

**FATIGUE CRACK GROWTH IN COMPLEX  
RESIDUAL STRESS FIELDS DUE TO SURFACE  
TREATMENT AND FOREIGN OBJECT DAMAGE  
UNDER SIMULATED FLIGHT CYCLES**

A thesis submitted to the University of Manchester for the degree of  
Doctorate of Philosophy in the Faculty of Engineering and Physical  
Sciences

**February 2012**

**Suraiya Zabeen**

**School of Materials**

## TABLE OF CONTENTS

<b>TABLE OF CONTENTS .....</b>	<b>2</b>
<b>Number of words: 43024 .....</b>	<b>4</b>
<b>List of Figures.....</b>	<b>5</b>
<b>List of Tables .....</b>	<b>17</b>
<b>Abstract.....</b>	<b>18</b>
<b>Declaration .....</b>	<b>19</b>
<b>Copyright Statement.....</b>	<b>19</b>
<b>Acknowledgements.....</b>	<b>20</b>
<b>Chapter 1 Introduction .....</b>	<b>23</b>
<b>Chapter 2 Background and Literature Review .....</b>	<b>26</b>
<b>2.1 Materials.....</b>	<b>26</b>
2.1.1 General Properties .....	26
2.1.2 Processing route and Microstructure .....	26
<b>2.2 Residual Stresses and their Measurement Techniques.....</b>	<b>28</b>
2.2.1 Residual Stress .....	28
2.2.2 Non-Destructive Measurement Techniques .....	29
2.2.3 Destructive Methods.....	36
2.2.4 Other Techniques .....	38
<b>2.3 Fatigue crack growth behaviour .....</b>	<b>39</b>
<b>2.4 Effect of residual stresses on fatigue crack growth .....</b>	<b>41</b>
<b>2.5 Foreign object damage and fatigue Life .....</b>	<b>42</b>
2.5.1 Residual stress distribution due to FOD .....	43
2.5.2 Effect of FOD induced Residual Stress on the fatigue life .....	47
2.5.3 Fatigue life reduction due to cyclic loading.....	50
<b>2.6 Mechanical Surface Treatment.....</b>	<b>56</b>
2.6.1 Laser Shock Peening (LSP) .....	57
2.6.2 Comparison between SP, LSP AND LPB .....	71
<b>2.7 Fatigue life assessment under LSP+FOD.....</b>	<b>75</b>
<b>Chapter 3 Experimental Method .....</b>	<b>81</b>

<b>3.1</b>	<b>Material and Specimen Geometry .....</b>	<b>81</b>
<b>3.2</b>	<b>Laser Shock Peening (LSP) Process .....</b>	<b>83</b>
<b>3.3</b>	<b>Simulation of Foreign Object Damage (FOD) .....</b>	<b>83</b>
<b>3.4</b>	<b>Fatigue Testing.....</b>	<b>85</b>
<b>3.5</b>	<b>Specimen Studied .....</b>	<b>87</b>
<b>3.6</b>	<b>Residual Stress Measurement Techniques .....</b>	<b>90</b>
3.6.1	Through thickness averaged Synchrotron X-ray Measurements.....	90
3.6.2	Depth Resolved Synchrotron X-ray Measurements on ID 31 .....	104
3.6.3	Contour Method .....	109
<b>Chapter 4</b>	<b>Results and Discussions .....</b>	<b>110</b>
<b>4.1</b>	<b>FOD damage Characterization.....</b>	<b>110</b>
<b>4.2</b>	<b>Residual stresses state in as-peened condition.....</b>	<b>114</b>
<b>4.3</b>	<b>Residual stress distribution in 0° and 45° Impact.....</b>	<b>116</b>
4.3.1	Through Thickness Transmission Measurements .....	116
4.3.2	Depth-Resolved Transmission Measurements .....	122
4.3.3	Contour Method Results and Comparison with the Synchrotron Results.	123
4.3.4	Summary.....	126
<b>4.4</b>	<b>Residual Strain relaxation behaviour under cyclic loading.....</b>	<b>127</b>
4.4.1	Effect of solely Low Cycle Fatigue on RS relaxation.....	127
4.4.2	Effect of Combined Cycle Fatigue on RS Relaxation.....	133
4.4.3	Discussion: CCF vs. LCF.....	137
4.4.4	Summary.....	141
<b>4.5</b>	<b>Fatigue crack growth behaviour in a residual stress field .....</b>	<b>142</b>
4.5.1	Effect of Low Cycle Fatigue Crack Growth on relaxation.....	142
4.5.2	Effect of Crack Growth under Combined Cycle Fatigue on relaxation .....	155
4.5.3	Summary.....	177
<b>4.6</b>	<b>FCG rate prediction.....</b>	<b>178</b>
4.6.1	Determination of stress intensity factor due to residual stress.....	178
4.6.2	Analytical model for FCG rate prediction.....	186
4.6.3	Comparison between predicted and experimental FCG rates .....	188
4.6.4	Summary.....	194
<b>4.7</b>	<b>Plastic Zone and Residual Stress Interactions .....</b>	<b>195</b>
4.7.1	Summary.....	202
<b>Chapter 5</b>	<b>Conclusions.....</b>	<b>203</b>
<b>Future Work</b>	<b>.....</b>	<b>207</b>

<b>REFERENCES .....</b>	<b>210</b>
<b>APPENDIX-II .....</b>	<b>226</b>
<b>APPENDIX-III.....</b>	<b>227</b>

**Number of words: 43319**

## List of Figures

Figure 2.1: Processing route for bi modal microstructure (schematically) (Sauer & Lutjering 2001).....	27
Figure 2.2: Ti-6Al-4V microstructure after $\alpha+\beta$ recrystallisation processing typical of aero-engine fan blade (Peters and Ritchie, 2000).....	28
Figure 2.3: Schematic representation of different type of residual macro and microstresses, where the process (source of RS) is shown on the left, the misfit in the centre and corresponding residual stress on the right hand side for each case (Withers & Bhadeshia 2001). ....	29
Figure 2.4: (a) Schematic illustration of the $\sin^2\psi$ technique. Only crystal planes perpendicular to the dashed line will diffract at a given $\psi$ angle (Withers 2007). (b) Lattice spacing ( $a_\psi$ ) is plotted as a function of $\sin^2\psi$ for TiAlN coating deposited on TS, HSS and WC-Co, the gradient of the linear curve determines residual stress inside the coating (Falub et al 2007), and (c) In-depth residual stress profile for as peened Udimet 720Li Ni superalloy and three conditions of thermal exposure measured by x-ray $\sin^2\psi$ method combined with layer removal (Kim et al 2005).....	32
Figure 2.5: Different types of $d$ versus $\sin^2\psi$ plots for (a) ideal biaxial stress state (b) in the presence of shear stress and (c) material with textured structure (Noyan & Cohen 1987). ....	33
Figure 2.6: Schematic representation of synchrotron measurement geometries: (a) $2\theta$ scanning; (b) low angle transmission; (c) white beam energy dispersive (Withers & Bhadeshia 2001). ....	35
Figure 2.7: Schematic representation of the principle of contour method, (a) The component with significant residual stress is cut into two halves, (b) RS is relaxed and the contour of the newly created surface deviate from planarity and (c) deformed contour is pushed into plane surface using FEM and stress is calculated by the post-processing of the result (Prime 2001).....	37

Figure 2.8: Schematic illustration of the three stages of fatigue crack growth (Dieter 1986) .....	40
Figure 2.9: Influence of (a) residual stress on the total stress and (b) stress intensity factor under combined cycle (Oakley & Nowell 2007). .....	41
Figure 2.10: General distribution of the hoop component of the residual stress, $\sigma_{\theta\theta}$ as found by experimental and numerical analysis around the FOD site (Boyce et al 2001). .....	44
Figure 2.11: Comparison of the residual strain distribution generated by a spherical impact between synchrotron X-ray diffraction and FEM in the hoop ( $\epsilon_{\theta\theta}$ ), radial ( $\epsilon_{rr}$ ) and surface normal ( $\epsilon_{zz}$ ) directions as a function of distance from the crater rim (Boyce et al 2001).....	44
Figure 2.12: (a) Elastic residual strain profiles around an FOD impact measured by high energy synchrotron X-ray Diffraction (left), and predicted strain profile (right), (b) Sample geometry showing the measurement plane and directions (Frankel 2009). .....	46
Figure 2.13 (a) Measured FWHM and (b) predicted plastic strain profiles (Frankel 2009). .....	46
Figure 2.14: Fracture surfaces after FOD and FOD+SR showing the effect of residual stress on fatigue. The FOD was created by firing 3 mm hardened steel cube at 200 m/s. (Ding et al 2007). .....	47
Figure 2.15: SEM image showing subsurface fatigue crack initiation. Sample had a leading edge radius of 0.38mm and FOD'd at 0° angle (Ruschau et al 2001). ...	48
Figure 2.16: Fatigue debit due to FOD in Ti-6Al-4V, compared with results from smooth bar samples (Peters & Ritchie 2000). .....	49
Figure 2.17: Comparison of experimental and predicted HCF threshold with or without considering residual stress (Oakley & Nowell 2007) .....	50
Figure 2.18: SEM and optical images of a simulated FOD damage, (a) across the section AA' and (b) across the section BB' (Ding et al 2007). .....	51

Figure 2.19: Effect of FOD damage depth on the HCF fatigue strength (Mall et al 2001). .....	53
Figure 2.20: Variation of normalised fatigue strength with damage depth produced by (a) 1.33 mm (b) 2.0 mm and (c) 0.5 mm diameter indents (Ruschau et al 2003). .....	54
Figure 2.21: Influence of impact angle on the fatigue strength of Ti-6Al 4V alloy for two stress ratios (Ruschau et al 1999). .....	55
Figure 2.22: Variation of normalised fatigue strength of Ti-6Al-4V with the impact velocity (Bache et al 2002) .....	55
Figure 2.23: Effect of impact velocity on the fatigue strength of Ti-6Al-4V ally at room temperature and 350°C (Bache et al 2003). .....	56
Figure 2.24: Laser system used for LSP treatment by MIC and LLNL (Hammersley et al 2000). .....	58
Figure 2.25: Schematic representation of the LSP process (Clauer 1996). .....	60
Figure 2.26: In-depth residual stress profile for 7075-T6 and 2024-T351 aluminium alloy (Clauer 1996). .....	61
Figure 2.27: Effect of using absorbent coating on the average surface residual stress of LSP treated 55C1 steel (Peyre et al 1998). .....	62
Figure 2.28: In-depth residual stress increases with power density but surface residual stress decreases by 100 MPa when power density is increased to 3 GW/cm <sup>2</sup> , as found for laser treated aluminium alloy A356. ....	63
Figure 2.29: Effect of laser power density on the fatigue life of LSP treated 7050 aluminium alloy under a maximum load of 390 MPa. Higher power density can reduce the fatigue life similar to the untreated sample (Liu et al 2007). .....	63
Figure 2.30: Effect of using multiple laser shot on the residual compressive stress in Ti-6Al-4V alloy (Dane et al 1998). .....	64

Figure 2.31: (a) Variation of surface residual stress with power density showing the effect of number of impacts, (b) Effect of shot impacts on the residual stress as a function of depth (Peyre et al 1996)..... 65

Figure 2.32: Influence of overlapping on the superficial residual stress state in 0.55% C steel (Masse & Barreau 1995)..... 65

Figure 2.33: Residual stress profile (in 2D) with 10% overlapping, showing LSP generated deep compressive stress layer at both top and bottom surfaces (Johnson et al 2005b)..... 66

Figure 2.34: Distribution of residual stress and the degree of cold working in Ti-6Al 4V after SP, Gravity peened, LSP and LPB treatments (Prev y et al 2001).... 68

Figure 2.35: Residual stress profile as a function of depth at a distance of (a) 0.5 mm and (b) 5 mm from leading edge (Ruschau et al 1999)..... 68

Figure 2.36: In-depth residual stress profile of LSP+SP treated Ti-6Al-4V samples at radial , axial and out of plane direction (King 2005)..... 69

Figure 2.37: Residual stress distribution due to LSP treatment in a leading edge specimen. Comparison between synchrotron X-ray diffraction and the contour method (Frankel 2009)..... 70

Figure 2.38: In-depth profiles for LSP treated Ti-6Al-4V at ambient temperature to show the effect of fatigue cycling (a) residual stress and (b) FWHM (Nalla et al 2003)..... 71

Figure 2.39: Comparison of residual stress and the degree of cold working in IN 718 following SP, LSP and LPB treatments (Zhuang and Halford 2001)..... 72

Figure 2.40: Effect surface treatment (LSP and SP) on the fatigue strength of notched and FOD'd Ti-6Al-4V simulated leading edge sample at R=0.1 and 0.8 (Ruschau et al 1999) ..... 74

Figure 2.41: Comparison of the High cycle fatigue behaviour in presence of FOD damage between laser shock peening and shot peening (Hammersley et al 2000). ..... 75

Figure 2.42: Fatigue limit stresses for 0° (with and without peening) and 45° FOD impacted specimen (with peening only) under LCF, HCF and combined cycle (LCF+HCF) fatigue. The corresponding notch depths are shown in the secondary Y-axis (Spanrad 2011). ..... 76

Figure 2.43: Fatigue crack growth rate as a function of crack length for 0 and 45° FOD impact with prior peening and 0° FOD without peening under (a) LCF cycles at R=0.1, (b) HCF cycles at R=0.7 and (c) CCF at R=0.1 and 0.7 and 1000 HCF cycles were incorporated on to 1 LCF cycle (Spanrad 2011). ..... 78

Figure 2.44: Variation of fatigue crack growth rate as a function of stress intensity factor range calculated with a standard single edge crack solution under: (a) LCF cycles at R=0.1, (b) HCF cycles at R=0.7 and (c) CCF at R=0.1 and 0.7 and 1000 HCF cycles were incorporated on to 1 LCF cycle (Spanrad 2011). 80

Figure 3.1: As-received microstructure of bimodal Ti-6Al-4V..... 81

Figure 3.2: (a) Laser shock peened four-point bend (4PB) simulated aerofoil specimen geometry (all dimensions are given in mm), where X and Y represent transverse and longitudinal directions respectively (b) Schematic of 0° and 45° FOD impact, shown on the cross-section of the sample along the mid XZ plane (c) a photograph of the specimen. .... 82

Figure 3.3: Schematic of the gas gun used to simulate FOD at Oxford University, UK (Nowell 2008) ..... 84

Figure 3.4: Schematic representation of the (a) 0° and 45° impact condition, (b) notch depth, d for a 0° impact and (c) notch depths for an asymmetric 45° impact..... 85

Figure 3.5: Schematic representation of (a) LCF, (b) HCF and (c) combined cycle fatigue (CCF) (Ding et al 2007). ..... 86

Figure 3.6: (a) Through thickness transmission experiment set up in 1-ID-C beamline at APS, Chicago, USA. The monochromator was selected to choose an energy of 65 keV or a wavelength of 0.1907Å..... 94

Figure 3.7: Scanning schedule for mapping 2D strain profiles in through thickness transmission. The blue rectangle represents the modified scanning arrangements used to save measurement time..... 96

Figure 3.8: A typical synchrotron run showing the DORIS beam current [mA] and beam lifetime [1/h] ..... 98

Figure 3.9: Experimental setup for thorough thickness transmission strain scanning of simulated leading edge Ti-6Al-4V sample on HARWI II beamline. 100

Figure 3.10: Comparison of the brilliance of various 3<sup>rd</sup> generation high-energy synchrotron radiation sources (Schell 2010)..... 103

Figure 3.11: Experimental setup for thorough thickness transmission strain mapping of simulated leading edge Ti-6Al-4V specimens at HEMS beamline at Petra III, Hamburg, Germany. .... 104

Figure 3.12: Experimental arrangement for depth resolved residual elastic strain scanning of FOD'd leading edge aerofoil specimens on Id-31 at ESRF..... 106

Figure 3.13: Schematic of gauge volume for depth resolved synchrotron measurement on ID 31. The monochromatic X-ray beam with energy of 51.8 keV was passed through a slit of  $0.4 \times 0.05 \text{ mm}^2$ . The diffracted beam was also passed through another slit of the same size before entering the detector at an angle  $2\theta=8.2^\circ$ . This setup resulted in a gauge volume of  $0.9 \times 0.4 \times 0.05 \text{ mm}^3$ . .... 107

Figure 3.14: Cross section of the sample leading edge, showing three lines of diffraction measurement points. The diamonds represent the centroid of the gauge volume used, and indicate the measurement locations and shape..... 108

Figure 4.1: Secondary Electron SEM images of the side view of (a)  $0^\circ$  FOD and (b)  $45^\circ$  FOD and top view of (c)  $0^\circ$  FOD and (d)  $45^\circ$  FOD showing the impact direction, exit and entry side for  $45^\circ$  FOD, loss of material and material pile up. Figure (c) also delineates the ❶ shallow, ❷ middle and ❸ deeper notch side in a  $45^\circ$  FOD..... 111

Figure 4.2: SEM images showing (a) material folding (b) material shear (c) microcracks and..... 112

Figure 4.3: (a) SEM image for a 0 degree impact (specimen S-1) taken from the cross-section at distance of 1 mm from the root of the notch, shows no drastic change of microstructure due to plastic deformation associated to FOD at the base of the impact crater. .... 113

Figure 4.4: The through-thickness averaged (at APS) and depth resolved (at ESRF) residual (a) strain and (b) stress profile in longitudinal and transverse directions in as-peened condition. .... 115

Figure 4.5: Through thickness averaged residual elastic strain map parallel to the leading edge in as FOD'd condition (a) for a 0° FOD impact with a damage depth of 1.5 mm (specimen S-1, see Table 3-2), (b) for 45° FOD with a damage depth of 0.82 mm (specimen S-7, see Table 3-3; in (b) residual strain data within 0.8 mm of the LE are discarded due to experimental error. .... 118

Figure 4.6: Residual elastic strain map normal to the leading edge in as FOD'd condition (a) for a 0° FOD impact with a damage depth of 1.5 mm (Specimen S-1) (b) for 45° FOD with a damage depth of 0.82 mm (Specimen S-7). .... 119

Figure 4.7: Longitudinal residual elastic stress maps calculated for Figure 4.5 and Figure 4.6 based on plane stress assumption, in as FOD'd condition for (a) 0° and (b) for 45° FOD impact, in (b) residual stress data within 0.8 mm of the LE are discarded due to experimental error. .... 120

Figure 4.8: 2D contour plots of FWHM (Degree) for  $(10\bar{1}2)$  diffraction peak from Ti- $\alpha$  phase in longitudinal direction of the specimen: (a) 0° and (b) 45° impacts. .... 121

Figure 4.9: The synchrotron residual strain profile parallel to the leading edge generated in as-peened condition and after 45° FOD impact (Specimen S-7). The notch depth is 0.82 mm. .... 122

Figure 4.10: Comparison of FWHM between as-peened and 45° FOD impact (Specimen S-7). .... 122

Figure 4.11: Contour method results for normalised (with respect to the yield strength) longitudinal residual stress distribution along the line of the FOD notch (a) after LSP (Specimen S-1), and (b) after LSP + 0° FOD (Specimen S-1)..... 124

Figure 4.12: Comparison of residual stress distribution, in longitudinal direction parallel to the leading edge, between synchrotron and Contour method: (a) in as-peened condition and (b) after LSP +0° FOD. Both were done in specimen S-1. .... 125

Figure 4.13: The depth-resolved residual strain profiles along the notch centreline ( $y=0$ ), parallel to the leading edge generated for a 45° FOD impact after applying 1000 LCF cycles under a maximum applied stress,  $S_{max} = 521$  MPa. The depth at the centreline of the notch for this specimen (S-9) and as-FOD'd specimen (S-7) are 0.62 mm and 0.82 mm respectively. .... 129

Figure 4.14: The depth-resolved residual strain distribution parallel to the leading edge along the notch centreline ( $y=0$ ), generated for a 45° FOD impact (S-9), after applying an additional  $10^5$  LCF cycles under a maximum applied stress,  $S_{max} = 586$ MPa. The notch depth for this specimen (S-9) is 0.62 mm..... 129

Figure 4.15: SEM image of the specimen S-9 (after applying an additional  $10^5$  LCF cycles at,  $S_{max} = 586$ MPa) showing multiple crack formation at the base of the notch..... 130

Figure 4.16: The FWHM plot in longitudinal direction for S-9, after  $10^3$  LCF cycles under a maximum applied stress,  $S_{max}=521$  MPa. .... 132

Figure 4.17: The FWHM plot in the longitudinal direction for S-9, after applying  $10^5$  LCF cycles under a maximum applied stress,  $S_{max}=586$  MPa..... 132

Figure 4.18: Residual elastic strain (a) parallel and (b) normal to the leading edge for a 0° FOD impact followed by 1 combined fatigue loading blocks (CCF=LCF: HCF=1:1000,  $S_{max}=435$  MPa and  $R_{LCF} = 0.1$  and  $R_{HCF} = 0.7$ ). The notch depth for this sample (S-2) is 1.55mm. Measurement locations are indicated by (+)..... 135

Figure 4.19: Comparison of residual elastic strain profiles parallel to the leading edge at the notch centre-line ( $y=0$ ) for a  $0^\circ$  FOD impact followed by 1 and 100 combined fatigue loading blocks (CCF=LCF: HCF=1:1000,  $S_{max}=435$  MPa and  $R_{LCF} = 0.1$  and  $R_{HCF} = 0.7$ ). The notch depth for this sample (S-2) is 1.55mm. .... 136

Figure 4.20: Average FWHM (from  $(10\bar{1}2)$  diffraction peak acquired on 1-ID-C beamline at APS) plot for post FOD and fatigue at N=1 block for specimen S-2. .... 136

Figure 4.21: The synchrotron residual strain profiles parallel to the L.E. generated for a  $45^\circ$  FOD impact after subjecting combined (LCF+HCF) fatigue cycles, N= 100 blocks, under  $S_{max}=430$  MPa. The notch depth for this specimen (S-8) is 0.78mm. The results are also compared with the residual strains in the as-FOD'd specimen (S-7)..... 138

Figure 4.22: The synchrotron residual strain profiles parallel to the L.E. generated for a  $45^\circ$  FOD impact after applying combined (LCF+HCF) fatigue cycles, N = 10 blocks, under  $S_{max} = 586$  MPa. The notch depth for this specimen (S-7) is 0.82 mm..... 138

Figure 4.23: The FWHM plot for S-8 in longitudinal direction, followed by combined (LCF+HCF) fatigue cycles, N= 100 blocks, under  $S_{max}=430$  MPa. .... 140

Figure 4.24: The FWHM plot for S-7 in longitudinal direction, after applying combined (LCF+HCF) fatigue cycles, N= 10 blocks, under  $S_{max}=586$  MPa. .... 140

Figure 4.25: (a) Through thickness averaged 2D residual strain ( $\times 10^{-6}$ ) map measured at HARWII, for a  $0^\circ$  FOD impact. The specimen (S-5) had a notch depth of 1.5 mm and a 0.56 mm crack was grown by applying low fatigue cycles of  $n= 20272$  using an applied stress of  $S_{max}=586$  MPa (Table 3-2)..... 143

Figure 4.26 (a): Through thickness averaged residual strain profiles, parallel to the leading edge generated for a  $0^\circ$  FOD impact after applying LCF fatigue cycles,  $n= 34300$  cycles, under  $S_{max}=586$  MPa. The notch depth for this specimen (S-6) is 0.78mm and  $\Delta a=5.3$ mm (Table 3-2)..... 147

Figure 4.27: (a) Effect of crack growth on relaxation under low fatigue cycles, when the crack length  $\Delta a=0.5$  (S-5), and 5.3mm under  $S_{max}=586$  MPa (S-6). The average notch depth is 1.5 mm and (b) Comparison of FWHM between as-FOD'd condition and after 5.3 mm crack (Table 3-2)..... 150

Figure 4.28 (a): Through thickness averaged 2D residual strain map measured on HEMS beamline, for a 45° FOD impact. The specimen (S-10) had a notch depth of 0.82mm and a 2.2 mm long crack was grown by applying LCF cycles of  $n=59641$  cycles and with a applied stress of  $S_{max}=586$  MPa (Table 3-3)..... 152

**Figure 4.29: (a)** A line plot of the longitudinal RS along the notch centerline for specimen S-10 with  $\Delta a = 2.2$  mm crack after 59641 LCF cycles at  $S_{max}=586$  MPa and (b) the corresponding FWHM plot. .... 154

Figure 4.30: Longitudinal depth resolved synchrotron residual strain profiles at a location of  $y=0$ , generated for 0° FOD impacts under combined (LCF+HCF) fatigue cycles at  $S_{max}=434$  MPa: (a) with a 0.7 mm crack after  $N= 1901$  blocks (S-2) and (b) with a 0.6 mm long crack after  $N= 2744$  blocks (S-3). The notch depths for specimen S-2 and S-3 are 1.55 mm and 1.49 mm respectively..... 156

Figure 4.31: FWHM plots in longitudinal directions for (a) specimen S-2 with  $\Delta a=0.7$  mm and (b) specimen S-3 with  $\Delta a=0.6$  mm ..... 157

Figure 4.32: SEM image for a 0° FOD impacted specimen (S-2) showing the actual direction of crack growth and the residual strain measurement line along notch centreline. Here the crack length,  $\Delta a=0.7$ mm..... 158

Figure 4.33: Through thickness averaged 2D residual strain map for a 0° FOD impact. The specimen (S-3) had a notch depth of 1.5mm..... 162

Figure 4.34: An SEM image showing the crack initiation and propagation under LCF + HCF loading in a 0° impacted specimen ( S-3)..... 166

Figure 4.35: Comparison of longitudinal residual strain variation, for a 0° FOD impact, under combined (LCF+HCF) fatigue cycles, at  $N= 1$  and 100 blocks (with no detectable cracks), and  $\Delta a=0.7$ mm under  $S_{max}=434$ MPa. The notch depth for this specimen (S-2) is 1.5mm..... 168

Figure 4.36: Effect of crack growth on relaxation under combined (LCF+HCF) fatigue cycles, when the crack length  $\Delta a=0.6, 1$  and  $2.1\text{mm}$  under  $S_{\text{max}}=434\text{MPa}$ . The notch depth for this specimen (S-3) is  $1.5\text{mm}$ . ..... 168

Figure 4.37: The synchrotron residual strain profiles, parallel to the leading edge generated for a  $45^\circ$  FOD impact after applying combined (LCF+HCF) fatigue cycles of  $N= 589$  blocks, under  $S_{\text{max}}=452\text{ MPa}$ . The notch depth for this specimen (S-12) is  $0.78\text{mm}$  and  $\Delta a=0.6\text{mm}$ : (a) RS variation along the thickness (b) comparison with the as-FOD'd condition. .... 170

Figure 4.38: (c) FWHM plot for specimen S-12 with  $\Delta a=0.6\text{ mm}$ . ..... 171

Figure 4.39: (a) The synchrotron residual strain profiles parallel to the leading edge generated for a  $45^\circ$  FOD impact after applying combined (LCF+HCF) fatigue cycles,  $N= 1439$  blocks, under  $S_{\text{max}}=430\text{ MPa}$ . The notch depth for this specimen (S-8) is  $0.78\text{mm}$  and  $\Delta a=2\text{ mm}$  and (b) the corresponding FWHM plot. .... 172

Figure 4.40: SEM image for a  $45^\circ$  impact containing  $2\text{ mm}$  long crack. The residual strains were measured along the white line and crack growth occurred along the black line which is deviated by an angle of  $20^\circ$  from the notch centreline. .... 173

Figure 4.41: (a) Longitudinal depth resolved residual strain profiles, generated for a  $45^\circ$  FOD impact after applying combined (LCF+HCF) fatigue cycles,  $N= 1262$  blocks, under  $S_{\text{max}}=434\text{ MPa}$ . The notch depth for this specimen (S-11) is  $0.78\text{mm}$  and  $\Delta a=7\text{mm}$  and (b) the corresponding FWHM plot. .... 174

Figure 4.42: SEM image for a  $45^\circ$  FOD impact with a  $7\text{ mm}$  crack showing residual stress measurement location and the crack path. .... 175

Figure 4.43: Longitudinal residual stress distribution for  $0^\circ$  and  $45^\circ$  impacts.. 180

Figure 4.44: Nominally applied maximum stress intensity factor,  $K_{\text{max}}$  with and without considering the shape function (S.F.), calculated for a typical applied stress of  $S_{\text{max}} = 435\text{ MPa}$ , and the variation of calculated  $K_{\text{res}}$  as a function of crack length for  $0^\circ$  and  $45^\circ$  FOD impact. .... 181

Figure 4.45: Determination of residual stress intensity factor range : (a) no residual stress. (b) when  $K_{min}+K_{res} > 0$  and (c) when  $K_{min}+K_{res} < 0$ ..... 182

Figure 4.46: Variation of the effective stress intensity factor range,  $\Delta K_{eff}$  as a function of crack length at  $R=0.1$  (LCF) and  $R=0.7$  (HCF) for (a) for  $0^\circ$  impact and (b)  $45^\circ$  impact..... 184

Figure 4.47: Effective R ratio as a function of crack length for LCF and HCF separately in a CCF block under  $S_{max} = 435$ , and also for solely LCF under  $S_{max} 586\text{MPa}$  for (a)  $0^\circ$  and (b)  $45^\circ$  impact..... 185

Figure 4.48: Variation of experimentally obtained Paris constant C with R ratio and the data fit to calculate the new constant  $C^*$  that is independent of R ratio. .... 188

Figure 4.49: Comparison of the predicted and experimental fatigue crack growth rate as a function of crack length for (a)  $0^\circ$  and (b)  $45^\circ$  FOD under and applied stress of  $S_{max}=586$  MPa in LCF loading. .... 190

Figure 4.50: Comparison of the predicted and experimental FCG rate as a function of crack length for (a)  $0^\circ$  and (b)  $45^\circ$  FOD under and applied stress of  $S_{max}=435$  MPa in CCF. .... 192

Figure 4.51: (a) Estimated variation of  $K_{max}$  and corresponding plastic zone size with crack length and (b) Forward and reverse plastic zone for both  $0^\circ$  and  $45^\circ$  impact, found using Equation 4-13 for CCF loading condition at  $S_{max} =435$  MPa . .... 198

Figure 4.52: SEM image showing the plastic zone ahead of the crack tip for an overloaded specimen (S-4,  $S_{max}>860\text{MPa}$ ) and heavily plastically deformed region at the crack tip and also at either side of the crack..... 200

Figure 4.53: (a) Longitudinal residual strain distribution for overloaded specimen (S-4,  $S_{max}>860\text{MPa}$ ) (b) corresponding FWHM showing high degree of plastic work around the cracked region. The X and Y axis represents the distance along the L.E. and from the L.E. respectively. .... 201

## List of Tables

Table 3-1: The chemical composition of Ti-6Al-4V alloy (in wt. %).....	82
Table 3-2 0° FOD specimens characterized at various synchrotron radiation sources.....	88
Table 3-3: 45° FOD specimens characterized at various synchrotron radiation sources.....	89
Table 3-4: The key parameters in four different synchrotron radiation source used in this study. ....	91
Table 4-1: Residual stress relaxation due to crack growth under LCF.....	146
Table 4-2: Residual stress relaxation due to crack growth under CCF.....	161
Table 4-3: Benchmark data for of the Paris Constant C with R ratio for Ti-6Al-4V of leading edge microstructure (Schofield 2011).....	187

## Abstract

**Abstract of the thesis is submitted by Suraiya Zabeen for the Degree of Philosophy entitled Fatigue Crack Growth in Complex Residual Stress Field due to Surface Treatment and Foreign Object Damage under Simulated Flight Cycles.**

**The University of Manchester**

**February 2012**

Foreign object damage (FOD) refers to the damage that generally takes place in aero engine fans and compressor blades, due to the ingestion of hard particles/debris during aeroplane take-off, taxiing, or landing. Such damage can reduce the fatigue life expectancy of the turbine engine components by 50%. Residual stresses and small microcracks induced by the high speed FOD impacts are two root causes that result in premature failure of these components. One way to mitigate the FOD related fatigue failure is to induce deep compressive residual stress into the surface. Among the available techniques that can induce such compressive residual stress, laser shock peening (LSP) has been found to be beneficial in improving the fatigue strength.

In this study aerofoil-shaped Ti-6Al-4V leading edge specimens were laser shock peened. Subsequently, FOD was introduced onto the leading edge specimen through ballistic impacts of a cube edge at angles of  $0^\circ$  and  $45^\circ$  to the leading edge. The effect of foreign object damage (FOD) on the pre-existing compressive residual stress field associated with the laser shock peening (LSP), and its change upon solely low cycle fatigue (LCF) as well as combined low and high cycle fatigue cycling has been studied. The residual stress distribution and their redistribution upon fatigue cycling were mapped around the FOD notch, using synchrotron X-ray radiation and the contour method.

The results suggest that under both impact angles, the FOD event superimposed a significant additional residual stress on top of the pre-existing stress associated with the LSP process. It has been observed that the FOD notch created by  $45^\circ$  impact was asymmetric in shape, and had differential notch depth between the entry and exit side. However, FOD damage that is created at  $0^\circ$  impact appeared as a sharp V notch. A higher amount of residual stresses were produced under  $0^\circ$  impact condition than at  $45^\circ$ . It has been found even though the FOD induced residual stresses relax, residual stresses due to LSP treatment remain highly stable even in the worst condition where a 7 mm long crack was grown from a  $45^\circ$  notch. The plastic zone sizes ahead of a crack tip was estimated for both  $0^\circ$  and  $45^\circ$  FOD impact, and the fatigue crack growth rates are predicted utilizing the measured residual stress distribution.

## Declaration

No portion of the work referred to in this thesis has been submitted in support of an application for another degree or qualification of this or any other university or other institute of learning.

## Copyright Statement

- i.** The author of this thesis (including any appendices and/or schedules to this thesis) owns certain copyright or related rights in it (the “Copyright”) and s/he has given The University of Manchester certain rights to use such Copyright, including for administrative purposes.
- ii.** Copies of this thesis, either in full or in extracts and whether in hard or electronic copy, may be made **only** in accordance with the Copyright, Designs and Patents Act 1988 (as amended) and regulations issued under it or, where appropriate, in accordance with licensing agreements which the University has from time to time. This page must form part of any such copies made.
- iii.** The ownership of certain Copyright, patents, designs, trade marks and other intellectual property (the “Intellectual Property”) and any reproductions of copyright works in the thesis, for example graphs and tables (“Reproductions”), which may be described in this thesis, may not be owned by the author and may be owned by third parties. Such Intellectual Property and Reproductions cannot and must not be made available for use without the prior written permission of the owner(s) of the relevant Intellectual Property and/or Reproductions.
- iv.** Further information on the conditions under which disclosure, publication and commercialisation of this thesis, the Copyright and any Intellectual Property and/or Reproductions described in it may take place is available in the University IP Policy (see <http://www.campus.manchester.ac.uk/medialibrary/policies/intellectual-property.pdf>), in any relevant Thesis restriction declarations deposited in the University Library, The University Library’s regulations (see <http://www.manchester.ac.uk/library/aboutus/regulations>) and in The University’s policy on presentation of Theses.

## Acknowledgements

First and foremost I would like to thank my supervisors Professor Philip Withers and Professor Michael Preuss for their invaluable advice, encouragement and support throughout this journey.

I would like to thank the Engineering and Physical Sciences Research Council (EPSRC) for financial support during my doctoral studies. Great thanks are extended to Rolls-Royce Plc for providing the specimens and technical assistance. Thanks are due to the institutions that allocated beamtime for this project: Advanced Photon Science (APS), Chicago, USA; HASYLAB of the DESY, Hamburg, Germany; PETRA III, DESY and also European synchrotron Radiation facility (ESRF), in Grenoble, France. Great thanks to all the scientists who supported me during these experiments.

I greatly acknowledge the help and support of Dr. Andy Fitch, the beamline scientist, ID 31, ESRF, without his help it would not be possible to generate the data presented in Section 4.5.2. Great thanks are extended to the following people for their substantial contribution to this research, be it technical support, discussion, or just supporting as a friend:

Dr Michael B. Prime

Dr. Andrew King

Dr. Darren Hughes

Dr Norbert Schell

Dr. Sam McDonald

Mr. Michael Faulkner

Dr. Bartlomiej Winiarski

Ms. Judith Shackleton

Dr. Andrew Winn

Dr. Chris Wilkins

Mr Kenneth Gyves

Dr. Kevin Tan

Dr. Philip Frankel

Dr. Richard Moat

Dr. Joe Kelleher

Dr. Kuvasani Govender

Dr. Leo Prakash

Dr. Alison Mark

Prof. Jie Tong

Dr. Sven Spanrad

Mr. Sanu Miah

Last, but not the least the continual inspiration and support of my family and friends are wholeheartedly and sincerely appreciated.

This Thesis is dedicated to my parents

## Chapter 1 Introduction

The structural integrity of aero engine components needs to be ascertained to ensure their safe and reliable operation, thereby avoiding any catastrophic failure. The aero engine system can fail from crack propagation, corrosion, fastener/bonding failure or any localized deformation over the plastic limit. Crack nucleation and propagation due to the application of repeated load cycles, well known as fatigue, is a well-established failure mechanism in engine components. Engine failures from high frequency vibratory loading cycles pose a critical challenge to both the military and civilian turbine engine sectors. This is why failure from high cycle fatigue (HCF) in combination with major loading cycles or low cycle fatigue (LCF), contact fatigue and foreign object damage (FOD) has been an increasing concern in the last half century.

Foreign object damage refers to the damage associated with the high speed impact of small, hard particles/debris during take-off, taxiing and landing of the aircraft. Such damage in the form of craters, nicks, dents, tears or gouges, can reduce the endurance strength by up to 50% (Nicholas 2006), and the number of cycles to failure at a given stress amplitude by several orders of magnitude. Naturally FOD damage tends to be especially severe for the low temperature (entry side) Ti alloy components of the aero engine.

Residual stresses are those stresses that can remain in the structure without any external applied load. These residual stresses are superimposed on the applied stress field, and can either reduce, or enhance, the fatigue life of the material depending on whether they are tensile or compressive in nature.

Based on this fact, one commonly employed means of increasing fatigue life is to introduce compressive residual stresses into the near surface region (Withers 2007). Among many other surface treatments, laser shock peening (LSP) has been shown to introduce compressive stresses to a much greater depth in Ti-6Al-4V alloy than conventional shot peening (King et al 2006, Nalla et al 2003). As a consequence it has been shown to be particularly beneficial in enhancing the fatigue resistance in the presence of FOD, (Ruschau et al 1999). Therefore,

knowledge of the residual stress and its effects in determining the fatigue life of aero engine components is critical.

It is well recognised that, FOD impact introduces significant amount of residual stresses, both compressive and tensile. The tensile residual stresses associated with FOD are one of the reasons for FOD related failure (Boyce et al 2001).

The beneficial effect from laser shock peening is mostly attributed to the compressive residual stress, therefore it is important to determine to which extent these compressive residual stresses are stable upon cyclic loading and crack growth under solely LCF and combined (LCF+HCF) cycle fatigue. The objective of this study is to address the following questions by experimentally measuring the residual stresses non-destructively using high energy synchrotron X-ray diffraction:

1. What is the residual stress distribution generated by the LSP treatment?
2. How does the FOD impact affects the original LSP'd residual stresses?  
Most importantly is there any tensile residual stress created by FOD ?
3. What is the effect of the impact angle on the residual stress field?
4. Are these residual stresses stable under cyclic loading?
5. How do the residual stresses redistribute upon fatigue crack growth under solely LCF and (LCF+HCF) loading conditions.
6. How the fatigue crack interacts with the residual stress?
7. Finally, how the residual stress results can be incorporated into the damage design practice to gain design credit? Can we predict the FCG rates using superposition principles?

## **Structure of the thesis**

Chapter 2 reviews various residual stress measurement techniques; laser shock peening (LSP) process and some published results on the measurement of residual stresses in LSP'd Ti-6AL-4V. This Chapter also discusses the previous work relating to as-FOD'd residual stresses and the effect of FOD in reducing the fatigue life of aerofoil components.

The experimental techniques used in this thesis are presented in Chapter 3. That includes through-thickness as well as depth-resolved transmission stress measurement techniques using constant wavelength synchrotron X-ray diffraction, and the contour method.

Chapter 4 presents the results and discussion in seven Sections comprising FOD damage characterizations, the residual stress distribution in as-peened condition and the re-distribution of these residual stresses upon FOD impact incident at two impact angles: 0° and 45°. Further, the relaxation of these beneficial residual stresses due to solely LCF and CCF types of fatigue loading and the fatigue crack growth behaviour in compressive residual stress field. Finally, predictions of the fatigue crack growth (FCG) rates employing the measured residual stresses are presented at the end of this Chapter.

An overview of the important conclusions drawn from this study, and some recommendations and suggestions for future work, are presented in Chapter 5 and Chapter 6 respectively.

## Chapter 2 Background and Literature Review

### 2.1 Materials

In this thesis, the fatigue life of LSP treated Ti-6Al-4V leading edge aerofoil samples are studied after subjecting them to simulated FOD damage. These samples are intended to replicate the leading edge of an aerofoil, both in terms of the through-thickness stress that can be imparted by peening treatments, and the fatigue crack growth response to applied cyclic loading. The processing method of Ti-6Al-4V including heat treatment conditions is elaborated in section 2.1.2.

#### 2.1.1 General Properties

The featuring properties of titanium base alloys are high specific strength, high specific modulus and good high-temperature capability. Ti- $\alpha$  has a high melting point, relatively low thermal conductivity and excellent resistance to corrosion even at temperatures up to 650°C (Polmear 1995). Two phase ( $\alpha + \beta$ ) Ti-6Al-4V is a widely used titanium alloy for aero engine compressor fan, blade, and aerofoil components. Ti-6Al-4V alloy shows a good creep resistance up to 350°C and so it can be used as an aerofoil material for static and rotating low-pressure compressor blades.

#### 2.1.2 Processing route and Microstructure

The microstructure and properties of Ti-6Al-4V alloy strongly depend on the processing parameters, which can lead to texture development resulting in anisotropic properties.

Four different types of thermo-mechanical routes are generally applied to Ti alloys:  $\beta$  annealing,  $\alpha + \beta$  recrystallisation,  $\beta$  processing, and through-transus processing to produce microstructures with various combinations of phases, enabling a wide range of useful properties. A bimodal microstructure is typically used for aero engine fan and blades, which is generally obtained through  $\alpha + \beta$  recrystallisation. Hence, this thermomechanical technique is discussed here briefly. Duplex or bimodal microstructures with equiaxed primary  $\alpha$  ( $\alpha_p$ ) and small recrystallised  $\beta$ -grains can be produced by this route. As shown schematically in Figure 2.1, processing steps consists of four distinct phases. Careful control of the process parameters is needed to

ensure optimum properties, as these have a significant influence in determining exact combination of phases.

The alloy is homogenised first above the  $\beta$  transus ( $996^{\circ}\text{C}$ ), which results in large equiaxed  $\beta$  grains, with both grain boundary  $\alpha$  and  $\alpha$ -plates within the  $\beta$  grains. In the second step, the alloy is heavily forged at  $938^{\circ}\text{C}$  and air cooled. Subsequently, the alloy is solution treated at about  $927^{\circ}\text{C}$  and air cooled. This is followed by a stress relieving heat treatment at  $705^{\circ}\text{C}$ . The final microstructure consists of primary  $\alpha_p$  phase surrounded by lamellar  $\alpha + \beta$  matrix. It should be noted here that the size and volume fraction of the  $\alpha_p$  phase controls the beta-grain growth by grain boundary pinning.

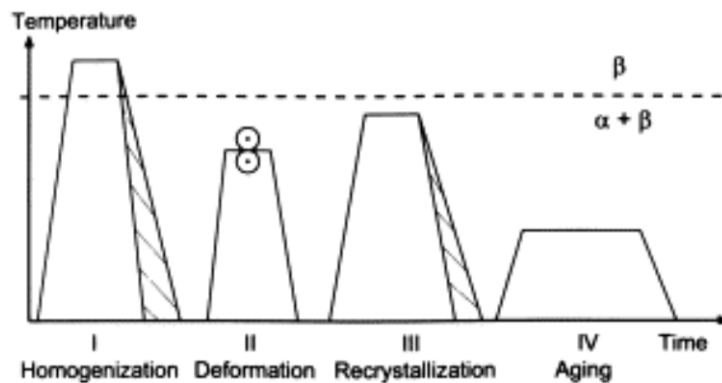


**Figure 2.1:** Processing route for bi modal microstructure (schematically) (Sauer & Lutjering 2001)

The primary  $\alpha_p$  grain size is about  $15\text{-}30\ \mu\text{m}$ . The  $\alpha_p$  volume fraction is reported as 50-60% (Sauer and Lutjering, 2001). This type of microstructure is also described as solution treated and overaged (STOA), Figure 2.2. (Peters and Ritchie, 2000).

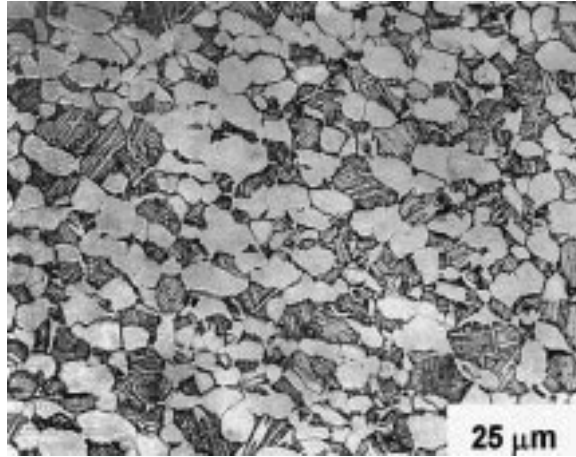


**Figure 2.2:** Ti-6Al-4V microstructure after  $\alpha + \beta$  recrystallisation processing typical of aero-engine fan blade (Peters and Ritchie, 2000).

## 2.2 Residual Stresses and their Measurement Techniques

### 2.2.1 Residual Stress

Residual stresses, which can be either compressive or tensile in nature, are those stresses that remain in the material without any external imposed load. These stresses are mainly generated in the body due to the mismatch associated with non-uniform plastic flow, steep thermal gradients and different types of phase transformation between regions of the material, component or assembly.

Depending on the scale over which they equilibrate, residual stresses are categorized into three different types (Macherauch & Kloss 1986) and shown in Figure 1 (Withers & Bhadeshia 2001).

**Type I** stresses are macroscopic, which are homogeneous over a length scale representative of the dimension of the material or component. These stresses can be alternatively called macrostress and denoted as  $\sigma^I$ . The net forces due to these stresses is balanced over a length scale representative of the dimension of the component itself.

**Type II** or intergranular stresses exist at the grain scale, and are generally present to some extent in all polycrystalline materials. This type of stress appears in the structure due to inhomogeneous plastic flow or thermal mismatch at the grain level, or the presence of more than one phase (precipitates) or phase transformation in the structure.

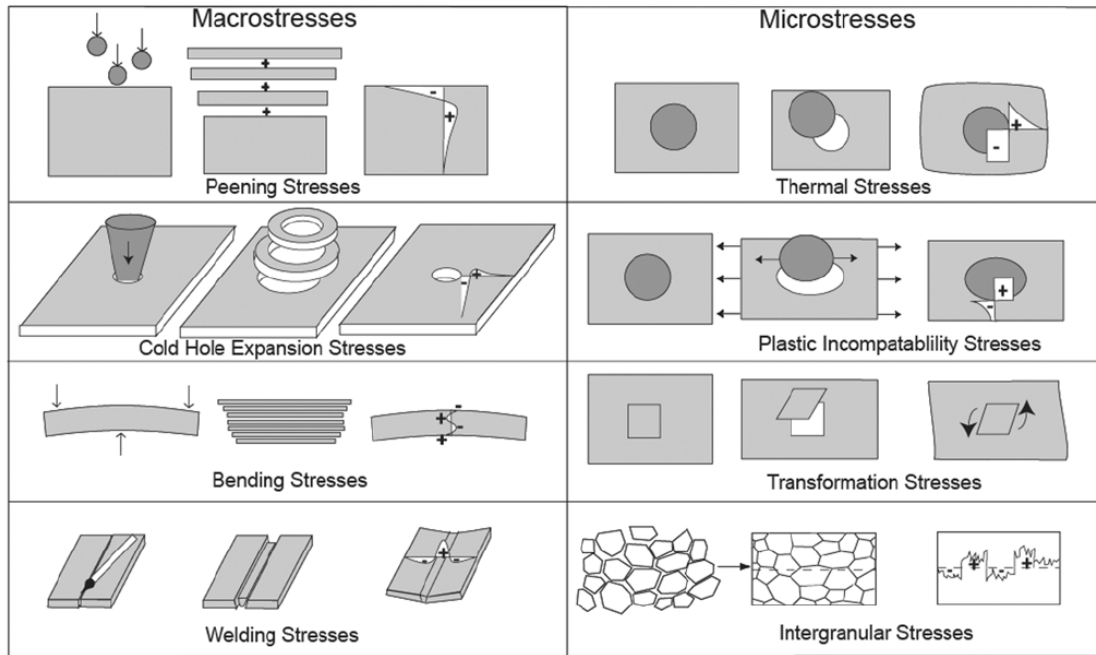


**Figure 2.3:** Schematic representation of different type of residual macro and micro stresses, where the process (source of RS) is shown on the left, the misfit in the centre and corresponding residual stress on the right hand side for each case (Withers & Bhadeshia 2001).

Many processing techniques introduce a significant amount of residual stress in the structure. Moreover, when these components are in use these existing residual stresses can be modified or new stresses can be created locally leading to premature or sometimes catastrophic failure of the parts. Therefore, it is important to measure the residual stress distribution accurately to predict the actual performance of a component. Both destructive and non-destructive methods are available for measuring residual stress as described in the following sections.

## 2.2.2 Non-Destructive Measurement Techniques

### 2.2.2.1 Diffraction Techniques

Among non-destructive techniques, diffraction is the most widely used and accurate method for quantifying residual stress fields within crystalline materials. Electron, X-ray photon and neutron beams are primary radiation sources for measuring the atomic lattice spacing. It is important to note here that the depth of penetration, spatial resolution and accuracy are the basic criteria to select a diffraction technique for characterising residual stress.

The principle of the diffraction technique is the same for each radiation source, and will be discussed before going into details of each diffraction technique.

#### 2.2.2.1.1 Bragg's law

Crystalline materials with periodic lattice structure can diffract an incident X-ray or neutron beam following Bragg's equation as given below:

$$d_{hkl} = \frac{\lambda}{2\sin\theta} \quad \text{Equation 2-1}$$

where  $d_{hkl}$  is the lattice spacing for a set of (hkl) planes in the lattice,  $\lambda$  is the wavelength of the incident beam and  $\theta$  is the diffraction angle associated with this set of (hkl) planes. Any deviation from the strain free lattice spacing or d-zero ( $d_{hkl}^0$ ), corresponds to elastic strain and is apparent as an angular shift ( $\Delta\theta$ ) in the diffraction peak position. It can be expressed as the following equation:

$$\varepsilon_{hkl} = \frac{d_{hkl} - d_{hkl}^0}{d_{hkl}} = -\cot\theta\Delta\theta \quad \text{Equation 2-2}$$

This elastic strain can then be directly converted to stress using appropriate elastic constants. Any plastic component of the strain does not modify the lattice spacing to a considerable extent, although it has a second order effect on the type II and type III (described in section 2.2) stress. However, besides stress, other factors such as local compositional change, geometrical effects or local change in temperature can result in variation in the measured strain (Withers et al 2007). Therefore, attention must be paid to these other possible sources of apparent strain during the measurement and analysis of the residual stress, and corrected for if necessary.

#### 2.2.2.1.2 Absorption of radiation

When any radiation is incident to a material surface, it can be absorbed depending on the material properties. As a result the intensity of the incoming radiation is reduced, affecting the maximum depth of penetration. If  $I_0$  is the initial intensity of an incident beam and  $I$  is the reduced intensity after travelling a distance  $x$  inside the material, then they can be related according to the equation (Cullity & Stock 2001):

$$I = I_0 \exp(-\mu x) \quad \text{Equation 2-3}$$

where,  $\mu$  is the linear absorption coefficient of the material for the type and wavelength of radiation in question.

### 2.2.2.1.3 Laboratory X-ray Diffraction

Laboratory X-Rays are produced when accelerated electrons with a very high velocity collide against a metallic target such as Cu, Mo, W *etc.* Two distinctive types of interaction occur between the accelerated electrons and target. When electrons hit the target they are rapidly decelerated, as a result energy with a range of wavelengths is emitted. This radiation is called continuous, white or bremsstrahlung radiation.

Additionally, when electrons interact with the target atom, radiation with wavelengths characteristic of the target metal is produced. Each shell of the atom (for example K, L, M *etc*) emits characteristic lines with a specific wavelength. All these lines form characteristic spectrum of the target metal (Cullity & Stock 2001). As a result of the electron bombardment a vacancy is created in the K shell, which is filled by an electron from any of the outer shells, thus giving rise to series of K lines.

Typically, only K lines are used in laboratory X-Ray diffraction as these have short wavelengths that are on the same scale as the (hkl) spacings in most metals, and thus generate diffraction peaks at convenient angles (Noyan & Cohen 1987). In addition, lines with longer-wavelength are more easily absorbed. Among the several lines in the K set, generally three strongest lines,  $K\alpha_1$ ,  $K\alpha_2$  and  $K\beta_1$  are used. In practice, the  $K\alpha_1$  and  $K\alpha_2$  lines may overlap to the point of being indistinguishable, and are referred to simply as the  $K\alpha$  line. In the case where only one line is to be used (such as  $K\alpha$ ), the X-Ray tube is operated above the K excitation voltage and a filter can be used to attenuate the  $K\beta$ .

### 2.2.2.1.4 $\sin^2\psi$ method

The history of the  $\sin^2\psi$  X-ray method for residual stress measurement is more than 80 years old (Lester & Aborn 1925). In this method, measurements are carried out over a range of inclination angles ( $\psi$ ) applying a very high scattering angle ( $2\theta$ ). By assuming a biaxial stress state under in-plane stress conditions, the lattice spacing ( $d_{\phi\psi}$ ) in a

given direction  $\phi\psi$  can be related to the principal stress by the following equation (Cullity & Stock 2001, Hauk 1997, Noyan & Cohen 1987):

$$\frac{d_{\phi\psi} - d_0}{d_0} = \varepsilon_{\phi\psi} = \left[ \left( \frac{1 + \nu}{E} \right)_{hkl} \sigma_{\phi} \sin^2 \psi \right] - \left[ \left( \frac{\nu}{E} \right)_{hkl} (\sigma_{11} + \sigma_{22}) \right] \quad \text{Equation 2-4}$$

If the above equation is rearranged and  $d_{\phi\psi}$  is plotted against  $\sin^2 \phi$  then the slope of the apparently linear curve gives a measure of the in-plane stress without using strain free lattice parameter,  $d_0$ , which is very difficult to measure directly. A practical example is given in

**Figure 2.4b** where this technique is exploited for TiAlN coating deposited on TS, HSS and WC-Co, and the lattice spacing ( $a_{\phi}$ ) is plotted against the  $\sin^2 \phi$  values; the gradient of the linear curve gives the residual stress present in the coating (Falub et al 2007).

This technique has also been used successfully to determine the residual stress relaxation in shot peened Ni superalloy,

**Figure 2.4c** (Kim et al 2005) and the residual stresses in laser shock peened Ti-6Al-4V alloy (Evans et al 2005).

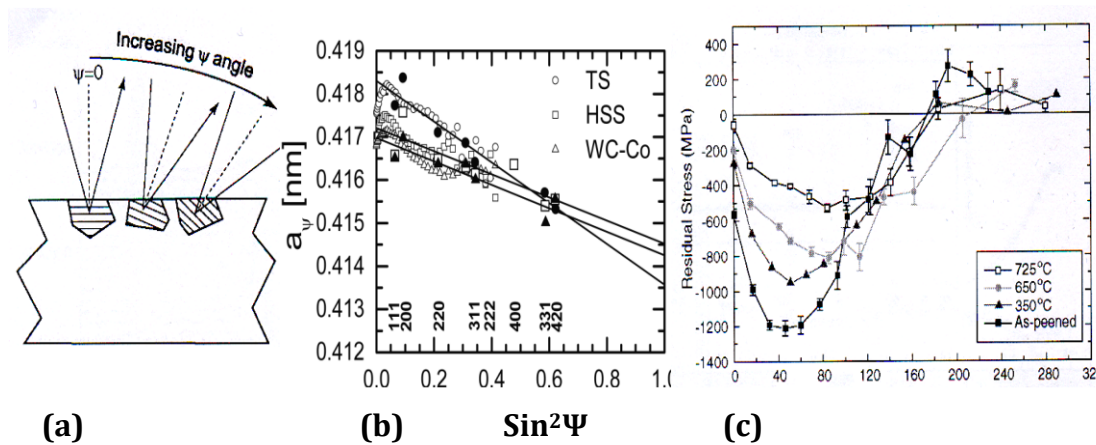
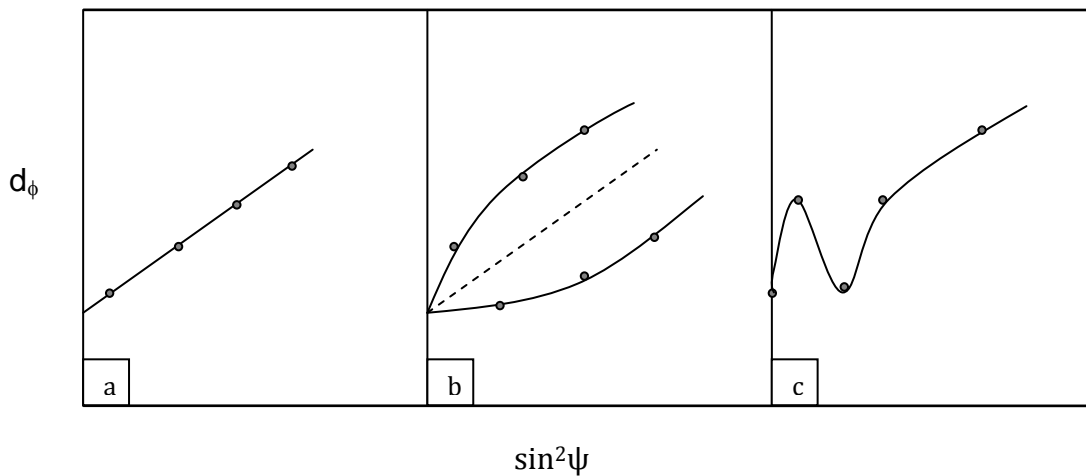


Figure 2.4: (a) Schematic illustration of the  $\sin^2 \psi$  technique. Only crystal planes perpendicular to the dashed line will diffract at a given  $\psi$  angle (Withers 2007). (b) Lattice spacing ( $a_{\phi}$ ) is plotted as a function of  $\sin^2 \psi$  for TiAlN coating deposited on TS, HSS and WC-Co, the gradient of the linear curve determines residual stress inside the coating (Falub et al 2007), and (c) In-depth residual stress profile for as peened Udimet 720Li Ni superalloy and three conditions of thermal exposure measured by x-ray  $\sin^2 \psi$  method combined with layer removal (Kim et al 2005).

It is important to note here that the linearity (as in Figure 2.5) of the  $d$  versus  $\sin^2 \psi$  curve may deviate due to (i) the presence of shear stress (curve will be split as in Figure 2.5b), (ii) the  $\psi$  angle of the diffractometer being misaligned during the measurement, (iii) preferred grain orientation (texture), as in Figure 2.5 and (iv) steep stress gradients, because increasing  $\psi$  angle decreases penetration depth, Figure 2.5 (Noyan & Cohen 1987).



**Figure 2.5:** Different types of  $d$  versus  $\sin^2 \psi$  plots for (a) ideal biaxial stress state (b) in the presence of shear stress and (c) material with textured structure (Noyan & Cohen 1987).

#### 2.2.2.1.5 High energy Synchrotron X-ray Diffraction

X-rays produced from a synchrotron source can offer a particularly high spatial resolution to resolve microstresses and deeper penetration compared to a laboratory X-Ray source. Synchrotron X-ray sources can produce photons with energies of more than 100 keV, which allows a larger depth of penetration to measure subsurface residual stress in the range of few mm to even few cm depending on the atomic number of the sample. For titanium, another benefit of using synchrotron X-Ray diffraction over neutron diffraction is a stronger diffracted beam.

There are two methods available for measuring residual strain using high energy synchrotron X-ray radiation. The first method is to acquire a single diffraction peak using monochromatic radiation, by measuring the diffracted beam intensity as a function of diffraction angle. A white X-ray beam incident on a double-bounce monochromator or focusing Laue monochromator and diffracted by satisfying Bragg's

law will produce a monochromatic beam. Because of absorption and incomplete diffraction in the monochromator elements, a monochromatic X-Ray beam has less intensity compared to the incident white beam (Noyan & Cohen 1987). However, this method provides the best diffraction peak resolution along with the opportunity to incorporate an analyser crystal before being detected by the detector, which removes sources of error arising from a thick or imperfectly positioned sample.

The second method is to acquire entire diffraction profiles at a fixed angle using a polychromatic white beam. In this case the diffracted beam is detected using multi-channel analyser crystal detector capable of detecting a range of photon energies. This method is suitable for dynamic in situ residual stress measurement such as shape memory related transitions. In addition, this method can be satisfactorily used to measure residual strain in textured material, where the intensity of a single diffraction peak may vary unacceptably, or otherwise be unrepresentative of the bulk material.

The wavelength of the diffracted beam,  $\lambda$  (in Angstroms) is related to the energy (keV) according to the following equation:

$$\text{Energy} = \frac{12.3975}{\lambda} \quad \text{Equation 2-5}$$

By combining Equation 2-1 and 2-5, it is clear that higher photon energy is associated with diffraction from smaller d-spacings and at a smaller scattering angle. The smaller angle, in turn, results in an elongated diamond shape gauge volume, with higher spatial resolution along the strain measurement direction but lower resolution in the beam propagation direction.

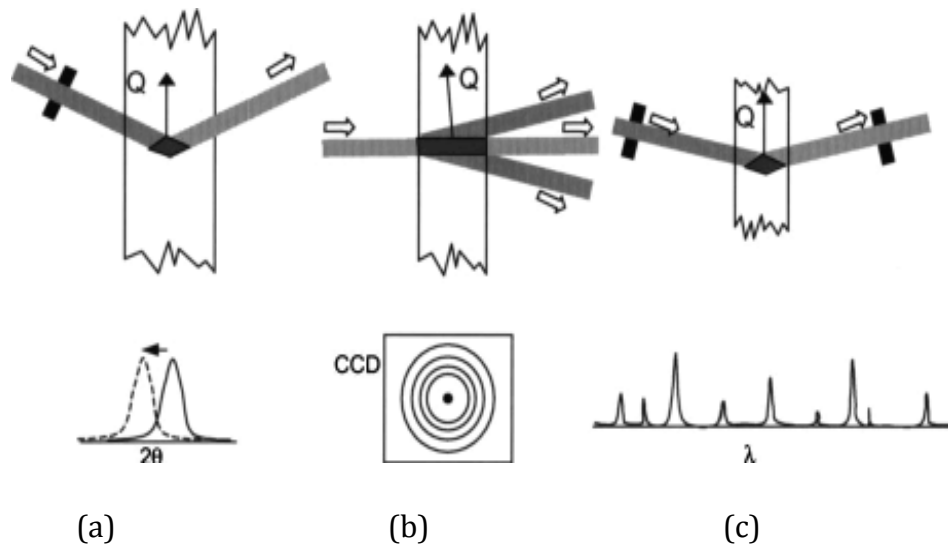


**Figure 2.6:** Schematic representation of synchrotron measurement geometries: (a)  $2\theta$  scanning; (b) low angle transmission; (c) white beam energy dispersive (Withers & Bhadeshia 2001).

### **2.2.3 Destructive Methods**

The destructive experimental techniques for measuring residual stress in materials include hole drilling, sectioning, curvature method, slotting, compliance, and a newly developed contour method. Such techniques involve measuring the distortion that results from cutting the material in some way, which necessarily relieves the residual stress perpendicular to the newly created surface. The original stress field is constructed from the distortion that originates due to the inherent residual stress relaxation that occurs. Though these techniques are widely applied for stress measurement, they are limited to measuring the macro-stress.

#### **2.2.3.1 Contour method**

This method of measuring residual stress is based on variation of Buckners' elastic superposition principle, Figure 2.7 (Prime 2001).

##### **2.2.3.1.1 Cutting**

In this method the sample to be measured is generally cut into two halves using wire electric discharge machine (EDM). This method is advantageous over other cutting method because i) it is capable of creating a very straight cut without removal of any additional material from the surface, ii) it does not involve any plastic deformation and iii) a negligible machining stress is induced in this case. However, this EDM cutting is limited to only electrically conductive materials.

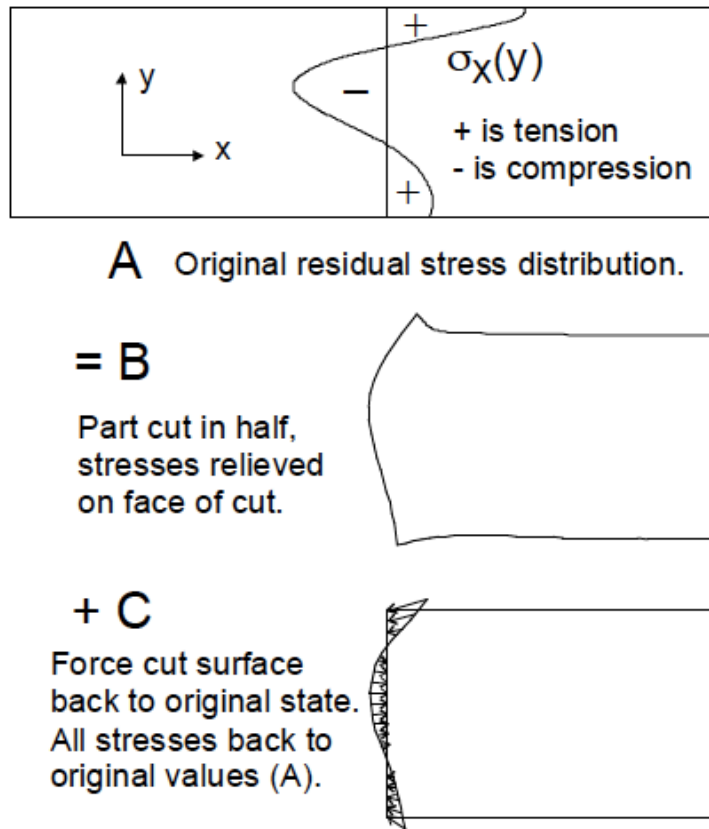


**Figure 2.7:** Schematic representation of the principle of contour method, (a) The component with significant residual stress is cut into two halves, (b) RS is relaxed and the contour of the newly created surface deviate from planarity and (c) deformed contour is pushed into plane surface using FEM and stress is calculated by the post-processing of the result (Prime 2001).

### 2.2.3.1.2 Contour Measurement

The contour of the newly created surface deviates from planarity due to the elastic relaxation of the intrinsic residual stresses. This deviation is then measured by using a touch probe or laser probe on a commercial Coordinate Measuring Machine (CMM) (Prime & Martineau 2002, Zhang et al 2004). It is to be noted here that the maximum resolution achievable from the best available touch probes is a few microns ( $0.6 \mu\text{m}$ ) which restricts its use to measuring higher levels of RS in reasonably large parts. Therefore, to overcome these difficulties a faster and more accurate laser based technique is developed (Kaplan 1997), and has been used for residual stress measurement (Zhao et al 2002).

#### 2.2.3.1.3 Stress Calculation

Finally, the contour of the surface is reversed and pushed back to the plane surface using finite element modelling. Boundary conditions are only applied to the direction normal to the cross-section, whereas other directions remain unconstrained. A single constraint is also required to help prevent rigid body motion. Finite element results are post processed to obtain a 2D stress profile perpendicular to the cut surface.

The residual stresses can thus be obtained directly from the measured surface contour without any need for inverse modelling procedures or prior assumptions about the stress field.

#### 2.2.4 Other Techniques

Many other methods are also available for residual stress measurement based on the fact that some property is directly related to the stress. These can be optical response in photoelasticity (Patterson 2001), magnetic properties in magnetoelasticity (Hyde et al 2000) or electrical properties (Blodgett et al 2005, Schoenig et al 1995), Raman excitation or photoluminescence (Molis & Clarke 1990, Young 2001), speed of sound in acoustoelasticity (Guz & Makhort 2000, Pao et al 1991), and change in temperature associated with adiabatic heating in thermoelasticity (Quinn et al 2004, Wong 2001). Being non-destructive, many of these methods have an added advantage; however, the conversion of these signals to specific stress components is not straightforward and depends mostly on the results from calibration experiments.

### 2.3 Fatigue crack growth behaviour

According to Linear Elastic Fracture Mechanics (LEFM), when a cyclic stress  $\sigma$  is applied to a material with a given R ratio, then for a crack length,  $a$ , the stress intensity factor for mode I crack growth can be given as:

$$K_{max} = Y\sigma_{max}\sqrt{\pi a} \quad \text{Equation 2-6}$$

and 
$$K_{min} = Y\sigma_{min}\sqrt{\pi a} \quad \text{Equation 2-7}$$

where, Y is the dimensionless parameter that depends on the specimen and crack geometry.

Therefore, the applied stress intensity factor range,  $\Delta K_{app}$  is:

$$\Delta K_{app} = K_{max} - K_{min} \quad \text{Equation 2-8}$$

Substituting Equation 2-6 and Equation 2-7 into Equation 2-8:

$$\Delta K_{app} = \sqrt{\pi a} (\sigma_{max} - \sigma_{min}) \quad \text{Equation 2-9}$$

Fatigue crack growth rate in a material can be described by the well-established Paris law, where FCG rate is proportional to the stress intensity factor range according to the following equation:

$$\frac{da}{dn} = C(\Delta K)^n \quad \text{Equation 2-10}$$

where,  $da/dn$  is the fatigue crack growth rate,  $\Delta K$  is the stress intensity factor, and C and n are the Paris constants. Fatigue crack growth behaviour is schematically illustrated in **Figure 2.8** where region I represents the stress intensity range  $\Delta K_{TH}$  below which no crack propagation occur, in region II crack grows linearly with the applied stress intensity factor range. Once  $\Delta K_{app}$  reaches the critical stress intensity factor,  $\Delta K_C$  of the material crack propagation occurs at a very fast rate and this is represented as region III.

Material fatigue is usually divided into two groups: high cycle fatigue (HCF) and low cycle fatigue. HCF can be defined as fatigue failure that occurs at low stress amplitude

and high frequencies, the number of cycles to failure is generally more than  $10^6$  cycles; whereas, LCF failure occurs at high stress amplitudes and low frequencies, in less than  $10^4$  cycles (Dieter 1986, Suresh 1998).

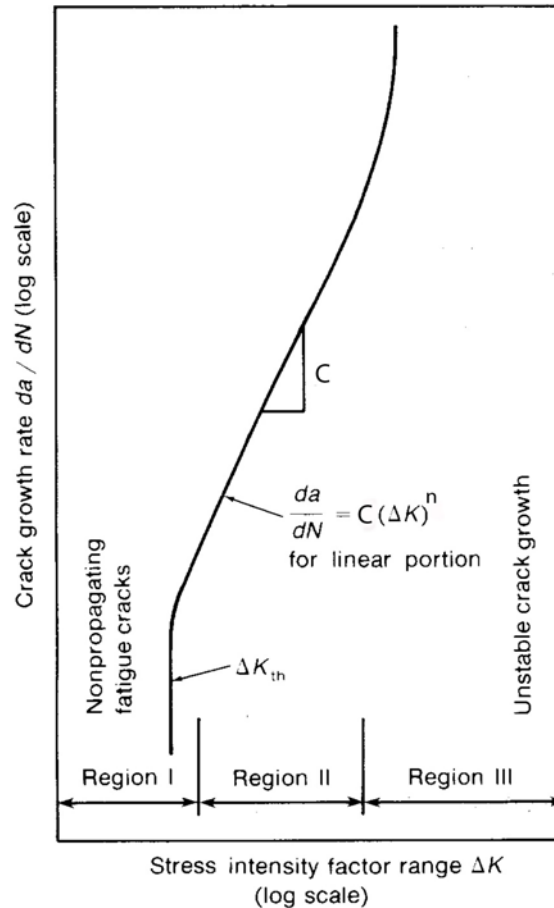


Figure 2.8: Schematic illustration of the three stages of fatigue crack growth (Dieter 1986)

A major proportion of aero-engine failure was found to be associated with high cycle fatigue that typically originates from vibrational stresses from the rotary motion of the engine components such as fans, compressors blades and discs. For that reason HCF has become of a greater concern as it has been identified as a major cause of engine failures. HCF life further worsens if the engine components are subjected to FOD. Most of the previous work has been carried out focusing on the deleterious effect of foreign object damage (FOD) under HCF or minor cycle fatigue. However, in reality LCF or major cycle loading arising from centrifugal and thermal stresses can play a significant role in determining the ultimate fatigue strength of the aerofoil components in combination with HCF. Ding et al (2007a) investigated the fatigue growth behaviour in

the presence of FOD under combined action of HCF and LCF on leading edge Ti-6Al-4V samples.

### 2.4 Effect of residual stresses on fatigue crack growth

Residual stresses influence the fatigue crack growth by accelerating or delaying the crack initiation and growth depending on their nature. Residual stresses are often regarded as being superimposed onto the applied stress to give an effective stress intensity factor. This is schematically represented in Figure 2.9 where profile (ii) represents the applied load cycle where no residual stresses are present in the structure. When a tensile residual stress field is superimposed onto the applied stress, the effective stress intensity factor becomes higher (profile iii). On the other hand, compressive residual stresses reduce the applied load and hence the stress intensity factor becomes lower (profile iii). Since negative stress intensity factors do not physically exist, only the positive part of the cycle is taken into account.

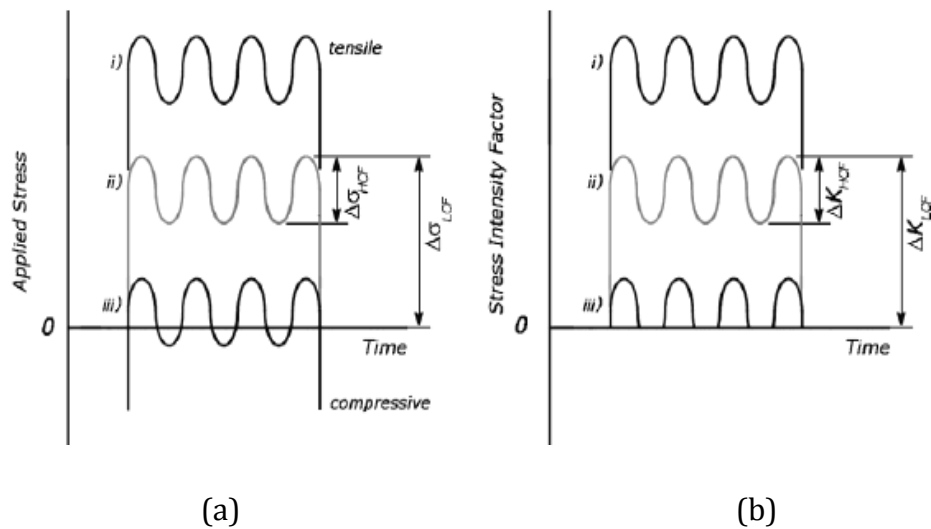


**Figure 2.9:** Influence of (a) residual stress on the total stress and (b) stress intensity factor under combined cycle (Oakley & Nowell 2007).

Therefore, the effective stress intensity factor can be simply defined as the following relation:

$$\Delta K_{eff} = \Delta K_{app} + K_{res} \quad \text{Equation 2-11}$$

Where,  $K_{res}$  is the stress intensity factor due to residual stress.

Fatigue crack growth in a residual stress field has been studied by many researchers both experimentally and numerically (Beghini & Bertini 1990, Beghini et al 1994, Chahardehi et al 2010, Edwards 2006, Farrahi et al 2006, Fitzpatrick & Edwards 1998, Ghidini & Donne 2007, Hatamleh et al 2007, John et al 2003, Liljedahl et al 2007, McClung & Newman 1999, McClung 2007, Ruschau et al 1999, Servetti & Zhang 2009, Tan et al 2004), especially in welded material. The most common way to take into account the effect of residual stress on the fatigue crack growth rate is to determine the stress intensity factor due to residual stress. Thus,  $\Delta K_{eff}$  can be determined according to Equation 2-11. The weight function method (WFM) and the finite element method are two commonly used techniques for estimating  $K_{res}$ . In this study WFM has been used to determine the  $K_{res}$  due to LSP+FOD'd residual stress and this is further explained in section 4.6.

## 2.5 Foreign object damage and fatigue Life

Foreign object damage (FOD) can be defined as the damage that generally occurs in the low temperature (entry) part of the aero engine compressor fans and blades, due to the ingestion of hard particles/debris during aeroplane take off, taxiing, or landing. Such damage in the form of craters, nicks, dents, tears or gouges (Nicholas 2006) significantly reduces the low, high and combined (both low and high) cycle fatigue strength of the turbine engine components (Ding et al 2007a, Hall et al 2008a, Martinez et al 2002, Nicholas 2006, Peters & Ritchie 2001b, Ruschau et al 2001, Witek 2011). This is why FOD has been an increasing concern for the last half-century.

The first step in studying FOD related fatigue failure is to simulate the FOD damage in the laboratory. Among the various damage simulation techniques that have been used recently such as EDM machining, quasi-static indentation, chisel indentation (pendulum), solenoid gun and the light gas gun method with the latter being the most effective in imparting damage representative of real FOD damage (Nicholas 2006). Therefore, in this study the light gas gun method has been chosen to induce FOD damage.

The majority of the previous works that used the light gas gun as a simulation method chose spherical hardened steel balls (Bache et al 2003, Boyce et al 2001, Peters & Ritchie 2000, Ruschau et al 2003) or glass beads (Martinez et al 2002, Ruschau et al

2001, Thompson et al 2001). However, some recent investigations used cubic impactors, which are considered to be the most effective in inducing worst case damage in the material (Ding et al 2007a). FOD damage characteristics created by spherical and cubic impactors are further explained in the following paragraphs.

Four factors associated with FOD have been identified that affect the fatigue life of the aero engine components. They are: (a) stress concentration related to the FOD geometry, (b) FOD-induced residual stresses, (c) presence of microcracks due to the impact and (d) microstructural damage such as shear band formation and local texturing (Birkbeck 2002, Peters & Ritchie 2000). A thorough investigation dealing with these parameters is crucial to assess their effect on the fatigue crack growth behaviour in the presence of FOD damage.

This section summarises some important results that have been published previously addressing the above mentioned issues that includes FOD damage characterization, typical residual stress fields generated by FOD impacts and a possible explanation of how these residual stresses affect the fatigue strength, and the effect of various impact parameters on the high and combined cycle fatigue strength.

The majority of previous work on FOD has been carried out using Ti-6Al-4V alloy, which is a commonly used alloy for aero engine compressor fans and blades.

### 2.5.1 Residual stress distribution due to FOD

The residual stress distribution associated with 0° FOD impacts (created by firing 3.2 mm diameter steel ball indenters at velocities of 200 and 300m/s) in Ti-6Al-4V has been measured using synchrotron X-ray diffraction and also predicted using dynamic FEM analysis (Boyce et al 2001). The general distribution of hoop residual stress,  $\sigma_{\theta\theta}$  is shown in Figure 2.10, and exhibits a wide region of compressive residual stress directly below the indent. The maximum compressive stress is found to be 1.5 times the yield strength, at a distance of half a crater diameter away. On the other hand, the balancing tensile residual stress appeared at two primary zones: i) a tiny but intense zone at the edge of the crater rim and ii) a wider region at a distance of half crater diameter away from the indent. In this case, the maximum stress is about 40% of the yield stress and is present well below the surface. Whether the damage is created by a quasi-static or ballistic mode impact, the general distribution of residual stress does not change over a

large scale (Boyce et al 2001). Only the magnitude of the residual stress was different. The comparison between measured and predicted residual strain distributions as a function of distance from the crater rim is given in Figure 2.11. In the hoop direction, which is typically the crack opening direction, the peak maximum residual strain is about -6000 microstrain, subsiding gradually with increasing distance from the crater rim. It seems that the FEM model captured the overall shape of the strain profiles in all three directions; however, the predicted strain values are higher than the experimental values. A similar residual stress distribution was predicted from numerical modelling by Chen (Chen 2005, Chen & Hutchinson 2001).

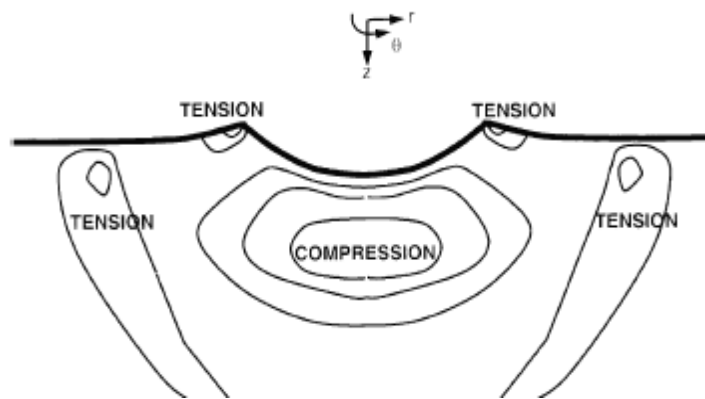


**Figure 2.10:** General distribution of the hoop component of the residual stress,  $\sigma_{\theta\theta}$  as found by experimental and numerical analysis around the FOD site (Boyce et al 2001).

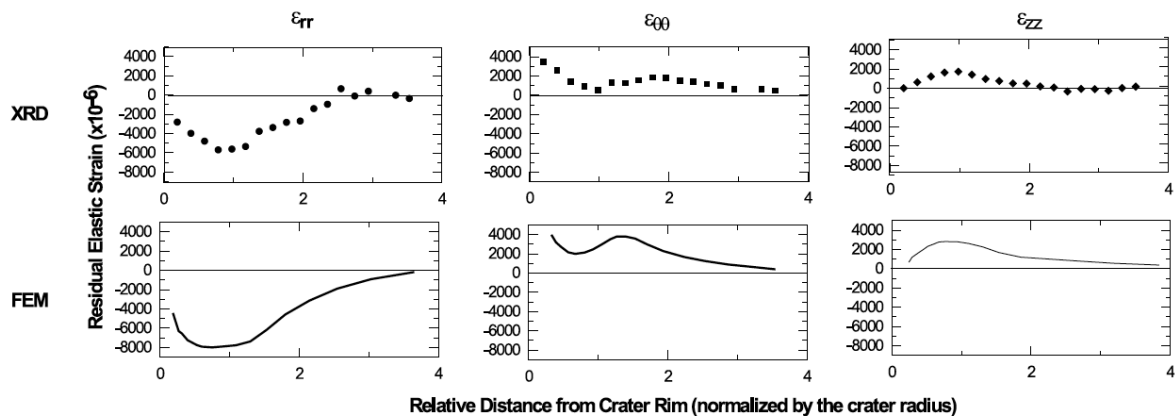


**Figure 2.11:** Comparison of the residual strain distribution generated by a spherical impact between synchrotron X-ray diffraction and FEM in the hoop ( $\epsilon_{\theta\theta}$ ), radial ( $\epsilon_{rr}$ ) and surface normal ( $\epsilon_{zz}$ ) directions as a function of distance from the crater rim (Boyce et al 2001).

Residual stresses due to a cubic impact (at an impact velocity of 277 m/s) were measured on a leading edge specimen using the laboratory X-ray technique ( $\sin^2\psi$ ) and synchrotron X-ray diffraction, and compared with the FEM prediction by Duó et al

(2007). Numerical predictions showed a fair qualitative agreement with the measured residual stress; however, poor quantitative agreement was found. Although high strain rate deformation and thermal softening is considered in the model, microstructural damage, the presence of microstructurally small cracks at the notch root as well as formation of shear bands were not taken into account. Nevertheless, both results confirm the presence of tensile residual stress (TRS) at the vicinity of notch root (Duó et al 2007).

Longitudinal residual strains due to cubic impacts have also been characterized in a recent study using high energy synchrotron X-ray diffraction (Frankel 2009) and compared with the predictions by the finite element modelling. FOD was simulated by dynamic impact, by firing a 3 mm steel cube indenter at an impact velocity of 200m/s onto the leading edge Ti-6Al-4V specimens. The strain distribution in the vicinity of the V notch is shown in Figure 2.12. Similar to that observed for spherical impact on flat plate specimen (Figure 2.11), a large compressive residual stress region was formed at the bottom of the notch. However, for the cubic impact, a tensile residual stress region appeared just below the compressive region. The magnitude of the peak compressive residual strain for the cubic impact is -4500 microstrain and the maximum value of the tensile residual stress is 2000 microstrain.

Comparison with the prediction suggests that even though there is similarity in shape between the measured and predicted strain profiles, the FEM model predicts higher strain values especially at the corners of the notch near the L.E., where a tensile residual stress was predicted. The diffraction peak FWHM map in as-FOD'd condition shows higher peak broadening surrounding the notch (Figure 2.13), which indicates higher plastic deformation in the vicinity of the notch.

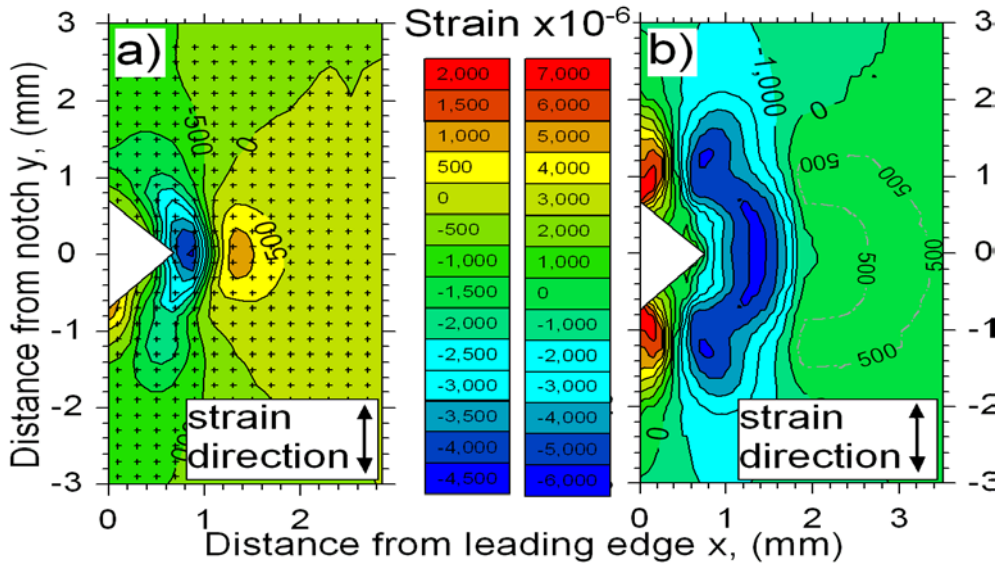
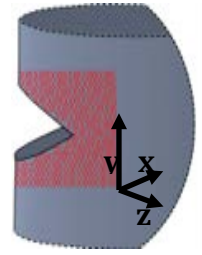


**Figure 2.12:** (a) Elastic residual strain profiles around an FOD impact measured by high energy synchrotron X-ray Diffraction (left), and predicted strain profile (right), (b) Sample geometry showing the measurement plane and directions (Frankel 2009).

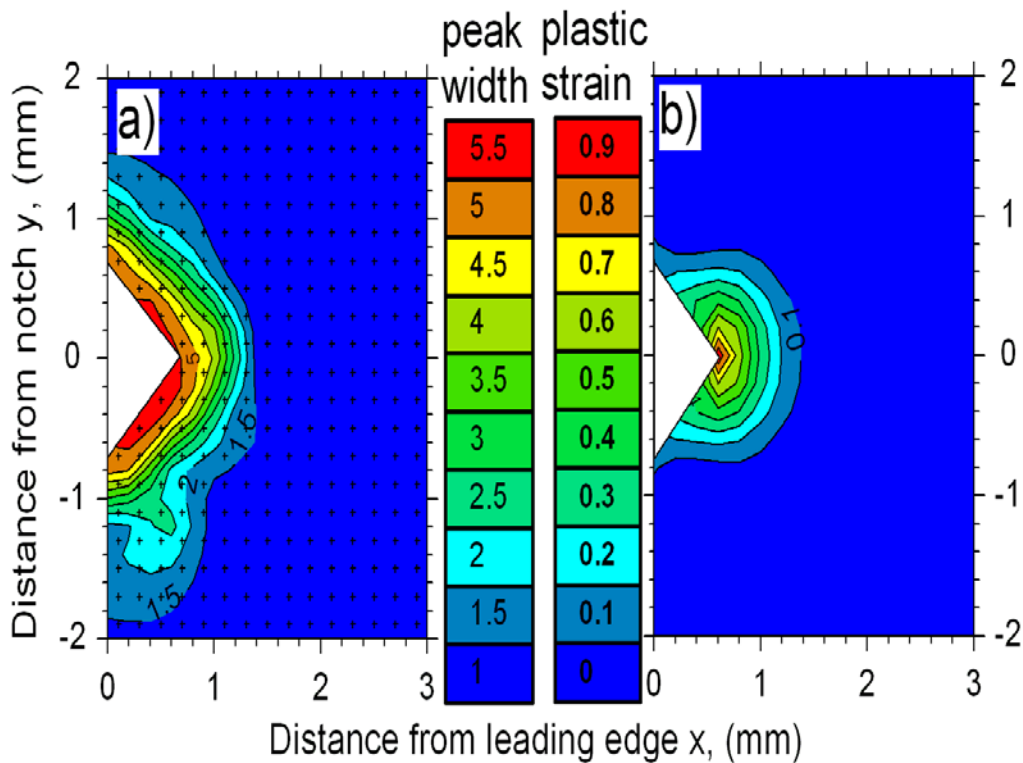


**Figure 2.13** (a) Measured FWHM and (b) predicted plastic strain profiles (Frankel 2009).

### 2.5.2 Effect of FOD induced Residual Stress on the fatigue life

In the previous section it has been observed that a significant amount of tensile residual stresses can be generated as a result of FOD impact. Numerical modelling of  $0^\circ$  impacts also predicted similar pattern of residual stress distribution, where compressive residual stresses were found below the FOD notch are balanced by a tensile residual stress field away from the notch site (Chen 2005). This compressive stress field may counterbalance the elastic stress concentration generated by the FOD notch when external cyclic load is applied. Evidence of this can be found in the work published by Ding et al (2007) where FOD'd (by firing 3 mm hardened steel cubes at 200 m/s) specimens were fatigued with and without stress relieving (SR) heat treatment. Not only was a longer fatigue life reported for the as-FOD'd specimen, but also crack initiation for this sample occurred at either sides of the indent that finally turned into quarter-elliptical shape (Figure 2.14a). Conversely, the FOD + SR specimen showed multiple crack initiation at the indent base that formed a semi-circular crack shape, Figure 2.14b. The residual stresses measurement of a similar FOD'd specimen by Frankel (2009) indeed showed evidence of compressive residual stress below the notch. This indicates that compressive residual stresses were inhibiting crack initiation at the base of the notch, resulting in slightly higher fatigue life for as-FOD'd specimens compared to FOD+SR specimens. However, Ruschau et al. (2003) found that fatigue strength only increased after stress relieving of FOD impacted specimens (created by 0.5 mm and 1.33 mm sized impactor at 305 m/s), whereas fatigue strength remained unchanged after stress relieving for FOD impact created by the largest size steel ball (2 mm diameter) at the same velocity.

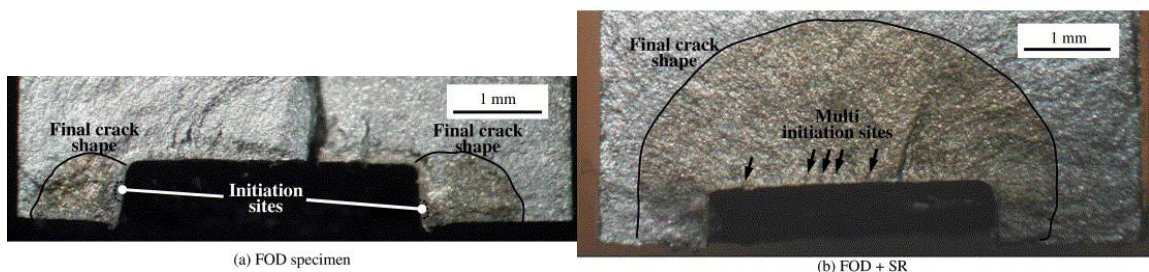


**Figure 2.14:** Fracture surfaces after FOD and FOD+SR showing the effect of residual stress on fatigue. The FOD was created by firing 3 mm hardened steel cube at 200 m/s. (Ding et al 2007).

On the other hand, the subsurface tensile region (below the compressive region) has been found to be a favourable crack nucleation site, if the tensile residual stress is higher in magnitude as shown in Figure 2.15.

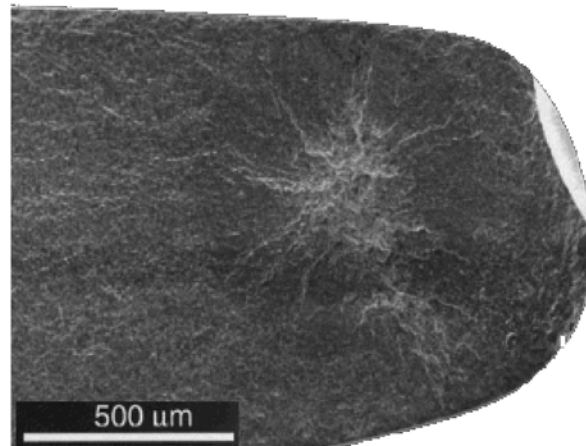


**Figure 2.15:** SEM image showing subsurface fatigue crack initiation. Sample had a leading edge radius of 0.38mm and FOD'd at 0° angle (Ruschau et al 2001).

It must be emphasized here that the magnitude of the compressive residual stress greatly depends on the impact velocity. Therefore, the crack initiation location also seems to be affected by this velocity. For example, for spherical FOD impacts that were created by low velocities (200-250m/s) crack initiation occurred at the base of the impact crater (possibly due to lower compressive RS), whereas for high velocity FOD impacts (250-300m/s) cracks initiated from the crater rim (at the FOD induced microcracks) (Peters & Ritchie 2000). Conversely, for cubic impacts (Figure 2.14) created at 200 m/s, crack initiation occurred at the two sides of the notch where pile up occurred. This might suggest that cubic impacts are more damaging than the spherical impacts.

Further evidence of FOD-induced residual stress affecting the HCF fatigue strength of Ti-6Al-4V alloy can be found in (Mall et al 2001), where FEM analysis showed that the effective stress and stress ratio is higher in the vicinity of the FOD notch than the far-field applied stress. They concluded the residual stress as well as the stress concentration generated by the FOD impact shape modify the applied stress ratio and mean stress in the region close to FOD sites. This may be one explanation of how the FOD induced tensile residual stresses reduce the fatigue strength. Fatigue life reduction associated with FOD has also been evaluated by Peters and Ritchie as shown in Figure 2.16 (Peters and Ritchie, 2000). This implies that tensile residual stress

produced by the FOD damage is detrimental to the HCF life whilst the compressive residual stresses present beneath the damage are not sufficient to compensate this reduction.

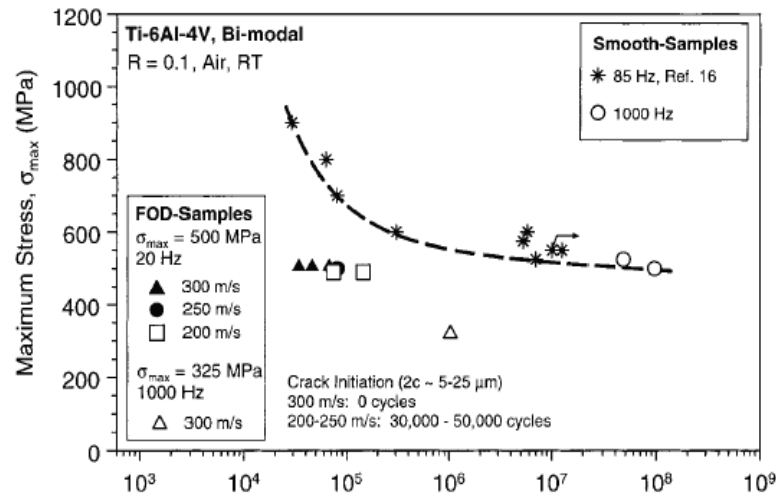


**Figure 2.16:** Fatigue debit due to FOD in Ti-6Al-4V, compared with results from smooth bar samples (Peters & Ritchie 2000).

HCF fatigue thresholds have been studied by Oakley & Nowell (2007) for Ti-6Al-4V blade-like samples at stress ratios  $R = 0.3$  and  $R = 0.8$ , with an elastic predictive approach based on short cracks propagating from a notch generated by FOD. The FE prediction is compared with the experimental results, with and without considering residual stresses. The results suggest that when residual stress was considered, predicted results agree with the experimental results, Figure 2.17 indicating that the effective stress and stress ratio in the vicinity of the FOD site is different from the far-field stress.

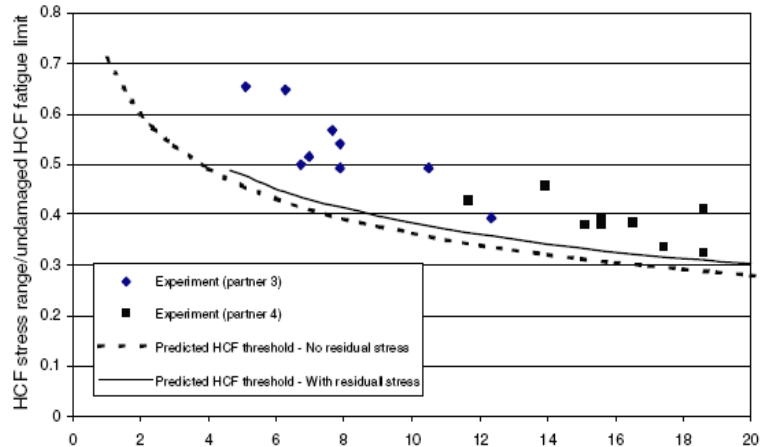


**Figure 2.17:** Comparison of experimental and predicted HCF threshold with or without considering residual stress (Oakley & Nowell 2007)

It is clear from the above discussion that FOD-induced residual stress can influence the mean stress in the cyclic load and in consequence accelerates or retards fatigue crack nucleation and growth.

### 2.5.3 Fatigue life reduction due to cyclic loading

Several researchers have reported the influence of FOD on the fatigue performance of material by performing experimental and numerical work (Bache et al 2003, Chen & Hutchinson 2001, Ding et al 2007a, Ding et al 2007b, Hall et al 2008a, Mall et al 2001, Martinez et al 2002, Nicholas 2006, Nowell 2008, Oakley & Nowell 2007, Peters & Ritchie 2000, Peters & Ritchie 2001a, Peters & Ritchie 2001b, Ruschau et al 1999, Ruschau et al 2001, Ruschau et al 2003, Thompson et al 2001).

In order to understand the effect of FOD damage on the fatigue life of the component it is important to analyse the effect of FOD damage characteristics such as the size and shape of the FOD damage, loss of material (LOM), plastic deformation and shear band formation on the fatigue behaviour of material. The characteristics of the FOD damage seems to depend on the size and shape of the impactor, impact velocity and impact angles. They are described in the following paragraphs.

#### 2.5.3.1 Effect of Impactors

Fatigue behaviour of the FOD'd material depends on the FOD geometry, which again greatly depends on the size and shape of the impactor. In general, a spherical shaped impactor creates smooth-surfaced, dent-shaped damage with no loss of material, or an irregular, jagged notch (still round shaped) with significant loss of material from the

notch surface (Thompson et al 2001). This implies that similar impact conditions can produce damage with different characteristics. For example a notch-like indentation may form either by plastic deformation or by loss of material (Thompson et al 2001). This demonstrates the uncertainty of simulating damages with exact features.

The geometry of a FOD notch also depends on the impact energy. For example, low energy impacts (velocities 237 m/s or lower) produced smooth indents where plastic deformation around the indent periphery, material pile up and shear band formation were reported (Bache et al 2002). For higher velocities, impact damage was associated with loss of material (LOM) that formed small notches. In this case evidence of shear deformation was found at the notch surface. Shear band formation was also reported by other researchers (Boyce et al 2001, Mall et al 2001) for spherical impacts.

On the other hand, a cubic impact on a leading edge specimen generally produces a V shaped notch with LOM and material pile up at both sides of the notch near the leading edge.

Ding et al (2007a) studied the effect of cubic impacts (created by firing 3.2 mm hardened steel cube at 200 m/s) and reported an irregular notch with material pile up, material distortion, folding, shear band formation and most importantly presence of microcracks, Figure 2.18. As mentioned earlier, these microcracks are the favourable sites for crack initiation and propagation in the following cyclic loading.

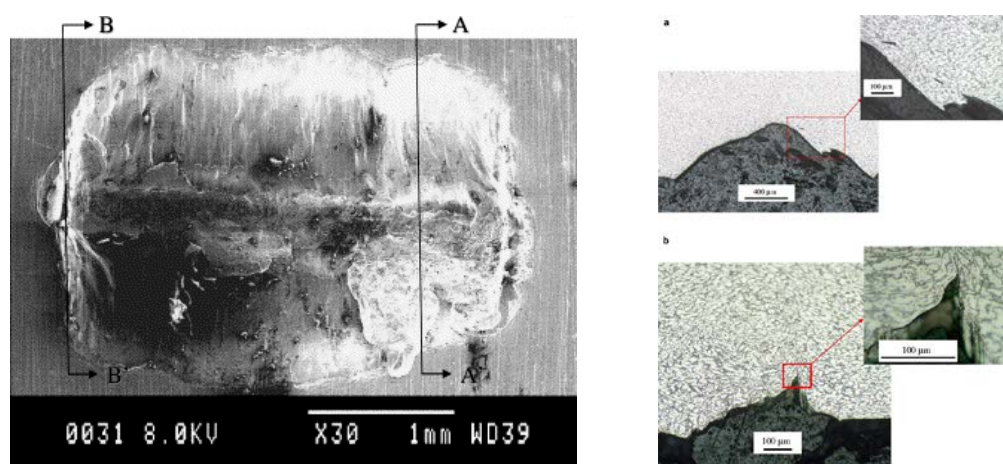


**Figure 2.18:** SEM and optical images of a simulated FOD damage, (a) across the section AA' and (b) across the section BB' (Ding et al 2007).

The depth of the impact damage generally depends on the size of the impactors. 1mm glass bead impactors created notches 0.1 to 0.2 mm deep notches (Martinez et al 2002), whereas 0.5 to 2.0 mm steel ball impactors resulted in a maximum notch depth of 0.75 mm. On the other hand, Ding et al (2007a) reported for cubic impacts, the notch depth and width is 0.59 to 0.68 mm, and 2.1 mm respectively.

#### 2.5.3.1.1 Influence of the FOD geometry

Attempts have been made to correlate the reduction in fatigue limit stress with the extent of physical damage such as macro and/or microscopic features at various FOD impact sites, by selecting damage depth as a criterion. However, no specific trend of decreasing fatigue limit has been found with increasing damage depth at either of the stress ratios  $R=0.1$  and  $0.5$  (Ruschau et al 2001). This can be attributed to the fact that similar impact conditions may produce damage with dissimilar characteristics. Therefore, consideration of solely damage depth is not an appropriate indicator to delineate the deficit in fatigue life. The FOD geometry or morphology has a significant influence in determining the fatigue life reduction of the component e.g. smooth 'dents' can be less detrimental than sharp irregular nicks of comparable size. However, in another study it has been shown that fatigue strength decreases with increasing notch depth (see Figure 2.20) (Ruschau et al 2003).

The effect of damage (quasi-static chisel indentation) depth has also been reported elsewhere (Mall et al 2001). Fatigue strength decreases with increasing damage depth up to 2 mm where major portion of fatigue life was expended in crack initiation rather than propagation of pre-existing cracks; whereas, fatigue strength did not reduce for depths greater than 2 mm where both crack initiation and propagation were observed, (see **Figure 2.19**).

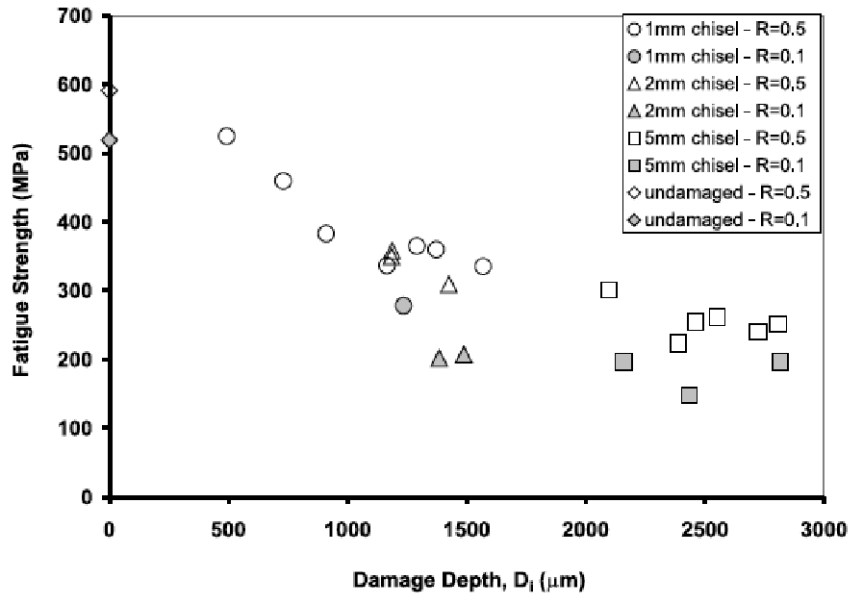
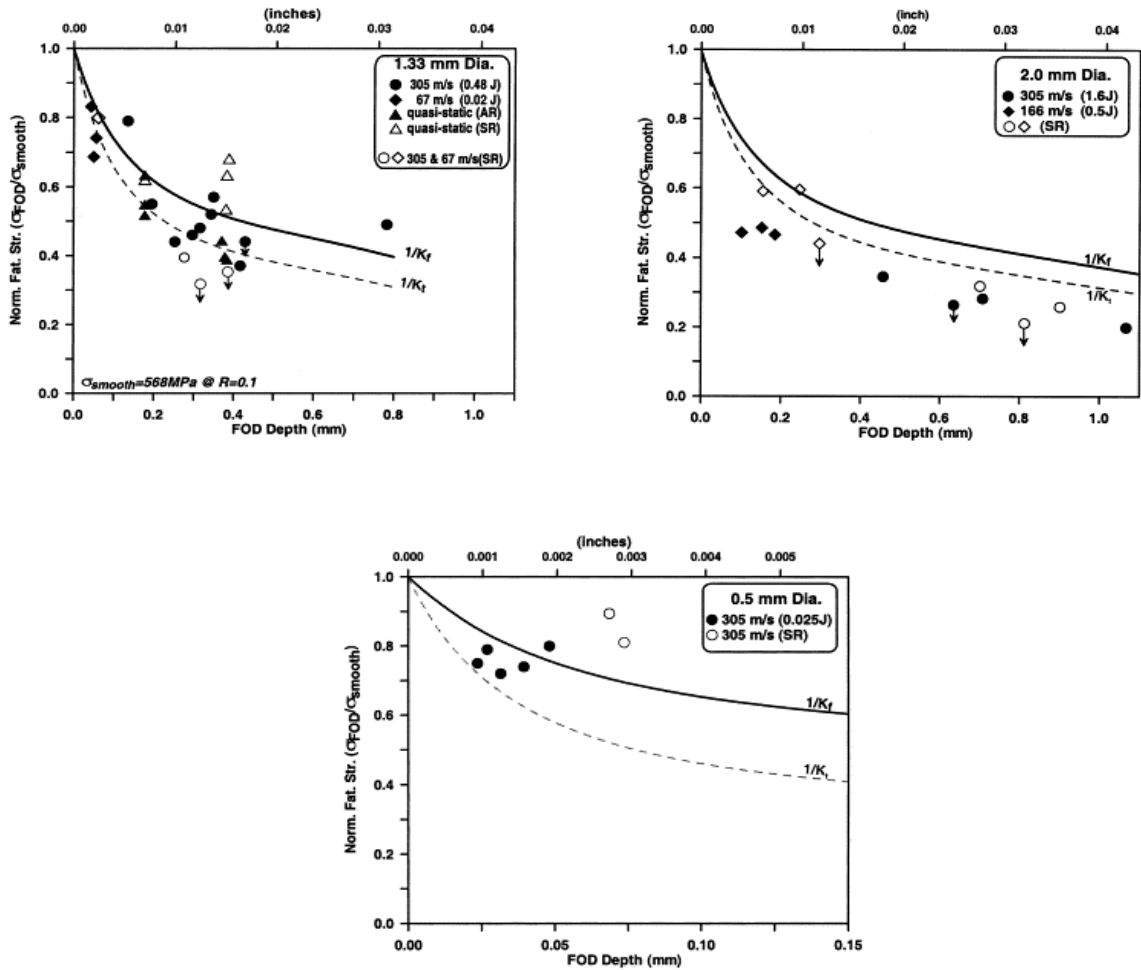


Figure 2.19: Effect of FOD damage depth on the HCF fatigue strength (Mall et al 2001).

Investigation of specimens that failed at the notch shows that when there are no tears or secondary notches present at the FOD sites, the fatigue failure mostly instigates near the deepest point of the crater. However, in their presence failure originates at a distance away from the notch, from a tear or notch. Similar work has been carried out with the same material but larger flat plate samples than the present study, which found that fatigue failure initiated at the crater rim (sample was FOD'd with 3.2 mm diameter steel indenter), and is in disagreement with the findings described above. The later FOD event was generated using higher kinetic energy resulting a tensile hoop stress at the crater rim, and hence give rise to fatigue crack nucleation at further cyclic loading. In comparison, dynamically impacted FOD damage using 1 mm diameter glass spheres on the edge of a sample with less than 1 mm thickness did not produce tensile hoop stress at the rim, and failed at the deepest point of the crater (Ruschau et al 1999).

Ruschau et al (2003) demonstrated the effect of FOD impactor diameter from 0.5 to 2.0 mm with impact velocities ranging from 60 to 500 m/s, on the HCF limit stress of the Ti-6Al-4V leading edge samples, Figure 2.20. They concluded that the loss of fatigue strength was more than 80% for largest impactor where damage showed significant loss of material.



**Figure 2.20:** Variation of normalised fatigue strength with damage depth produced by (a) 1.33 mm (b) 2.0 mm and (c) 0.5 mm diameter indents (Ruschau et al 2003).

### 2.5.3.2 Effect of impact angle

Ruschau et al (1999) investigated the fatigue depreciation of Ti-6Al-4V leading edge fan blade specimens due to FOD event, simulated by ballistic shot using 1 mm diameter glass spheres at a nominal velocity of 305 m/s at various impact angles (0-60°), as well as different leading edge thickness. More loss in fatigue life is found for off-axis (30°) impacts, than 0° impact for both the stress ratios  $R=0.1$  and  $0.5$ , as shown in Figure 2.21.

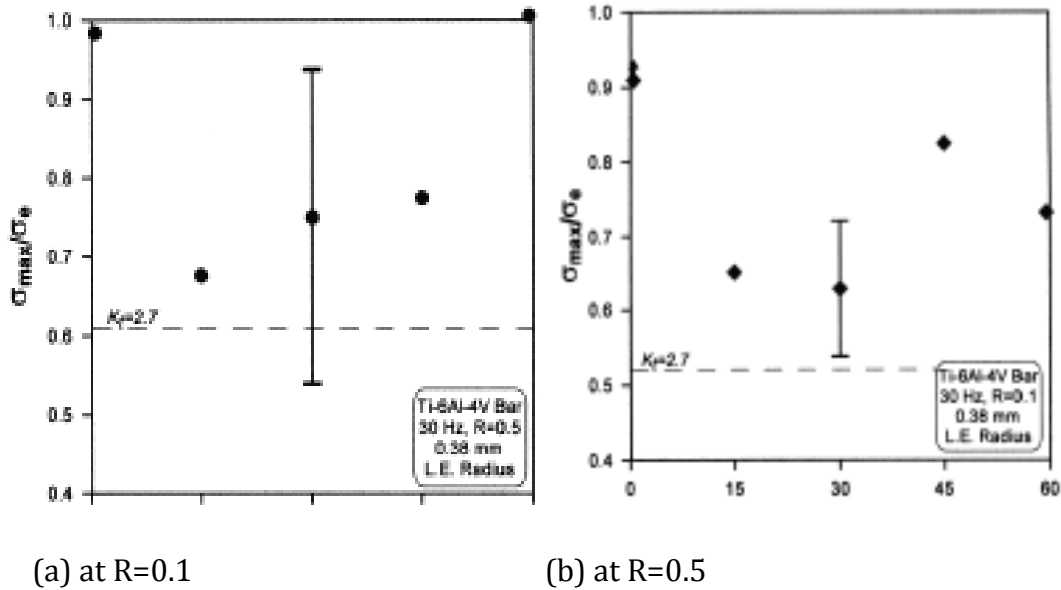


**Figure 2.21:** Influence of impact angle on the fatigue strength of Ti-6Al 4V alloy for two stress ratios (Ruschau et al 1999).

The higher fatigue damage for off-axis impact can be explained in light of the analytical modelling result (Boyce et al 2001) that predicts the presence of a relatively small tensile stress field at the entry side of the FOD damage site along with large compressive stress field. Such a tensile field may facilitate further fatigue crack nucleation and propagation.

### 2.5.3.3 Effect of impact velocity

Fatigue strength was found to be decreased with increasing impact velocity Figure 2.22 (Bache et al 2002). The fatigue debit exceeded 70% of the original fatigue strength of the alloy, for the highest energy impact.

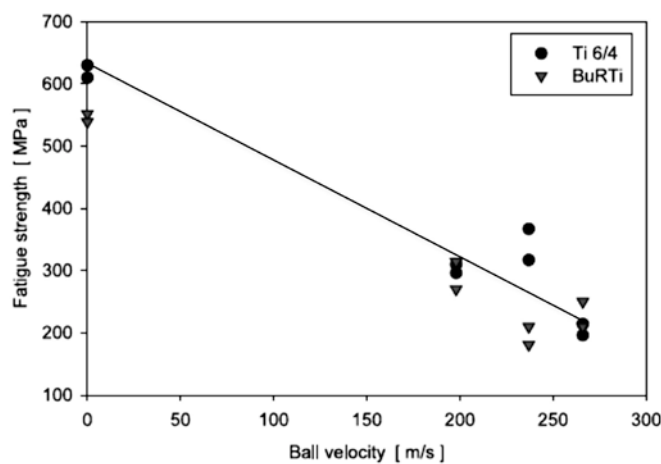


**Figure 2.22:** Variation of normalised fatigue strength of Ti-6Al-4V with the impact velocity (Bache et al 2002)

FOD was simulated by shooting 2 mm diameter steel balls at impact velocities of 120 - 266 m/s (Bache et al 2003). SEM images showed shear deformation and plastic pile up for low energy indents (impact velocity  $\leq 237$  m/s). Conversely, for high energy impacts, LOM was noticed at the notch surface.

Comparison of the fatigue strength at room temperature and 350°C (the maximum working temperature for the alloy) suggests that fatigue strength decreases with increasing impact velocity; however, fatigue strength seems to be insensitive to temperature as shown in Figure 2.23.

It is worth noting here that high speed impacts are generally associated with microstructurally small cracks and/or crack like discontinuities from where fatigue cracks may nucleate and grow under subsequent cyclic loading leading to failure. Hence, it is reasonable that fatigue strength decreases with increasing impact velocity.

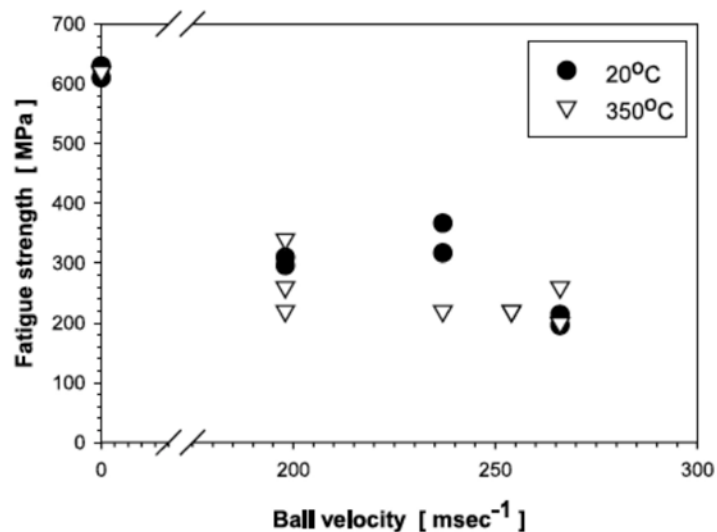


**Figure 2.23:** Effect of impact velocity on the fatigue strength of Ti-6Al-4V alloy at room temperature and 350°C (Bache et al 2003).

## 2.6 Mechanical Surface Treatment

For aerofoil components, damage like fatigue and corrosion cracking are generally initiated at the surface under cyclic loading that includes a tensile component in the cycle. Therefore, treating the surface to induce a compressive residual stress layer is

beneficial in improving the fatigue life of the component (McClung 2007). Depending on the level of the compressive residual stress, it does not only prevent the crack initiation but also retard the propagation rate of small cracks. Furthermore, corrosion (stress corrosion cracking) and wear resistance are also enhanced by surface treatment.

Among the various mechanical surface treatment techniques available for aero engine components are coating, plating, heat treatment for surface hardening, ion implantation and shot peening (SP). Shot peening is a widely used mechanical surface treatment technique to enhance the fatigue life of a component, yet this process has several limitations. The extent of compressive residual stress is limited in depth, e.g. the maximum depth was found to be 0.25 mm (Montross et al 2002) for softer material (aluminium alloys) and even less for harder materials. Also, the peening process induces a large degree of cold work that can damage the microstructure and is favourable in relaxation of this beneficial compressive stress. In addition to that, the peened surface is considerably rough and needs to be modified prior to its application. This further processing predominantly reduces the compressive stress layer.

A desire to overcome these limitations has been the driving force to develop advanced mechanical surface treatment technologies such as laser shock peening (LSP) and low plasticity burnishing (LPB). Both of these processes are capable of introducing much deeper compressive stress layers with a low degree of strain hardening in the surface material.

In this work, focus is given to LSP induced residual stress characterization and consequent fatigue life enhancement for Ti-6Al-4V alloy. This study extensively reviews the above mentioned technique in terms of the basic principle, associated parameters, their influence on the residual stress, measured residual stress profiles for a number of alloys.

## **2.6.1 Laser Shock Peening (LSP)**

### **2.6.1.1 Basic LSP process**

#### **2.6.1.1.1 Laser System**

High energy laser pulses can induce plastic deformation in the surface of a material by generating shock waves. This fact was first recognized in the early 1970s and since then

the process has been gradually developed (White 1963). LSP has become a potential process for enhancing the fatigue life of the aero engine components after the discovery of a new laser system, as the original Nd-glass pulsed laser system was relatively slow in laser generation – approximately eight minutes per cycle (Vaccari 1992).

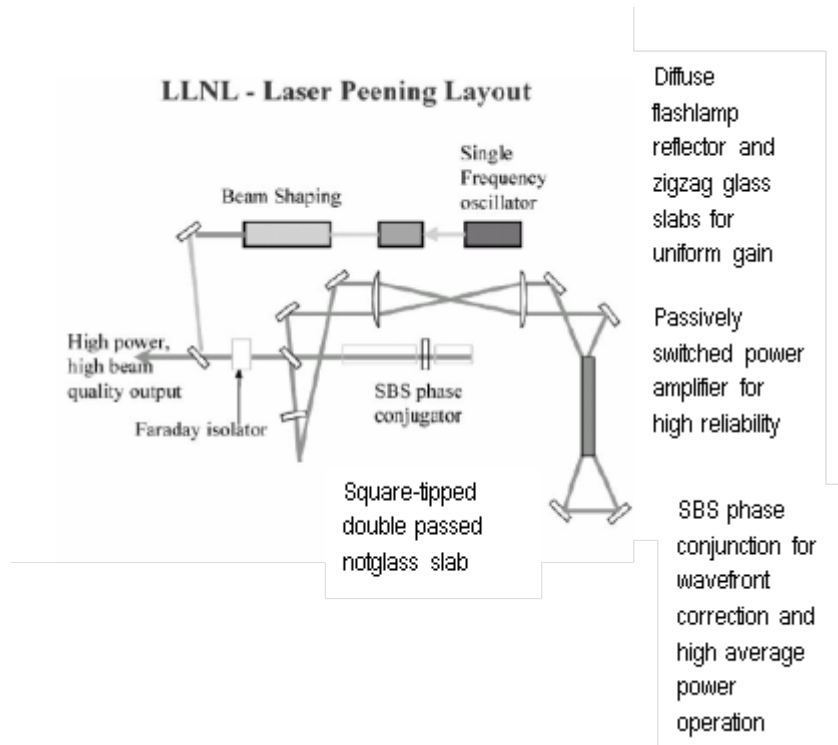


**Figure 2.24:** Laser system used for LSP treatment by MIC and LLNL (Hammersley et al 2000).

For a successful laser peening process, the laser generation system should be able to produce laser beams with energies in the level of 10-500 J/pulse with a pulse length smaller than 100 ns (Montross et al 2002). Q-switched laser systems, based on a neodymium-doped glass or yttrium aluminium garnet (YAG) lasing rod operating at 1064 wavelength, were developed to meet these requirements. Subsequently, this system has been further modified and a fast firing Q-switched system was developed at the Lawrence Livermore National Laboratory and employed by Metal Improvement Co. Inc (MIC), Figure 2.24. In this system about 3% (Nd) doped yttrium lithium fluoride crystal is used as the laser source.

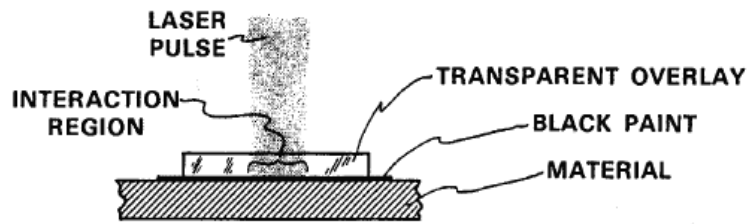
For the current investigation, all the Ti-6Al-4V 4P bend samples were laser treated by MIC.

#### 2.6.1.1.2 Process

Laser shock peening (LSP) is a mechanical surface treatment process utilized to increase the fatigue and fretting resistance of metals and alloys. Another application of this process is strain hardening of thin-sectioned material. LSP is also suitable to treat fatigue critical areas such as localized treatment along holes, notches, keyways, fillets, splines, welds, and other regions with high stress.

A high energy laser pulse is employed to generate a compressive residual stress into the surface of the material. The laser system consists of a high energy neodymium-glass laser capable of generating about 15-30 nanosecond pulses with an energy of 50 joules or more. Figure 2.25 represents a schematic of the working principle of the LSP process. The area for laser treatment is first overlaid by an opaque layer such as a black coating, which is then covered by another transparent layer (water is usually used for this purpose) as shown in Figure 2.25a.

The high energy laser beam passes through the transparent layer and strikes the opaque layer, which is then immediately vaporized. Further incoming laser energy is trapped into this vapour, causing heating and expansion between the transparent layer and the surface to be treated. The transparent layer restricts the plasma and creates a high pressure on the surface. Consequently a shock wave is propagated inside the material. The parameters for the peening process are set to produce a stress level well above the yield stress of the material. Hence, surface material is plastically deformed which leads to strain hardening and compressive residual stress at the surface of the component.



a. Surface area to be laser shocked, showing the laser beam and overlays.

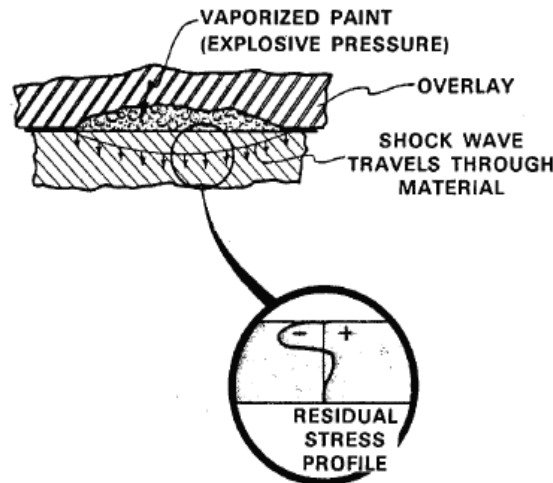


**Figure 2.25:** Schematic representation of the LSP process (Clauer 1996).

### 2.6.1.2 Effect of controlling process parameter

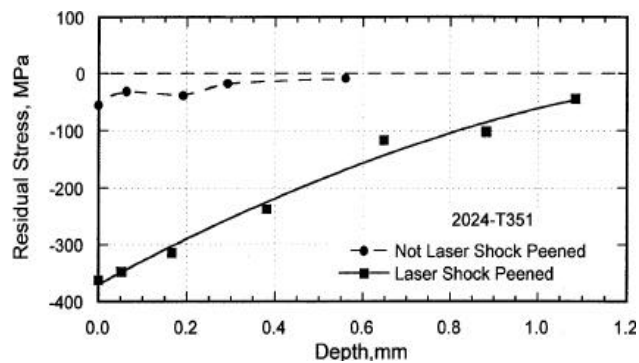
The level of the compressive residual stress, both in terms of magnitude and depth below the surface, depends on the optimization of the process parameters such as laser spot size, shape, laser energy (J), wavelength (nm), pulse duration (ns), area of the laser spot (cm<sup>2</sup>) *etc.* Among these parameters, Fluence (energy/area J/cm<sup>2</sup>) and laser power density are critical in ensuring the effectiveness of the peening process.

Along with the above peening parameters residual stress is also largely dependent on the mechanical properties of the material to be treated as well as the geometry of the sample, use of absorbent coating, multiple laser shocks and overlapping of the laser spots. The effect of these factors is described in section 2.6.1.2.

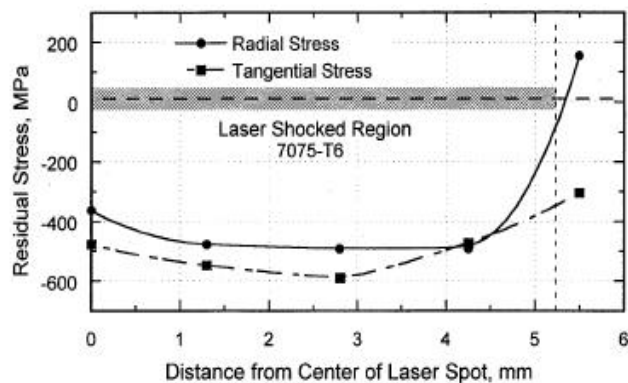
The laser peening process can be controlled by using Almen strips similar to the SP process, digital monitoring and data logging as employed by MIC (Hammersley et al 2000).

### 2.6.1.3 LSP Induced Residual stress

LSP produces a relatively uniform residual stress across the surface of the treated part. The magnitude of the surface stress increases with increasing intensity of the peening condition, eventually reaching a limiting value and then remaining constant. The depth of the residual stress beneath the surface is usually greater than that created in a normal shot peening (SP) process as described earlier. The intensity of the processing condition, material properties and other factors control the actual depth. A depth of 0.5 to 1 mm can easily be achieved without any severe degradation of the surface, which is a common scenario in the case of SP processes. LSP generates a maximum stress at the surface and the stress magnitude gradually decreases with increasing distance from the surface. This again makes LSP more advantageous than SP, where compressive residual stress (CRS) reaches maximum at a distance away from the surface and then decreases with increasing depth, Figure 2.26 (Clauer 1996).



(a)



(b)

**Figure 2.26:** In-depth residual stress profile for 7075-T6 and 2024-T351 aluminium alloy (Clauer 1996).

### 2.6.1.3.1 Influence of absorbent coatings

Absorbent coatings are used for mainly two reasons: i) to protect the surface of the material from the thermal effect of ablation (Fairand & Clauer 1976) ii) and to increase the pulse pressure on the surface (Peyre et al. 1997). As mentioned in Figure 2.27, a high tensile stress can form in the case of LSP treatment with no protective coating whereas a significant amount of compressive residual stress is successfully created by using absorbent coating (Peyre et al 1998). The generation of balancing tensile residual stress is also evident at a distance away from the treated area (Masse & Barreau 1995). In fact, the absorbent coating retains the laser energy enhancing the pulse pressure to transmit a high pressure (1-6 GPa) (Fabbro et al 1990) shock wave into the material. For example, even with a high power density, only a slight compressive residual stress was achieved when a Hadfield steel is LSP'd without any absorbent coating (Chu et al 1995).

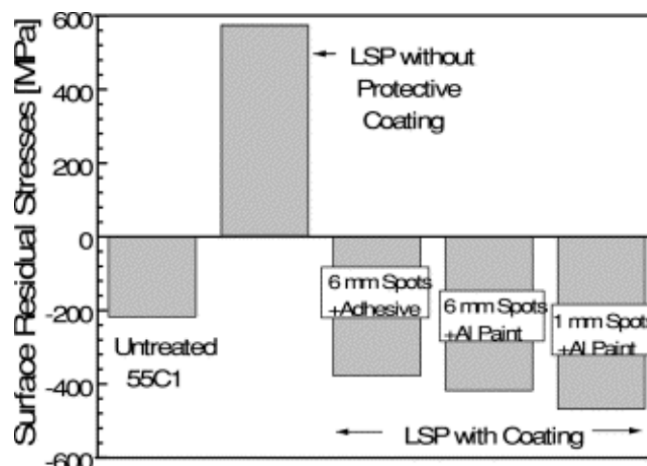


**Figure 2.27:** Effect of using absorbent coating on the average surface residual stress of LSP treated 55C1 steel (Peyre et al 1998).

### 2.6.1.3.2 Effect of laser power intensity

The effect of power density or fluence on the residual stress development was studied by Peyre et al. (1996) on A356-T6 cast aluminium alloy. It was found that the magnitude of the residual stress increased with power density, reaching a maximum threshold, and then decreased with a further increase in power density as a result of surface release waves. However, the depth of compressive RS continued to increase with the power density, Figure 2.28. A further investigation with 7050 aluminium showed that, when the power density is above a critical value (that varies according to the material to be treated and the system used) it can lead to internal cracking of the

laser treated component (Liu et al 2007). These cracks propagate under subsequent cyclic loading, thereby reducing the fatigue life of the component, Figure 2.29.

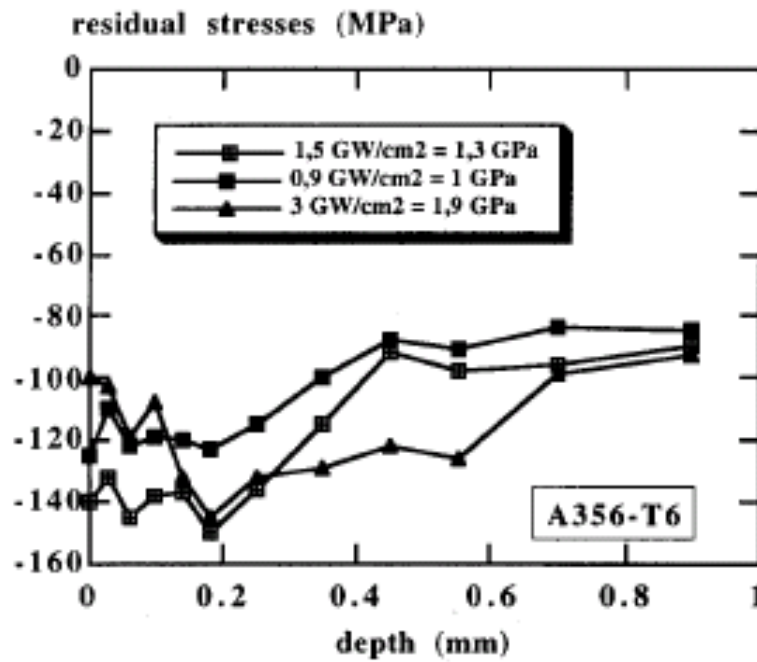


Figure 2.28: In-depth residual stress increases with power density but surface residual stress decreases by 100 MPa when power density is increased to 3 GW/cm<sup>2</sup>, as found for laser treated aluminium alloy A356.

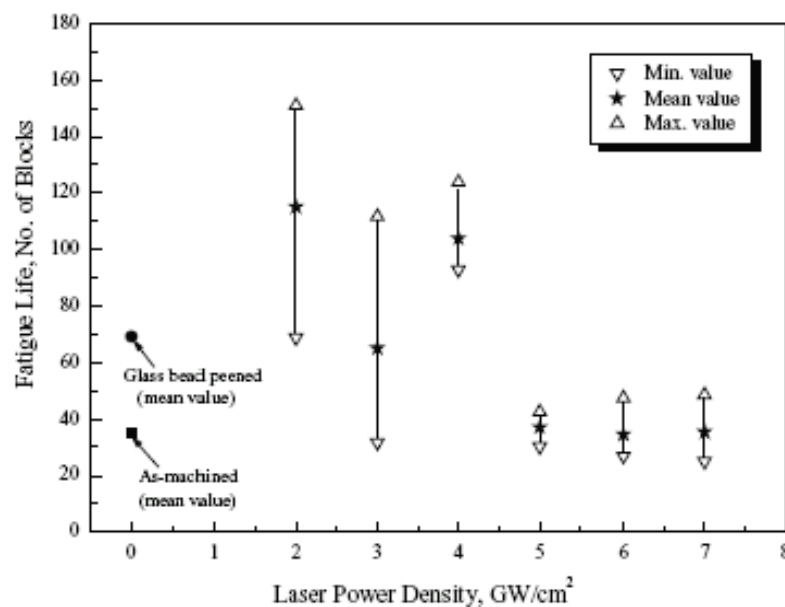
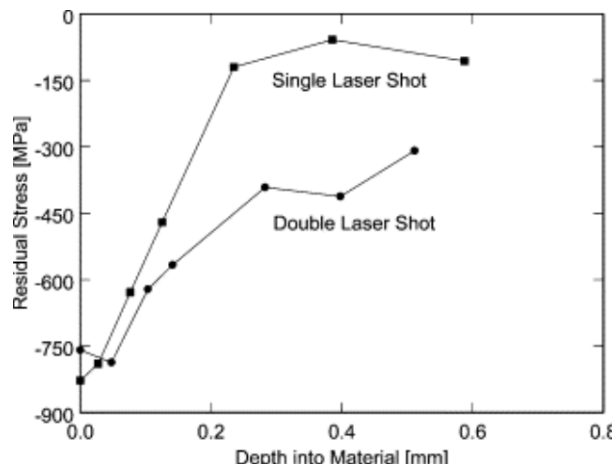


Figure 2.29: Effect of laser power density on the fatigue life of LSP treated 7050 aluminium alloy under a maximum load of 390 MPa. Higher power density can reduce the fatigue life similar to the untreated sample (Liu et al 2007).

### 2.6.1.3.3 Influence of multiple laser shock

The depth of the compressive residual stress layer can be increased by employing consecutive shots. Dane et al (1998) investigated the influence of multiple laser shock on Ti-6Al-4V alloy treated at the same spot size and with a power density of  $200 \text{ J/cm}^2$ , and a pulse duration of 30 ns. The result is shown in Figure 2.30. It can be seen that although the surface CRS is slightly less compressive with two successive laser shots, at a depth of 0.2 to 0.6 mm the magnitude of the CRS is at least twice that of the single laser shot.



**Figure 2.30:** Effect of using multiple laser shot on the residual compressive stress in Ti-6Al-4V alloy (Dane et al 1998).

For a 7075 aluminium alloy, the depth and magnitude of the residual compressive stress is found to be increased with the increase in number of laser impacts, Figure 2.31. Using a constant power density of  $4 \text{ GW/cm}^2$ , a single impact generates compressive stress of 170 MPa, while a double impact raises this stress value to 240 MPa and for a triple impact the stress value found was 340 MPa (Peyre et al 1996). Similar results were found for 0.55% carbon steel and 4340 steel (Clauer 1996).

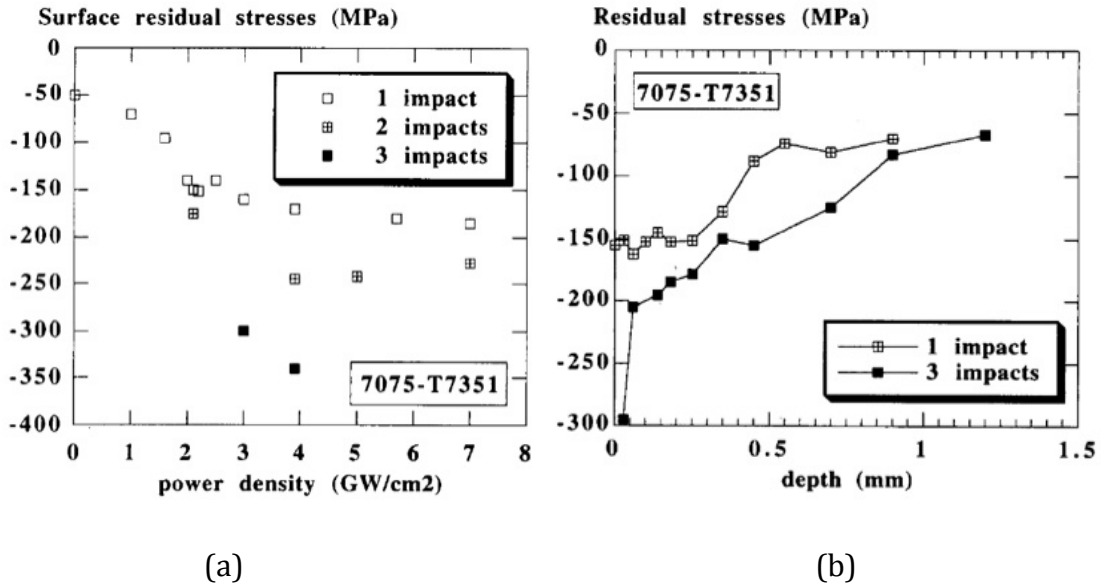


**Figure 2.31:** (a) Variation of surface residual stress with power density showing the effect of number of impacts, (b) Effect of shot impacts on the residual stress as a function of depth (Peyre et al 1996)

#### 2.6.1.3.4 Effects of overlapping of laser spots

From several investigations with many metals and alloy systems, such as steel (Peyre et al 1998); aluminium alloy: A 356, 7075, 7049-T73 (Rankin et al 2003); titanium alloys: Ti-6Al-4V (Ruschau et al 1999) etc., it was found that the overlapping of laser spots is beneficial in peening larger areas or larger components as even modern high performance laser systems are limited in the areas treated per pulse. According to the results reported so far, a uniform distribution of compressive residual stress can be achieved by overlapping without any deterioration of the properties. When overlapping was increased from 10% to 25%, a more homogeneous CRS layer was found for 0.55%C steel (Masse & Barreau 1995), Figure 2.32.

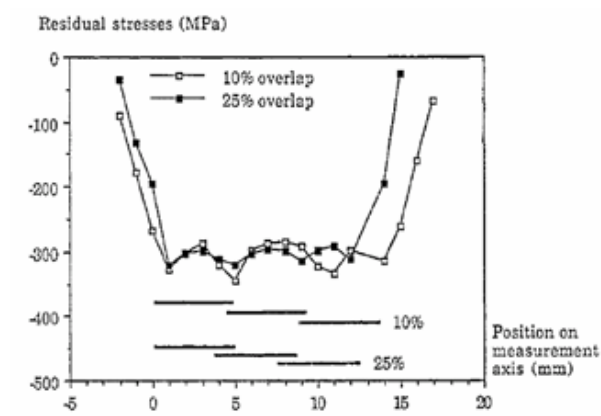


**Figure 2.32:** Influence of overlapping on the superficial residual stress state in 0.55% C steel (Masse & Barreau 1995).

Rankin et al. (2003) also studied the influence of overlapping using 7049-T73 alloy and found that although increased overlapping from 10% to 50% has the potential to enhance the plastically affected depth, the magnitude of the CRS remains unaffected.

Another study was carried out with 7075 aluminium on the residual stress distribution and the surface topography using synchrotron and neutron diffraction and also contour method. The residual stress distribution as measured by contour method shows a deep compressive stress layer at the peened surface for 10% overlapping. As both top and bottom surfaces were treated by LSP, and a compressive stress layer is present in both surfaces (Figure 2.33). It can be observed that the compressive stress is balanced by the tensile residual stress below the compressive stress region and at the edges of the plate.

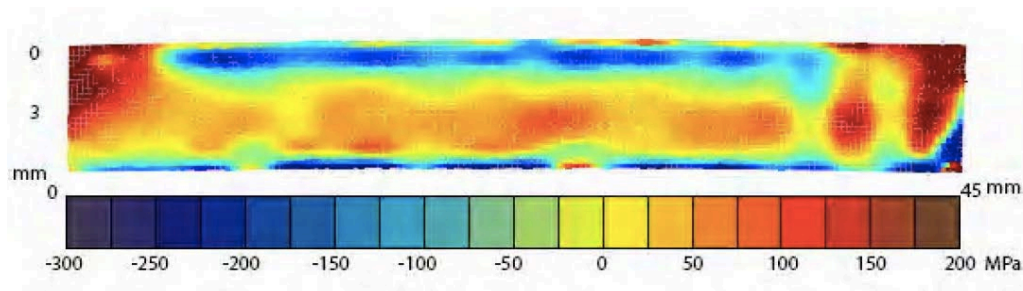


**Figure 2.33:** Residual stress profile (in 2D) with 10% overlapping, showing LSP generated deep compressive stress layer at both top and bottom surfaces (Johnson et al 2005b).

#### 2.6.1.4 Application to the aero-engine materials

It is now evident that LSP improves the fatigue life of the components. Several investigations have been carried out using aluminium alloy, steel and titanium, and found this process effective in slowing down the fatigue crack growth rate and even arresting pre-existing cracks. LSP has been found to be beneficial in improving the fatigue life of welded components where tensile residual stresses exist.

For the current study, Ti-6Al-4V simulated leading edge aerofoil samples were LSP treated and subjected to simulated FOD. The distribution of residual stress due to LSP and their redistribution due to FOD were characterized, and the consequence of the complex residual stress on the fatigue crack growth was evaluated under combined cycle (LCF+HCF) conditions.

LSP has been applied in various metals and alloys such as cast iron and powder metallurgy iron alloys, steel (Masse & Barreau 1995), aluminium alloys (Clauer et al 1983, Liu et al 2007, Peyre et al 1996, Tan et al 2004, Yang et al 2001) , nickel base alloys (Forget et al. 1993) and titanium alloys (Chahardehi et al 2010, Clauer 1996, El-Dasher et al 2006, Evans et al 2005, Golden et al 2007, King et al 2006, Martinez et al 2003, Nalla et al 2003, Ruschau et al 1999, Shepard et al 2001, Srinivasan et al 2009, Zhang et al 2010).

#### **2.6.1.4.1 LSP of Titanium alloys**

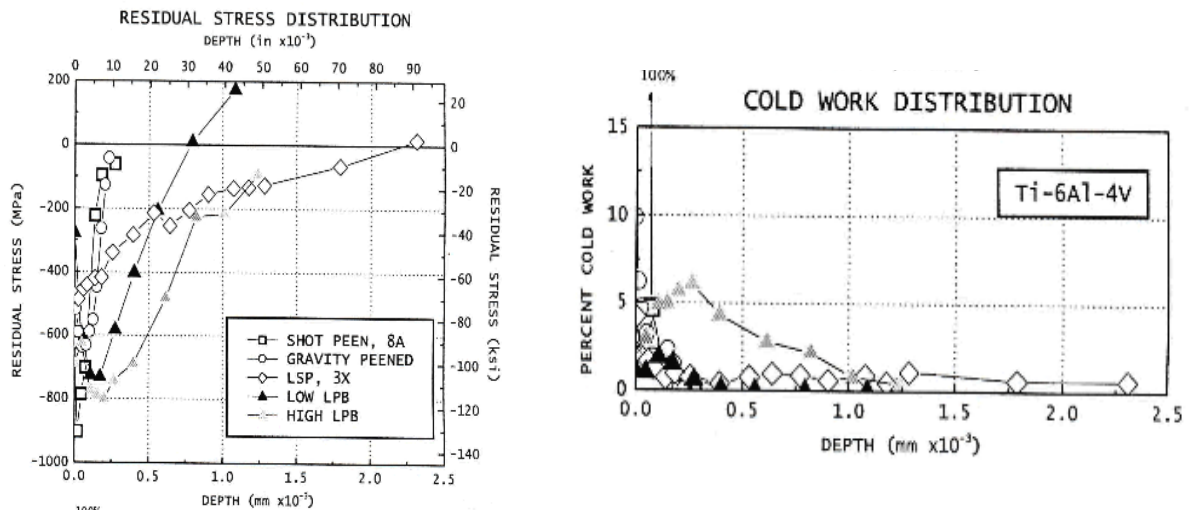
In this work, laser shock peening induced residual stress has been investigated in the titanium based fan blade alloy Ti-6Al-4V. Some basic metallurgical aspects about titanium alloys are discussed in the materials Section 1.2. In this section the postulated literature relating to the laser shock peening of Ti-6Al-4V are reviewed, focusing on the enhancement of fatigue behaviour in the presence of notches or simulated foreign object damage (FOD).

The residual stress distribution and cold work state were measured by Prevey et al. (Prevéy et al 2001) for gravity peening, LSP, SP, low and high LPB treated Ti-6Al-4V alloy, and the comparison is shown in Figure 2.34. The residual stress profiles reveal the maximum attainable depth of compression for LSP treated specimen with a surface stress magnitude of -600 MPa. Although the depth of the CRS layer was greatest for the LSP treatment, the surface compressive stress is lower in magnitude compared to other processes. Hence, the process parameters are required to be optimized properly as a surface stress of about -800MPa (Dane et al. 1998) can be achieved for the same alloy system. The absence of tensile residual stress at a depth 2.25 mm away from the surface can also be considered as beneficial from the fatigue life point of view.

Figure 2.34 also shows a comparison of the distribution of cold working between the four surface treatment techniques mentioned above. Compared to LPB, LSP treatment shows a lower degree of cold working at the surface.

Ruschau et al (1999) examined the effect of LSP induced residual stress on the fatigue crack growth rate of Ti-6Al-4V simulated leading edge aerofoil samples. Laser peening was conducted using a spot size of 5.6 mm diameter with a 30% overlapping and each spot was hit three times to ensure an adequate depth of compressive stress zone. The

residual stress was measured using X-ray diffraction combined with layer removal technique.

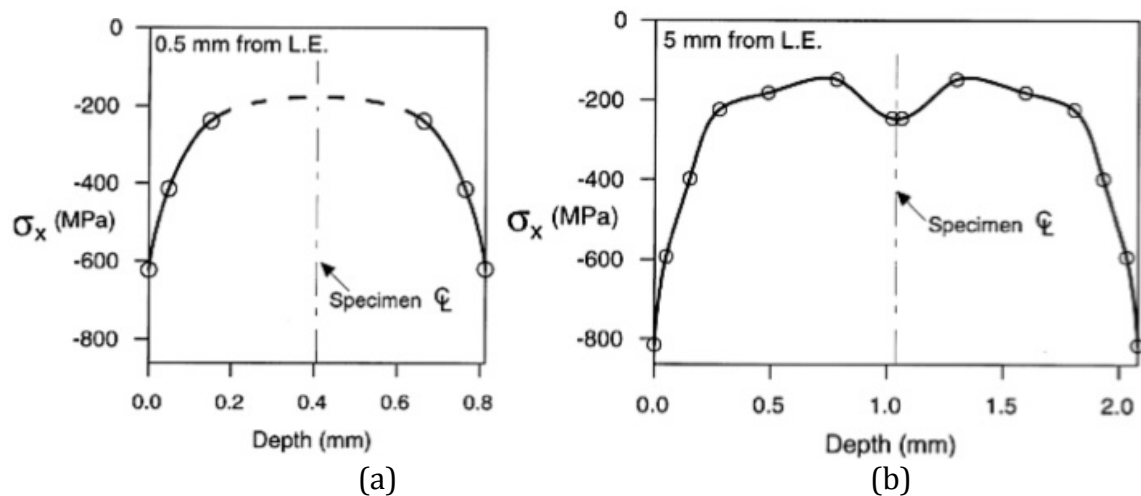


(a) Residual stress profile

(b) Variation in cold working

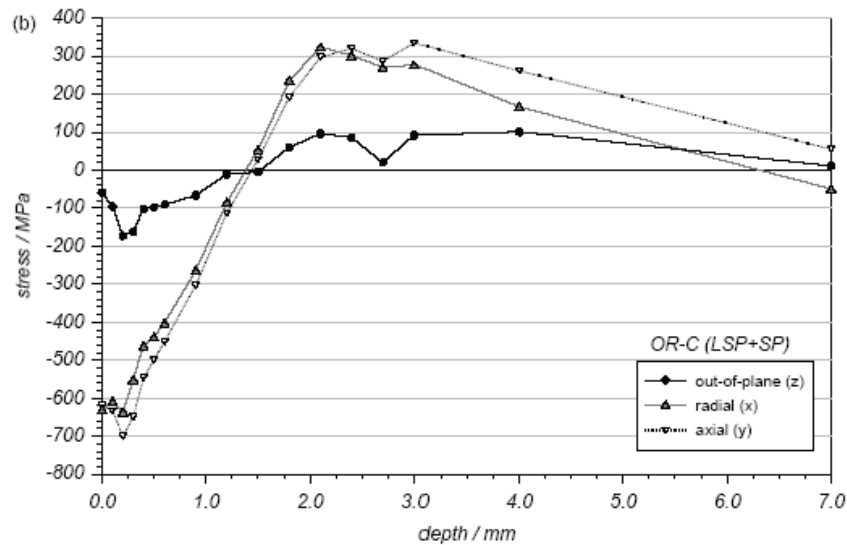
**Figure 2.34:** Distribution of residual stress and the degree of cold working in Ti-6Al 4V after SP, Gravity peened, LSP and LPB treatments (Prevéy et al 2001).

Figure 2.35 shows the residual stress profile measured at 0.5 mm and 5 mm away from the leading edge (as the sample was tapered, residual stress was expected to vary with the thickness). A compressive stress zone was observed across the whole thickness at both locations with a maximum of -600MPa at a distance of 0.5mm, and -800 MPa at a distance of 5 mm from the leading edge. For both cases, the highest level of stress was present at the surface which seemed to be less compressive with increasing depth (Ruschau et al 1999).



**Figure 2.35:** Residual stress profile as a function of depth at a distance of (a) 0.5 mm and (b) 5 mm from leading edge (Ruschau et al 1999).

King (2005) studied the residual stress distribution of laser peened wide chord fan blade (WCFB) samples at the root section. Synchrotron X-ray diffraction was used to map in-depth residual stress profile in three directions, axial, radial and out of plane, Figure 2.36. A maximum compressive residual stress of -600 MPa was found in radial direction at the surface, which is comparable to the other findings. A balancing tensile residual stress appeared at a distance of 1.3 mm below the surface, and then increased to reach a maximum value of 300 MPa, followed by a gradual decrease with further increase in depth.



**Figure 2.36:** In-depth residual stress profile of LSP+SP treated Ti-6Al-4V samples at radial, axial and out of plane direction (King 2005).

On the other hand, Frankel (2009) reported a lower level of compressive residual stress for simulated leading edge Ti-6Al-4V specimens. LSP induced residual stress distribution was measured by synchrotron and the contour method. The comparison, shown in Figure 2.37, infers that both the contour method and X-ray diffraction techniques provide a compressive residual stress of about -350 MPa at the surface that gradually decreases with increasing distance from the leading edge. The balancing tensile residual stress appeared at a distance of 6 mm from the leading edge that subsided to zero at a distance far away from the leading edge.

From the results presented above on the residual stresses associated with LSP treatment on Ti-6Al-4V it seems that the magnitude of the residual stress at the surface and the overall distribution of residual stress greatly depends on the LSP processing

parameters. It is therefore necessary to optimize the processing parameters to obtain a desirable residual stress distribution.

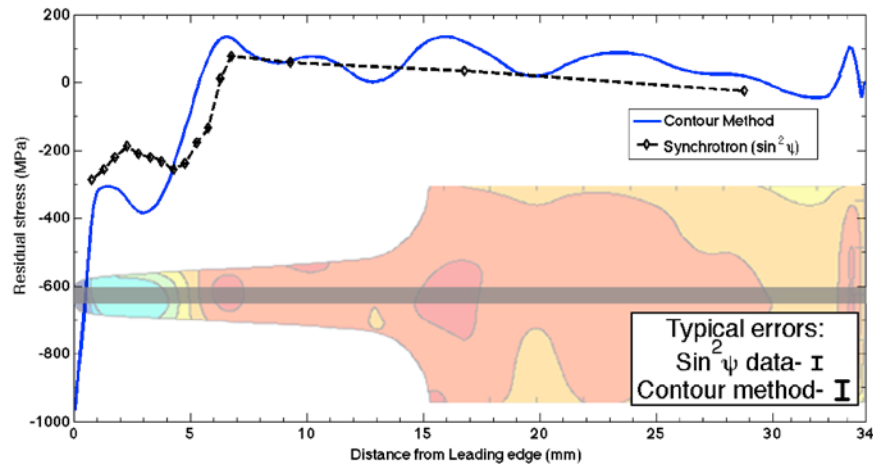
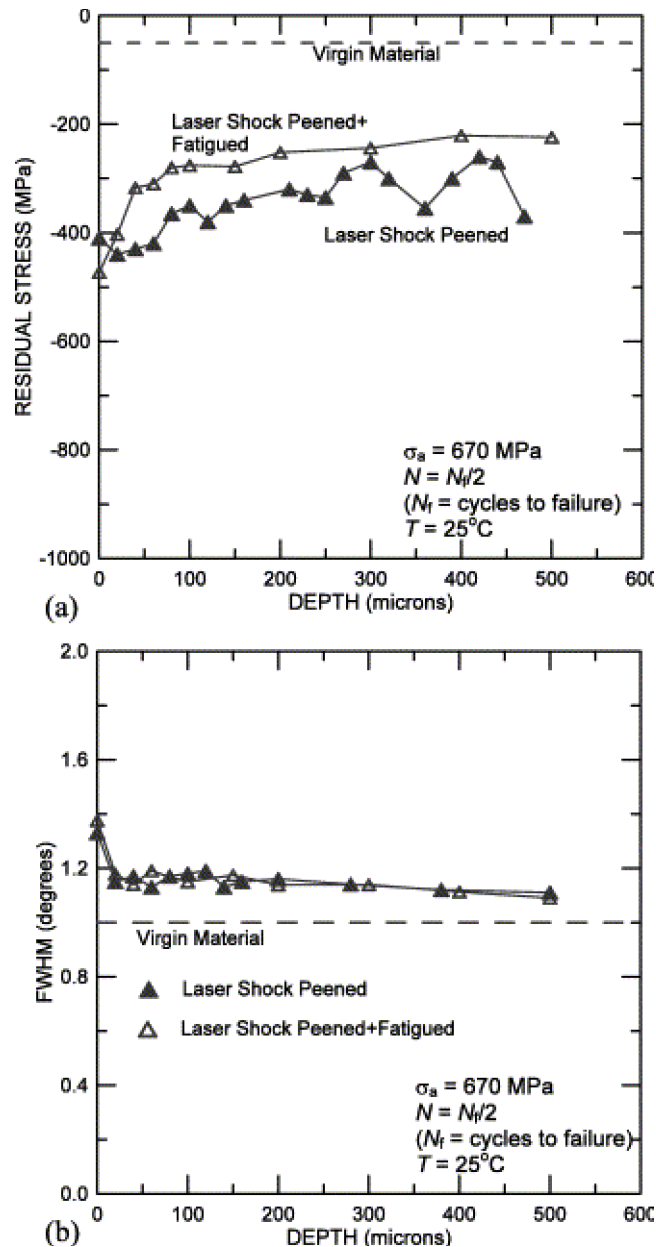


Figure 2.37: Residual stress distribution due to LSP treatment in a leading edge specimen. Comparison between synchrotron X-ray diffraction and the contour method (Frankel 2009).

The effect of the LSP process on the fatigue life of Ti-6Al-4V has been studied at the room temperature by Nalla (2003). LSP was carried out employing a power density of 7GW/cm<sup>2</sup>, pulse length of 18 ns and number of impacts used was two. The residual stress profile was measured using X-ray diffraction combined with the layer removal method. Fatigue testing was conducted at R=-1 at a frequency of 5Hz at 25°C. Figure 2.38a shows the variation of residual stress with the depth below the surface at ambient temperature. The maximum compressive residual stress in as-peened state at the surface is -400MPa that sharply decreased with increasing depth within the first 75  $\mu\text{m}$  and then remained roughly constant afterwards. Even though the compressive residual stress became more compressive at the surface after fatigue, 20% relaxation was observed overall.



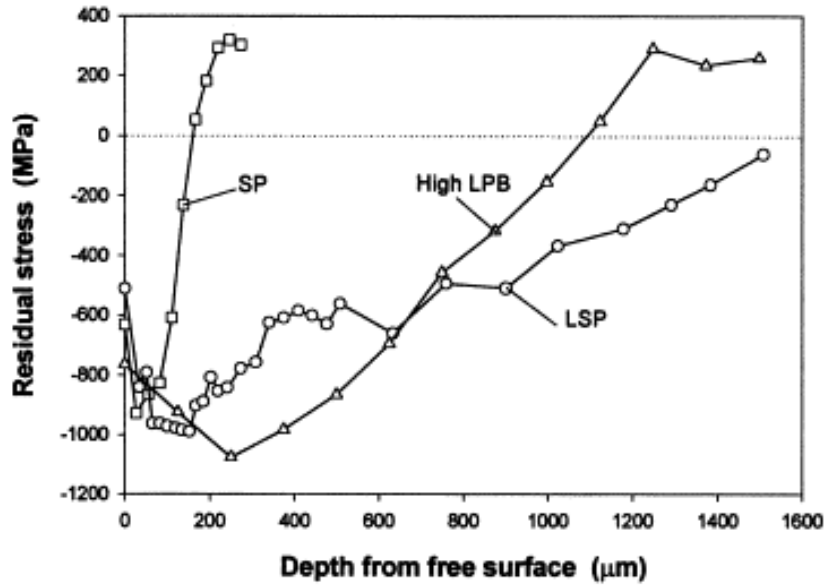
**Figure 2.38:** In-depth profiles for LSP treated Ti-6Al-4V at ambient temperature to show the effect of fatigue cycling (a) residual stress and (b) FWHM (Nalla et al 2003).

## 2.6.2 Comparison between SP, LSP AND LPB

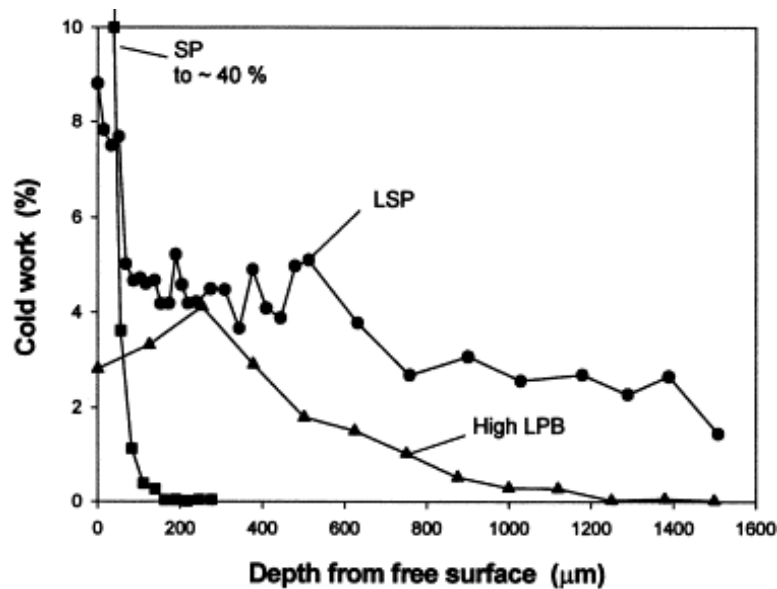
### 2.6.2.1 Residual stress profile

The major difference between SP and LSP, includes the depth of the plastically deformed layer or CRS layer. Zhuang and Holford (2001) compared the residual stress distribution and associated degree of cold work for SP, LSP and LPB treated nickel base alloy IN 718, Figure 2.39 (Zhuang and Halford 2001). As can be seen from the figure, a higher level of compressive stress can be induced by SP but the depth of the stress layer below the surface is much lower compared to LSP and high LPB. For

both SP and LPB a tensile residual stress is found beneath the compressive stress region whereas the LSP induced residual stress curve exhibits no tensile residual stress at 1.5mm below the surface. SP generated a high degree of cold working (up to 40%) at the surface in contrast to other two processes.



(a) In -plane distribution profile



(b) Variation in cold working

**Figure 2.39:** Comparison of residual stress and the degree of cold working in IN 718 following SP, LSP and LPB treatments (Zhuang and Halford 2001).

A higher stress gradient for SP is also observed compared to that obtained for the LSP process. Similar result was also found by Dane et al. (1998) with the same alloy.

### 2.6.2.2 Residual Stress relaxation

The beneficial compressive residual stress induced by surface treatment process can be relaxed under subsequent fatigue loading (mechanical relaxation) or elevated temperature application (thermal relaxation). Mechanical relaxation primarily depends on the following factors (Zhuang & Halford 2001):

- The magnitude and gradient of the initial residual stress
- The extent of cold working
- Mean fatigue stress ratio, stress amplitude and number of cycles
- Material stress-strain response and the level of cyclic work hardening or softening

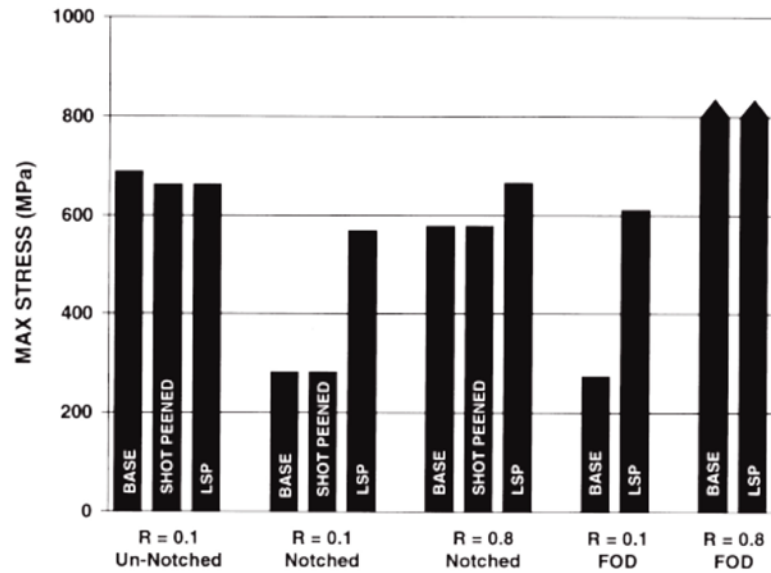
The mechanism of residual stress relaxation is still under investigation. However, it has been observed that the rate of thermal relaxation of residual stress depends on the extent of cold working at the surface (Nalla et al 2003, Prevèy 2000). Thermal relaxation of several surface treatment techniques is compared. It is observed that higher degree of cold working, as in the case of SP, leads to accelerated thermal relaxation, compared to LSP and LPB that generated low degree of cold working.

### 2.6.2.3 Effect of LSP+FOD

There are a few results available in the literature that show that LSP improves the fatigue life in the presence of FOD. However, no systematic study on the residual stress measurements on LSP+FOD condition, and their relaxation behaviour has been reported thus far.

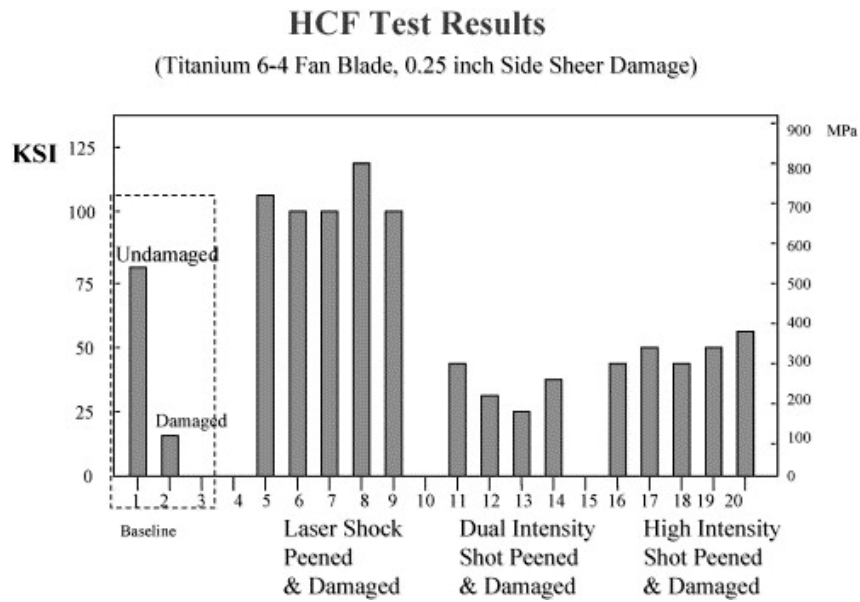
Fatigue testing was conducted at  $R=0.1$  and  $R=0.8$  for un-notched, notched and FOD'd samples (Ruschau et al 1999), and the effect of SP and LSP was compared with the untreated samples, Figure 2.40. The results show that for lower R ratios, fatigue life of a FOD'd specimen noticeably improves when treated by the LSP process, whereas the fatigue life remains almost unaffected at higher R ratio. This behaviour can be explained in terms of, at lower stress ratios, the fatigue cyclic stress is lower than the pre-existing residual stress due to LSP treatment (which is  $-600\text{MPa}$  at the surface). The fatigue crack growth is therefore suppressed by the superposition of the compressive residual stresses. On the other hand, at higher stress ratios, fatigue crack

growth rate is governed by the higher applied cyclic stress, hence fatigue life remains insensitive to the LSP stress.



**Figure 2.40:** Effect surface treatment (LSP and SP) on the fatigue strength of notched and FOD'd Ti-6Al-4V simulated leading edge sample at R=0.1 and 0.8 (Ruschau et al 1999).

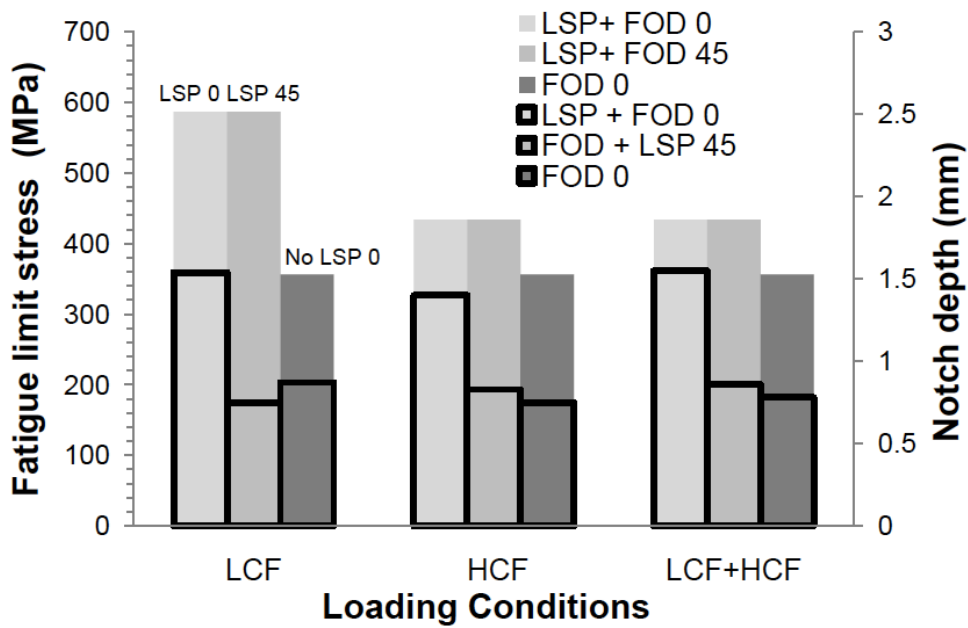
Laser peening has also been found to increase the fatigue life of the FOD'd specimen dramatically, Figure 2.41, compared to the shot peening process (Hammersley et al 2000).



**Figure 2.41:** Comparison of the High cycle fatigue behaviour in presence of FOD damage between laser shock peening and shot peening (Hammersley et al 2000).

## 2.7 Fatigue life assessment under LSP+FOD

Fatigue experiments were carried out by our research partner at the University of Portsmouth (Spanrad 2011). Some important results are summarized in this section to have a better understanding of the effect of solely LCF and CCF on the residual stress relaxation associated with peening and FOD impact; and the redistribution of these stresses in subsequent fatigue crack growth under low and combined cycle fatigue as presented in the following Chapters. Fatigue limit stresses can be defined as that stress below which a material can undergo an infinite number of fatigue cycles without failure. The fatigue limit stress for bimodal Ti-6Al-4V alloy has been reported as 500 MPa. Fatigue limit stress in peened and impacted specimens are shown in Figure 2.42, together with the corresponding notch depth in framed symbols. Compared with the unpeened 0° FOD, it is clear that in all fatigue loading conditions, LSP has noticeably improved the fatigue performance of the material in presence of FOD impact.



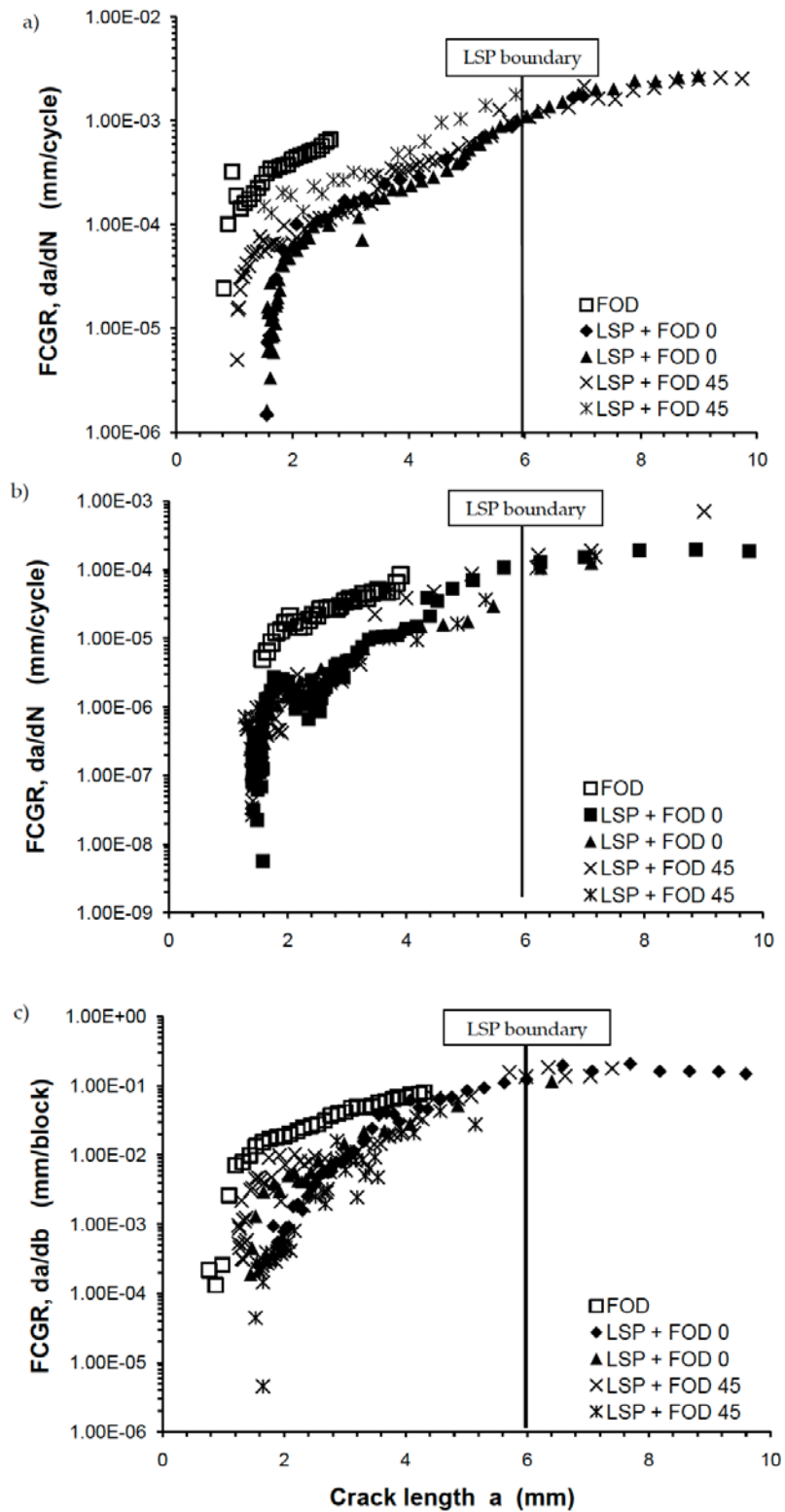
**Figure 2.42:** Fatigue limit stresses for  $0^\circ$  (with and without peening) and  $45^\circ$  FOD impacted specimen (with peening only) under LCF, HCF and combined cycle (LCF+HCF) fatigue. The corresponding notch depths are shown in the secondary Y-axis (Spanrad 2011).

Figure 2.42 also suggests that the stress required to initiate and propagate fatigue crack under HCF and CCF is similar with a value of 435 MPa, whereas a 35% higher stress was required under LCF type of loading. This might be due to the compressive residual stresses associated with peening and FOD impact as seen in section 4.3.1. It is known that residual stresses modify the maximum and minimum i.e. mean applied stress rather than the total stress range or stress intensity range. This suggests that at low R values the beneficial effect from the compressive residual stress is prevalent. Similar results were also found by Ruschau et al. (1999) for  $30^\circ$  FOD impact on L.E. specimen after peening; where at  $R=0.1$  fatigue life is improved significantly but no improvement was observed at  $R = 0.8$  compared with the as-FOD'd condition (Ruschau et al 1999). An attempt was made to calculate the stress intensity factor by our research partner (Spanrad 2011).

It is important to note here that for  $45^\circ$  FOD impacts the notch depth at the deeper side is about 1.6 mm, which is similar to that for  $0^\circ$  FOD specimens. Researchers have shown that the fatigue life generally decreases with increasing notch depth (Mall et al 2001, Ruschau et al 2003). Here, however, it is shown that even though the notch depth for  $0^\circ$  FOD specimen was twice as deep as  $45^\circ$  FOD specimens, the fatigue limit stresses

in both cases are the same. This discrepancy might be attributed to the fact that here for 45° FOD specimens, average notch depth (average depth between the shallow and the deeper notch side) is reported as 0.8mm, whereas crack initiation and propagation occurs first from the deeper side of the notch. Hence, for an asymmetric notch with variable notch depth at the entry and exit side of the impactor on the specimen, averaging the notch depth may be misleading. Therefore, the depth at the deeper side should be reported in the fatigue life assessment of the aerofoil components instead of the average notch depth for 45° FOD specimens.

The fatigue crack growth rate behaviour with the crack length  $a$  is shown in Figure 2.43 for LSP+FOD specimens under three loading conditions. The beneficial effect of laser shock peening treatment is evident for both 0° and 45° FOD impacts over the as-FOD'd condition. It is noted that the as-FOD'd data presented here is for 0° impact angle and the applied load used was 20% less than that for LSP+FOD specimens. Most importantly the FOD notch depth is ~0.8 mm, which is half that of peened and FOD'd specimens. It would be more appropriate to compare the LSP+FOD data with the as-FOD'd data having similar notch depth.



**Figure 2.43:** Fatigue crack growth rate as a function of crack length for  $0$  and  $45^\circ$  FOD impact with prior peening and  $0^\circ$  FOD without peening under (a) LCF cycles at  $R=0.1$ , (b) HCF cycles at  $R=0.7$  and (c) CCF at  $R=0.1$  and  $0.7$  and 1000 HCF cycles were incorporated on to 1 LCF cycle (Spanrad 2011).

It would be more appropriate to compare the LSP+FOD data with the as-FOD'd data having similar notch depth.

Figure 2.44 shows the fatigue crack growth rate,  $da/dN$  or  $da/db$  as a function of stress intensity factor range,  $\Delta K$  for LCF, HCF and CCF loading condition for unpeened FOD'd and peened FOD'd specimens both for  $0^\circ$  and  $45^\circ$  impact. It is evident from the plots that in all loading conditions residual stresses induced by LSP increase the  $\Delta K$  value, hence improves the fatigue life despite the twice as deep as notch in LSP+FOD specimens. Only under LCF condition, Figure 2.44a  $45^\circ$  impact condition is more damaging than  $0^\circ$ . This may be attributed to the higher amount of residual stress as observed for  $0^\circ$  impact (see section 4.3 for the corresponding residual stress results). At high R ratio,  $R=0.7$ , Figure 2.44b the effect of such difference in residual stress between  $0^\circ$  and  $45^\circ$  diminishes, and crack growth data for two impact conditions merge together. Similar observation can be made for CCF loading, Figure 2.44c where crack growth data for  $45^\circ$  FOD specimen are scattered. This infers that the effect of residual stress is dominant in low R ratio compared to high R ratio as also reported in previous studies (Thompson et al 2001). Figure 2.44c also suggest that under combined cycle fatigue, the onset of  $\Delta K$  value is  $\sim 30 \text{ MPa}\sqrt{\text{m}}$ , nearly double compared to the unpeened FOD condition.

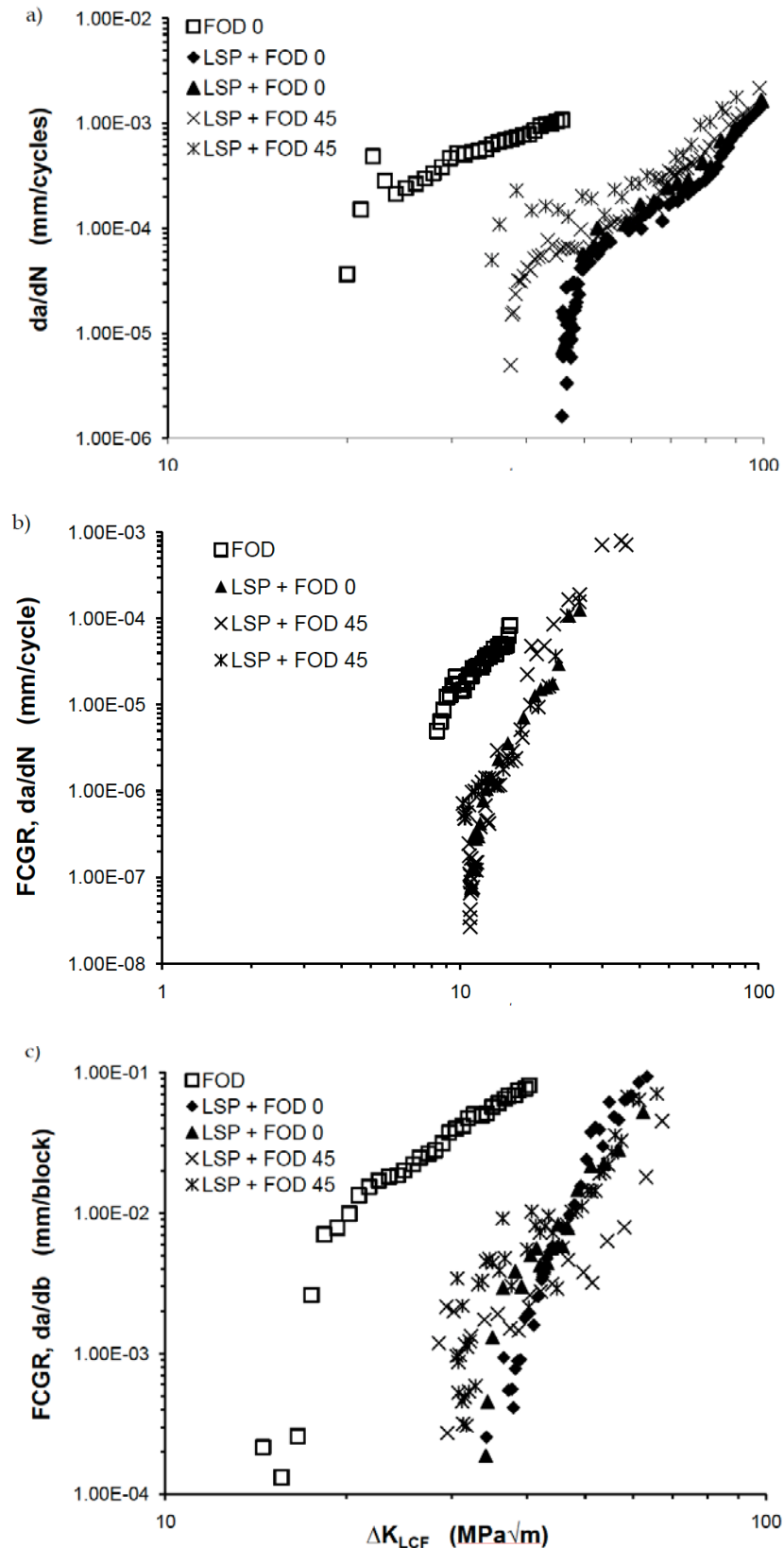


**Figure 2.44:** Variation of fatigue crack growth rate as a function of stress intensity factor range calculated with a standard single edge crack solution under: (a) LCF cycles at  $R=0.1$ , (b) HCF cycles at  $R=0.7$  and (c) CCF at  $R=0.1$  and  $0.7$  and 1000 HCF cycles were incorporated on to 1 LCF cycle (Spanrad 2011).

## Chapter 3 Experimental Method

### 3.1 Material and Specimen Geometry

Ti-6Al-4V is widely used for aero-engine compressor blades and is thus studied here. Full details of the alloy and the manufacturing process have been discussed previously (section 2.1). In brief, the manufacturing process involves forging above the  $\beta$  transus of the material, then in the  $\alpha+\beta$  phase field to produce a bimodal microstructure comprising  $\sim 60\%$  of primary  $\alpha$  and 40% (by volume) of lamellar colonies of  $\alpha+\beta$ , Figure 3.1. The alloy is subsequently solution treated at about  $927^\circ\text{C}$  and then stress relieved at  $705^\circ\text{C}$  for 2 hours. Finally, the specimens were machined from the forged blanks. The specimens were supplied by Rolls-Royce plc. The room temperature mechanical properties of Ti-6Al-4V can be represented by Young's modulus,  $E=103\text{GPa}$ ; yield strength,  $\sigma_Y = 860\text{MPa}$ ; and ultimate tensile strength,  $\sigma_{\text{UTS}} = 980\text{MPa}$  (Spanrad 2011). The chemical composition of the alloy is given in Table 3.1 (Rolls-Royce standard MSRR 8610).

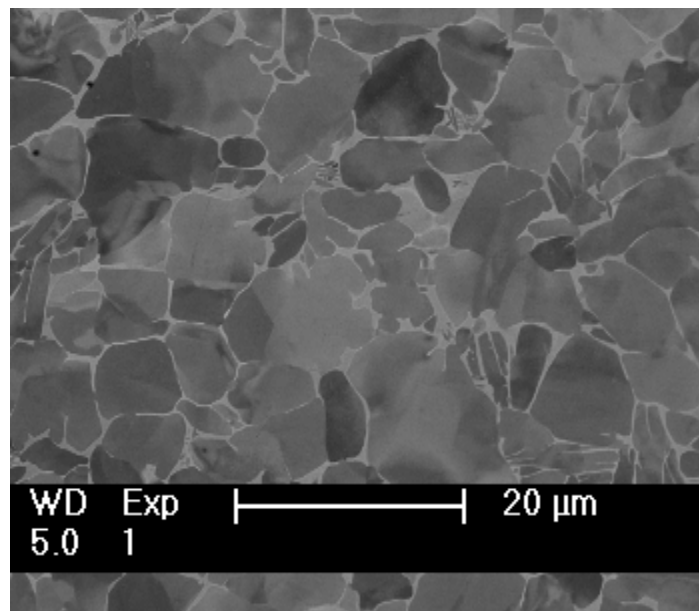


*Figure 3.1: As-received microstructure of bimodal Ti-6Al-4V.*

**Table 3-1:** The chemical composition of Ti-6Al-4V alloy (in wt. %)

Elements	Al	V	Fe	C	O	N	Y	H
MSRR	5.50 -	3.5 - 4.5	< 0.3	< 0.08	0.14 -	< 0.03	< 0.005	0.01
8610	6.75				0.23			25

Foreign Object Damage (FOD) generally occurs at the leading edge of the turbofan blades and low temperature compressor blades situated at the front end of aero-engines. Therefore, the specimen geometry has been designed to simulate a generic leading edge of an aero-engine fan or compressor blade, as illustrated in Figure 3.2a.

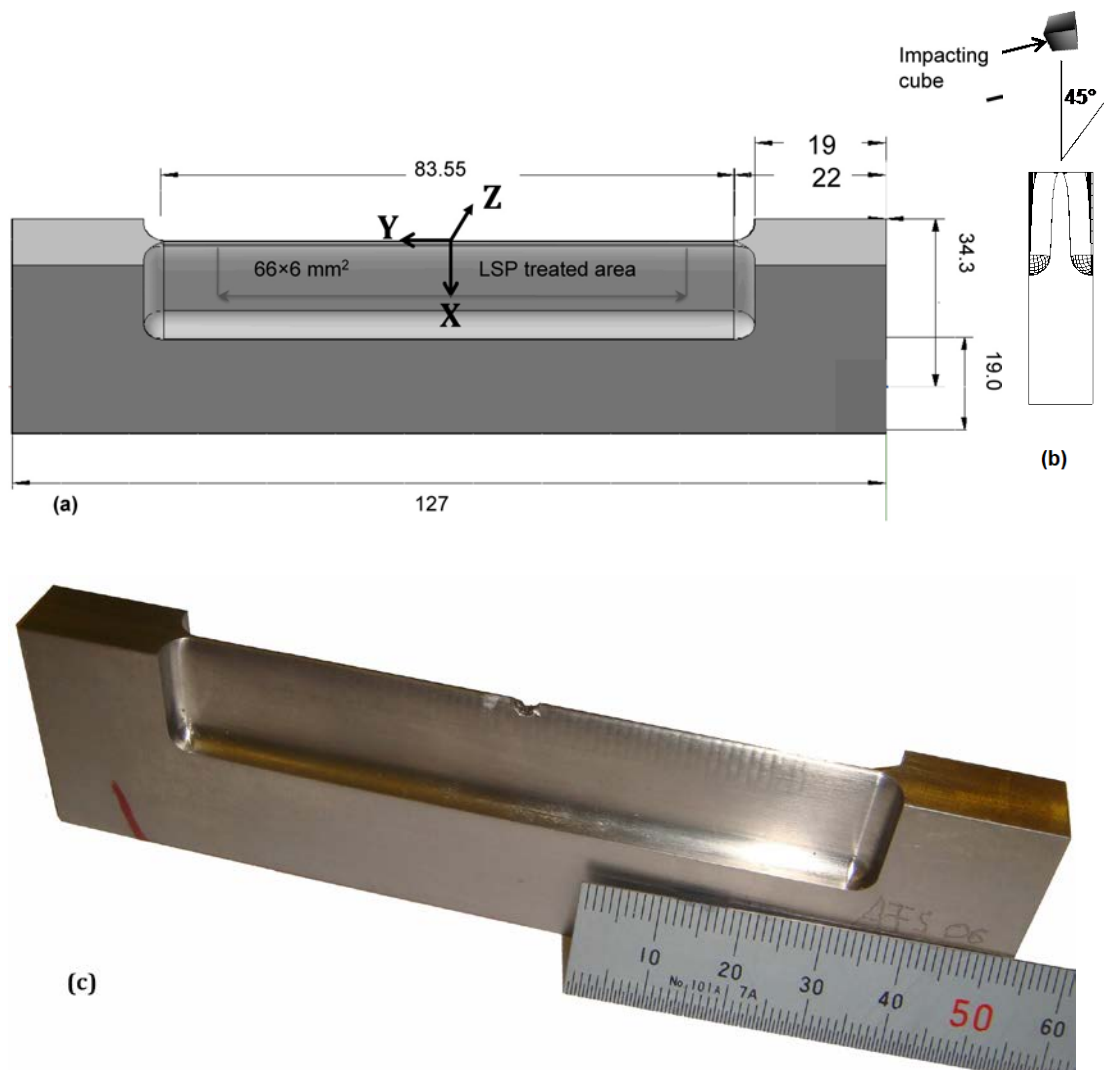


**Figure 3.2:** (a) Laser shock peened four-point bend (4PB) simulated aerofoil specimen geometry (all dimensions are given in mm), where X and Y represent transverse and longitudinal directions respectively (b) Schematic of 0° and 45° FOD impact, shown on the cross-section of the sample along the mid XZ plane (c) a photograph of the specimen.

The aerofoil specimen has a leading edge section with a circular tip of a radius,  $r = 0.53$  mm, which is tapered elliptically to join with the rectangular section. The joining edge has a circular radius,  $r = 3$  mm. The maximum thickness of the tapered leading edge part is 3 mm and the thickness of the surrounding rectangular part is 3 times as thick to provide enough constraint and to prevent buckling during the subsequent four-point bend (4PB) fatigue testing. The leading edge of the specimen is laser shock peened over the area shown in Figure 3.2a.

### **3.2 Laser Shock Peening (LSP) Process**

The machined samples were laser shock peened (details can be found elsewhere, (Ruschau et al 1999)) over the leading edge by Metal Improvement Company, USA at a power density of  $10 \text{ GW/cm}^2$ , using a spot size of  $3 \times 3 \text{ mm}^2$ , 50% overlap and 200% coverage, with a pulse duration of 27 ns. The LSP'd region extends 6 mm from the leading edge and over 66mm of the leading edge.

### **3.3 Simulation of Foreign Object Damage (FOD)**

To simulate FOD damage condition that occurs as a result of ingested particles at high velocities and strain rates, the specimens were ballistically impacted using a light compressed gas gun at the Department of Engineering Science, Oxford University, UK. The gas gun was equipped with a 2 litre gas cylinder connected to a 2.5 m long sleeved barrel, Figure 3.3. The details of the damage simulation technique is described elsewhere (Nowell et al 2003). To replicate the 'worst case' damage, hardened steel cubes were chosen with a hardness value between Rockwell C 62 and 64. The steel cube was mounted in a nylon sabot to prevent rotation and to ensure that the steel cubes hit onto the leading edge of each specimen in the centre of the gauge length, either with edge first or point first. The specimens to be impacted were mounted in a cross-vice that could be rotated and translated using a motor-driven system with micrometre precision. Two impact angles were chosen for this study:

0° FOD impact: Where a 3.2 mm hardened steel cube was directed at an angle of 0° to the leading edge (parallel to the transverse 'x'

direction) with an impact velocity of 200 m/s. In this case, the cube hit the specimen with edge first.

45° FOD impact: Where a 4.8 mm hardened steel cube was directed at an angle of 45° to the leading edge with an impact velocity of 250 m/s. In this case the cube was orientated to hit the specimen with point first.

The nominal impact velocities as mentioned above were within 8% of the recorded velocity. Note the difference in impact velocities and the size of the projectile between the two impact conditions. The notch depth for each specimen was measured from the profile view of the notch taken by an optical microscope. Figure 3.4 illustrates the notch depth,  $d$ , measured from the tip of the leading edge to the root of the notch, for a 0° impacted specimen. Specimens impacted at 45° are associated with an asymmetric notch with a shallower depth,  $d_1$  at the entry side and deeper depth,  $d_2$  at the exit side as shown in Figure 3.4.

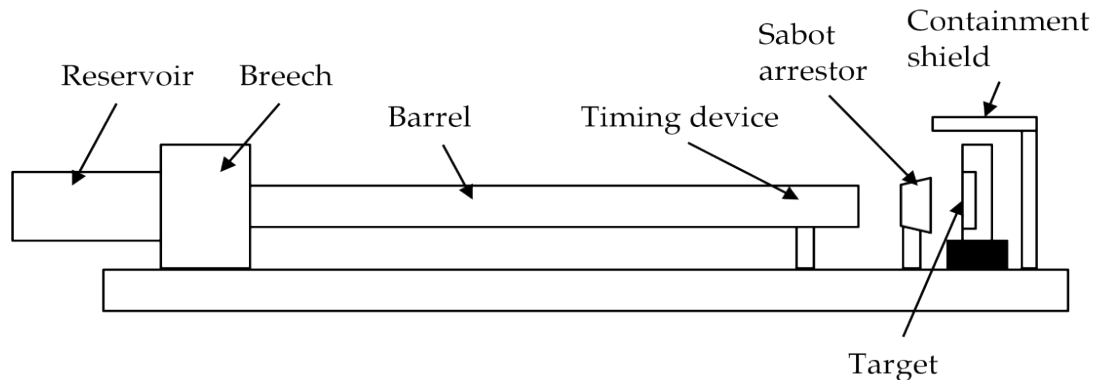


**Figure 3.3:** Schematic of the gas gun used to simulate FOD at Oxford University, UK (Nowell 2008)

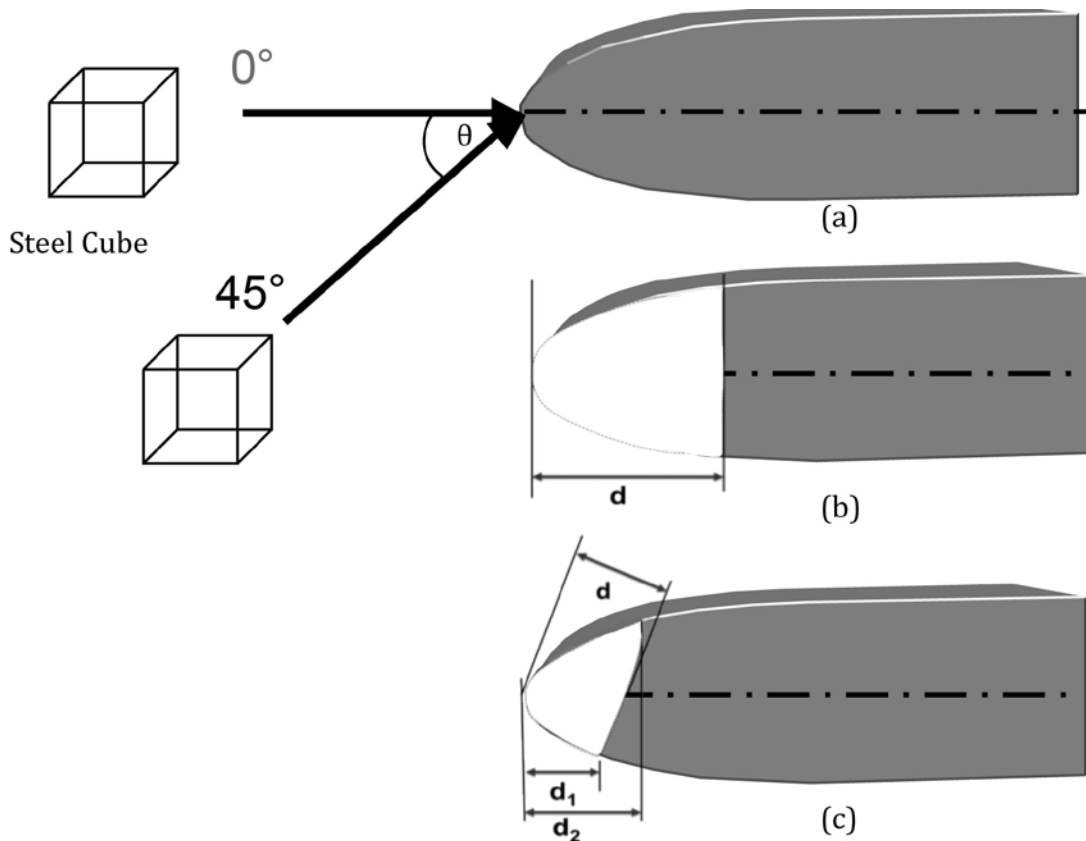


Figure 3.4: Schematic representation of the (a)  $0^\circ$  and  $45^\circ$  impact condition, (b) notch depth,  $d$  for a  $0^\circ$  impact and (c) notch depths for an asymmetric  $45^\circ$  impact.

### 3.4 Fatigue Testing

The fatigue testing of all specimen studied in this project was carried out by our research partner at the University of Portsmouth (Spanrad 2011). A servo-hydraulic twin-actuator 100kN fatigue testing machine designed for high cycle (HCF) and low cycle (LCF) load applications was used for the fatigue experiments. Experiments were carried out at room temperature under block loading of combined LCF and HCF cycles with 1000 HCF cycles superimposed upon 1 LCF cycle, representing a simplified flight spectrum. A combine cycle loading block is schematically represented in **Figure 3.5**. The crack growth was monitored using a direct current potential drop (DCPD) system with nanovoltmeters. The crack lengths were verified post testing from the fracture surfaces. Full experimental procedures may be found in (Hall et al 2008b, Spanrad 2011).

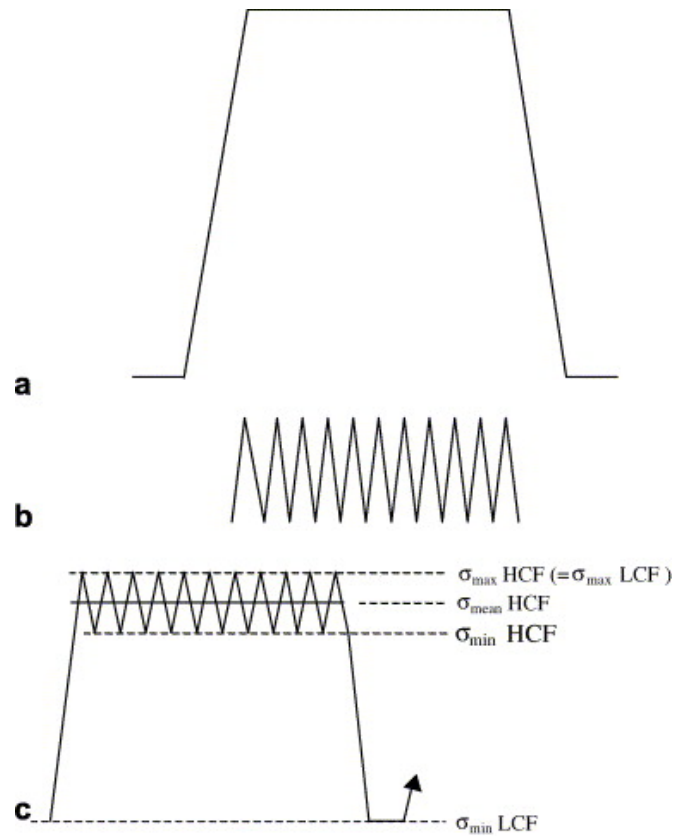


Figure 3.5: Schematic representation of (a) LCF, (b) HCF and (c) combined cycle fatigue (CCF) (Ding et al 2007).

### **3.5 Specimen Studied**

The specimens studied in the current investigation and the corresponding fatigue loading conditions is presented in Table 3-2 and Table 3-3 for **0° and 45°** FOD impact respectively.

Table 3-2 0\* FOD specimens characterized at various synchrotron radiation sources

Spec ID	Wave-form	Applied Stress (MPa)	1 <sup>st</sup> prep. (APS)	2 <sup>nd</sup> prep. (ESRF 1)	3 <sup>rd</sup> prep. (HARWI-II)	4 <sup>th</sup> prep. (ESRF 2)	5 <sup>th</sup> prep. (HEMS)
S-1			Untested				
S-2	LCF+HCF	434	N=1 block,	N=100 blocks	-	$\Delta a = 0.7$ mm N= 1901 blocks	-
S-3	LCF+HCF	434	-	$\Delta a_f = 0.6$ mm N=2744	$\Delta a = 1.0$ mm N=2979	-	$\Delta a = 2.1$ $\Delta N = 421$
S-4	OVERLOAD	>860	-	-	-	-	Overload
S-5	LCF	586	-	-	-	$\Delta a = 0.56$ mm n=20272cycles	-
S-6	LCF	586	-	-	-	-	$\Delta a = 5.3$ mm n=34313Cycles

Table 3-3: 45° FOD specimens characterized at various synchrotron radiation sources

Spec ID	Waveform	App. Stress (MPa)	1st prep. (APS)	2nd prep. (ESRF)	3rd prep. (HARWI-II)	4th prep. (ESRF)	5th prep. (HEMS)
S-7	No Loading, LCF+HCF		Untested		-	N=10 blocks $S_{\max}=586$ MPa	-
S-8	LCF+HCF	430		N=100 blocks	-	$\Delta a=2$ mm N= 1439 blocks	-
S-9	LCF	521/586		n=1000, $S_{\max}=521$ MPa	-	n=10 <sup>5</sup> $S_{\max}=586$ MPa	-
S-10	LCF	586	-	-	-	-	$\Delta a=2.2$ mm, n=59641
S-11	LCF+HCF	434	-	-	-	$\Delta a=7$ mm N=1262 blocks	-
S-12	LCF+HCF	452		$\Delta a_f= 0.6$ mm N=589 blocks*	-	-	-

## **3.6 Residual Stress Measurement Techniques**

### **3.6.1 Through thickness averaged Synchrotron X-ray Measurements**

Residual elastic strains have been mapped in laser shock peened leading edge samples using high energy synchrotron X-ray diffraction in as peened, as FOD'd and after subjecting to various fatigue loading conditions.

Through thickness averaged residual strain measurement were carried out initially at the Advanced Photon Science (APS), Chicago, USA; afterwards at the Hamburger Synchrotronstrahlungslabor, HASYLAB of the Deutsches Elektron-Synchrotron, DESY, Hamburg, Germany, and also at PETRA III, DESY. Even though identical principles were applied for all three above mentioned synchrotron facilities, each experiment was slightly different in certain aspects that will be discussed later. Important parameters regarding the synchrotron source, insertion device used for the specific beamline, monochromator and detector are given in Table 3-4 for the four beamlines used for this project.

Table 3-4: The key parameters in four different synchrotron radiation source used in this study.

Synchrotron Source	APS *	HASYLAB** DORIS III	HASYLAB* ** PETRA III	ESRF****
Energy GeV	7.00	4.45	6.084	6.00
Initial positron beam current (mA)	100	140 (5 Bunches)	80 (in top-up mode)	200
Cicumference (m)	1104	289.2	2304	844
Beamline	(1-ID-C)	HarWI II	P07 HEMS	ID31
<b>Insertion Device: Wiggler/Undulator</b>				
Type	3.3 Undulator	Hard X-ray wiggler	Standard 2m	3 Ex-vacuum
Magnet Type	A	Hybrid	Hybrid	
Period Length (mm)	33	110	29	Two 35 and one 32
Number of Period	72	35	69	
Total Length (m)	2.4	4	2	1.6
Max. Magnetic Field (T)	0.70	1.98	0.81	0.64
Max Deflection Parameter K	2.17	20.3	2.2	
Total radiated Power (kW)	-	29	7.5	
Power Density (kW/mrad <sup>2</sup> )	-	32	0.19 W/murad <sup>2</sup>	
Critical Energy (keV)	23.5	26.7	3.45	
Min Gap (mm)	11	14	10.9	11
Phase Error (rms)	<8 degrees	-	Calc. with 0	

**Monochromator**

<b>Type</b>	Si(111) Bent Double- Laue	Tempered Si(111) Bent Double- Laue	Si (111)	Si (111) Double Crystal
<b>Energy Range (keV)</b>	50-130	20-200	DCM 30-200 SBM 53.3/87.1	5-60
<b>Energy used (keV)</b>	65	65	53.3	
<b>Initial Beam Size (mm<sup>2</sup>) (h×v) FWHM</b>		10×10	0.3×0.5	0.5–2.5 mm (h) by 0.1-1.5 mm (v)
<b>Beam Used (mm<sup>2</sup>)(h×v)</b>	0.2×0.1	0.2×0.1	0.2×0.1	0.2×0.1
<b>Photon Flux (photons mm<sup>-2</sup> s<sup>-1</sup>)</b>		10E14/s in 0.1% BW	In EH1 SBM App 10E08/s	1.5×10 <sup>12</sup> at 0.43 Å

**Detector**

<b>Type</b>	MAR345	MAR555	MAR345	Position Sensitive Detector
<b>Channel Size (µm)</b>	100×100	140×140	100×100	
<b>Active area (mm)</b>	Ø345	430×345	Ø345	
<b>Resolution (pix)</b>	3450	3072×2560	3450	
<b>Total read-out time</b>	Up to 80s	1200 ms	Up to 80s	

\* (Dejus et al 1994, Lai et al 1993, Shastri et al 1998)

\*\* (Fitch 2004, Laclare 1994)

\*\*\* (Beckmann et al 2003, Bouchard et al 1998, Lathe et al 2006, Lippmann et al 2007, Liss et al 2003, Neseemann et al 1995)

\*\*\*\* (Balewski et al 2004, Schell et al 2008)

### 3.6.1.1 Advanced Photon Science

An initial experiment was carried out on the 1-ID-C beamline at APS. A monochromatic synchrotron X-ray beam with 65 keV energy or 0.1907 Å wavelength was selected using a Si (111) Bent Double Laue monochromator. The measurement was carried out in through thickness transmission geometry with a small  $2\theta$  scattering angle of 6.6°. Figure 3.6(a) and (b) shows the experimental set up. As LSP treatment induces a steep stress gradient that is further augmented by the FOD impact, a high spatial resolution was required to accurately measure the strain variation in the vicinity of the FOD damage. Therefore, the incident beam size was specified by a rectangular slit size of 0.2 mm in the horizontal direction and 0.1 mm in the vertical direction. Figure 3.7 shows the scanning arrangements of the measurement points taken for specimen S-1, S-2 and S-7 (see Table 3-2 and Table 3-3)

The samples were aligned by determining the co-ordinates of the FOD notch root and the edges of the notch. This was accomplished by an intensity scan of the samples as a function of position. No images were acquired at this stage. The volume of the illuminated region was  $0.1 \times 0.2 \times 2.0 \text{ mm}^3$ , adequate to capture a sufficient number of grains properly oriented for the diffraction. For each specimen, about 900 individual measurement points were collected. The diffracted beam from the specimen was captured employing a MAR-345 image plate detector as shown in Figure 3.6b, where a complete Debye-Scherrer ring was acquired for each point.

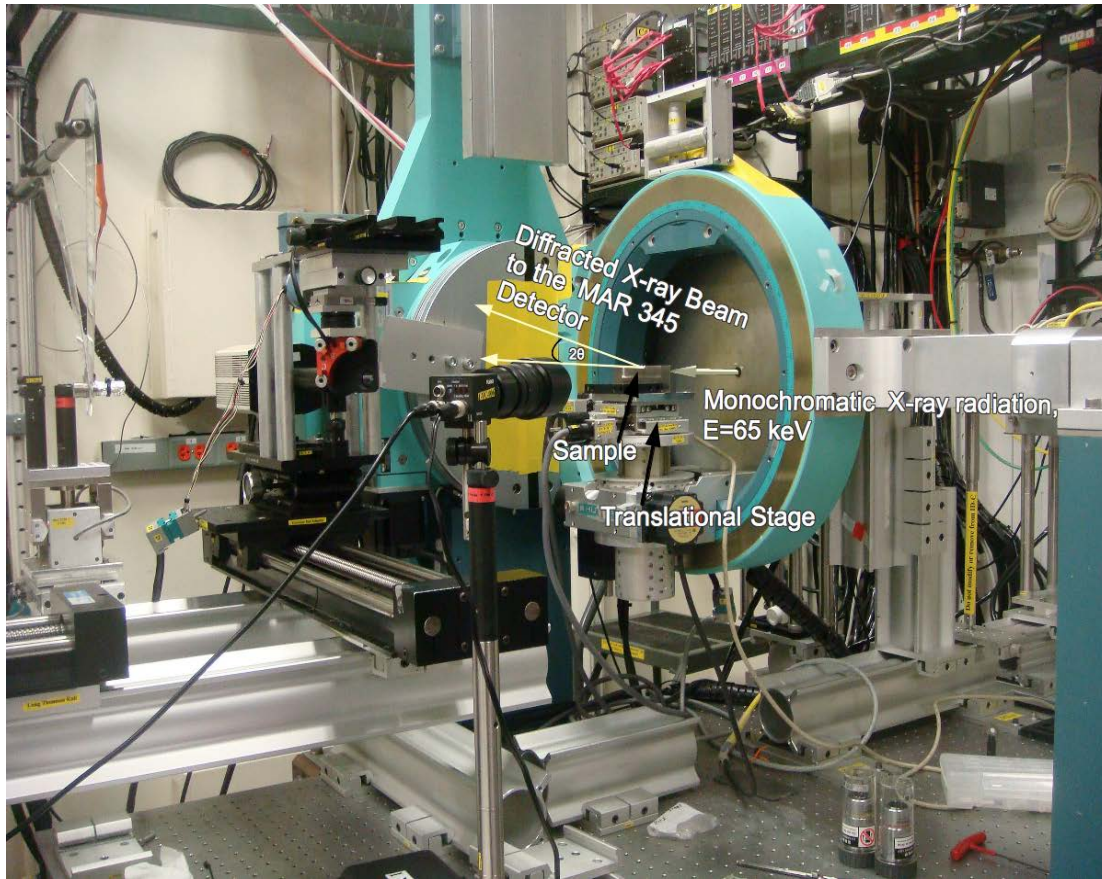


**Figure 3.6:** (a) Through thickness transmission experiment set up in 1-Id-C beamline at APS, Chicago, USA. The monochromator was selected to choose an energy of 65 keV or a wavelength of  $0.1907\text{\AA}$ .

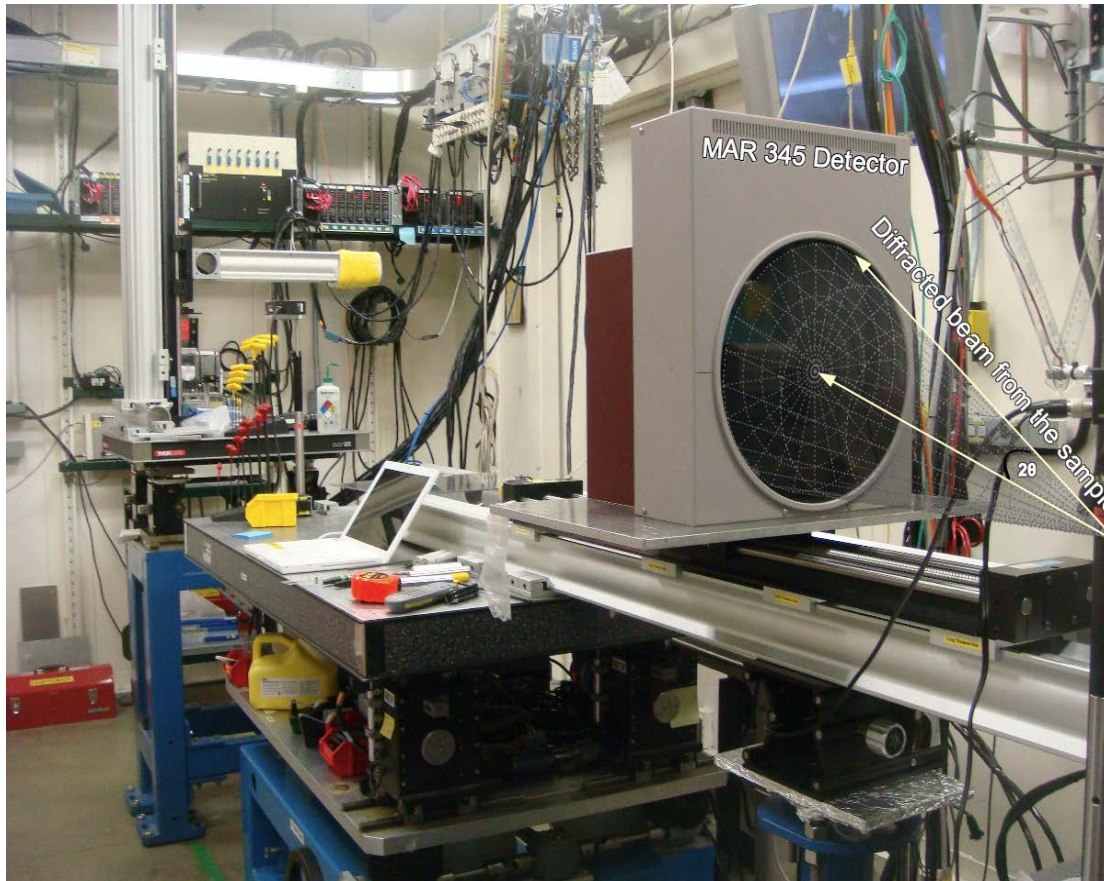


**Figure 3.6: (b)** The detector setup used in the APS experiment. The sample to detector distance was 1170 mm.

The pixel size of the detector was  $100\ \mu\text{m} \times 100\ \mu\text{m}$  (horizontal  $\times$  vertical). Since an image plate detector was used to collect the complete diffraction ring no slits were used for the diffracted beam. Therefore, it was possible to calculate the strains in both the longitudinal and transverse directions with respect to the leading edge. Three samples were measured in this experiment: 1)  $0^\circ$  LSP+FOD (S-1), 2)  $45^\circ$  LSP+FOD (S-7) and 3)  $0^\circ$  LSP+FOD (S-2) after applying one combined fatigue cycling block (see Table 3-2 and Table 3-3)

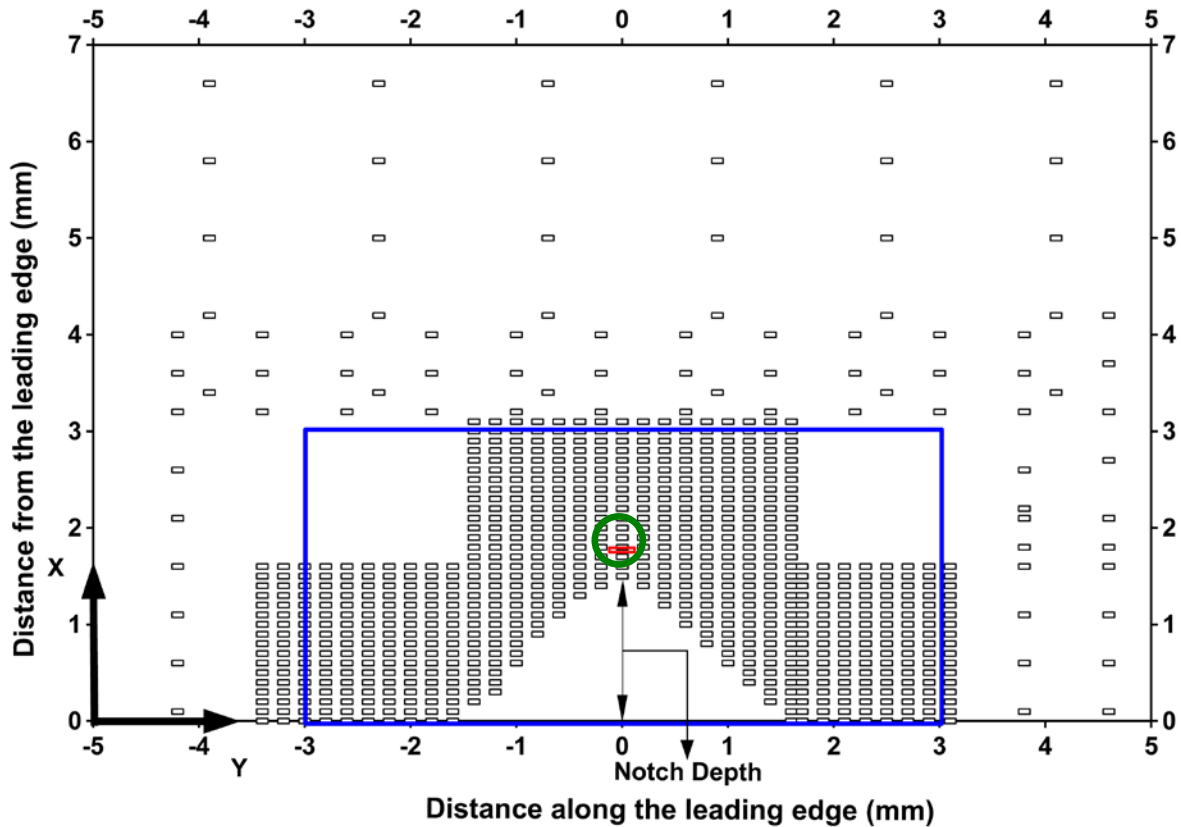


**Figure 3.7:** Scanning schedule for mapping 2D strain profiles in through thickness transmission. The blue rectangle represents the modified scanning arrangements used to save measurement time.

### Data Processing

The raw 2D diffraction images from the beamline were corrected and integrated by a data reduction program, fit2D (Hammersley et al 1996). Since the detector system introduces distortion into the recorded data, calibration of the beam centre as well as detector tilt was necessary. For this purpose, a  $\text{CeO}_2$  reference powder standard was applied over the intended region of the scan, to obtain reflections from the standard along with the reflection from Ti-6Al-4V. The utilization of the standard reference was also useful in determining any systematic error introduced by the sample misalignment (e.g. see (Evans 2007)). Once calibration and determination of beam centre and detector tilt was correctly established, the subsequent step was to convert each 2D pixel image to a 1D line spectra. This was achieved by integrating over a segment of  $\pm 10^\circ$  at an azimuthal position of  $0^\circ$  to obtain peak shift and hence strain in the longitudinal direction (Figure 3.2) of the specimen. The same procedure was repeated at an azimuthal position of  $90^\circ$  for strain along the transverse direction of the sample. The resulting spectra are the distribution of

intensity as a function of  $2\theta$ , and was assumed to be a Gaussian function and fitted by a Matlab fitting routine. The fitting routine provided peak centre position in terms of  $2\theta$  position, which was then used to calculate the desired  $d$  spacing according to the Bragg equation:

$$\lambda = 2d \sin(\theta) \quad \text{Equation 3-1}$$

Strains were calculated from the peak shift of  $(10\bar{1}2)$  diffraction peak from Ti- $\alpha$  phase due to its low tendency to be affected by intergranular strain .

From the  $d$  spacing, strains,  $\varepsilon$  were calculated according to the following equation:

$$\varepsilon = \frac{d - d_0}{d_0} \quad \text{Equation 3-2}$$

where,  $d_0$  is the strain free lattice parameter. Various methods of determination of  $d_0$  are available in the literature (Withers et al 2007). For this study the  $d_0$  was initially measured at a location far away from the LSP treated region, which was assumed to be stress free. However, it was found that the  $d_0$  value measured at this region did not provide a stress free value for  $d_0$ . Therefore, a new  $d_0$  value was determined by assuming bi axial stress state condition at the leading edge. This new value correlates well with the  $d_0$  value measured in a small cubic sample cut out of the sample.

Once strains are calculated both in the longitudinal and transverse direction, stresses were calculated assuming bi-axial stress state. The equations are as follows:

$$\sigma_{xx} = \frac{E}{1-\nu^2} (\varepsilon_{xx} + \nu\varepsilon_{yy})$$

and

$$\sigma_{yy} = \frac{E}{1-\nu^2} (\varepsilon_{yy} + \nu\varepsilon_{xx}) \quad \text{Equation 3-3}$$

where,  $\sigma_{xx}$  and  $\sigma_{yy}$  are the stresses in transverse and longitudinal directions respectively in the sample,  $\varepsilon_{xx}$  and  $\varepsilon_{yy}$  is the strain in the corresponding direction, E is the Young's Modulus and  $\nu$  is the Poisson's ratio. For Young's Modulus, a value of 103 GPa and for Poission's ratio, 0.3 was used.

## 3.6.1.2 HARWI-II

At this synchrotron facility there are two storage rings available, where synchrotron radiation is emitted from accelerated electrons or positrons. The storage rings are called DORIS III and the new PETRA III. The second strain scanning experiment was carried out in through thickness transmission mode using high energy constant wavelength synchrotron radiation from DORIS III storage ring. The ring is operated with a particle energy of 4.5 GeV and a positron current of 80-150mA. Since the DORIS III was not running in continuous “top up” mode, the beam current typically decays with a lifetime of 10-20 hours. Therefore, injection is required periodically to help maintain the beam current within an optimal range. A typical beam decay is shown in Figure 3.8 that exhibits DORIS beam lifetime per hour and current. The initial beam current was 140 mA, which was then decreased over a period of 6 hours to around 85-90 mA, and then accelerated particles were injected to recover the beam loss. The beam current instability of DORIS III has been addressed over the last two decades, and a series of technical and mechanical measures have been employed to improve the beam conditions that are discussed and can be found in the literature (Brinker & Kaul 2004, Neseemann et al 1995).

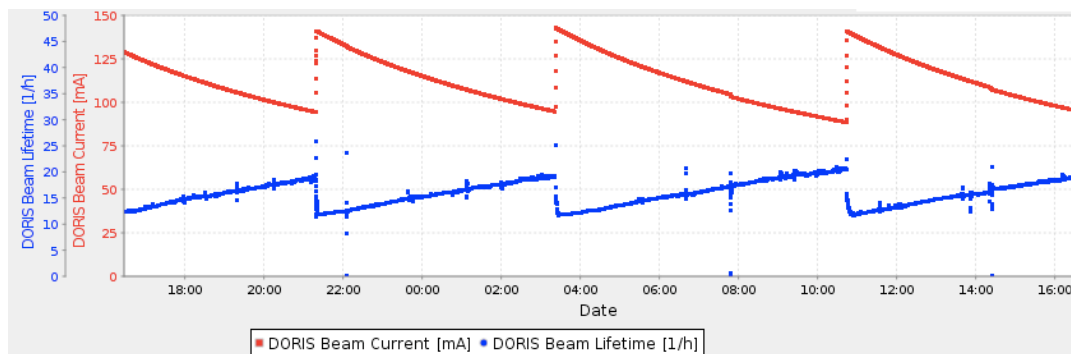


**Figure 3.8:** A typical synchrotron run showing the DORIS beam current [mA] and beam lifetime [1/h]

At DORIS III, a new High Energy Engineering Materials Science beamline, HARWI II (Hard Radiation Wiggler), is operated by the GKSS Forschungszentrum Geesthacht, Germany. The second experiment was carried out on this beamline which is equipped with a wiggler insertion device to deliver high energy X-rays with a photon energy range from 20-250

keV. Important parameters of this wiggler are included in Table 3-4. A monochromatic X-ray radiation was selected with an energy of 65 keV and a wavelength of 0.1907Å by employing a double Laue type monochromator (Si (111) reflection) to deliver an initial beam size of 10×10 mm<sup>2</sup>. The beam size was narrowed down to 0.2 mm in the horizontal and 0.1 mm in the vertical direction using a three-stage motor driven slit system. Figure 3.9 shows the experimental set up. The specimens were placed on the aligned tower (sample stage), which can be linearly translated by 1000 mm in the x-direction (horizontal, ⊥ to the beam), ±250 mm in the y-direction (horizontal, to the beam), ±200 in the z-direction (vertical) with a resolution of 0.05 mm in the x direction and 0.01 mm in the other two directions (Beckmann et al 2003). There was no surface preparation applied to the specimens. In this set up, the longitudinal axis of the leading edge sample was perpendicular to the incident beam, which penetrated through the full thickness of the specimen before emerging from the opposite side of the specimen. In this case, the total irradiated volume was 0.2×0.1×(1.8 to 3.0) mm<sup>3</sup> that contained approximately 1600 grains; sufficient enough to provide statistically viable number of favourably oriented grains for diffraction. A total of seven peaks were measured within a 2θ range of 3° to 8°. Among them, five peaks are from the reflection of (10 $\bar{1}$ 0), (0002), (10 $\bar{1}$ 1), (10 $\bar{1}$ 2) and (11 $\bar{2}$ 0) planes from Ti-α phase and two of them from the reflection of (110) and (200) planes from Ti-β phase. Since the β phase fraction in this material is less than 10%, any strain contribution from the β phase was not taken into account.



**Figure 3.9:** Experimental setup for thorough thickness transmission strain scanning of simulated leading edge Ti-6Al-4V sample on HARWI II beamline.

As described before, strains were calculated from the displacement of the  $(10\bar{1}2)$  diffraction peak from Ti- $\alpha$  phase. The diffracted X-ray beam was detected by a MAR 555 Flat panel detector from MAR Research, Nordersted, Germany. A complete Debye-Scherrer ring was acquired for each point. The selenium-coated detector has an active area of  $430 \times 350$  mm (with a diagonal of 555 mm), with a larger number of pixels:  $3072 \times 2560$  pixels (1 pixel =  $140 \mu\text{m}$ ) and a dynamic range of 18 bit (0:260.000). The function of the Se layer in this detector is to convert the diffracted photon into an electron. This unique characteristic of the Se layer with highly sophisticated read-out system provided a high spatial and excellent signal to noise ratio. Although the read out time of the MAR555 detector is only 1200 ms, much faster than the MAR345 image plate detector, the actual time taken to record each image was approximately two minutes due to an error in the detector software.

On average, 600 measurement points are acquired for each sample. Due to the limited availability of the experimental time, two samples, S-3 and S-5 were measured in this

experiment, both were LSP treated and contained 0° FOD notch. As shown in Table 3-2, specimens S-3 and S-5 were fatigue cycled with a maximum load of  $S_{\max} = 434$  MPa and  $S_{\max} = 586$  MPa respectively, and contained a retained crack length of  $\Delta a = 1$  mm and  $\Delta a = 0.5$  mm respectively.

### **Data Acquisition**

At HARWI II, SPEC utility system was used to operate the sample environment for moving the motor position, both for slit system and sample stage, diffractometer data control. Since each measurement point took approximately two minutes (exposure time of 20 s, detector read out time 90 sec), manual data collection at each location on the sample would be tedious. Therefore, a script was written that contained a series of commands to automate the complete measurement cycle for each sample. The script included commands for positioning the beam to the specified motor position, in the x and z directions; the y direction was along the beam and kept fixed; checking for the injection: this step was required to ensure the availability of the desired level of beam current (70 mA at the DORIS III ring) to stop recording invalid data; if the photon flux was less than 200 (Unit), no data was recorded and measurement only continued once the beam had recovered.

In the script, the measurement locations were specified by a fine rectangular grid around the FOD notch where maximum residual stress variation was expected, with a step size of 0.2 mm in the x direction (longitudinal direction in the sample) and 0.1 mm in z direction (transverse in the sample). This arrangement involved the measurement of some empty space within the notch. Additionally, two coarse rectangular grids were specified adjacent to the fine grid with a step size of 1 mm in both directions to generate the background strain profile.

### **Data Processing**

The raw 2D diffraction images from the beamline were corrected and integrated by a data reduction program, fit2D (Hammersley et al 1996). Since the detector system introduces distortion into the recorded data, calibration of the beam centre as well as detector tilt was necessary. For this purpose, a CuO<sub>2</sub> reference powder standard was applied over the intended region of the scan, to obtain reflections from the Standard along with the

reflection from Ti-6Al-4V. The utilization of the standard reference was also useful in determining any systematic error introduced by the sample misalignment. Once calibration and determination of the beam centre and detector tilt was correctly established, the subsequent step was to convert the resulting 2D pixel image to a 1D line spectra. From this step onwards, the same procedure was followed as described in Section 3.6.1.1 to obtain the strains.

### 3.6.1.3 PETRA III

The third experiment was carried out at the High Energy Material Science (HEMS) beamline at the 3<sup>rd</sup> generation synchrotron radiation source, PETRA-III at Desy, Hamburg, Germany. Important parameters regarding the storage ring and beamline are listed in Table 3-4. The storage ring is operated with a particle (positron/electron) energy of 6 GeV to provide a beam current of 100 mA. PETRA III is a unique synchrotron radiation source that provides high particle energy, a small beam emittance together with high flux and brilliance compared to other 3<sup>rd</sup> generation synchrotron sources employed in this study, Figure 3.10. The flux is characterized by number of photons per second and brilliance is number of the photon flux divided by the beam size, divergence and energy band width (BW) and usually given in units of photons/S mm<sup>2</sup> mrad<sup>2</sup> 0.1% BW. The unrivalled low emittance of 1nmrad (horizontal) and 0.01 nmrad (vertical), which allowed a small beam size to be selected with sufficient flux density to characterize a thick sample with sub-micron level resolution.

The beamline HEMS is equipped with a 4.5 m long in-vacuum undulator (U19-5) that allows a tunable energy range between 30-300 keV (Schell et al 2008). At the time when this experiment was carried out the beamline was still under development; hence, it was operating only in two energy modes: 53.3 and 87.1 keV. The selection of 53.3 keV energy over the relatively higher energy option was based on the fact that the spectral resolution decreases with increasing incident beam energy.

As discussed before, a small beam-size was required for this experiment to capture the sharp residual stress gradient created by the notch. Therefore, a box shaped beam was defined with the 3 step slit system with a size of 0.2 mm in the horizontal direction and 0.1 mm in the vertical direction that delivered  $2 \times 10^8$  photons/S mm<sup>2</sup> mrad<sup>2</sup> 0.1% BW

sufficient enough to penetrate a 9 mm thick Ti-6Al-4V specimen with high spatial resolution.

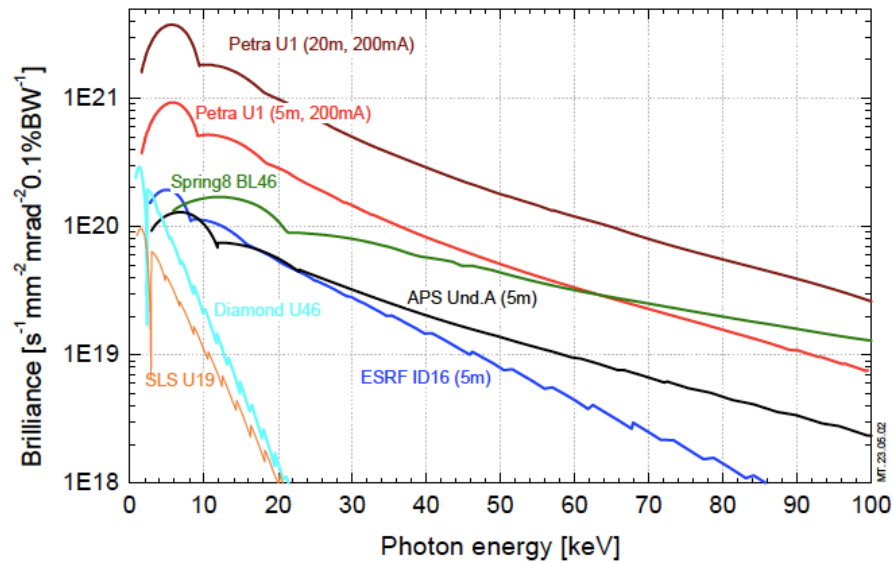
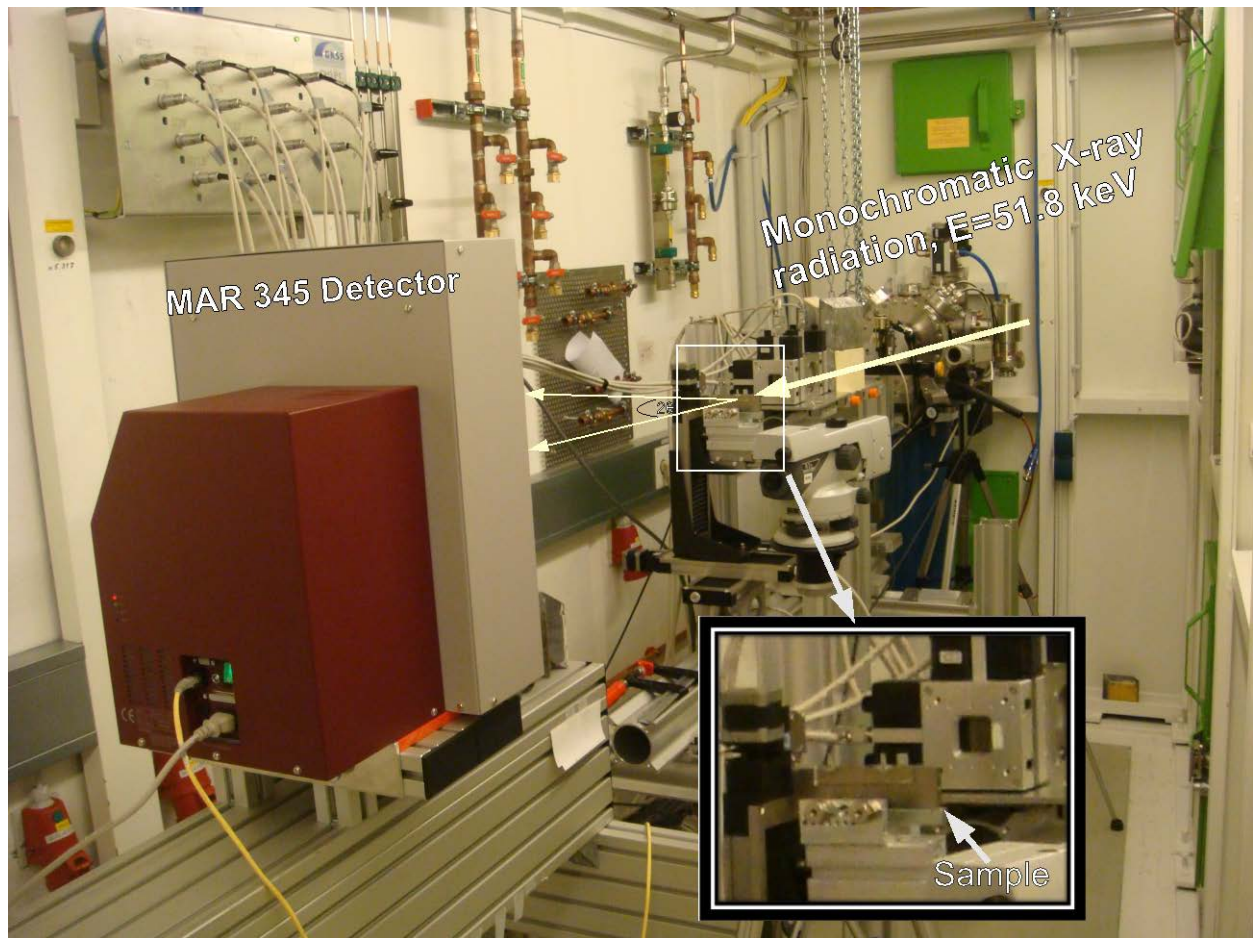


Figure 3.10: Comparison of the brilliance of various 3<sup>rd</sup> generation high-energy synchrotron radiation sources (Schell 2010).

Four samples, S-4, S-3, S-6 and S-10 were measured on the P07, HEMS beamline at PETRA III. Figure 3.11 shows the experimental setup. Each specimen was mounted on the sample stage capable of linear translational movement in X, Y and Z directions.



**Figure 3.11:** Experimental setup for thorough thickness transmission strain mapping of simulated leading edge Ti-6Al-4V specimens at HEMS beamline at Petra III, Hamburg, Germany.

The specimen was placed so that its longitudinal direction (Y) aligned perpendicular to the incoming beam and the Z direction was along the beam. This geometry allowed all the reflections from suitably oriented crystal planes at that illuminated volume to be averaged and the diffracted X-ray beam emerged from the other side of the specimen. A MAR-345 image plate detector was used to capture a complete Debye-Scherrer ring for each measurement point. The data from this experiment was processed as described previously in Section 3.6.1.1.

### 3.6.2 Depth Resolved Synchrotron X-ray Measurements on ID 31

Constant wavelength synchrotron X-ray diffraction measurements were made on the 45° FOD specimens on ID 31 beamline at the European Synchrotron radiation facilities (ESRF).

ID 31 was chosen particularly to investigate 45° impact condition to resolve any residual strain variation across the thickness. Six leading edge aerofoil specimens were measured as listed in Table 3-3. The residual strains were mapped in as-FOD'd condition as well as after subjecting to solely low cycle fatigue and combined cycle fatigue. Two separate experiments were performed on ID 31. On the first visit, S-7, S-9, S-12 and S-8 were measured. On the second visit S-9, S-7, and S-8 was re-mapped with a higher number of cycles applied to them. In addition, S-11 with a 7 mm crack was also investigated. The corresponding fatigue loading conditions are also provided in Table 3-3.

A monochromatic synchrotron X-ray beam was selected (50.8keV, 0.244Å) by a Si (111) double crystal monochromator, to ensure an optimised configuration of enough flux to get maximum possible counts and enough penetration to enable the measurement in transmission geometry. The displacement of the  $(10\bar{1}2)$  diffraction peak from Ti- $\alpha$  phase was measured at a diffraction angle ( $2\theta$ ) of 8.2°. To define the illuminated volume in the specimen, two slits of dimensions 0.4 × 0.05 mm<sup>2</sup> were used on the incident and diffracted beam. This resulted in an elongated gauge volume that was 0.9 mm long, 0.4 mm wide and 0.05 high, Figure 3.13. A rectangular shaped slit opening ensured high spatial resolution necessary to resolve strain variation across the depth, and also allowed a sufficient photon flux to be attained reducing the counting time to 3 minutes per measurement point. In the previous study on the residual strain measurement in as-FOD'd (without peening) condition,

From Figure 2.12, the width of the peak compressive region has been found to be approximately 0.8 mm (Frankel 2009). Therefore, to ensure excellent resolution, a smaller beam width needs be selected so that the interrogated volume of grains remains within this region (as shown by the green circle in Figure 3.7). For that reason a 0.4 mm wide beam has been selected in the longitudinal direction of the specimen.

To examine the residual strain variation across the thickness of 45° FOD specimens, three line scans were measured along the thickness direction: one along the mid thickness and the other two lines were 0.67 mm away from the surface of the sample on either side as shown in Figure 3.14. A highly dense step-size of 0.1 mm was used just below the notch up to 3 mm from the notch root, thereafter sparsely distributed measurement points were

taken.

The experimental set up is shown in Figure 3.12. A VAMAS sample positioning apparatus was used to mount the specimens as a set of 3, aligned parallel with one another with a spacing of approximately 5 mm (Pirling et al 2006). This entire assembly was attached to the translational sample stage that allowed linear movement in X, Y, and Z directions. To obtain the longitudinal strain component ( $\epsilon_{yy}$ ), the specimens were placed vertically with respect to the longest axis (Y axis) and aligned perpendicular to the axis of the incident beam. For measurement of transverse strain ( $\epsilon_{xx}$ ), the assembly was remounted by rotating through an angle of  $90^\circ$ .

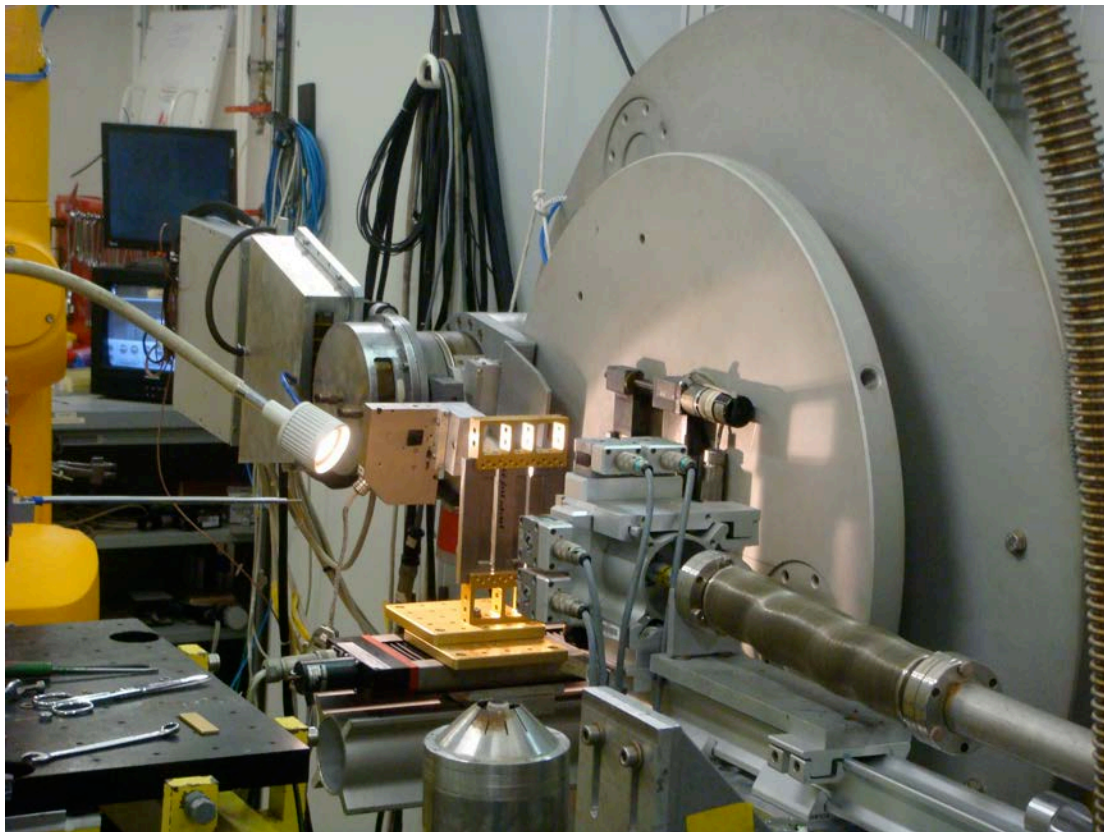


*Figure 3.12: Experimental arrangement for depth resolved residual elastic strain scanning of FOD'd leading edge aerofoil specimens on Id-31 at ESRF.*

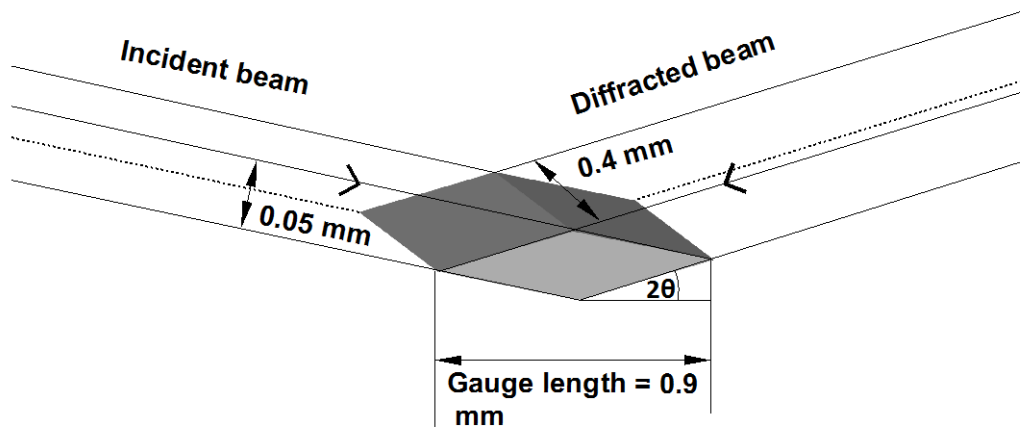


**Figure 3.13:** Schematic of gauge volume for depth resolved synchrotron measurement on ID 31. The monochromatic X-ray beam with energy of 51.8 keV was passed through a slit of  $0.4 \times 0.05 \text{ mm}^2$ . The diffracted beam was also passed through another slit of the same size before entering the detector at an angle  $2\theta=8.2^\circ$ . This setup resulted in a gauge volume of  $0.9 \times 0.4 \times 0.05 \text{ mm}^3$ .

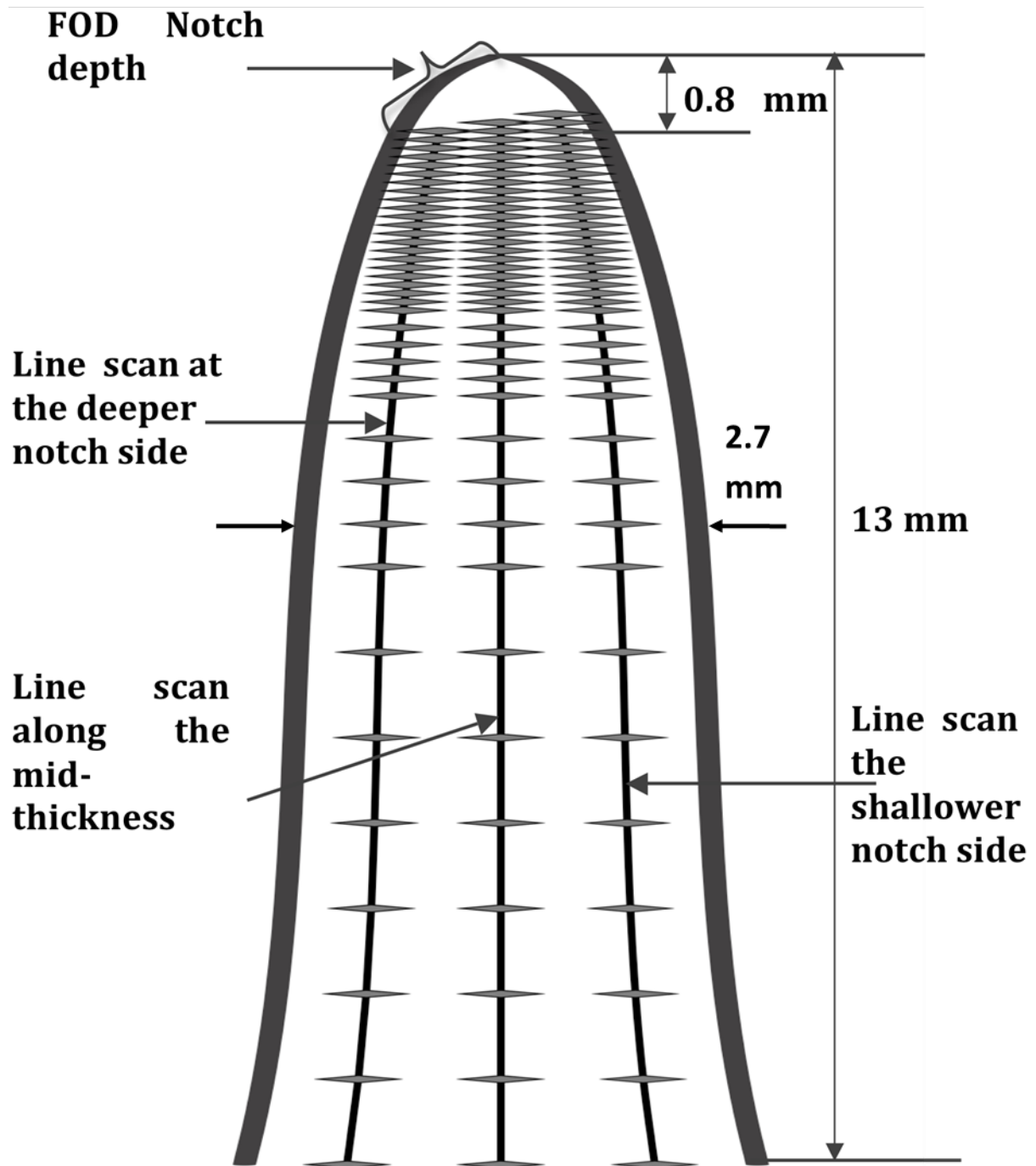


**Figure 3.14:** Cross section of the sample leading edge, showing three lines of diffraction measurement points. The diamonds represent the centroid of the gauge volume used, and indicate the measurement locations and shape.

The diffracted beam that emerged from the other side of the specimen was passed through an analyser crystal and then registered on the central detector of the 9-channel

multianalyser stage. The use of the analyser crystal was particularly suitable for assessing the residual stress of specimens impacted at 45°. Without an analyser crystal asymmetric and irregular notch shape that might cause incomplete gauge volume leading to pseudo peak shift to be detected (Owen 2002).

The distribution of diffracted intensity as a function of  $2\theta$  was assumed to be a Pseudo-Voigt peak shape and fitted using Large Array Manipulation Program (LAMP) to determine the centre of the peak position and also the full width half maximum (FWHM). ID 31 provides a very narrow peak with an instrumental broadening of around 0.003° (Masson et al 2001) that makes it suitable to fit with a Pseudo-Voigt function. On the other hand, Gaussian function was used for the previous experimental data analysis involving 2D detector setup.

### 3.6.3 Contour Method

To validate the synchrotron X-ray measurements, and also to evaluate the through thickness stress variation, complementary residual stress measurements were carried out using the contour method, which has been described in detail by Prime (2001). In order to obtain maps of the longitudinal stress across the section due to LSP and the changes introduced by the FOD, a 0° FOD'd specimen was clamped firmly and electro-discharge wire cut (300 µm diameter brass, skim cut settings) in two locations: firstly along the centre-line of the notch ( $y = 0$ ) and secondly far from the notch ( $y = 22$  mm) (see Figure 3.2). The resulting surface contours were measured by using a NanoFocus *µscan*® profilometer equipped with a confocal laser sensor on both sides of the cut surfaces to assess deviation from planarity arising from the elastic relaxation of the intrinsic residual stress. Each half was scanned with a point density of 10 µm × 10 µm. The acquired surface displacement data was then processed using MATLAB® routines developed by Xiong (2008). The processing steps include cleaning outliers, aligning, averaging datasets from two halves and fitting the surface using spline fitting. Then ABAQUS CAE software was used to create a finite element model for the half of the specimen and exported as an input file to read into MATLAB by another script (Johnson 2004, Johnson 2008). Finally the stresses required to return the surface to flatness were calculated.

## Chapter 4 Results and Discussions

### 4.1 FOD damage Characterization

The ballistic damage imparted by the 0° and 45° FOD impacts have been characterized by scanning electron microscopy (SEM) using a Zeiss EVO60 VPSEM and are presented in Figure 4.1. As described in section 3.3, to create FOD damage at impact angles (0° & 45°), impactor mass and velocity has been varied to adjust the impact energy imparted onto the specimen. Since FOD simulation is a highly uncertain process, a significant difference was observed not only between different impact conditions but also from sample to sample impacted under identical conditions in terms of the appearance of the damage crater. A typical wide V shaped notch was evident for all 0° FOD specimen (Figure 4.1a), whereas an asymmetric V shape was observed for specimen impacted at 45° angle with variable notch depth at the entry and exit side of the impactor (Figure 4.1b), which is likely to be due to off axis impact angle. The average notch depths for the FOD damage were measured from the profile view and found to be 1.49 mm for the 0° notch (see Table 3-2), and 0.82 mm in the shallower side and 1.5 mm at the deeper side for the 45° notch (see Table 3-30 and APPENDIX-II). The common features observed for both types of impacts include loss of material (LOM), material folding at the rim near the L.E. (shown in Figure 4.1c), material shear, and microcracks. Of importance to note here is that although less LOM is evident in 45° notches, more microcracks were observed for this type of impact. Also, as can be observed in Figure 4.1b, the traversing path of the impacting tool is evident for the 45° impact suggesting that material is pushed away by the impactor from the entry side (deep) to the exit side (shallow). Material shear at the notch surface is observed as shown Figure 4.3a. An important characteristic of ballistic impact damage is the formation of micronotches and microcracks (Figure 4.2c and d) at the periphery and also at the root of the notch. These cracks can grow to fully-fledged fatigue crack upon subsequent fatigue loading, which can lead to failure of the component. (Peters & Ritchie 2000).

Further FOD damage characterization results can be found elsewhere (Spanrad & Tong 2011).

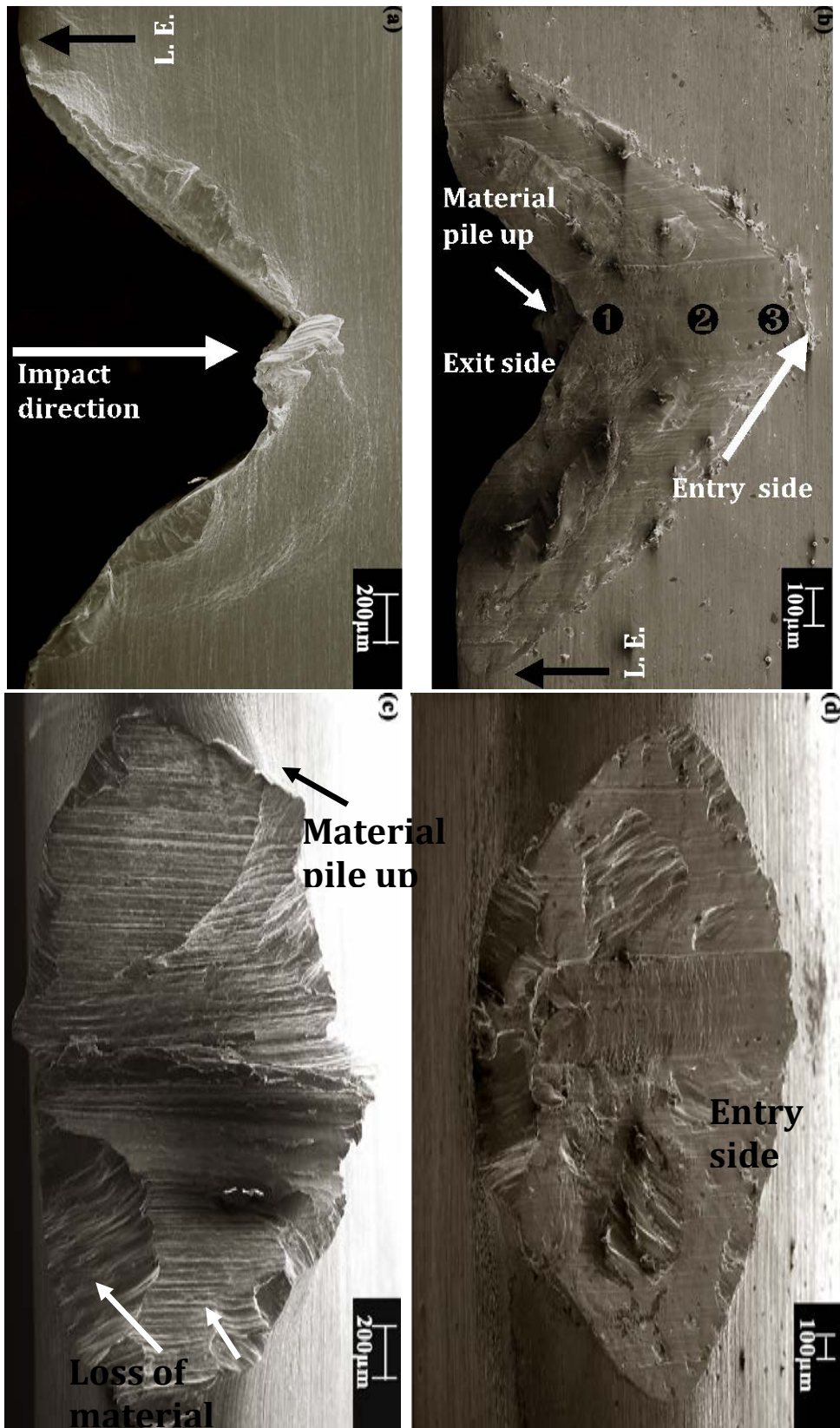


**Figure 4.1:** Secondary Electron SEM images of the side view of (a) 0° FOD and (b) 45° FOD and top view of (c) 0° FOD and (d) 45° FOD showing the impact direction, exit and entry side for 45° FOD, loss of material and material pile up. Figure (c) also delineates the ① shallow, ② middle and ③ deeper notch side in a 45° FOD.

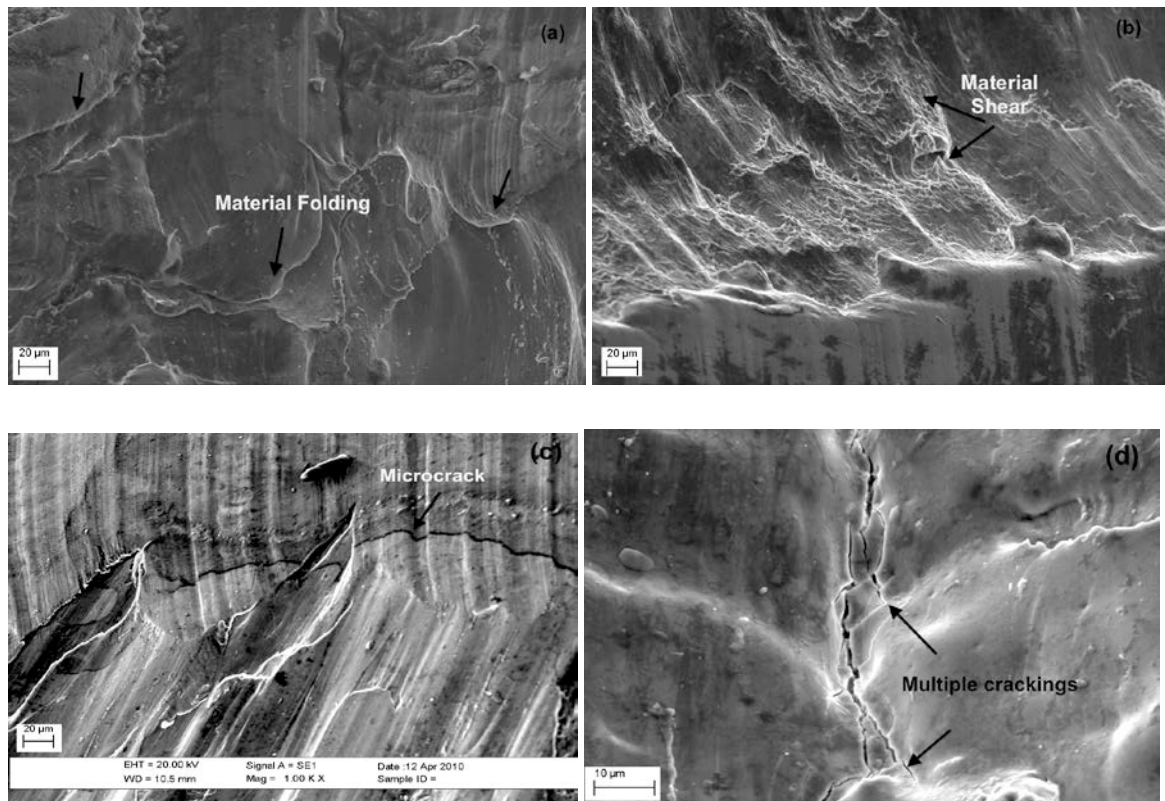


**Figure 4.2:** SEM images showing (a) material folding (b) material shear (c) microcracks and (d) multiple cracking observed for 45° FOD impact condition.

Figure 4.3a shows the microstructure at the FOD notch root for specimen S-1. No severe microstructural degradation is evident in this case. To further investigate the microstructural damage and plastic deformation an EBSD pattern is acquired at a distance of 1mm from the base of the notch, Figure 4.3b, that shows the local mis-orientation map.

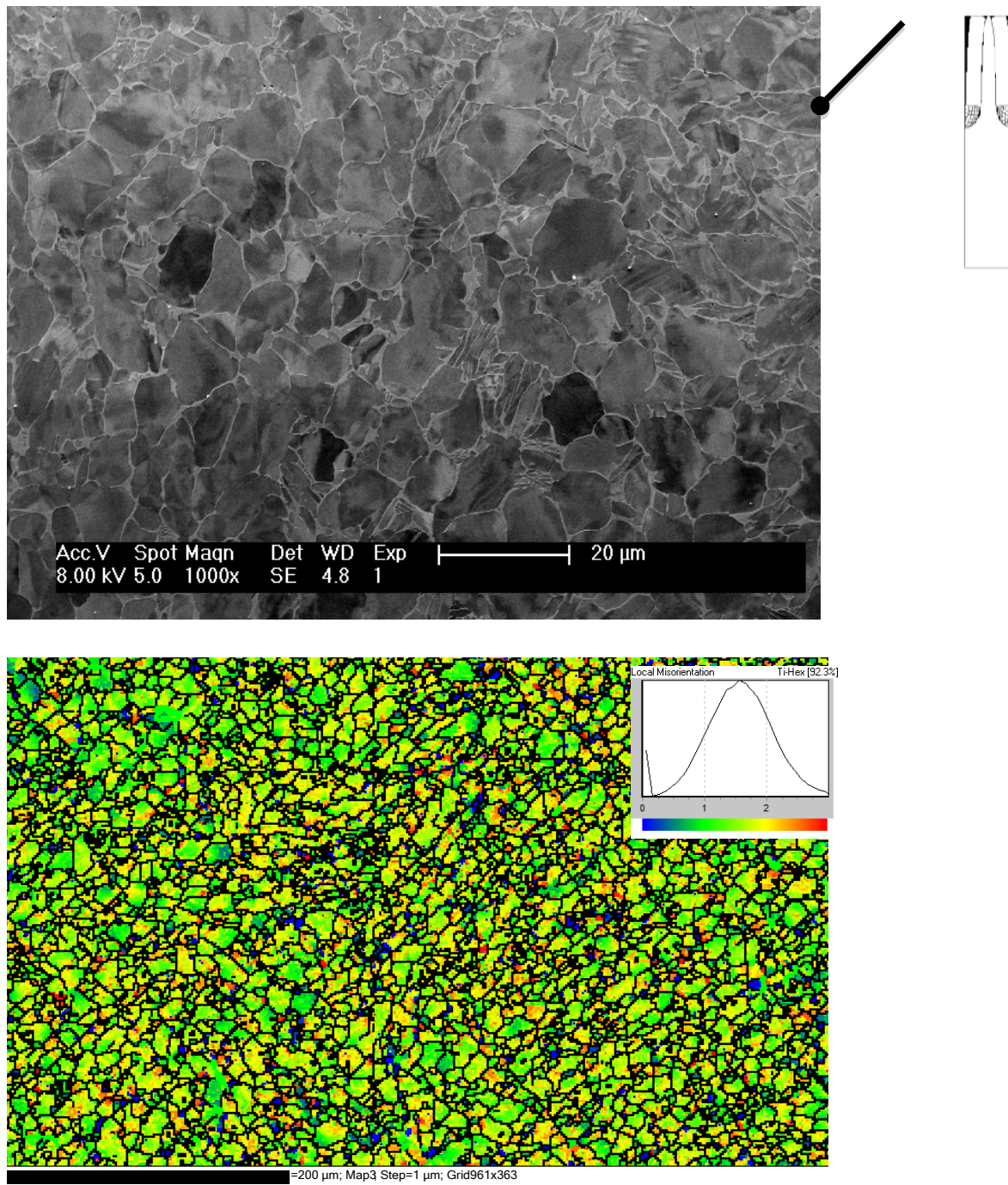
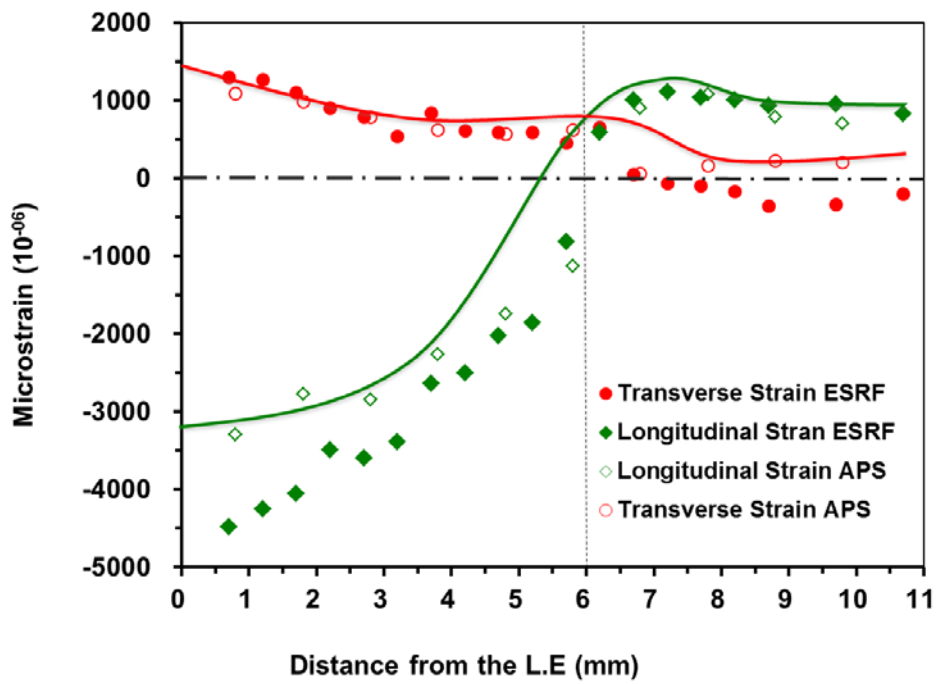


**Figure 4.3:** (a) SEM image for a 0 degree impact (specimen S-1) taken from the cross-section at distance of 1 mm from the root of the notch, shows no drastic change of microstructure due to plastic deformation associated to FOD at the base of the impact crater.

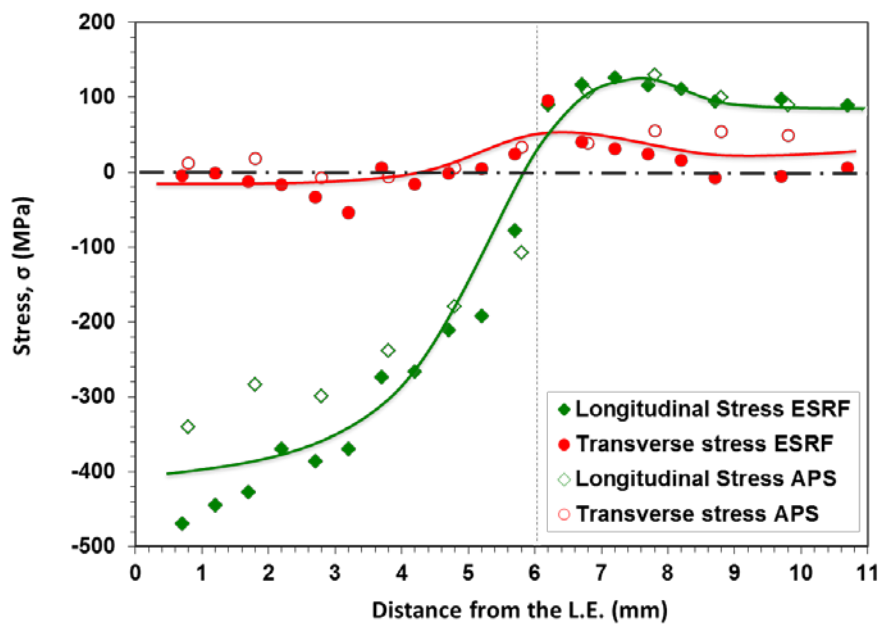
(b) The EBSD pattern for at the same distance shows the local mis-orientation map.

## 4.2 Residual stresses state in as-peened condition

The through-thickness averaged residual strain profile acquired by the synchrotron XRD technique (experimental setup is described in section 3.6.1.1 and 3.6.2) in the as-peened condition is shown in Figure 4.4a. The residual stresses arising from the LSP treatment were calculated according to the procedure described in section 3.6.1.1, and shown both parallel ( $\sigma_{yy}$  stress component), and normal ( $\sigma_{xx}$ ) to the leading edge in Figure 4.4b. The maximum longitudinal (crack-closing) compressive stress is approximately 55% of the yield stress and located at a distance of 0.7 mm from the L.E. The residual stress then gradually decreases with increasing distance from the LE as the profile thickens, becoming tensile at 6 mm from the L.E. (this corresponds well with the extent of the LSP treated area). The balancing tensile stress, which is  $\sim 0.12\sigma_y$ , diminishing towards zero further away from the LE. Previous researchers have measured the LSP induced residual stresses on Ti-6Al-4V thin slice (Korsunsky et al 2006), and on simulated leading edge aerofoil shaped specimens using laboratory X-ray diffraction combined with layer removal technique (Ruschau et al 1999), and using synchrotron X-ray diffraction (Frankel 2009). Ruschau et al (1999) found a maximum surface compressive residual stress of  $0.86\sigma_y$  at a distance of 1 mm from the leading edge. On the other hand, the maximum compressive stress at the same location was found to be  $0.3\sigma_y$  (Frankel 2009). The tensile stresses outside the peened region do not seem to vary significantly.



(a)



(b)

**Figure 4.4:** The through-thickness averaged (at APS) and depth resolved (at ESRF) residual (a) strain and (b) stress profile in longitudinal and transverse directions in as-peened condition.

### 4.3 Residual stress distribution in 0° and 45° Impact

#### 4.3.1 Through Thickness Transmission Measurements

The effect of 0° FOD on the longitudinal and transverse residual strain distribution are shown in Figure 4.5a and Figure 4.6a respectively. The strains are converted into stresses (see section 3.6.1.1 for details), and the corresponding stress map is presented in Figure 4.7a. Two observations can be made from this stress plot: firstly a large compressive stress region was formed directly beneath the notch reaching 0.8 times the yield stress ( $\sigma_y$ ) approximately 0.4mm beneath the notch and secondly a small region of low level tensile stress is evident near the flanks of the impact crater. Comparison with previous stress maps around FOD damage in unpeened systems such as, for a quasi-static FOD on flat plate geometry as in (Boyce et al 2001) and ballistic impact on leading edge specimen (Frankel 2009) suggest similar stress features. However, the prior LSP has biased the stress variations significantly towards compression. Most importantly, the sub-surface large tensile stress region observed after FOD on a previously unstressed aerofoil (Frankel 2009) as can be seen in Figure 2.12, is not evident in LSP+FOD condition. Given that this tensile region has been a location for the initiation of damage beneath FOD under fatigue (Ruschau et al 2001), and also upon approaching this tensile region a fatigue crack may accelerate resulting in the premature failure of the component. This may explain why LSP can increase fatigue resistance to FOD (Ruschau et al 1999).

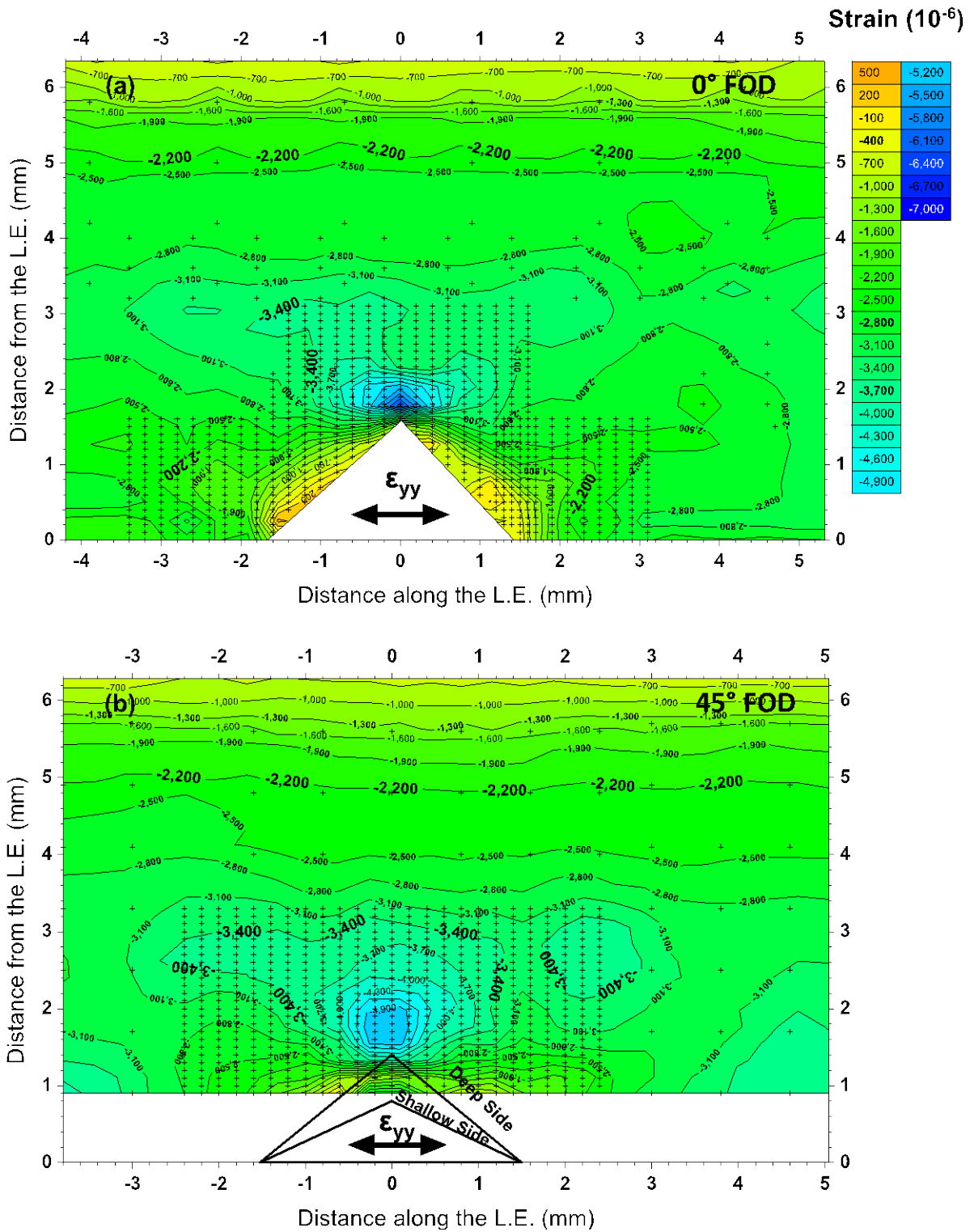
Furthermore, the current results are in agreement with those of Frankel (2009) also for cube edge impact, showing a compressive peak directly beneath the FOD tip (see Figure 2.12), rather than at a distance 1.5xcrater radius away as observed for spherical FOD (Boyce et al 2001).

Figure 4.5b and Figure 4.7b show the residual strain and corresponding stress maps respectively around a 45° FOD impact (specimen S-7, see Table 3-3). The 45° impact resulted in asymmetric damage with a higher loss of material observed for the entry side than for the exit side this is in agreement to small glass sphere impact (Ruschau et al 2001) and is due to the orientation of the cube edge. The damage depths at the shallower side and deeper side are approximately 0.8 mm and 1.5 mm respectively. As our synchrotron X-ray measurements are averaged through the aerofoil thickness any variation in the through-

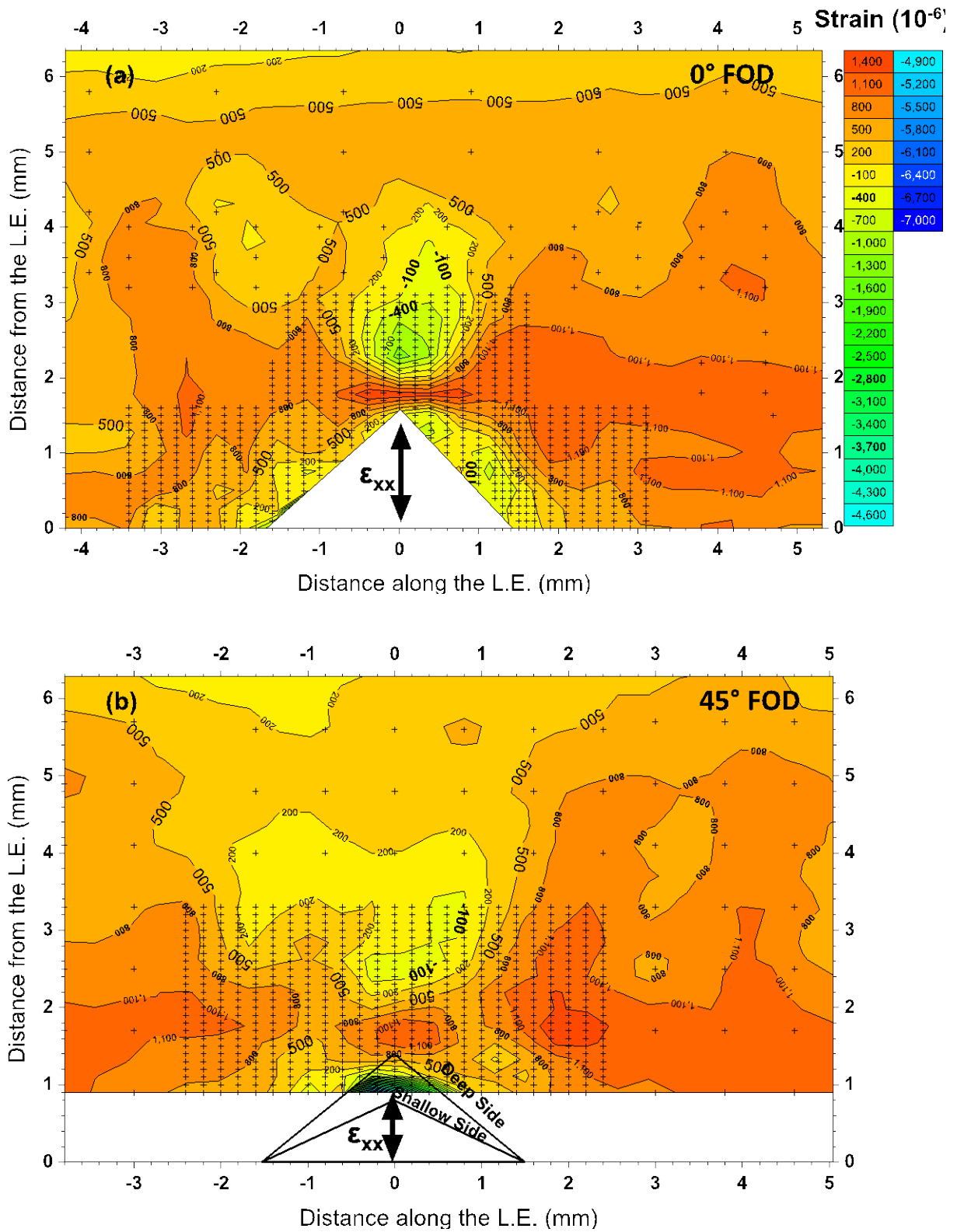
thickness direction is not captured in the current study. It is noteworthy that the depth-resolved study presented in section 4.4.1 through 4.5 shows a significant through thickness stress variation for 45° FOD impacts, which is discussed later. The comparison of residual stress distribution between 0° and 45° crater suggest that the main difference lies in the magnitude of the local maximum compressive stress, which is about  $0.6\sigma_Y$  in the case of 45° impact compared to  $0.8\sigma_Y$  for 0° impact, which is probably due at least in part to the different impact depths.

Figure 4.6 shows the transverse residual strain map for 0° and 45° FOD impact.

The broadening (FWHM) of diffraction peaks has long been used as a measure of plastic work (Warren & Averbach 1950, Warren & Averbach 1952). Figure 4.8 shows the full width half-maximum (FWHM) maps for (a) 0° and (b) 45° impact. It is clear that a significant level of plastic deformation was introduced by the high-energy impact. A highly plastically deformed region, approximately 3 times higher than the LSP'd plasticity is observed surrounding the FOD notch.



**Figure 4.5:** Through thickness averaged residual elastic strain map parallel to the leading edge in a FOD'd condition (a) for a  $0^\circ$  FOD impact with a damage depth of 1.5 mm (specimen S-1, see Table 3-2), (b) for  $45^\circ$  FOD with a damage depth of 0.82 mm (specimen S-7, see Table 3-3; in (b) residual strain data within 0.8 mm of the LE are discarded due to experimental error).



**Figure 4.6:** Residual elastic strain map normal to the leading edge in as FOD'd condition (a) for a 0° FOD impact with a damage depth of 1.5 mm (Specimen S-1) (b) for 45° FOD with a damage depth of 0.82 mm (Specimen S-7).

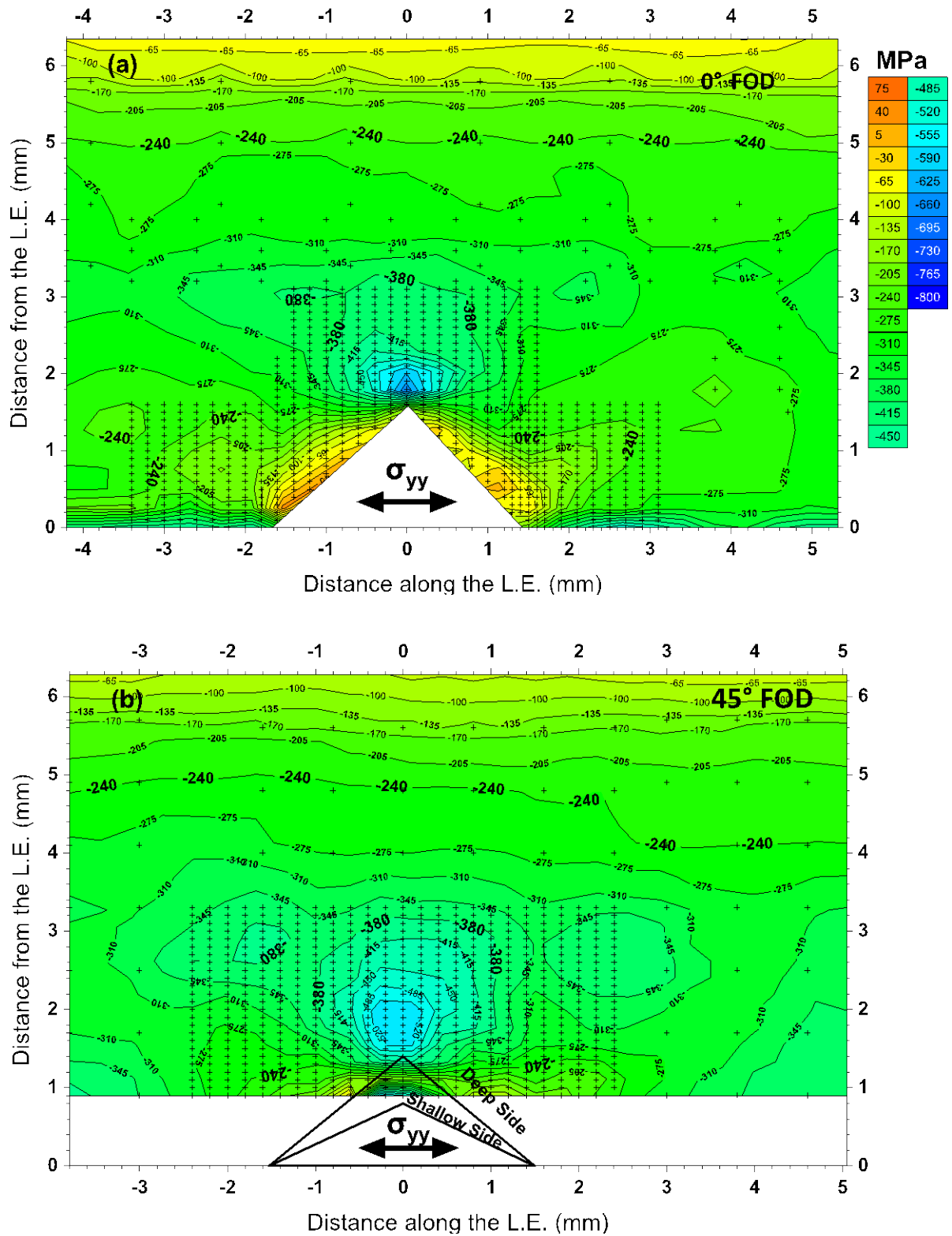


**Figure 4.7:** Longitudinal residual elastic stress maps calculated for Figure 4.5 and Figure 4.6 based on plane stress assumption, in as FOD'd condition for (a) 0° and (b) for 45° FOD impact, in (b) residual stress data within 0.8 mm of the LE are discarded due to experimental error.

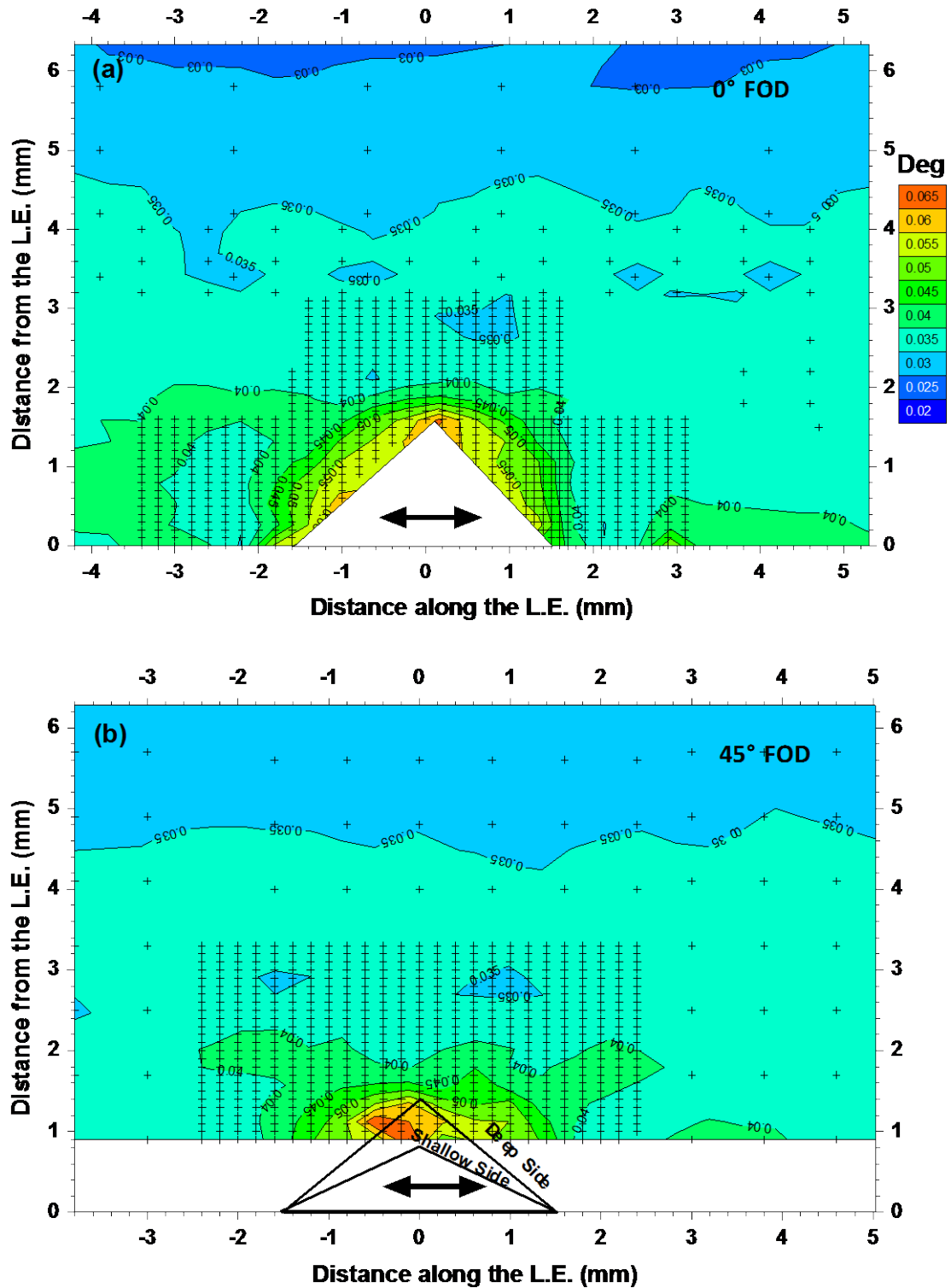


Figure 4.8: 2D contour plots of FWHM (Degree) for  $(10\bar{1}2)$  diffraction peak from Ti- $\alpha$  phase in longitudinal direction of the specimen: (a) 0° and (b) 45° impacts.

4.3.2 Depth-Resolved Transmission Measurements

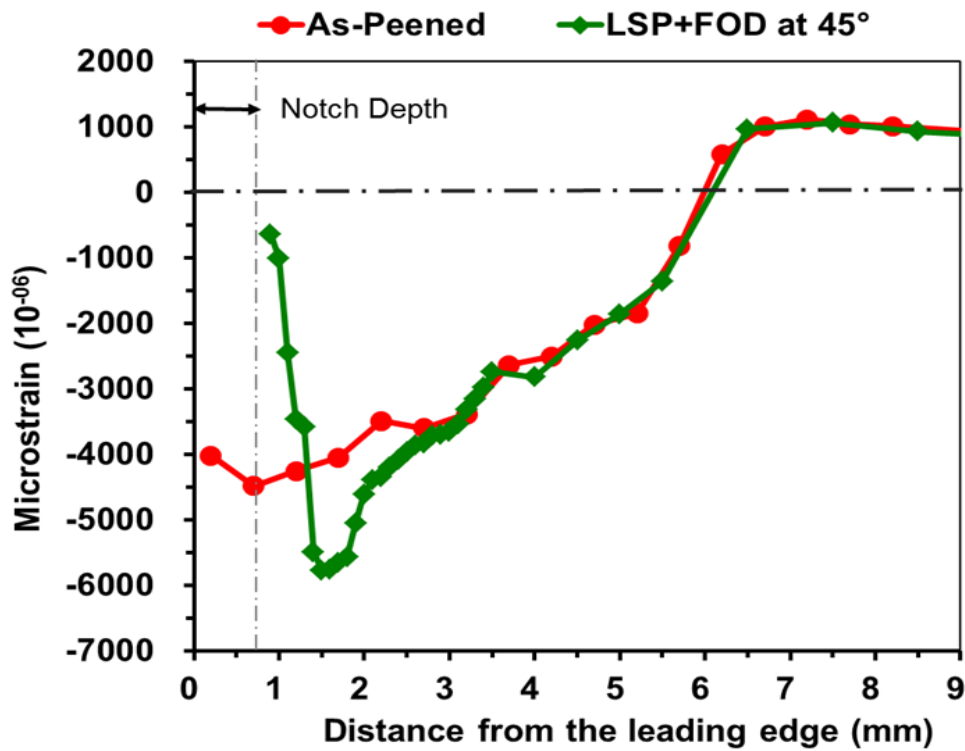


Figure 4.9: The synchrotron residual strain profile parallel to the leading edge generated in as-peened condition and after 45° FOD impact (Specimen S-7). The notch depth is 0.82 mm.

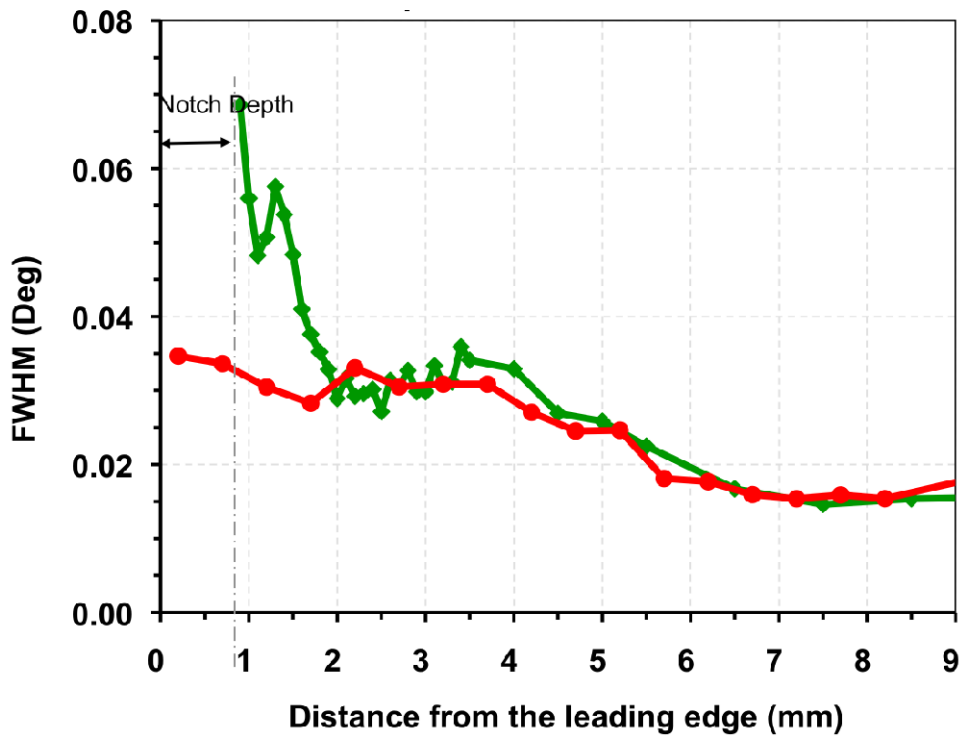


Figure 4.10: Comparison of FWHM between as-peened and 45° FOD impact (Specimen S-7).

### 4.3.3 Contour Method Results and Comparison with the Synchrotron Results

The contour method was applied to evaluate the through-thickness stress variation in parallel to the L.E. (experimental details are described in section 3.6.3), both prior and subsequent to FOD. Figure 4.11a shows the 2D contour map of the residual stress distribution in as peened condition. A maximum stress of  $\sim 0.5\sigma_Y$  was observed at the tip of the LE that becomes slightly tensile outside the peened region and decays with the distance from the L.E. A comparison between contour method and synchrotron diffraction for stress profiles associated with LSP is presented in Figure 4.12a. Note that for this purpose, the stresses were averaged through the whole thickness of the specimen to match with the synchrotron result. As this plot suggests, the stress profile obtained by the destructive CM corresponds well with the non-destructive synchrotron results in terms of the overall shape of the stress profile, the compression/tension cross-over point which appears at the edge of the peened region (6 mm from the LE), and the far-field stress. However, the CM results do show a slightly higher value of peak compressive stress compared to the synchrotron data. Also, the stress gradient is somewhat steeper in the former compared to the later.

To evaluate the 2D residual stress field associated with FOD in LSP'd specimen (Specimen S-7), the stress measurement was carried out along the x-z plane containing the notch tip ( $y=0$ ). The result, presented in Figure 4.11b exhibits a highly compressive zone at the base of the notch, similar to that measured by synchrotron diffraction. The level of compression decreases with increasing distance from the LE. In contrast to the results of Frankel (2009) on unpeened samples, no significant tensile stress region is observed below this region. It is important to note here that little through thickness stress variation is observed for the  $0^\circ$  impact (Figure 4.11b), justifying our use of through-thickness synchrotron stress profiling. The comparison with the synchrotron result is also provided in Figure 4.12b, where the difference in the magnitude of the maximum compression between those two methods is  $< 0.1 \sigma_Y$ .

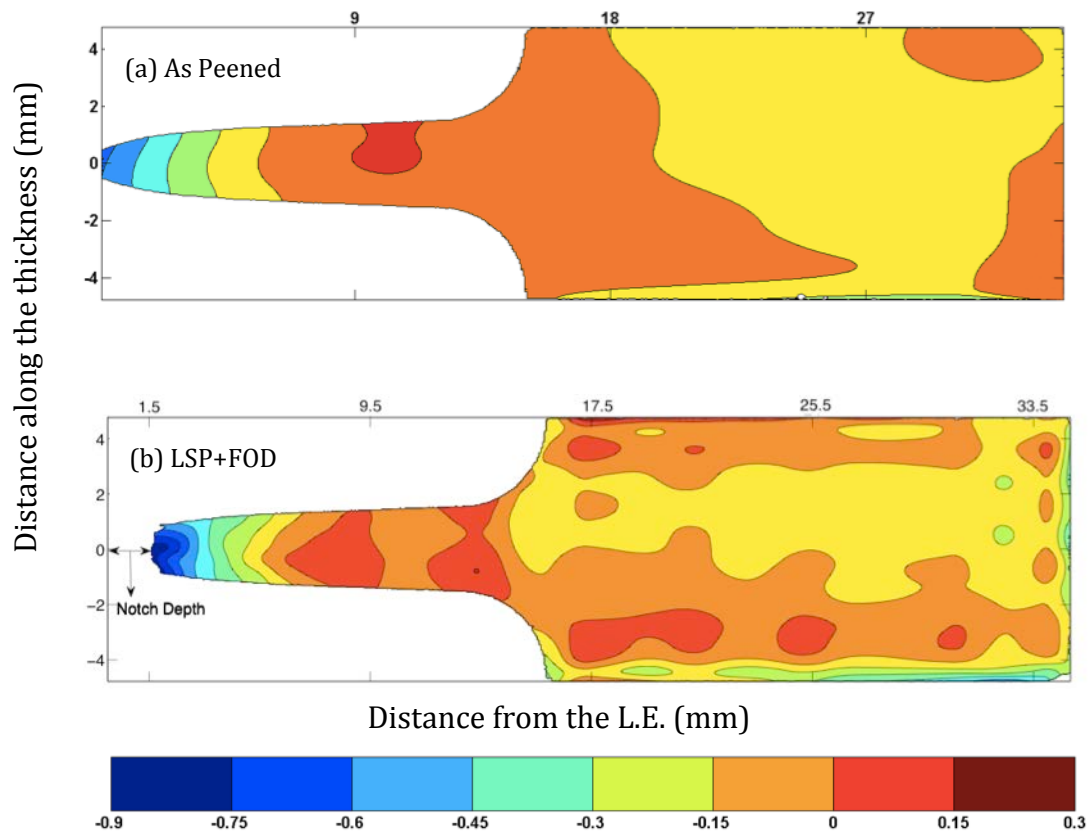
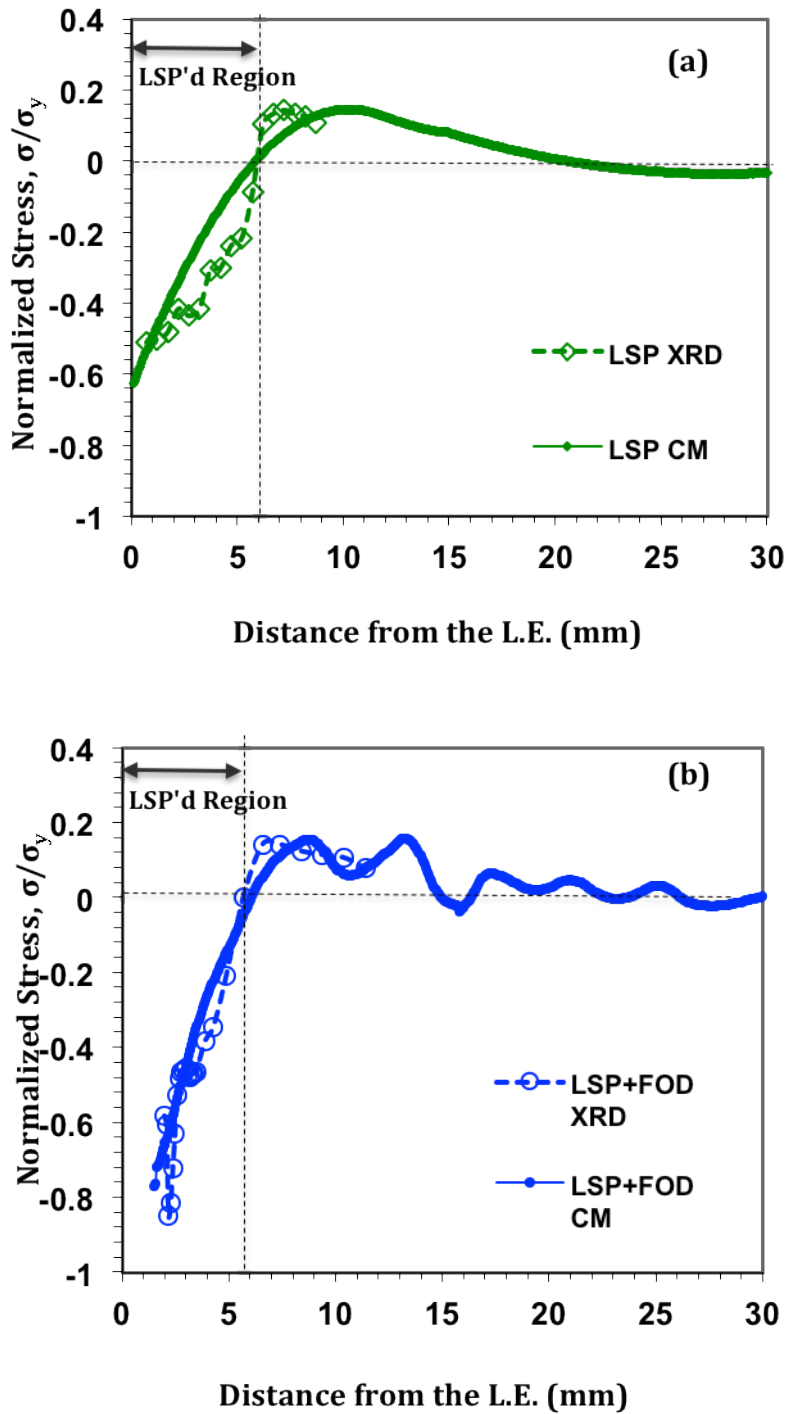


Figure 4.11: Contour method results for normalised (with respect to the yield strength) longitudinal residual stress distribution along the line of the FOD notch (a) after LSP (Specimen S-1), and (b) after LSP +  $0^\circ$  FOD (Specimen S-1).



**Figure 4.12:** Comparison of residual stress distribution, in longitudinal direction parallel to the leading edge, between synchrotron and Contour method: (a) in as-peened condition and (b) after LSP + 0° FOD. Both were done in specimen S-1.

#### 4.3.4 Summary

The residual stress distribution around 0° and 45° FOD damages have been characterised by the synchrotron X-ray technique. The contour method was applied to the 0° FOD specimen and the results are compared. Laser shock peening introduces compressive residual stresses with a value of  $0.5 \sigma_Y$  in the longitudinal direction (crack opening direction) of the aerofoil specimen.

High speed FOD impacts, both 0° and 45° superimposed additional residual stresses onto the initial LSP'd stresses predominantly at two key locations: a) a small tensile region at the flanks of the notch and b) a large compressive zone directly below the notch. The maximum compression observed was in the level of  $-0.8\sigma_Y$  and the maximum tension was  $0.2 \sigma_Y$ . No significant variation in terms of the size, shape or the position of these stress features were observed between 0° and 45° FOD notch. The magnitude of the compressive stresses introduced by a 0° impact was found to be slightly higher than that introduced by a 45° impact. It can also be observed that unlike 45° impact condition residual strains do not vary significantly along the thickness. This infers that head-on impacts create a mostly homogeneous strain distribution along the thickness of the specimen in compared the 45° impact.

The  $\sigma_{yy}$  stress variation along the notch centreline was measured using the contour method for only LSP treatment, and also for a 0° FOD specimen. The line profiles were taken along the centreline. The stress profile generated by the contour method agrees well with that obtained by synchrotron diffraction technique. A small discrepancy of about 100 MPa was observed between the two results at the root of the notch which is largely due to the incapability of the contour method to provide correct stress near the surface.

FOD damage characterisation for both 0° and 45° impact showed the evidence of loss of materials, material pileup, material folding, and the presence of microcracks.

#### 4.4 Residual Strain relaxation behaviour under cyclic loading

Residual stresses introduced by LSP and subsequently by ballistic impacts are likely to influence the mean applied stress during cyclic loading and hence can affect the fatigue life of the material. If the compressive residual stresses as shown in section 4.3 are stable, they may provide a good level of protection against static mechanical loading, cyclic loading (Fatigue), crack growth, and thermal exposure. Many studies can be found in the literature confirming this for shot peening, and also laser shock peening in Ti-6AL-4V (Altenberger et al 2002, Bache et al 2003, Ding et al 2007a, Jayaraman et al 2005, King et al 2006, Martinez et al 2002, Pasta & Reynolds 2008, Peters & Ritchie 2001a, Zhang et al 2010). However, the relaxation of LSP+FOD residual stress has hardly been reported. Therefore, to allow for these residual stresses in the damage tolerant design, it is imperative to determine the stability of the LSP+FOD residual stresses under various conditions. In this study the relaxation behaviour of the residual stresses has been evaluated under cyclic loading and crack growth. This section presents the experimental results and discussion involving the relaxation behaviour under solely low cycle fatigue (LCF) and combined (LCF+HCF) cycle fatigue (CCF) type of loading where no detectable (by Direct Current Potential Difference (DCPD) system see e.g. (Spanrad 2011)) cracks were present. All the specimens and their corresponding fatigue loading conditions are summarised in Table 3-2 for 0° and Table 3-3 for 45° FOD impacts respectively.

##### 4.4.1 Effect of solely Low Cycle Fatigue on RS relaxation

Since FOD at a 45° angle is generally considered to be the worst case damage, the residual stress redistribution due to solely LCF has been examined for only 45° impacts.

##### 4.4.1.1 Residual Stress Response of 45° FOD specimens under LCF

The residual stress relaxation for a 45° FOD impact under solely LCF loading was studied using synchrotron X-ray diffraction on ID 31, ESRF.

Figure 4.13 shows the depth-resolved residual strain distribution as a function of distance from the L.E. for a 45° FOD impact after the application of 1000 LCF cycles under a maximum applied stress of  $S_{max} = 521$  MPa (specimen S-9, see Table 3-3), along with the strain profile in the as-FOD'd condition (specimen S-7). Note that in as-FOD'd

condition the strains were acquired along the mid-thickness of the specimen using the same gauge volume. The peak compressive residual strain (CRS) of  $-5000 \times 10^{-6}$  appeared at a distance of 1 mm from the L.E, which is around 15% less than the corresponding peak CRS in the as-FOD'd condition. At a distance of 2 mm from the L.E. the relaxation is as high as 60%. Beyond 3 mm from the L.E., the strain profiles were largely remained unaffected. The residual strain relaxation observed in this case is mainly due to the higher applied stress. It should be noted here that the (average) notch depth for the as-FOD'd specimen (S-7) is 0.2 mm deeper than the fatigued specimen (S-9) at the centre of the notch, and because the magnitude of the peak compressive residual strain increases with the depth of the notch, it is likely that the initial residual strain distribution was less in specimen S-9 prior to fatigue. Therefore, the difference in the residual strain observed here may be at least partly due to the difference in notch depth between two specimens.

To assess the effect of solely LCF, the specimen (S-9) was subjected to additional fatigue cycles up to  $10^5$  cycles with increasing load from  $S_{\max} = 521\text{MPa}$  to  $S_{\max} = 586\text{MPa}$  (specimen S-9), and residual strains were measured again. The results are shown in Figure 4.14. Now a direct comparison can be made between Figure 4.13 and Figure 4.14 to delineate the combined effect of (i) applied load and (ii) solely LCF cycles, where the latter causes 20% relaxation of the compressive residual strain with a peak at 2mm from the L.E.

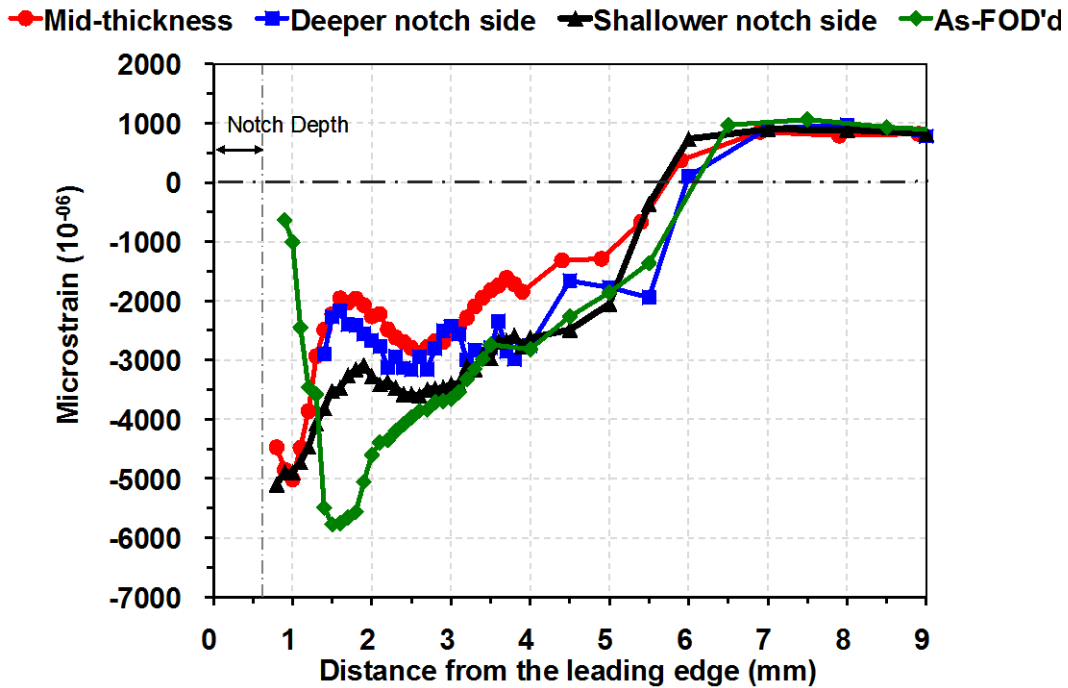


**Figure 4.13:** The depth-resolved residual strain profiles along the notch centreline ( $y=0$ ), parallel to the leading edge generated for a  $45^\circ$  FOD impact after applying 1000 LCF cycles under a maximum applied stress,  $S_{max} = 521$  MPa. The depth at the centreline of the notch for this specimen (S-9) and as-FOD'd specimen (S-7) are 0.62 mm and 0.82 mm respectively.

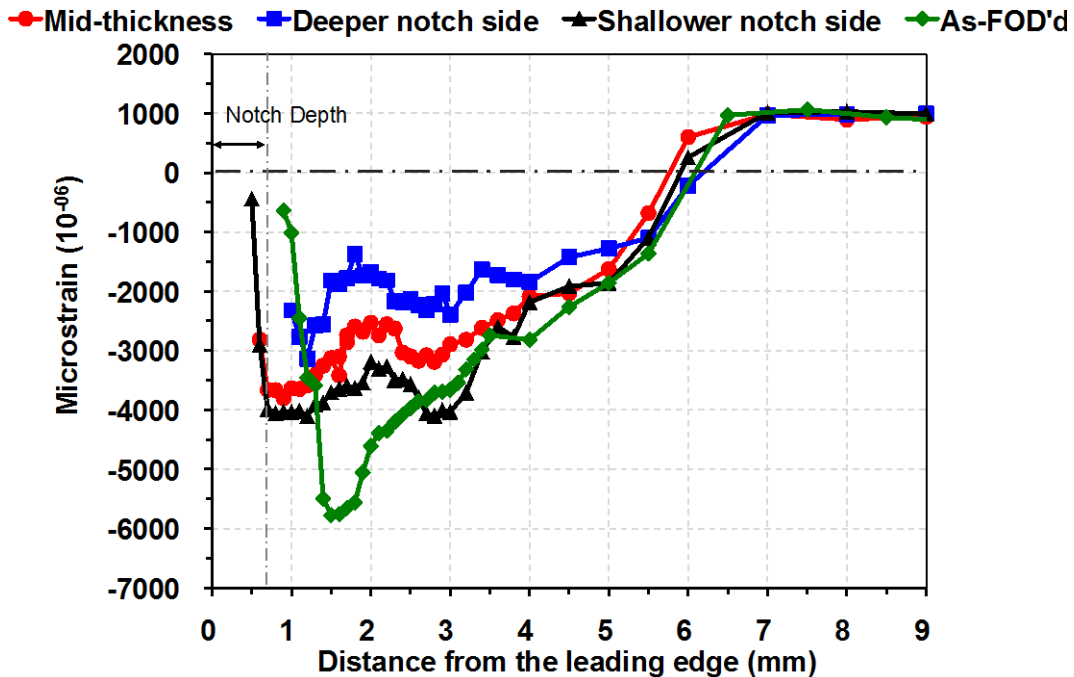


**Figure 4.14:** The depth-resolved residual strain distribution parallel to the leading edge along the notch centreline ( $y=0$ ), generated for a  $45^\circ$  FOD impact (S-9), after applying an additional  $10^5$  LCF cycles under a maximum applied stress,  $S_{max} = 586$  MPa. The notch depth for this specimen (S-9) is 0.62 mm.

Significant difference in the strains values has been observed along the thickness. Some important features in Figure 4.13 and Figure 4.14 are highlighted below:

- Solely LCF cycles introduced higher compressive residual stresses at the notch root compared to the as-FOD'd impact.
- A significant through thickness strain variation has been observed with more relaxation in the deeper notch side than the shallower notch side. This may be associated with the higher stress concentration effects at the deeper side. This agrees well with the observation of crack initiation at the deeper side by Spanrad (2011) and also elsewhere (Thompson et al 2001). Although no cracks have been detected for specimen S-9 by DCPD system, evidence of microcracking has been found in the SEM (Figure 4.15) at the notch root.
- Even though peak compressive stress at the notch root has been relaxed by 20%, after  $10^5$  cycles, at a distance of 1.8 mm from the L.E. the residual strains at the shallower side and mid-thickness of the notch became more compressive. This may be due to nonuniform material deformation along the thickness. This could also be due to the presence of short undetected cracks that caused stress concentration at 1.55 mm, and so reducing stress at notch and increasing stresses at 1.8 mm. Figure 4.15 supports this inference.
- Relaxation stretches to a distance of 4 mm from the L.E. in both cases.

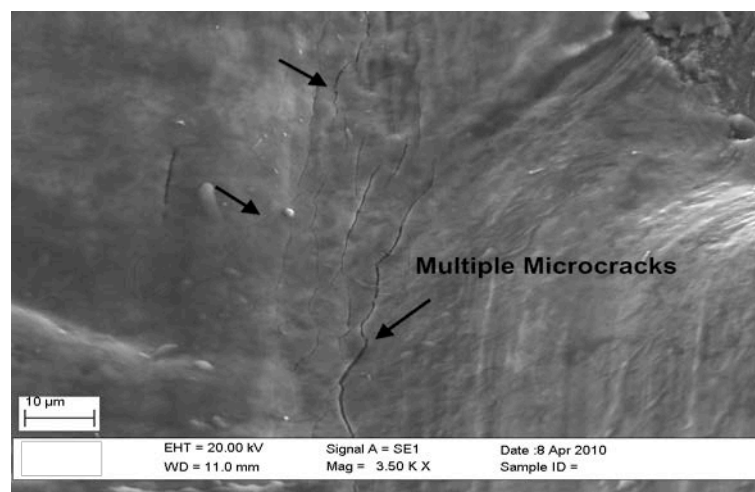


**Figure 4.15:** SEM image of the specimen S-9 (after applying an additional  $10^5$  LCF cycles at,  $S_{max} = 586\text{MPa}$ ) showing multiple crack formation at the base of the notch.

## **FWHM**

The FWHM of the fitted peaks were also plotted as a function of distance from the L.E. for two loading conditions in the longitudinal directions as shown in Figure 4.16 and Figure 4.17 respectively. Clearly, in the longitudinal direction solely LCF fatigue loading resulted in 20% reduction in the FWHM compared to the as-FOD'd condition. This may be attributed to the redistribution of dislocation substructure upon fatigue loading. Researchers found similar results in shot peened AISI 4140 steels peak width decreases with increasing number of cycles under fully reversed condition ( $R=-1$ ) (Holzapfel et al 1998). When the specimen was subjected to  $10^5$  cycles, a slightly increased peak broadening was observed near the notch in the longitudinal direction. For  $10^3$  cycles, deeper notch side exhibited unusually higher peak broadening (65%) in the transverse direction indicating high stress concentration at this side due to the larger notch depth, and also the possibility of initiation and early stage crack growth of FOD induced microcracks ( see Figure 4.15) under LCF. It has been found that such high speed impacts can generate microcracks  $< 10 \mu\text{m}$  (Boyce et al 2001, Frankel 2009) in the specimen that can grow under subsequent cyclic loading. Such microstructurally small cracks are difficult to detect by DCPD system even though the resolution of such a system is reported as  $2.5 \mu\text{m}$  (Ding et al 2007a). This might infer that FOD induced microcracks might have grown under LCF loading contributing to the relaxation observed here.

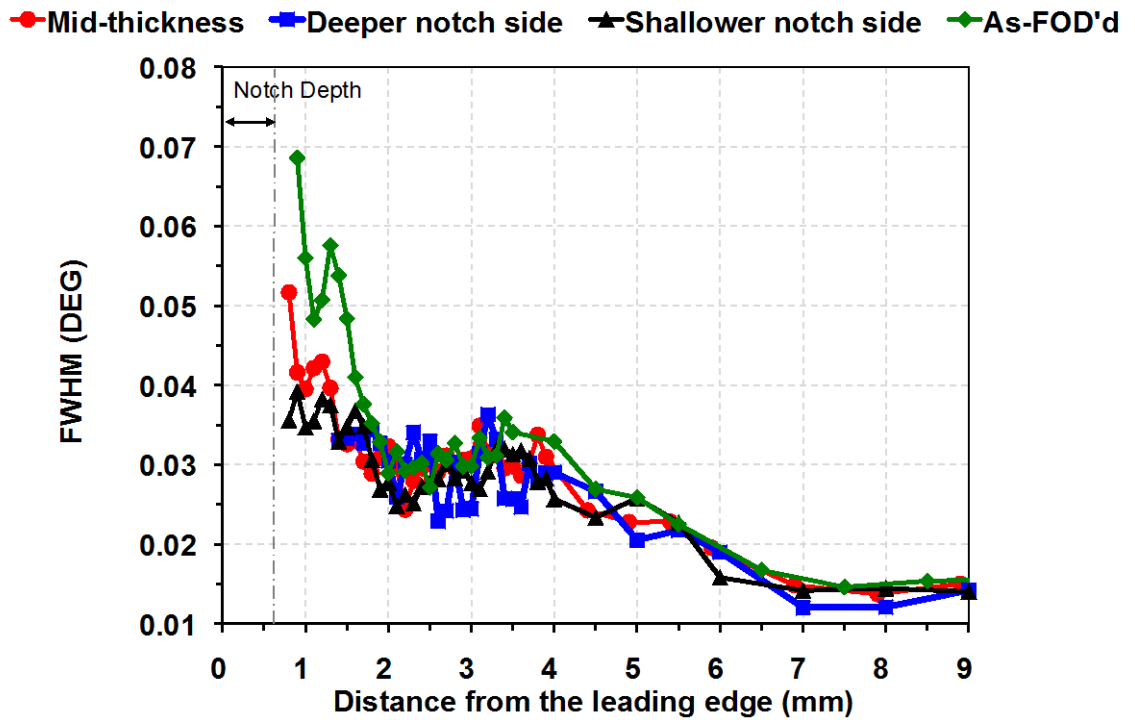


Figure 4.16: The FWHM plot in longitudinal direction for S-9, after  $10^3$  LCF cycles under a maximum applied stress,  $S_{max}=521$  MPa.

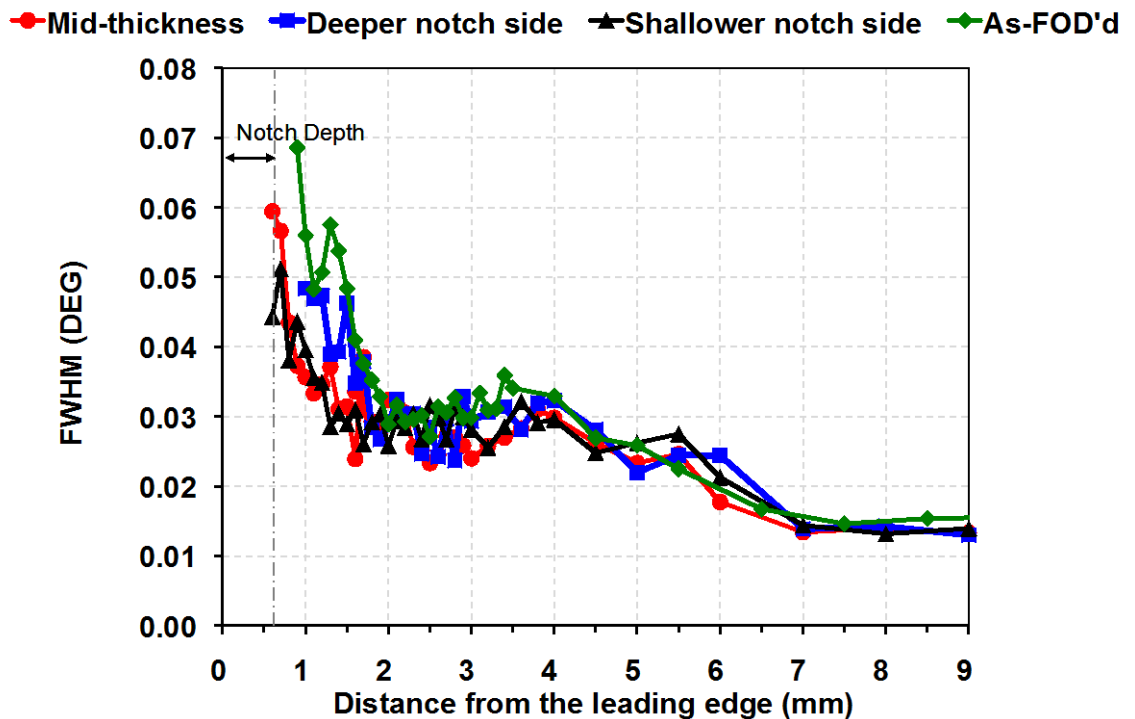


Figure 4.17: The FWHM plot in the longitudinal direction for S-9, after applying  $10^5$  LCF cycles under a maximum applied stress,  $S_{max}=586$  MPa.

#### 4.4.2 Effect of Combined Cycle Fatigue on RS Relaxation

Aero-engine rotating components such as fans and blades are generally subjected to high frequency vibratory loading (HCF), which is superimposed onto low frequency centrifugal loading (often at high stress). Therefore, knowledge of residual stress rearrangement either in LCF or HCF loading is not sufficient to understand whether the beneficial compressive stresses from LSP treatment are stable during service. For that reason the residual stress relaxation behaviour for both 0° and 45° FOD impacts has been investigated under combined (LCF+HCF) cycle loading (see Figure 3.5 for the definition of CCF), and the results are presented in this section.

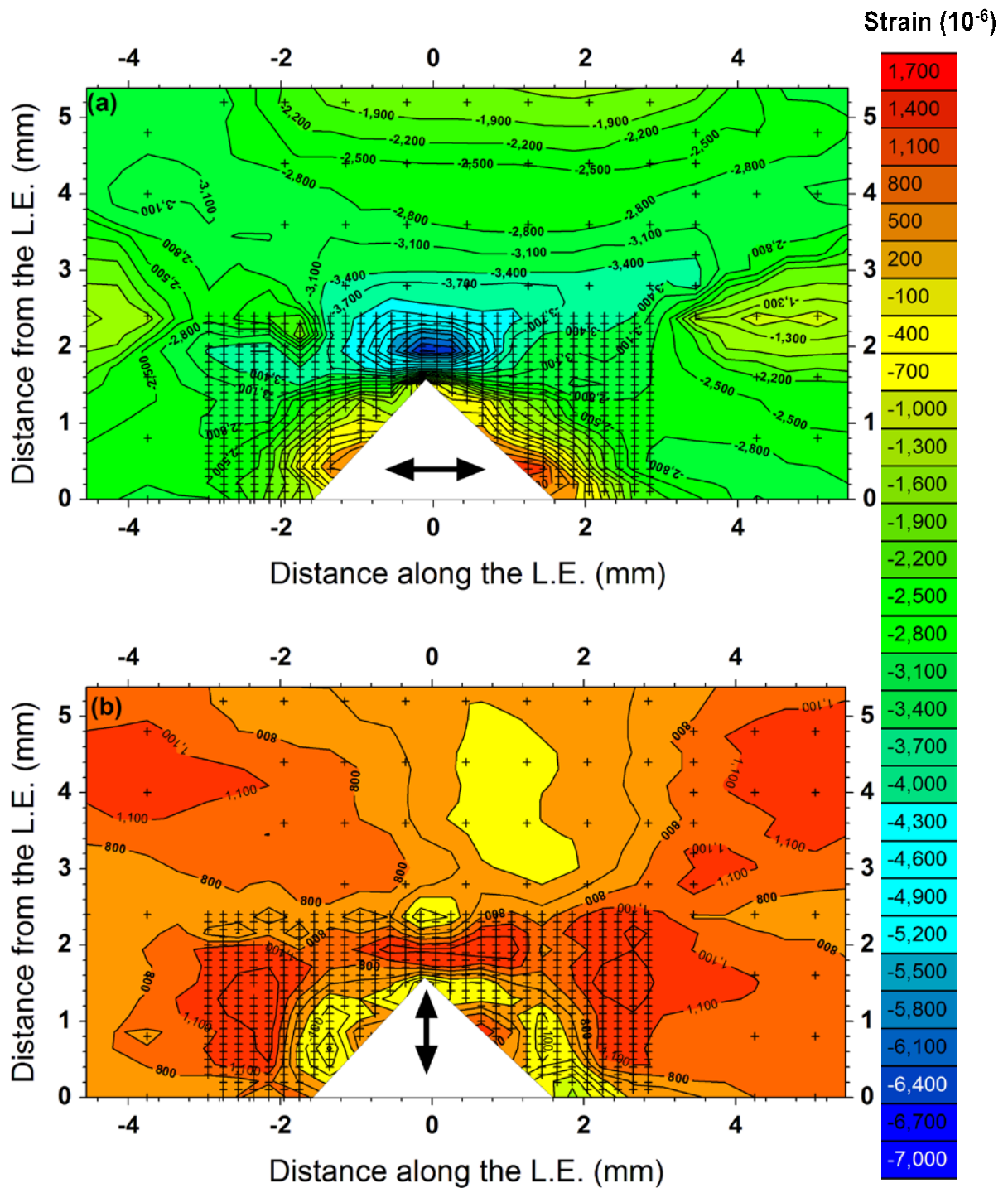
##### 4.4.2.1 Residual Stress Response of 0° FOD to Combined Cycle Fatigue

Figure 4.18a shows the 2D residual strain map obtained on 1-Id-C beamline at APS, for a 0° FOD impact after a single block of combined LCF and HCF loading cycles (ratio of LCF and HCF = 1:1000; maximum applied Stress  $S_{max} = 435\text{MPa}$  and  $R = 0.1$  and  $0.7$  for LCF and HCF, respectively). Comparison with the as-FOD'd (S-1) residual strain map in Figure 4.5 suggest no relaxation for  $N=1$  block. It is important to note that the two specimens in Figure 4.5 and Figure 4.18 are different specimens. The notch in the sample represented in Figure 4.18 is 0.06 mm deeper than in the sample mapped for Figure 4.5 due to the variability of the FOD impact process. The deeper notch depth resulted in a larger compressive strain field at the bottom of the notch. It has been reported that, for Ti-6Al-4V, the applied stress needs to be  $0.54 \times \sigma_y$  (at  $R=0.1$  and  $N=1$  cycle) for strain relaxation to occur under fatigue loading conditions, whilst at  $0.35 \times \sigma_y$ , little relaxation was observed (Boyce et al 2003). Even though the current test condition is about  $0.56 \times \sigma_y$  there is no evidence of relaxation after the fatigue cycles. The effect of fatigue loading might have been overshadowed by the difference in notch depths between the two samples. Figure 4.18b shows the residual elastic strains perpendicular to the leading edge measured post FOD and fatigue loading. Again, there seems no apparent evidence of strain relaxation after a block of 1000 HCF cycles on a LCF cycle, given the difference in the damage depths of the two samples. In this case also the area beyond 3 mm from the L.E. remained unchanged.

When the specimen was further fatigue loaded with  $N = 100$  blocks, whilst keeping the maximum applied stress constant no relaxation was observed as shown in Figure 4.19. This suggests that 1 or 100 CCF blocks are not sufficient to cause any relaxation under an applied

stress of  $0.35 \times \sigma_y$ . This suggests that LSP induced residual stresses are highly stable. This agrees well with the results published by Nalla et al (2003) where only 20% stresses are shown to be relaxed after applying half number of cycles of the total cycles to failure ( $N=0.5N_f$ ) at a stress amplitude of  $\sigma_a=0.7 \sigma_y$  under complete reverse bending

Figure 4.20 exhibits the average FWHM map for S-2 followed by  $N=1$  cycles. Similar to the as-FOD'd condition, twice as much as peak broadening can be noticed in the vicinity of the notch compared to the far field broadening. There is almost no effect observed after the first cycle.



**Figure 4.18:** Residual elastic strain (a) parallel and (b) normal to the leading edge for a  $0^\circ$  FOD impact followed by 1 combined fatigue loading blocks ( $CCF=LCF$ :  $HCF=1:1000$ ,  $S_{max}=435$  MPa and  $R_{LCF} = 0.1$  and  $R_{HCF} = 0.7$ ). The notch depth for this sample (S-2) is 1.55mm. Measurement locations are indicated by (+).

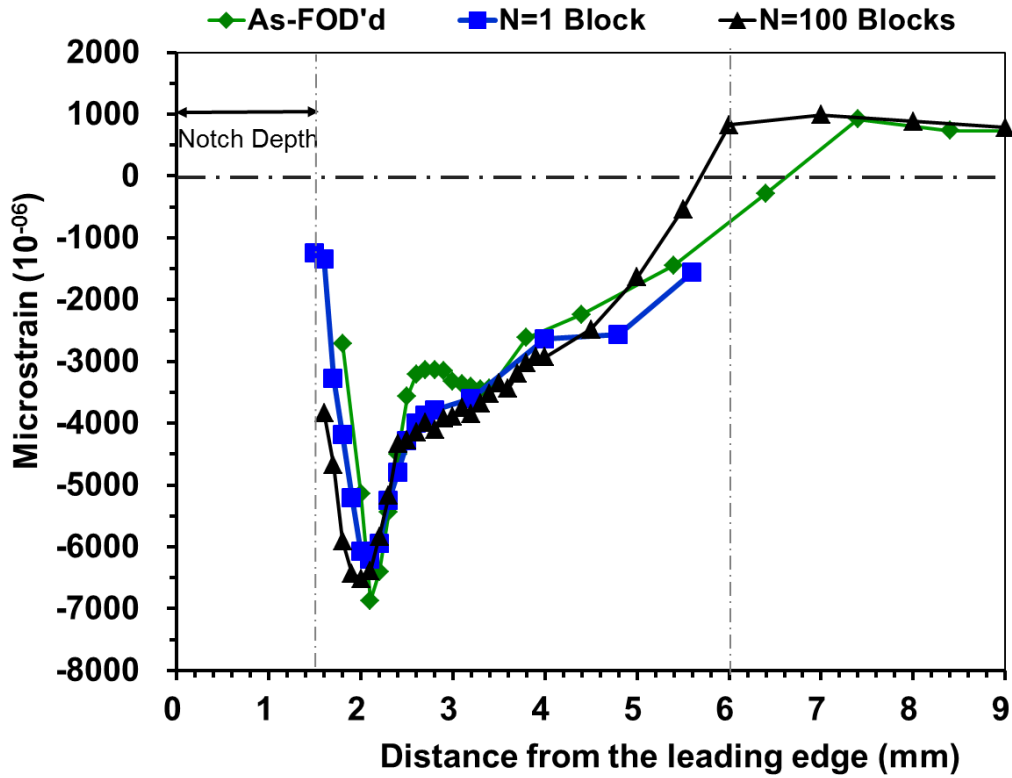


Figure 4.19: Comparison of residual elastic strain profiles parallel to the leading edge at the notch centre-line ( $y=0$ ) for a  $0^\circ$  FOD impact followed by 1 and 100 combined fatigue loading blocks (CCF=LCF: HCF=1:1000,  $S_{max}=435$  MPa and  $R_{LCF} = 0.1$  and  $R_{HCF} = 0.7$ ). The notch depth for this sample (S-2) is 1.55mm.

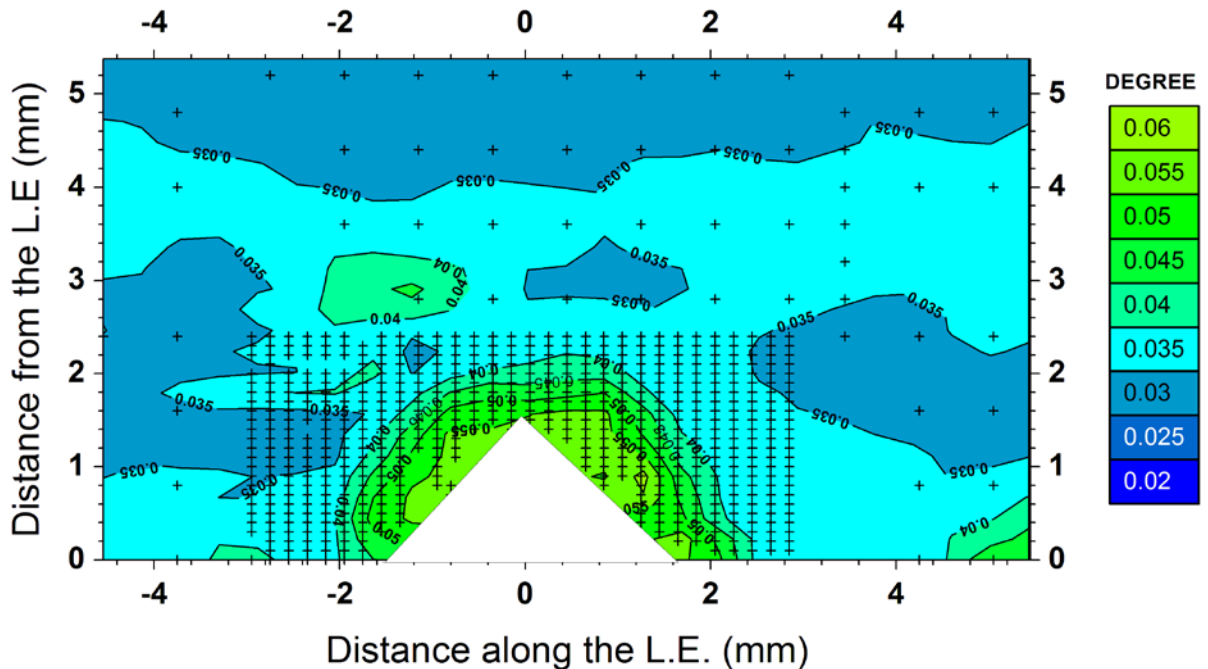


Figure 4.20: Average FWHM (from  $10^{-2}$ ) diffraction peak acquired on 1-ID-C beamline at APS) plot for post FOD and fatigue at N=1 block for specimen S-2.

#### 4.4.2.2 Residual Stress Response of 45° FOD specimens to CCF

The residual strain relaxation under CCF type of loading was evaluated for 45° FOD impact on ID 31, ESRF. Figure 4.21 exhibits residual strain profiles for a specimen that underwent N=100 blocks with  $S_{max}=430$  MPa (see Table 3-3). Comparison with the as-FOD'd condition suggest no significant relaxation of LSP+FOD'd residual stress has taken place. However, when the applied stress was increased by 36%, 30% residual strains shakedown occurred after only 10 CCF blocks as shown in Figure 4.22. This suggests that applied stress has a greater effect on relaxation than the number of cycles, be it LCF or CCF.

#### 4.4.3 Discussion: CCF vs. LCF

Comparison of the effect of the combined cycle fatigue with the solely LCF cycles (result presented in section 4.4.1.1) suggest that applied stress is a predominant factor in relaxation than the total number of applied fatigue cycles.

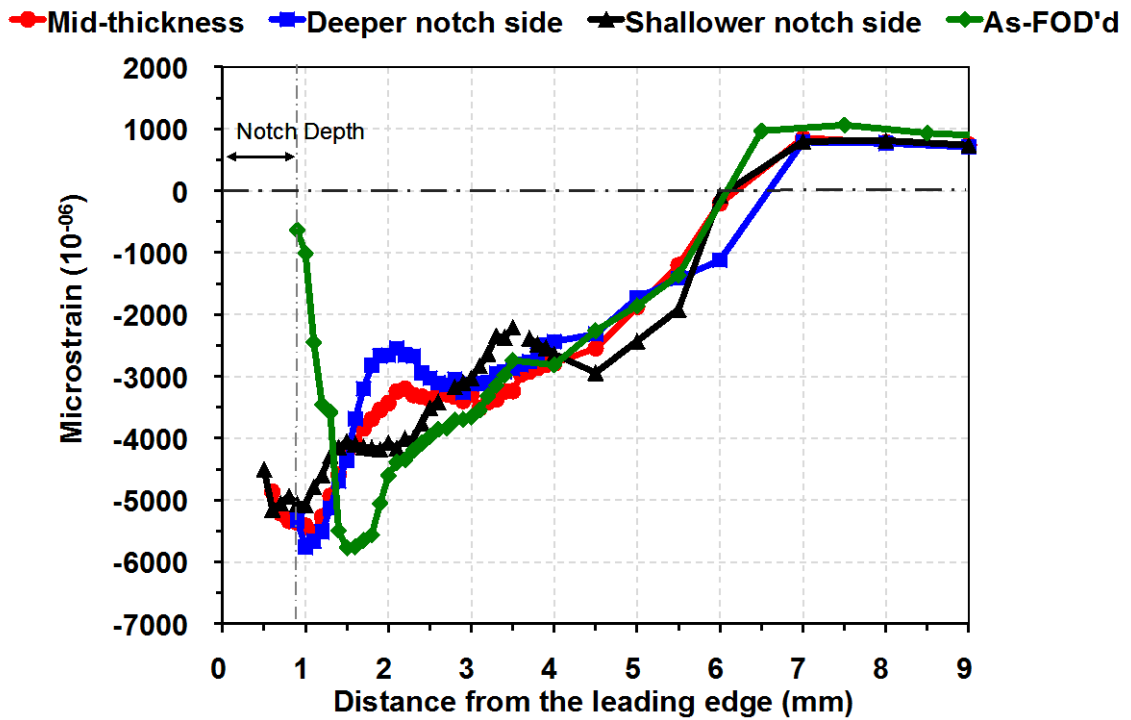


**Figure 4.21:** The synchrotron residual strain profiles parallel to the L.E. generated for a 45° FOD impact after subjecting combined (LCF+HCF) fatigue cycles,  $N= 100$  blocks, under  $S_{max}=430$  MPa. The notch depth for this specimen (S-8) is 0.78mm. The results are also compared with the residual strains in the as-FOD'd specimen (S-7)

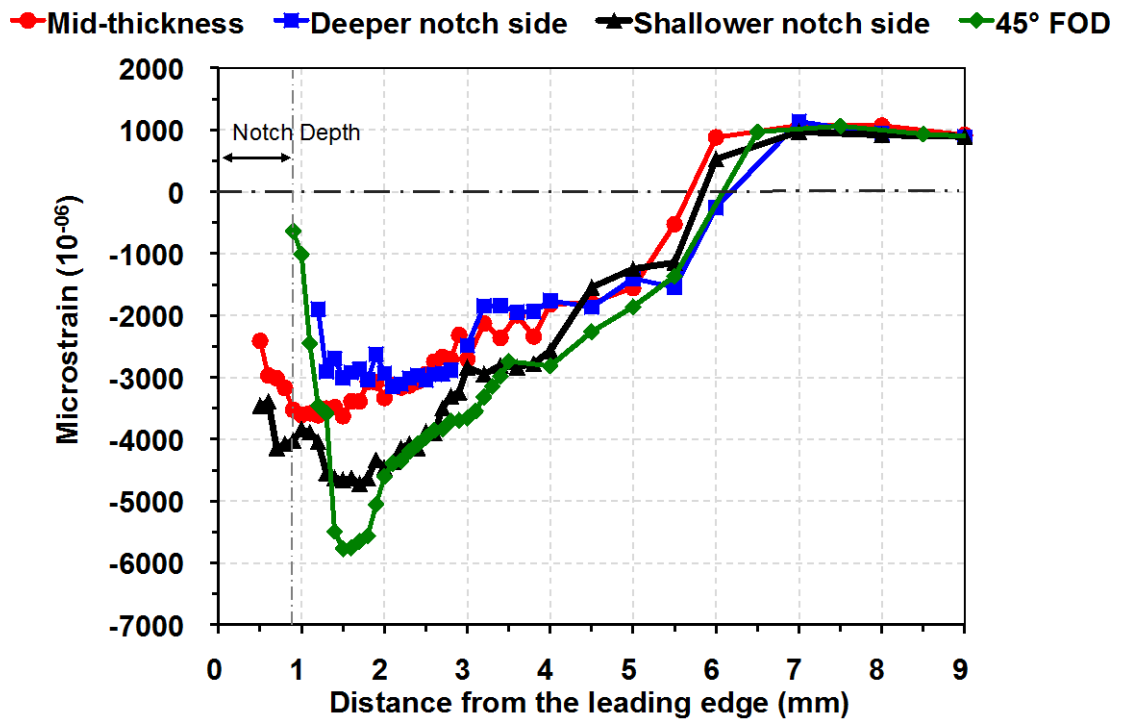


**Figure 4.22:** The synchrotron residual strain profiles parallel to the L.E. generated for a 45° FOD impact after applying combined (LCF+HCF) fatigue cycles,  $N = 10$  blocks, under  $S_{max} = 586$  MPa. The notch depth for this specimen (S-7) is 0.82 mm.

Figure 4.24 shows the FWHM plot for S-7 only after 10 blocks. Note that the line shown here for as-FOD'd condition was acquired from the same specimen before fatigue cycling. Therefore, direct comparison is possible in this case. Clearly it is evident that the peak width is largely unaffected after  $N=10$  blocks under a maximum applied stress of  $0.7 \times \sigma_y$ . This result is in agreement with those presented above, and suggests that the diffraction peak width decreases with increasing number of fatigue cycles before crack initiation. Now comparison of this result with Figure 4.23 indicate that higher applied stress may cause the redistribution of the residual stress even at small number of CCF type fatigue loading, without changing the overall cold work in the specimen. However, the degree of cold work is reduced with increasing number of cycles. Similar results were also found experimentally on shot peened AISE 4340 steel (Torres & Voorwald 2002) and numerically by (Zhuang & Halford 2001).

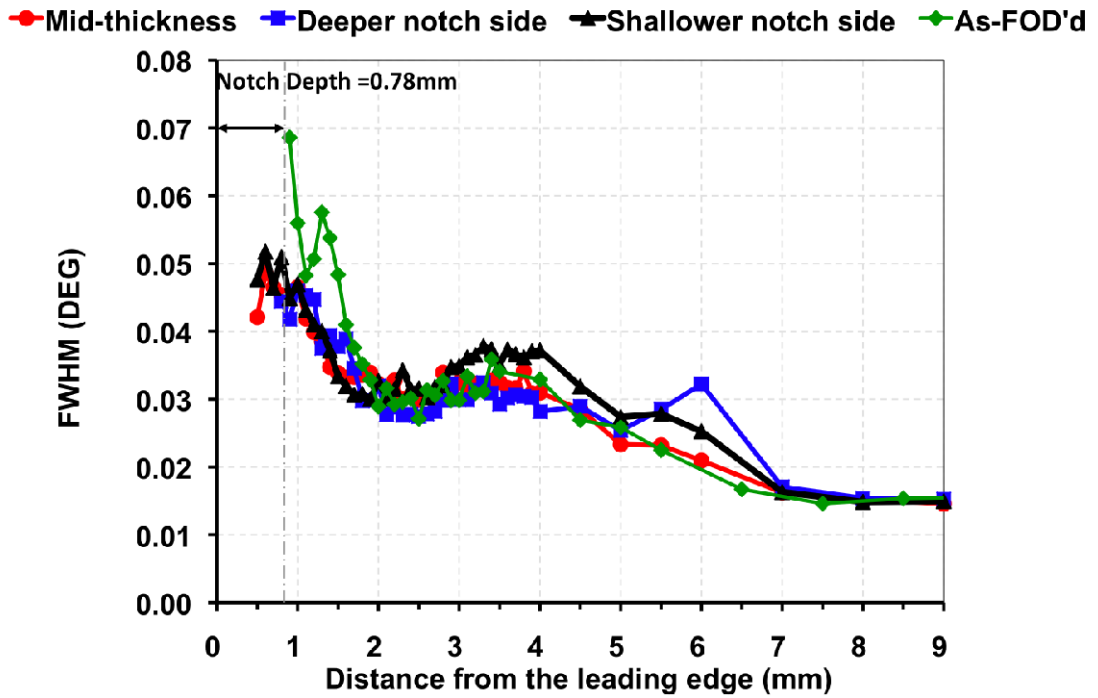


**Figure 4.23:** The FWHM plot for S-8 in longitudinal direction, followed by combined (LCF+HCF) fatigue cycles,  $N=100$  blocks, under  $S_{max}=430$  MPa.

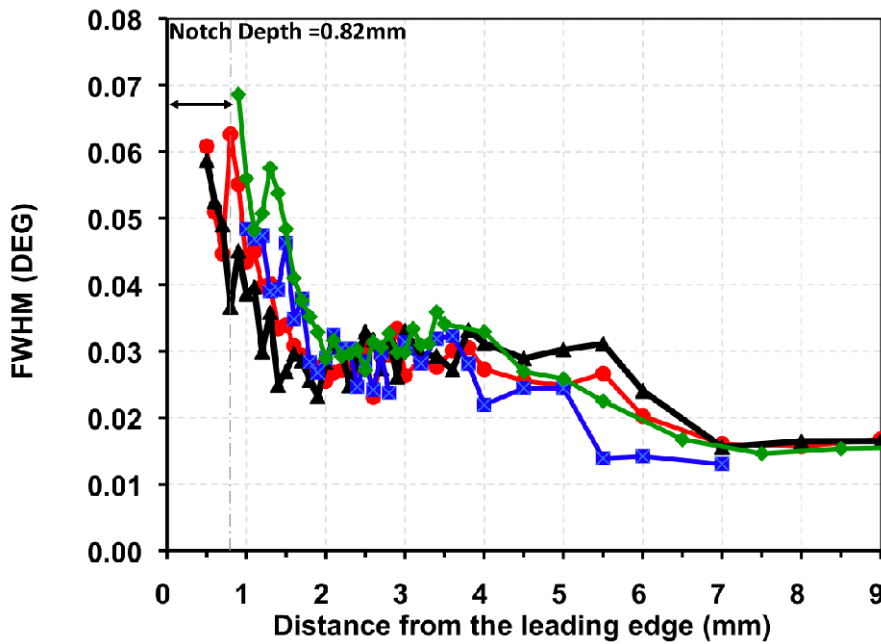


**Figure 4.24:** The FWHM plot for S-7 in longitudinal direction, after applying combined (LCF+HCF) fatigue cycles,  $N=10$  blocks, under  $S_{max}=586$  MPa.

#### **4.4.4 Summary**

A thorough evaluation has been carried out to determine the effect of various types of fatigue loading, on the relaxation of the residual strains associated with FOD impact on LSP'd simulated leading edge specimens in two impact conditions. For 0° impacted specimens no significant relaxation was observed under the fatigue loading condition studied here. Due to the limited availability of the specimen the effect of just LCF, and also relaxation under CCF at an applied stress of  $0.7 \times \sigma_y$ , was not investigated here. However, for the 45° impact condition a thorough investigation has been carried out. Based on the results presented here, it can be inferred that the level of the applied stress is more effective in RS relaxation than the number of cycles. From the FWHM plots it is evident that even though higher applied load is necessary to cause relaxation, the degree of plasticity adjacent to the notch reduced only when the specimens were subjected to the higher number of cycles.

## 4.5 Fatigue crack growth behaviour in a residual stress field

The residual stresses associated with laser shock peening and FOD impacts are likely to be subject to relaxation and redistribution when a fatigue crack propagates through the material. A significant amount of relaxation may necessarily reduce the beneficial effect of LSP treatment by enhancing the fatigue crack growth rate. Therefore, it is important to evaluate the relaxation of these beneficial compressive residual stresses and the rate at which they relax as a function of crack length for both 0° and 45° FOD. In this section the residual strain relaxation behaviour is delineated for various crack lengths ranging from short ( $a < 1$  mm) to long ( $a > 1$  mm) cracks under solely LCF as well as combined cycle fatigue loading conditions.

### 4.5.1 Effect of Low Cycle Fatigue Crack Growth on relaxation

#### 4.5.1.1 Residual stress relaxation for 0° FOD

In order to study the residual stress redistribution associated with short crack growth upon application of LCF, a 0° impacted specimen (S-5) was low cycle fatigued to  $n = 20,270$  cycles such that a crack of length  $\Delta a = 0.56$  mm was grown (Table 3-2). The residual strain redistribution was measured on HARWII using the through thickness transmission technique as described in Section 3.6.1. Figure 4.25 exhibits the residual strain distribution in the longitudinal direction of the specimen. Similar strain features to the as-FOD'd condition can be observed with a large compressive zone at the tip of the notch. No significant relaxation was evident for short crack growth. By contrast, for long crack growth at  $\Delta a = 5.3$  mm, studied in specimen S-6 (Table 3-2), the size and intensity of the large compressive region was substantially reduced as shown by the 2D residual strain distribution map given in Figure 4.26a.

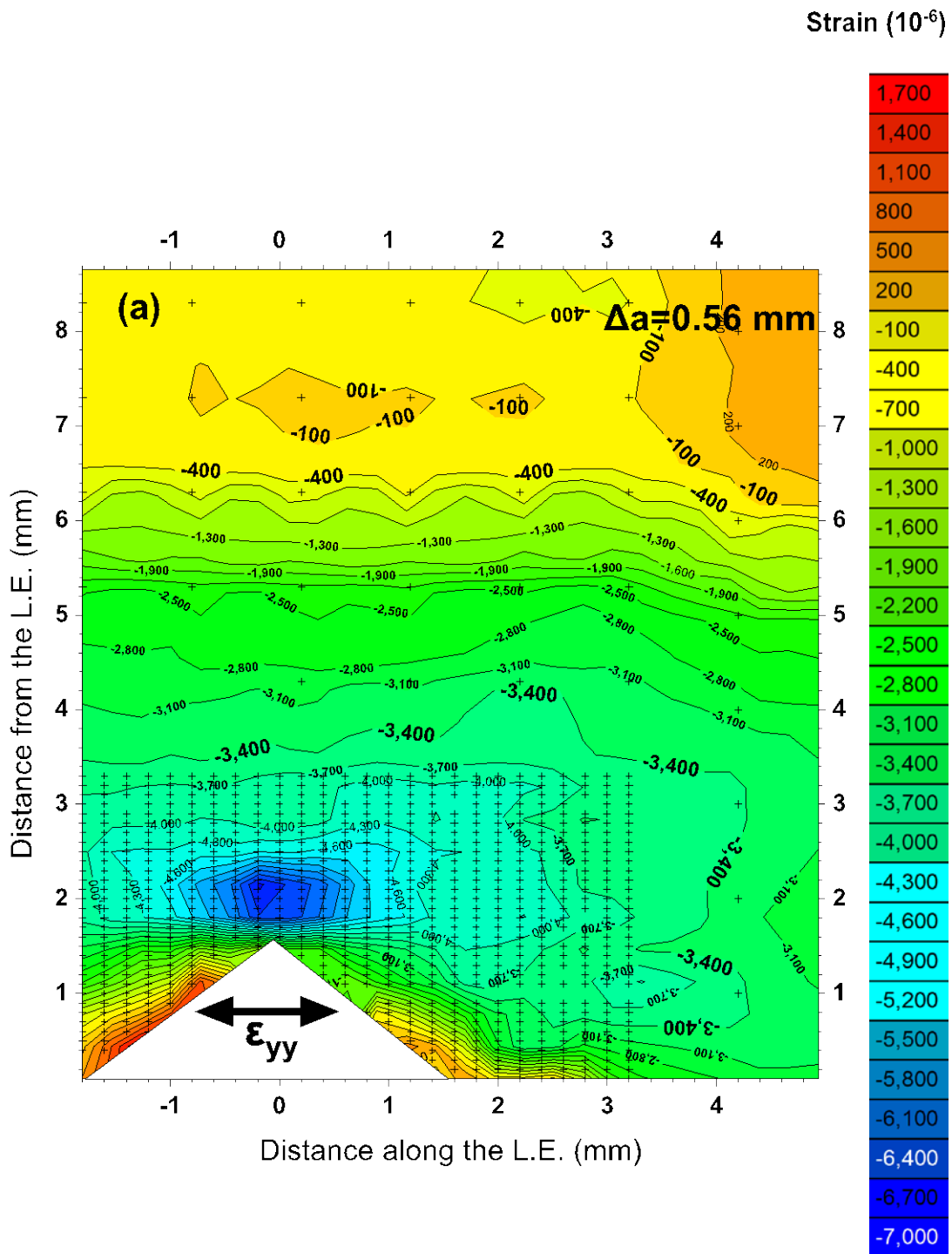
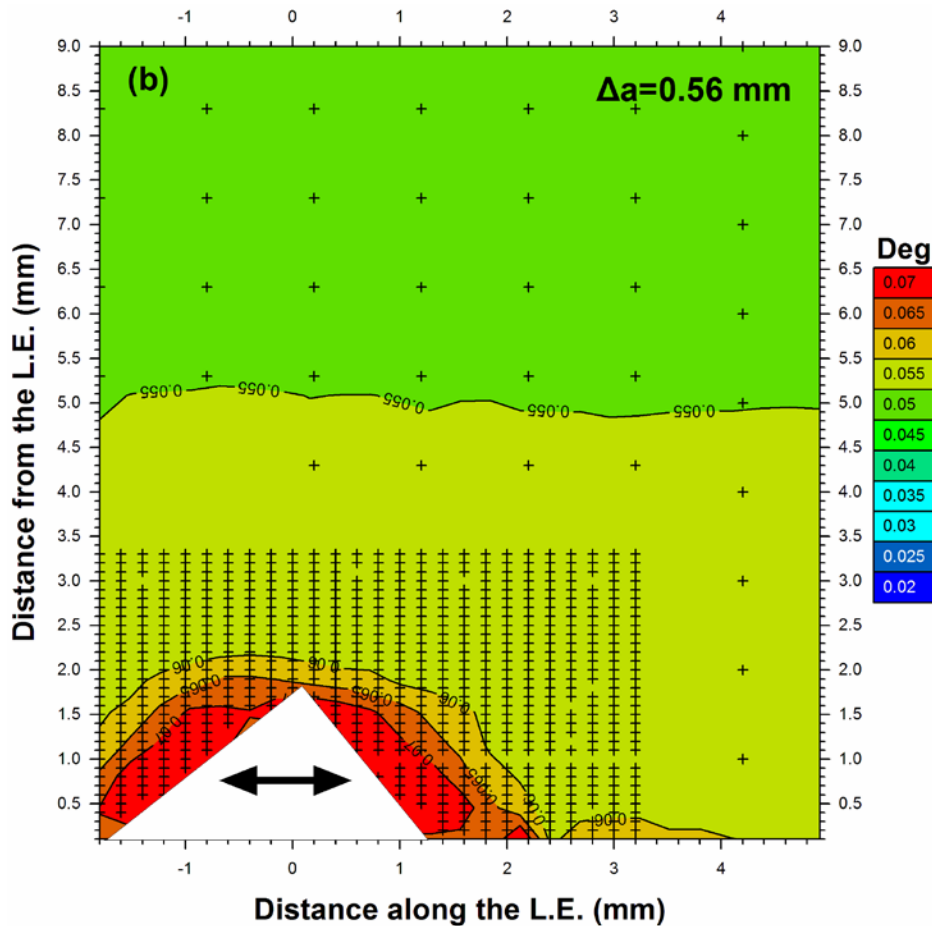


**Figure 4.25:** (a) Through thickness averaged 2D residual strain ( $\times 10^{-6}$ ) map measured at HARWII, for a  $0^\circ$  FOD impact. The specimen (S-5) had a notch depth of 1.5 mm and a 0.56 mm crack was grown by applying low fatigue cycles of  $n = 20272$  using an applied stress of  $S_{max} = 586$  MPa (Table 3-2).



(b) FWHM plot for specimen S-5 with a crack length,  $\Delta a = 0.56$  mm.

From Figure 4.25a and Figure 4.26a, 1D RS profiles as a function of distance from the L.E., were acquired at a location of  $y=0$  (which is the most probable location for crack initiation and propagation), and compared with the as-FOD'd RS profile in Figure 4.27a. Comparison with the as-FOD'd condition suggests that under an applied load of 586 MPa, when a shorter crack was grown with large number of LCF cycles, the residual stresses remained essentially unchanged; whereas the long crack ( $\Delta a=5.3$  mm) resulted in 28% relaxation in the peak compressive residual strain. The corresponding SEM image showing the crack initiation location and growth direction is shown in Figure 4.26b for 5.3 mm long crack.

Increasing relaxation with crack length is not surprising. However, the important finding here is that significant compressive residual stresses along the crack

faces remain, despite growing a 6.8 mm long crack. This may be associated with the global effect of the LSP induced compressive stress holding the crack faces shut. Furthermore, crack tip plasticity induced compression region is evident in Figure 4.26a along the crack path, noticeable after 5 mm from the L.E where the LSP'd residual stresses are less compressive.

Plasticity-induced crack-closure is a well-recognized phenomenon that occurs under cyclic loading (McClung & Newman 1999). Crack tip shielding takes place from the compressive residual stresses associated with plastic deformation at the crack tip. At low R ratios such crack-closure effect generally dominates. For this reason, it has been observed that when a 6.8 mm long crack was grown at  $R=0.1$ , plasticity-induced residual compression was evident along the crack faces. More precisely, in Figure 4.26a at the crack tip (at 6.8 mm from the L.E.), the initial RS originating from LSP was 2000 microstrain which was modified by the interaction of crack to -2000 microstrain. This effect may be attributed to the crack tip induced plasticity.

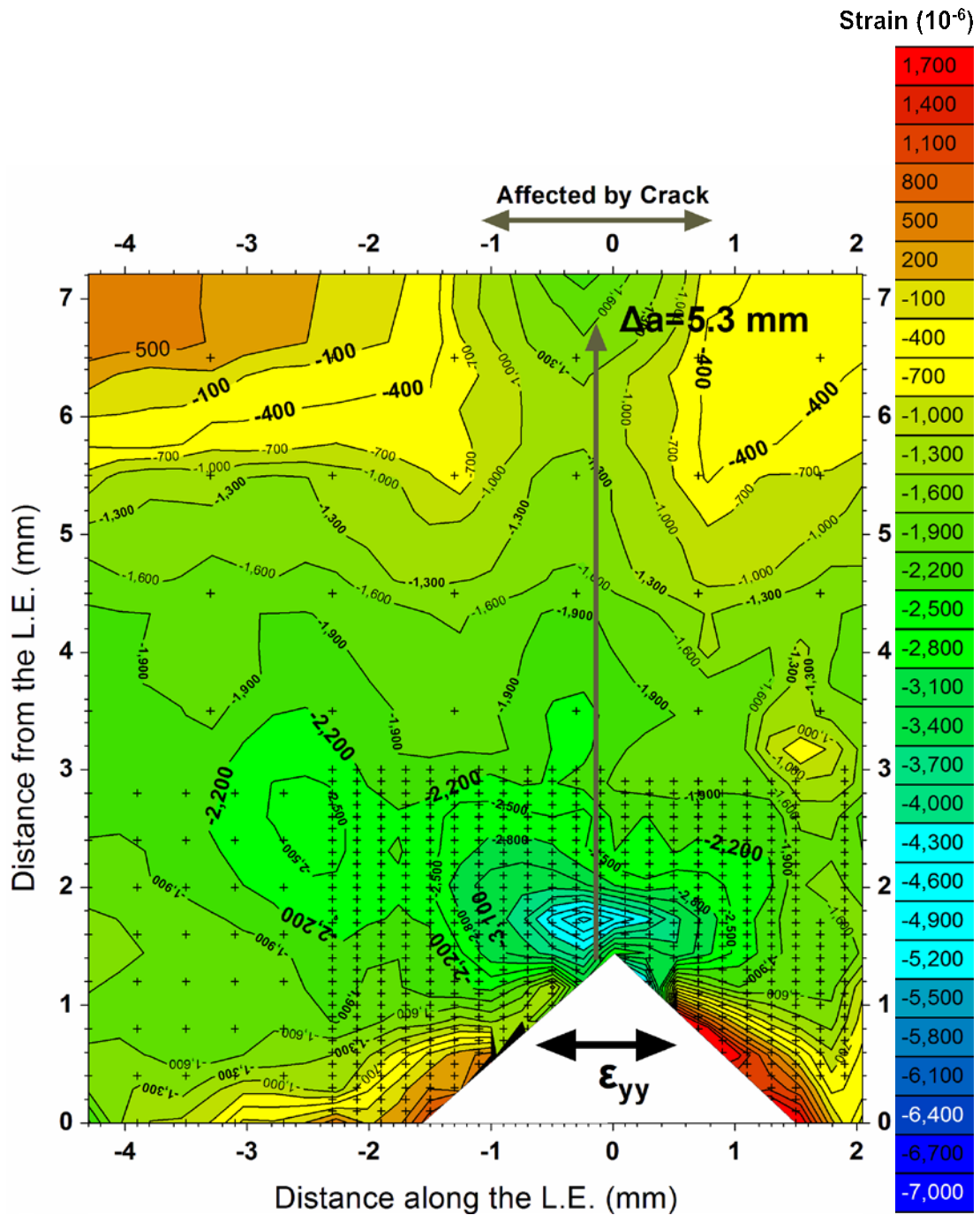
From the above discussion it is clear that relaxation due to crack growth is a local effect. However, global relaxation may occur if the applied stress ( $\geq 0.7 \sigma_y$ ) is higher (see Figure 4.14).

Table-4-1 summarizes the fatigue loading conditions and the corresponding relaxation of the peak compressive residual stress for both short and long cracks.

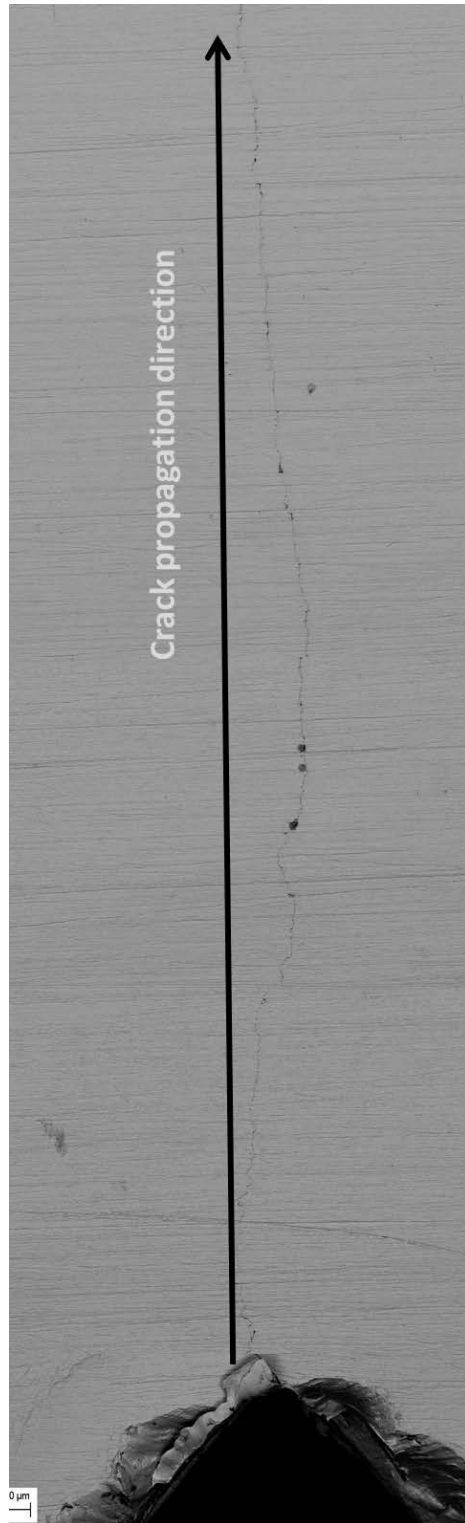
FWHM maps were also obtained and presented in Figure 4.25b and Figure 4.26c for 0.56 mm and 5.3 mm long crack respectively, and the comparison with the as-FOD'd condition is shown in Figure 4.27b. Near the notch root 20% higher value of FWHM was introduced due to crack growth which dropped sharply with increasing distance from the L.E. Beyond 3 mm from the L.E. the level of peak width becomes similar for two specimens. Since plastic deformation is at least one reason to increase the FWHM, this may suggest that early stage crack growth confers additional plasticity into the region near the notch root.

**Table 4-1: Residual stress relaxation due to crack growth under LCF**

Sample ID	$\Delta a$ (mm)	n (Cycles)	$S_{max}$ (MPa)	Relaxation of peak compression %
<b>0° FOD</b>				
S-5	0.5	20270	586	Not significant
S-6	5.3	34310		28%
<b>45° FOD</b>				
S-10	2.2	59641	586	29%



**Figure 4.26 (a):** Through thickness averaged residual strain profiles, parallel to the leading edge generated for a  $0^\circ$  FOD impact after applying LCF fatigue cycles,  $n = 34300$  cycles, under  $S_{max} = 586 \text{ MPa}$ . The notch depth for this specimen (S-6) is  $0.78 \text{ mm}$  and  $\Delta a = 5.3 \text{ mm}$  (Table 3-2).



*(b) An SEM image of the specimen (S-6) showing the crack initiation location and the crack growth direction.*

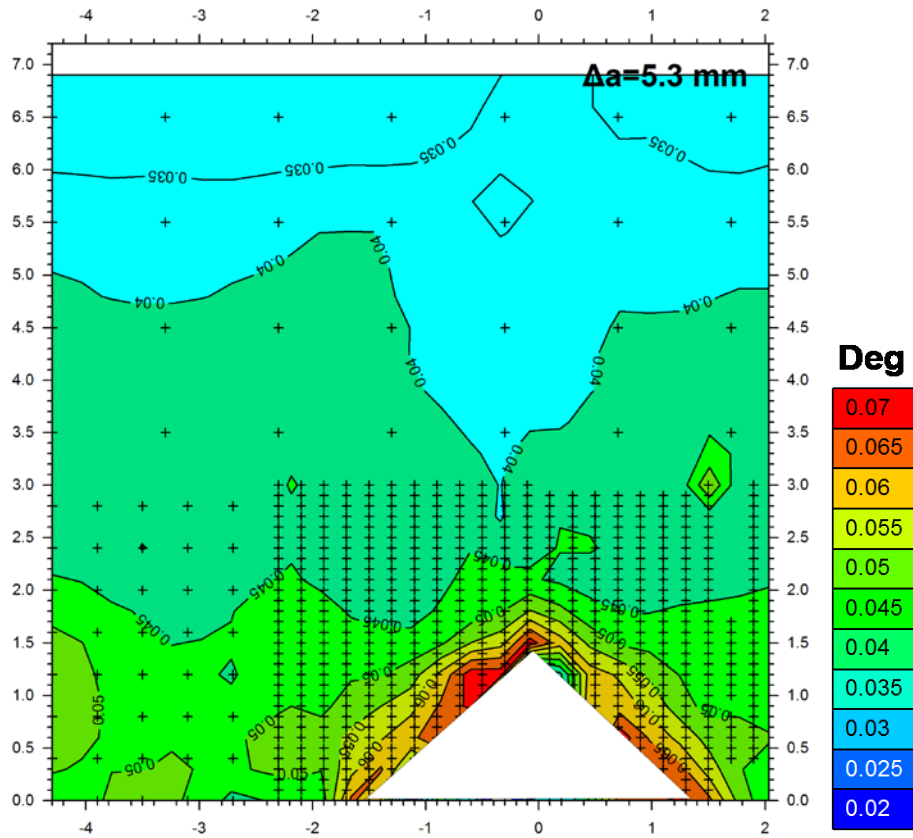
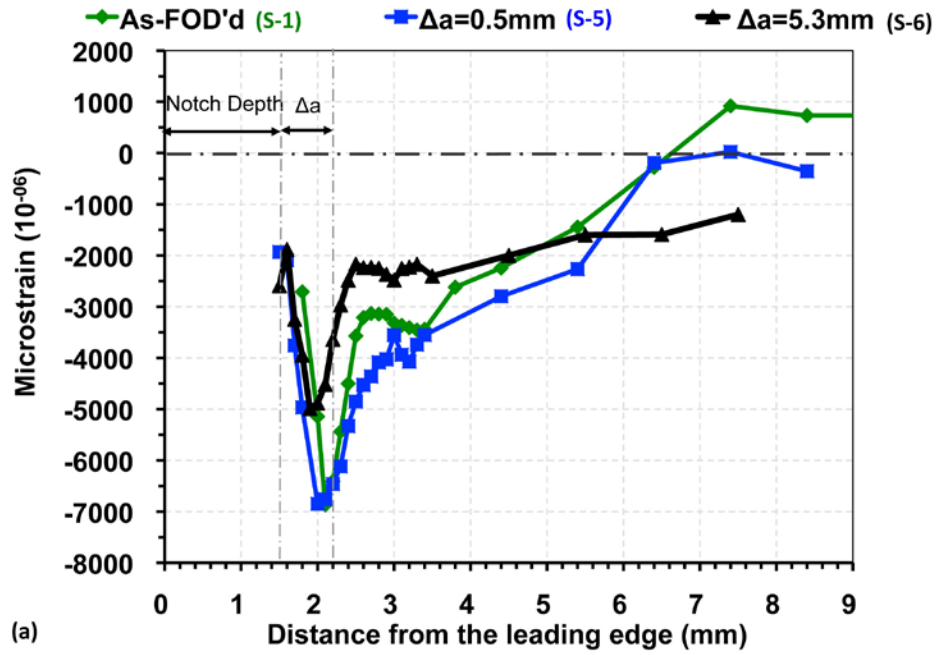
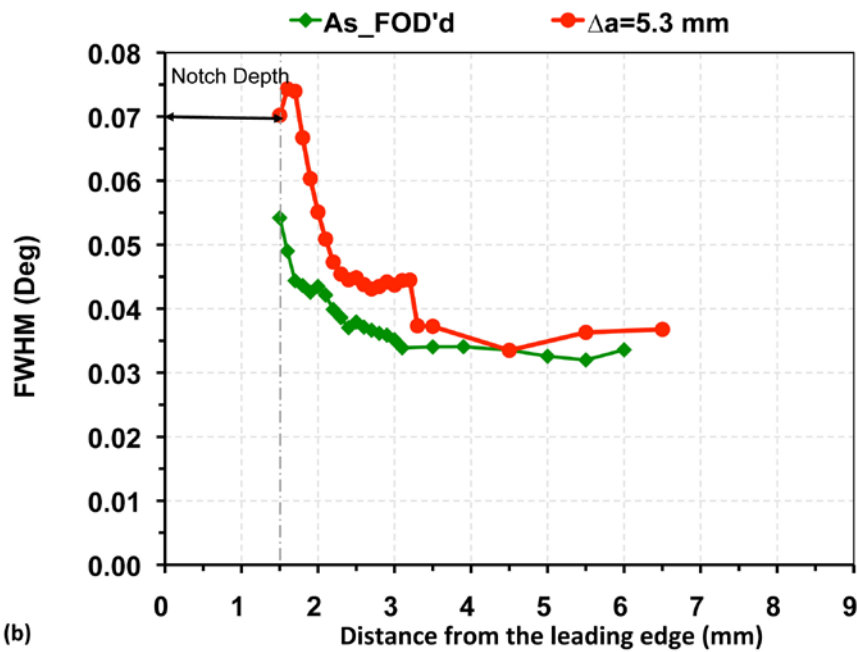


Figure 4.26 (c): FWHM Plot for specimen S-6 having a 5.3 mm long crack.



(a)



(b)

**Figure 4.27:** (a) Effect of crack growth on relaxation under low fatigue cycles, when the crack length  $\Delta a=0.5$  (S-5), and 5.3mm under  $S_{max}=586$  MPa (S-6). The average notch depth is 1.5 mm and (b) Comparison of FWHM between as-FOD'd condition and after 5.3 mm crack (Table 3-2).

**4.5.1.2 Residual Stress Response of 45° FOD Impact during Crack Growth**

Residual stress relaxation along the crack path has also been studied for the 45° impact condition. Figure 4.28a shows the 2D residual strain distribution of  $\epsilon_{yy}$  residual strain component for a 45° impacted specimen containing a 2.2 mm crack (see Figure 4.28b for the SEM image of the crack). Due to time constraints only one side of the notch was mapped. In comparison with the as-FOD'd condition, Figure 4.29a shows 29% relaxation of residual stress after 2.2 mm long crack growth.

The relaxation in the peak compressive residual stress is also tabulated in Table 4-1. Now these results can be correlated with the relaxation behaviour observed under solely LCF, to ascertain the residual strain relaxation due only to the crack growth because total residual stress relaxation = Cyclic relaxation + Relaxation due to crack growth. As shown in Figure 4.14, 48% relaxation was observed after  $10^5$  cycles, whereas, with a 2.2 mm long crack only 28% stress was relaxed after  $3.4 \times 10^4$  cycles. This may suggest that the total number of applied major cycle is a more significant contributing factor to the residual stress relaxation than relaxation from crack growth above.

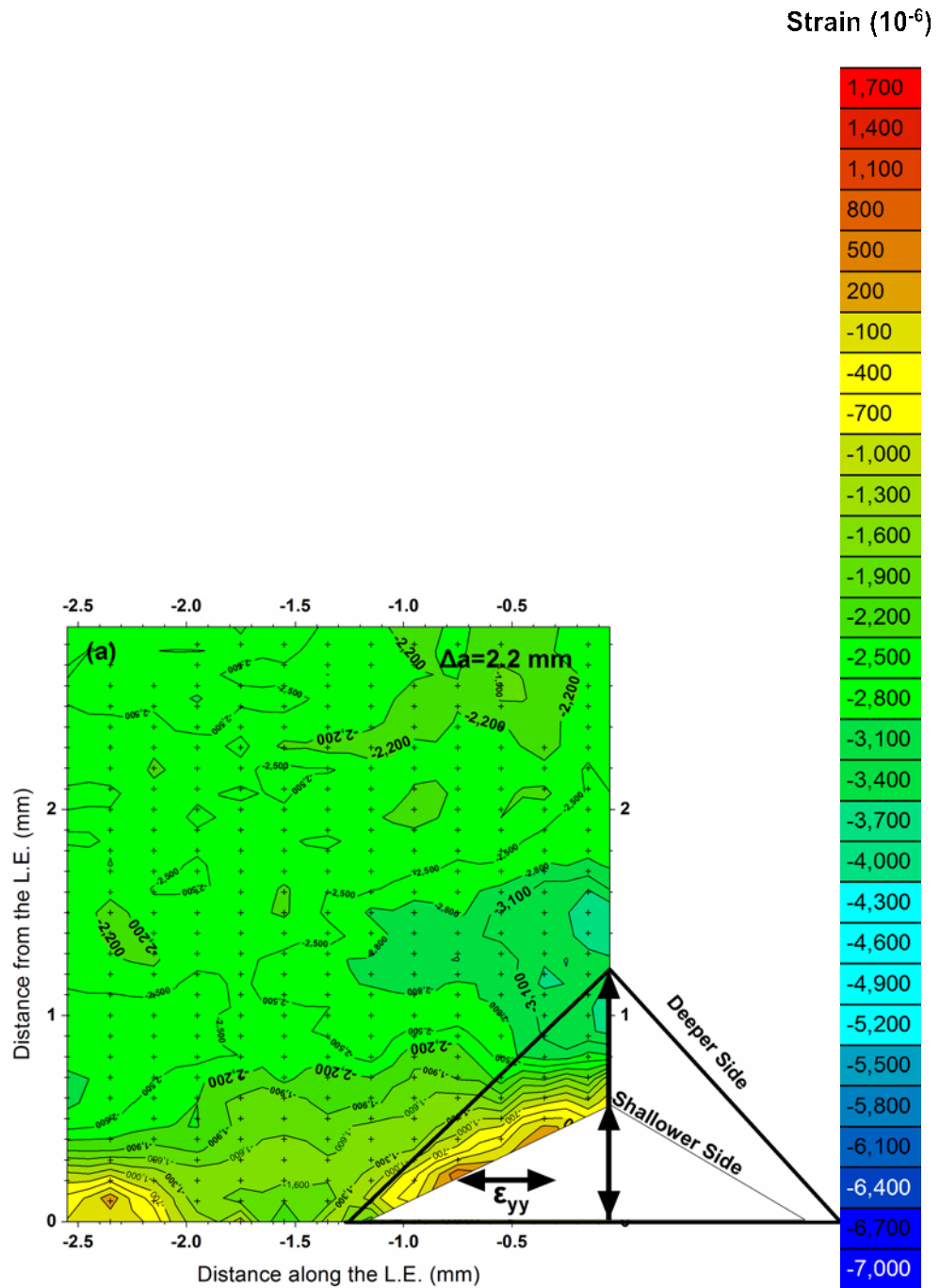
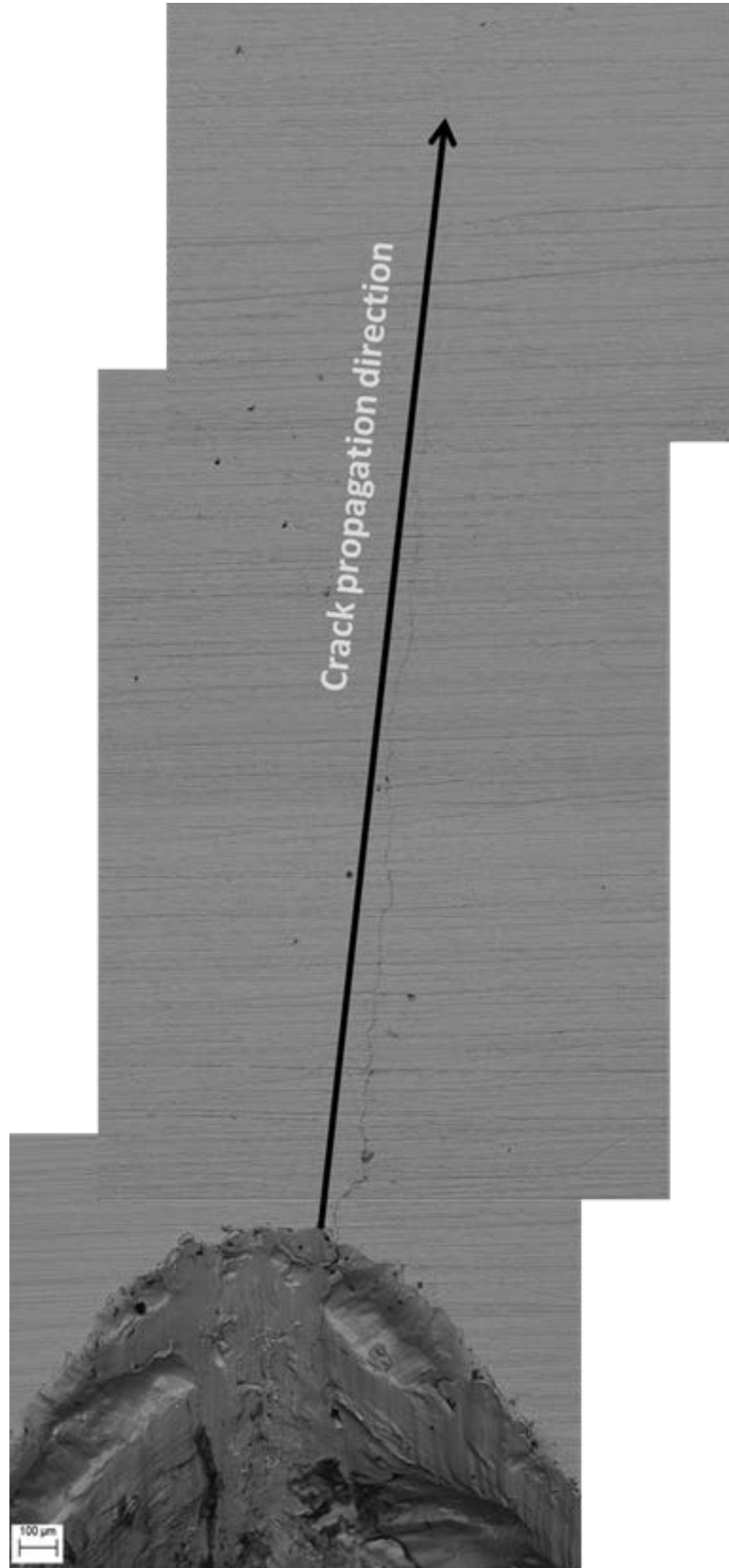
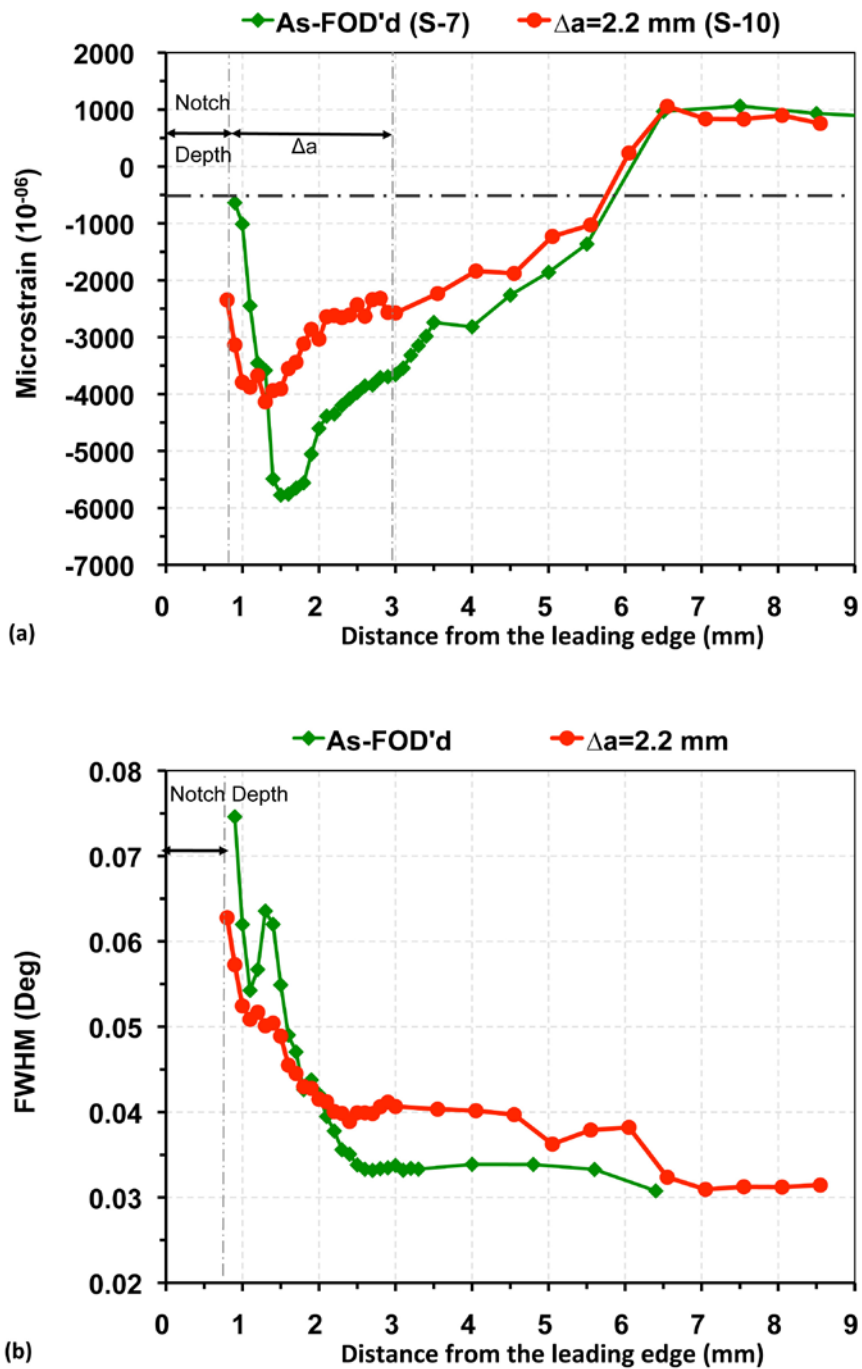


Figure 4.28 (a): Through thickness averaged 2D residual strain map measured on HEMS beamline, for a  $45^\circ$  FOD impact. The specimen (S-10) had a notch depth of 0.82mm and a 2.2 mm long crack was grown by applying LCF cycles of  $n=59641$  cycles and with a applied stress of  $S_{max}=586$  MPa (Table 3-3).



*(b )An SEM image of the specimen (S-10) showing the crack initiation location and the crack growth direction.*



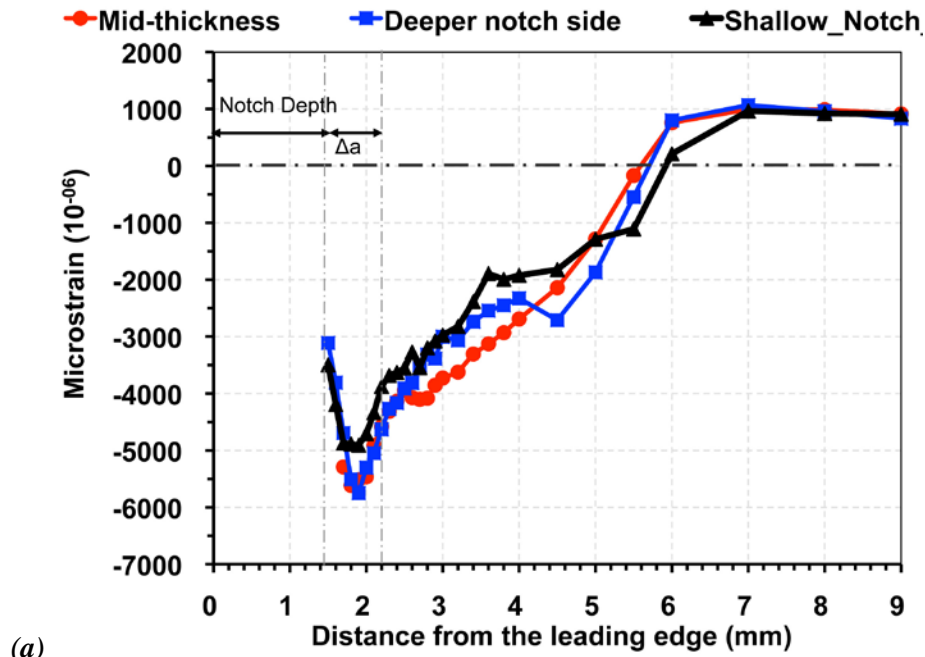
**Figure 4.29:** (a) A line plot of the longitudinal RS along the notch centerline for specimen S-10 with  $\Delta a = 2.2$  mm crack after 59641 LCF cycles at  $S_{max}=586$  MPa and (b) the corresponding FWHM plot.

#### 4.5.2 Effect of Crack Growth under Combined Cycle Fatigue on relaxation

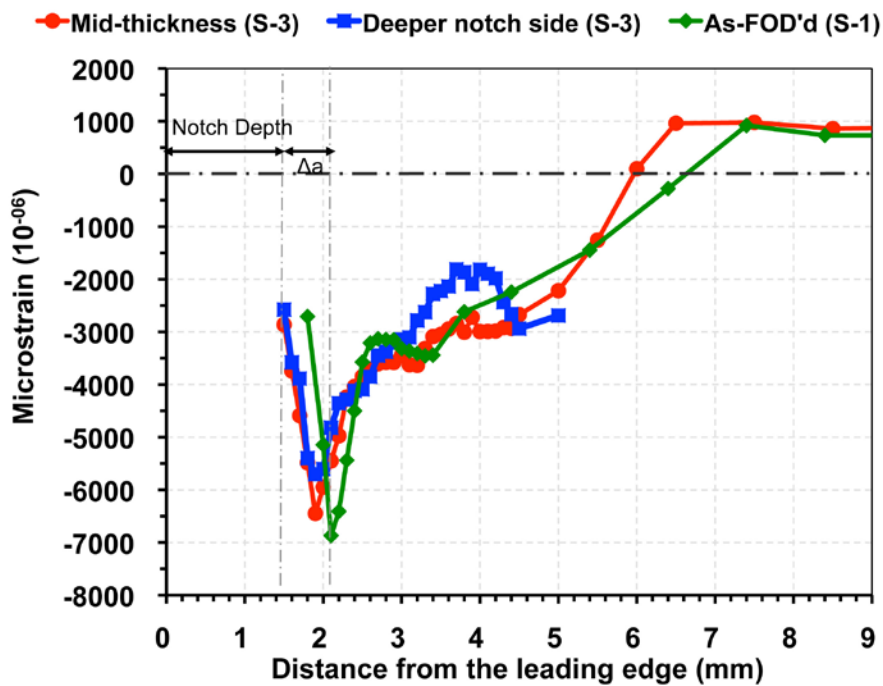
In the previous section, relaxation due to crack growth under solely LCF has been presented. Actual loading cycles in an aero-engine are typically a combination of both LCF and HCF. For that reason the residual stress relaxation caused by crack growth was studied under combined cycle fatigue (LCF+HCF). The analysis of the residual stress effect is often based on the straightforward superposition technique where residual stresses are simply added to the applied stress to get an effective applied stress at a location. When the applied stress is large enough such that the effective applied stress exceeds the yield stress of the material the compressive residual stress would be expected to relax. Later on, these results can be incorporated to the crack growth rate prediction model to assure a safe prediction in the damage tolerance design. The prediction of the expected fatigue crack growth rate is made in section 4.8 and compared with the experimental crack growth rate.

##### 4.5.2.1 Residual Stress Relaxation for Cracked 0° FOD specimens under CCF

The residual strain relaxation was studied for both short  $a < 1$  mm and long  $a > 1$  mm cracks under combined cycle fatigue. Two head-on (0° FOD) specimens namely S-2 and S-3 were investigated to study the relaxation due to short crack growth behaviour, for which the later had a 0.06 mm deeper notch than the former. Figure 4.30a and Figure 4.30b show the depth resolved residual strain profiles and FWHM, obtained on ID-31 ESRF, for specimen S-2 with 0.7 mm long crack and S-3 with 0.6 mm crack respectively. It is evident that 17% relaxation occurred in the peak compressive residual stress for specimen S-2, whereas only 7% relaxation was observed for S-3 specimen along the centreline of the notch. This is because of the difference in location where cracks were initiated and the direction at which they grew (see Figure 4.34). This is further elaborated as below.



(a)



(b)

**Figure 4.30:** Longitudinal depth resolved synchrotron residual strain profiles at a location of  $y=0$ , generated for  $0^\circ$  FOD impacts under combined (LCF+HCF) fatigue cycles at  $S_{max}=434$  MPa: (a) with a 0.7 mm crack after  $N= 1901$  blocks (S-2) and (b) with a 0.6 mm long crack after  $N= 2744$  blocks (S-3). The notch depths for specimen S-2 and S-3 are 1.55 mm and 1.49 mm respectively.

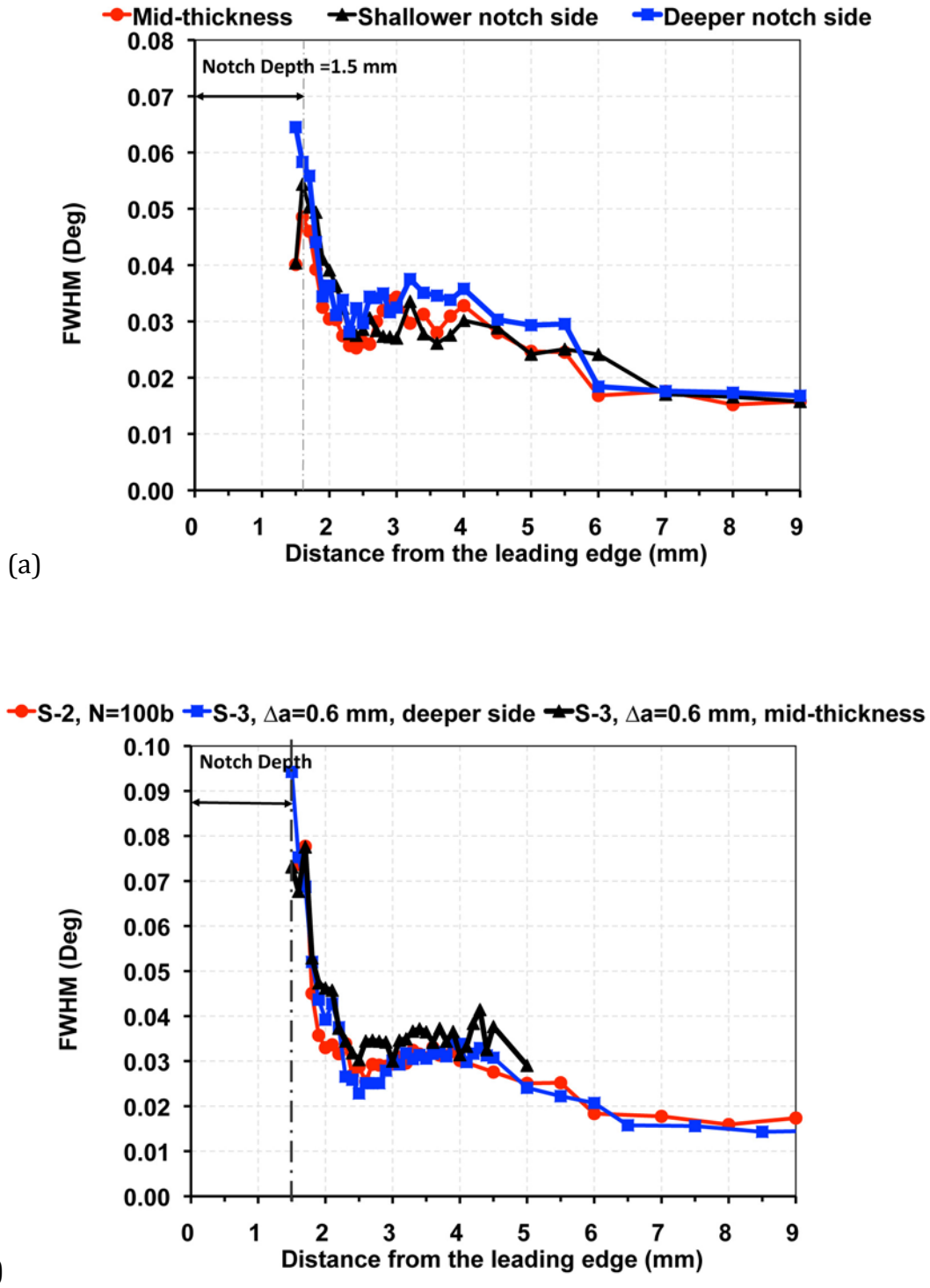


**Figure 4.31:** FWHM plots in longitudinal directions for (a) specimen S-2 with  $\Delta a=0.7$  mm and (b) specimen S-3 with  $\Delta a=0.6$  mm

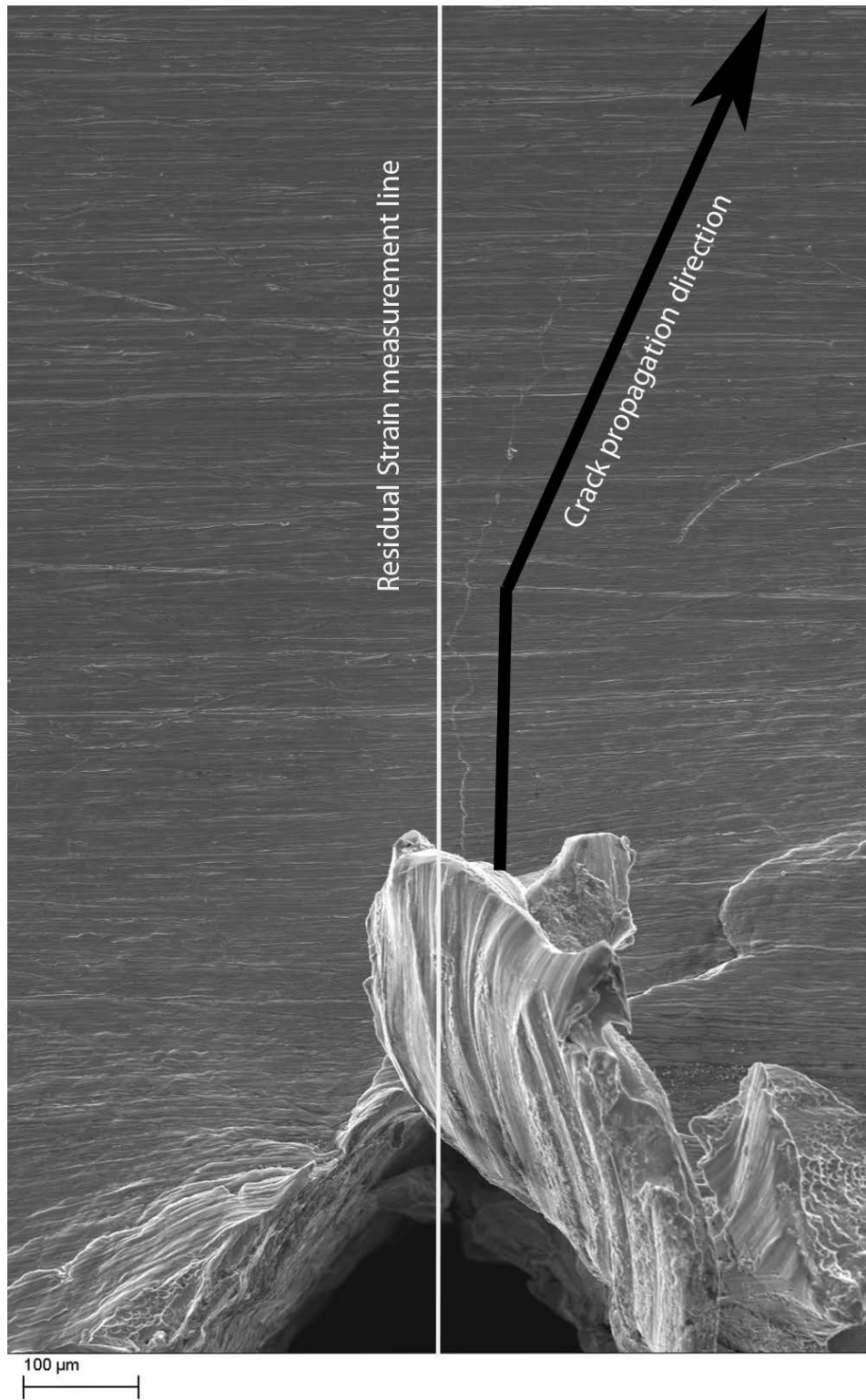


**Figure 4.32:** SEM image for a  $0^\circ$  FOD impacted specimen (S-2) showing the actual direction of crack growth and the residual strain measurement line along notch centreline. Here the crack length,  $\Delta a=0.7\text{mm}$ .

An SEM investigation suggests that in specimen S-2, Figure 4.32, the crack initiated approximately at the notch centre and subsequently grew along the centreline for the first 0.45mm. Upon approaching the region of large compressive zone below the notch (see corresponding 2D strain plot in Figure 4.18a), the crack deviates by an angle of 20° from the notch centreline and propagated along a less compressive region. On the other hand, in specimen S3, crack initiation occurred 100µm away from the notch centre (see Figure 4.34) which is then deviated by an angle of 10°. As a result, the strain profiles given in Figure 4.30, do not represent the residual strain redistribution along the crack path and this might explain why there is no significant relaxation compared to specimen S-2. However, this shows that the residual strain relaxation due to crack growth is indeed localized.

To evaluate the residual strain relaxation arising from long crack growth, the crack in specimen S-3 was propagated further to crack lengths of 1 mm and 2.1 mm, and the residual stress field was mapped in each case. Instead of a 1D line scan that may not provide a true picture of the strain distribution along the crack path, 2D residual stress maps were taken. For the 1 mm long crack, Figure 4.33a, it can be observed that no significant reduction in the peak compressive stress occurred. It is worth noting here that at the right hand side of the notch (flank) residual stresses are not tensile as that at the left hand side, which suggests that crack growth might have occurred along this side resulting in the relaxation of the tensile residual stresses. Figure 4.33b exhibits the 2D residual strain map for S-3 containing 2.1mm crack. Following a further 1 mm crack growth the residual strain distribution has changed significantly compared to that of the 1 mm crack. Note that here the crack was at left hand side of the notch. This is because the two maps were acquired at two different beamlines and the specimen was placed differently with respect to the CCD camera. It seems that 7% relaxation occurred along the notch centreline. It can also be observed that crack growth along the right hand side of the notch side left the residual strain distribution asymmetric with the strains being lower at this side. To understand this anomaly, the specimen was examined under the SEM microscope and the crack

is shown in Figure 4.34. It shows that initially, crack growth occurred close to the notch centre-line (up to 0.6 mm from the notch root), subsequently the crack changed its direction and grew sharply for 0.2 mm and finally changed its direction, and grew along a direction perpendicular to the leading edge.

Another observation can be made comparing the short and long crack growth results; the amount of relaxation increases with the crack length. Also, it can be argued that the large compressive stress region present below the notch may explain why the crack initiates a few hundred micrometres away from the notch centreline and/or to deviate the crack path along a more favourable region from a residual stress viewpoint.

Figure 4.33c and Figure 4.33d show the FWHM maps for 1 mm and 2.1 long cracks respectively. An increased peak broadening is only evident in the vicinity of the notch.

**Table 4-2: Residual stress relaxation due to crack growth under CCF.**

Sample Id	$\Delta a$ (mm)	N (Blocks)	$S_{max}$ (MPa)	Relaxation in peak compression %
<b>0° FOD</b>				
S -2	0.7	1901	434	17%
S -3	0.6	2744		No Significant Relaxation
S -3	1	2979		
S -3	2.1	3400		7%
<b>45° FOD</b>				
S-12	0.6	589	452	-10%
S-8	2	1439	430	30%
S-11	7	1262	434	32%

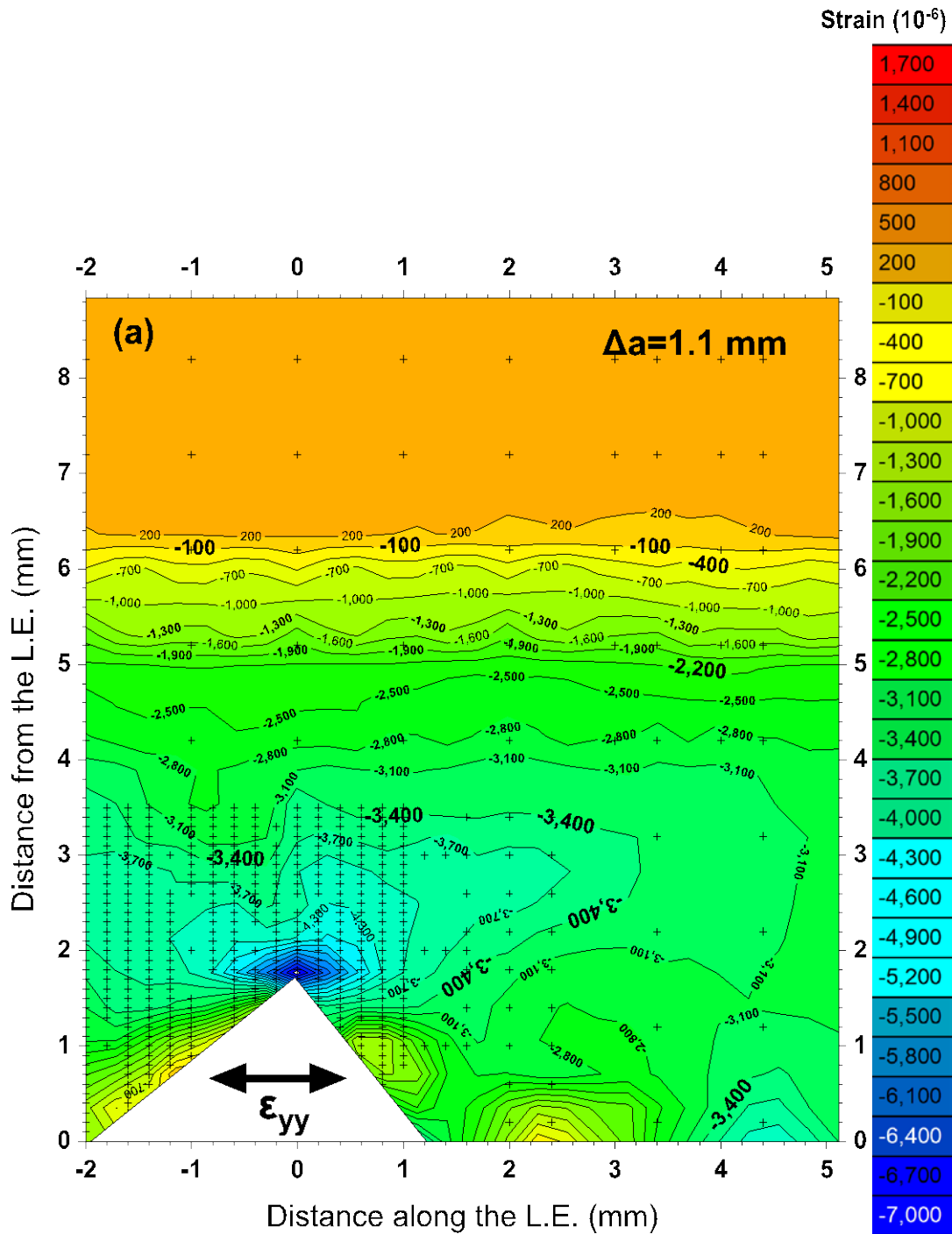


**Figure 4.33:** Through thickness averaged 2D residual strain map for a  $0^\circ$  FOD impact. The specimen (S-3) had a notch depth of 1.5mm

(a): Crack length,  $\Delta a = 1\text{mm}$ ,  $N = 2979$  blocks and  $S_{max} = 434\text{MPa}$ ,

NOTE: Corresponding line plots can be found in the Discussion section

(Figure 4.36).

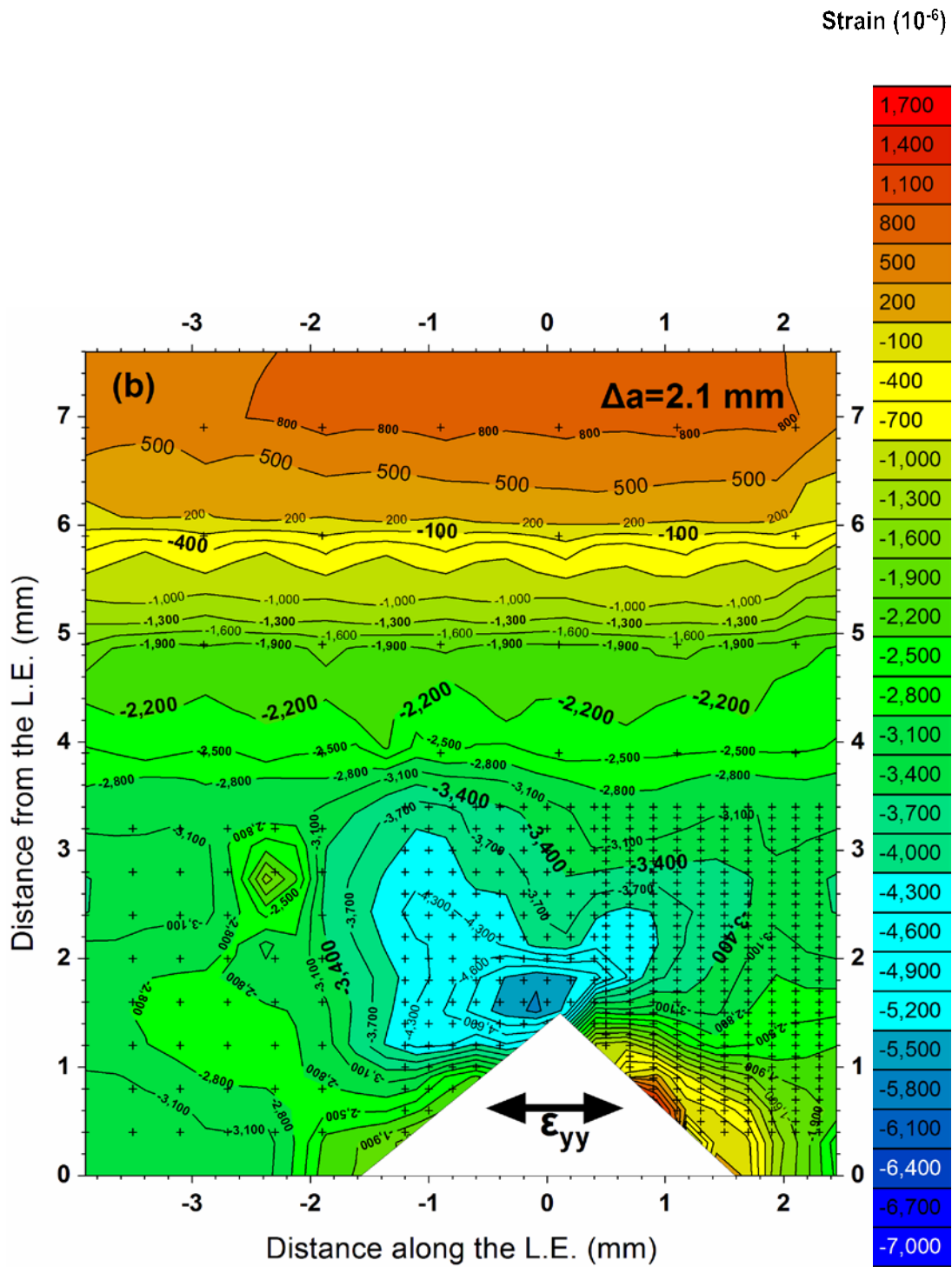


Figure 4.33 (b):  $\Delta a = 2.1 \text{ mm}$   $N = 3400$  blocks, applied stress of  $S_{max} = 434 \text{ MPa}$ .

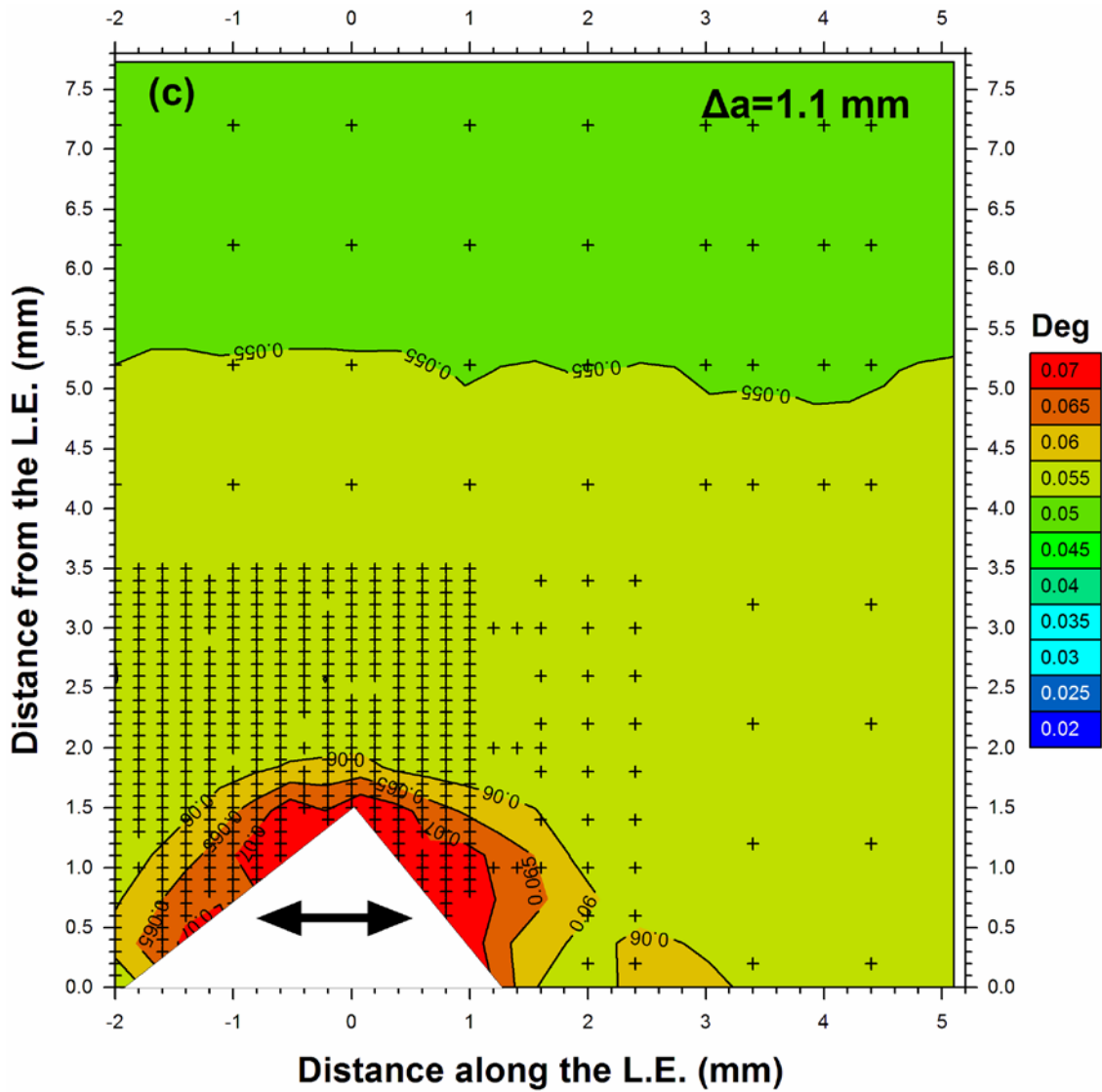


Figure 4.33 (c): FWHM plot for  $\Delta a = 1 \text{ mm}$   $N = 2979$  blocks, applied stress of  $S_{max} = 434 \text{ MPa}$ .

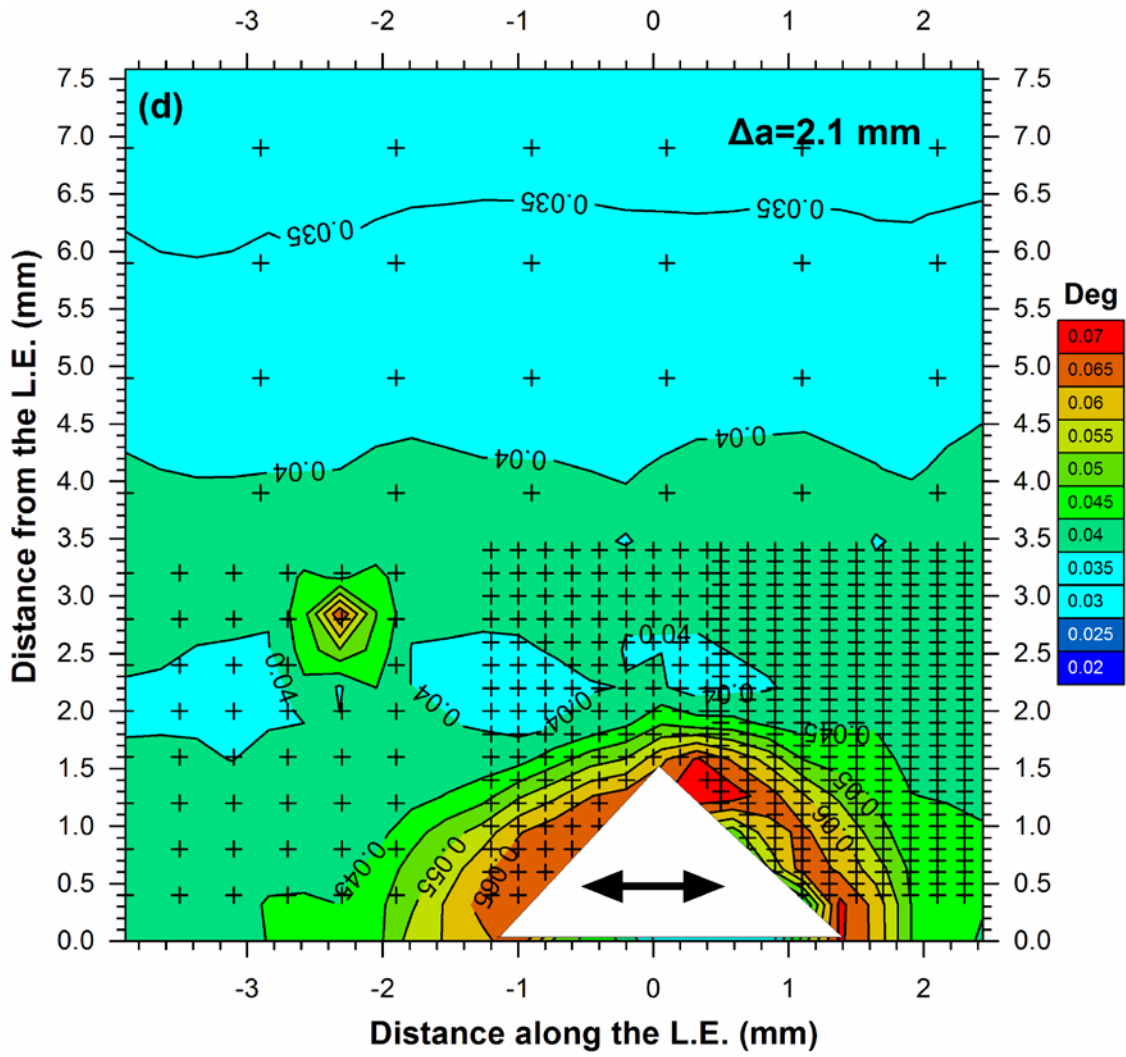
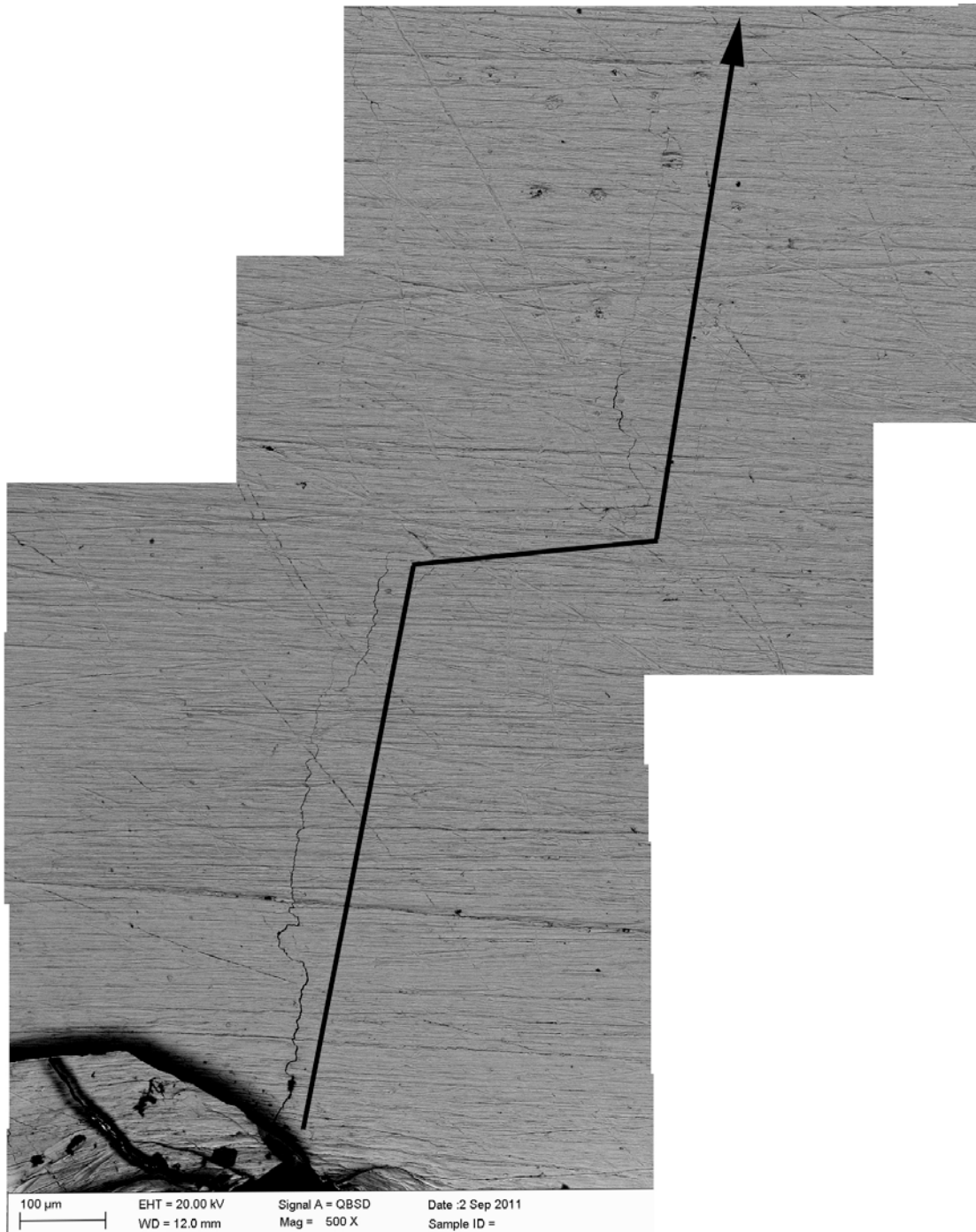


Figure 4.33 (d): FWHM Plot for specimen S-3 having a 2.1 mm long crack.



**Figure 4.34:** An SEM image showing the crack initiation and propagation under LCF + HCF loading in a  $0^\circ$  impacted specimen ( S-3).

**4.5.2.2 The evolution of RS with crack growth in a specimen**

Due to the fact that FOD impact testing has a degree of expected scatter, it was not possible to achieve identical damage characteristics in specimens despite using the same impact velocity and impact angle. In order to carry out a parametric study where only one or two parameter is varied and the rest are kept constant,, it is important to make a comparison between specimens that are nominally identical. Since identical FOD damage cannot be guaranteed for successive nominally identical conditions, residual strain measurements were carried out on the same sample (S-2) through different stages of fatigue cycling to confirm the relaxation behaviour observed. Figure 4.33 shows the comparison of residual strain profiles under solely combined cycle fatigue loading and also for a short crack. It is clearly evident that the residual strains are essentially unrelaxed by N=1 or 100 CCF blocks; however, it is clear that the residual strain has been relaxed by approximately 17 % when a 0.7mm long crack was grown. This suggests that residual strains associated with LSP are highly stable under solely CCF loading and reduce by a relatively small amount, and once a small crack has started to propagate.

In order to study the long crack growth behaviour on a single specimen (S-3) were measured at 3 different crack lengths, 0.6, 1 and 2.1mm. No significant RS relaxation is evident for  $\Delta a=0.6$  mm and  $\Delta a=1$  mm along the notch centrelines. However, for a longer crack with  $\Delta a = 2.1$  mm, only 7% relaxation in the peak compressive residual stress was observed. Possible reasons have already been discussed.

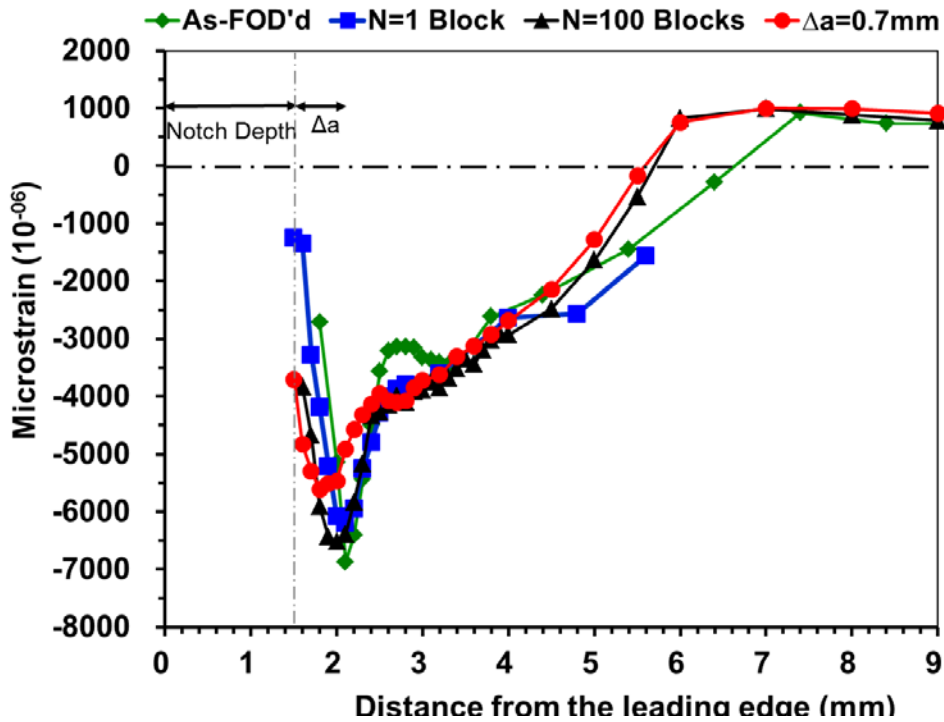


Figure 4.35: Comparison of longitudinal residual strain variation, for a  $0^\circ$  FOD impact, under combined (LCF+HCF) fatigue cycles, at  $N=1$  and 100 blocks (with no detectable cracks), and  $\Delta a=0.7\text{mm}$  under  $S_{max}=434\text{MPa}$ . The notch depth for this specimen (S-2) is 1.5mm.

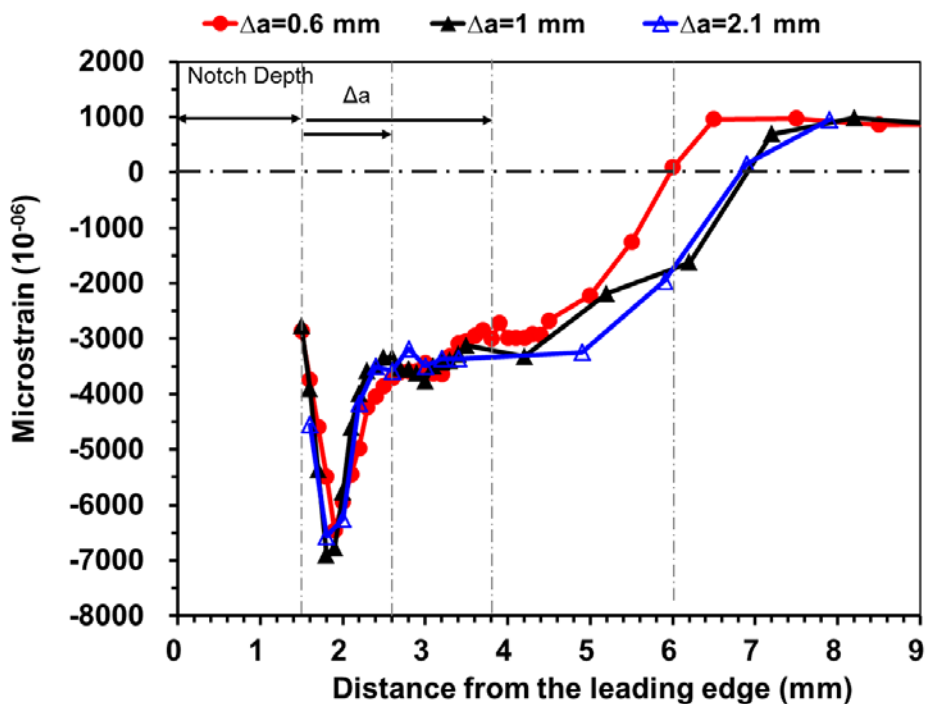


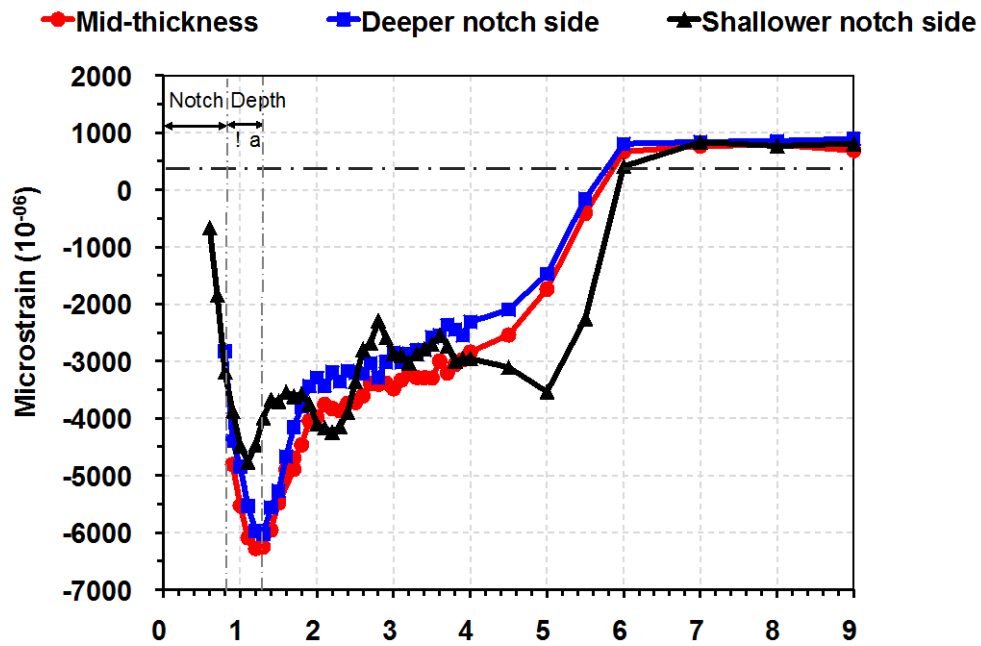
Figure 4.36: Effect of crack growth on relaxation under combined (LCF+HCF) fatigue cycles, when the crack length  $\Delta a=0.6, 1$  and  $2.1\text{mm}$  under  $S_{max}=434\text{MPa}$ . The notch depth for this specimen (S-3) is 1.5mm.

**4.5.2.3 Residual Stress Relaxation for 45° FOD during crack propagation**

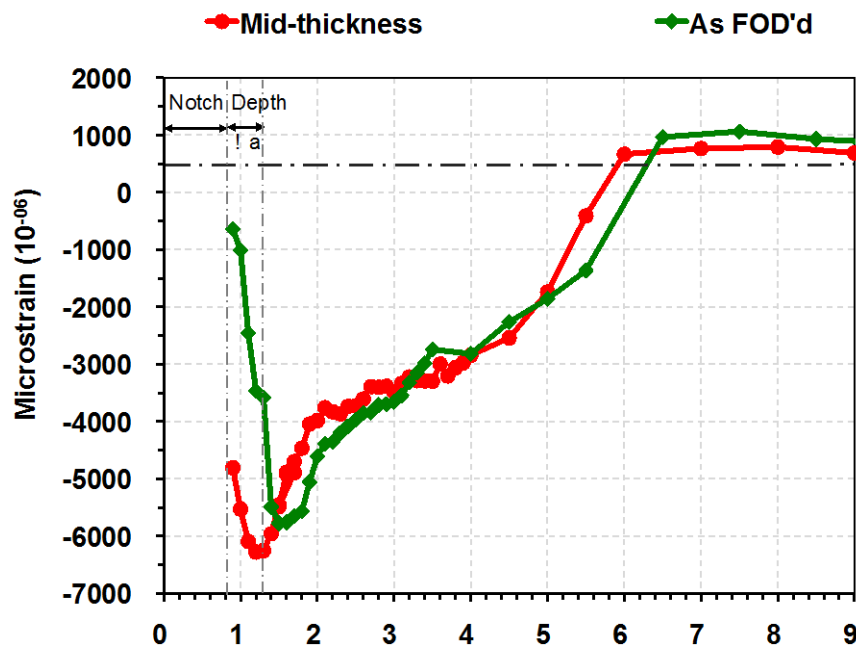
Residual strain relaxation was also studied for 45° FOD impact condition for both short and long crack lengths. Figure 4.37a shows the depth resolved residual strain distribution due to 0.6 mm crack growth. Comparison with the as-FOD'd condition reveals that the value of maximum compressive strain at a distance of 1.1 mm from the L.E is slightly more compressive. This may be associated with the crack tip plasticity (Elber 1971). Surprisingly, in contrast to what has been seen for the solely LCF or CCF condition, residual strains at the shallower side of the notch has more relaxed compared to the deeper notch side. Unfortunately, no SEM images were taken for this specimen; therefore the actual reason for this observation could not be confirmed.

The strain along ( $y=0$ ) is shown in Figure 4.39 for  $\Delta a = 2$  mm and Figure 4.41 for  $\Delta a = 7$  mm respectively. The peak compressive residual strain was observed to decrease by 30% for a 2 mm long crack, as shown in Figure 4.39a and by 32% relaxation for a 7 mm long crack, Figure 4.41a. From these results it may appear that the amount of residual strain relaxation did not increase with increasing crack length. However, in reality, instead of growing along the notch centreline, the crack propagated along a diverged route. Note that strain profiles given for two crack lengths were acquired for two different specimens (S-12 and S-8). In both cases cracks were initiated at the centre of the notch and subsequently deviated by an angle of about 20° to the notch centre-line. It seems that the crack tends to deviate as it approaches the large compressive stress region created by the FOD impact. This observation has an important implication in understanding the experimental crack growth data for these specimens.

Table 4-2 summarizes the fatigue loading conditions and the corresponding relaxation of the peak compressive residual stress for both 0° and 45° FOD impacts. The maximum relaxation is found to be ~30% for long crack growth in both impact conditions. The major part of the beneficial compressive residual stress still remains in the specimen when a crack exceeds the extent of the LSP'd region. 0° impacted specimens are more resistant to crack growth than the 45°



(a)



(b)

**Figure 4.37:** The synchrotron residual strain profiles, parallel to the leading edge generated for a 45° FOD impact after applying combined (LCF+HCF) fatigue cycles of  $N= 589$  blocks, under  $S_{max}=452$  MPa. The notch depth for this specimen (S-12) is 0.78mm and  $\Delta a=0.6$ mm: (a) RS variation along the thickness (b) comparison with the as-FOD'd condition.

due to (i) the asymmetric notch geometry and (ii) the higher level of residual stress in the former.

Also presented in Figure 4.39 for  $\Delta a = 2$  mm and Figure 4.41 for  $\Delta a = 7$  mm two lines at  $y=0.8$  mm that correspond to a line towards the edge of the notch and is close to the distance by which the cracks have deviated from  $y=0$ .

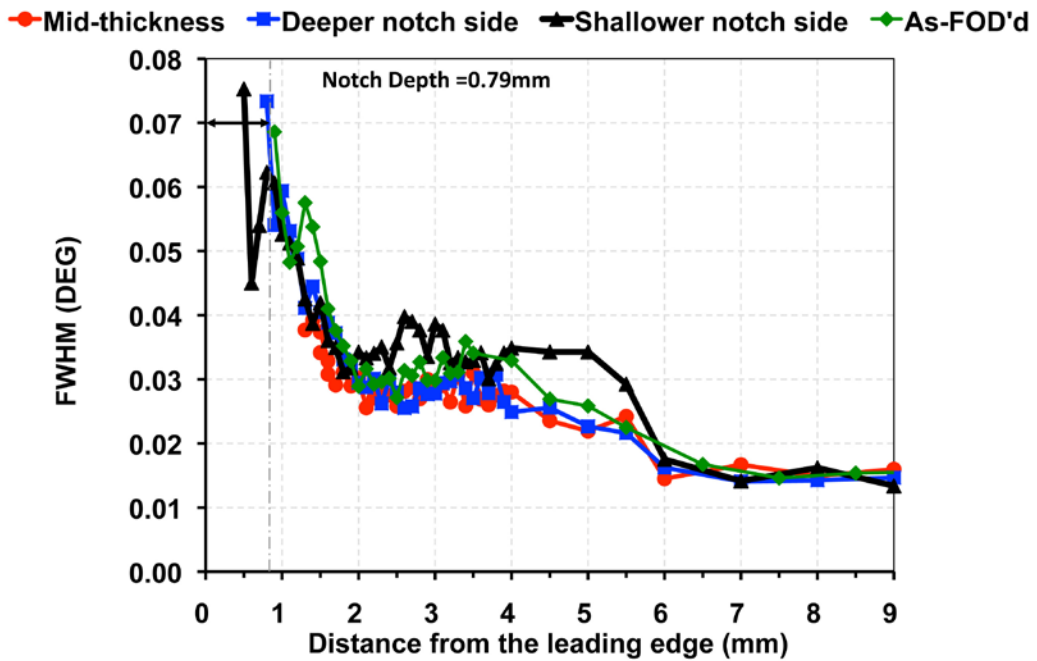
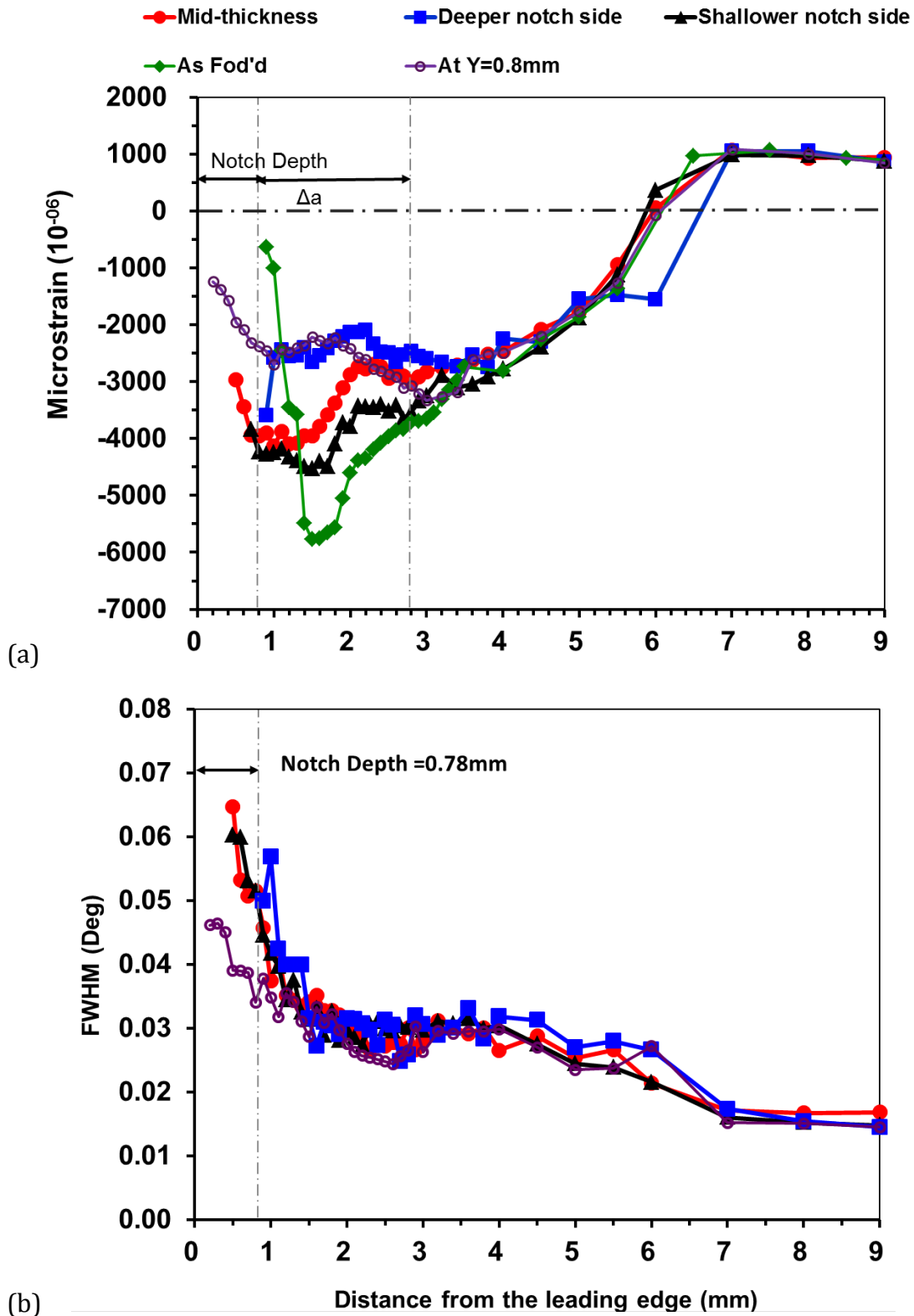
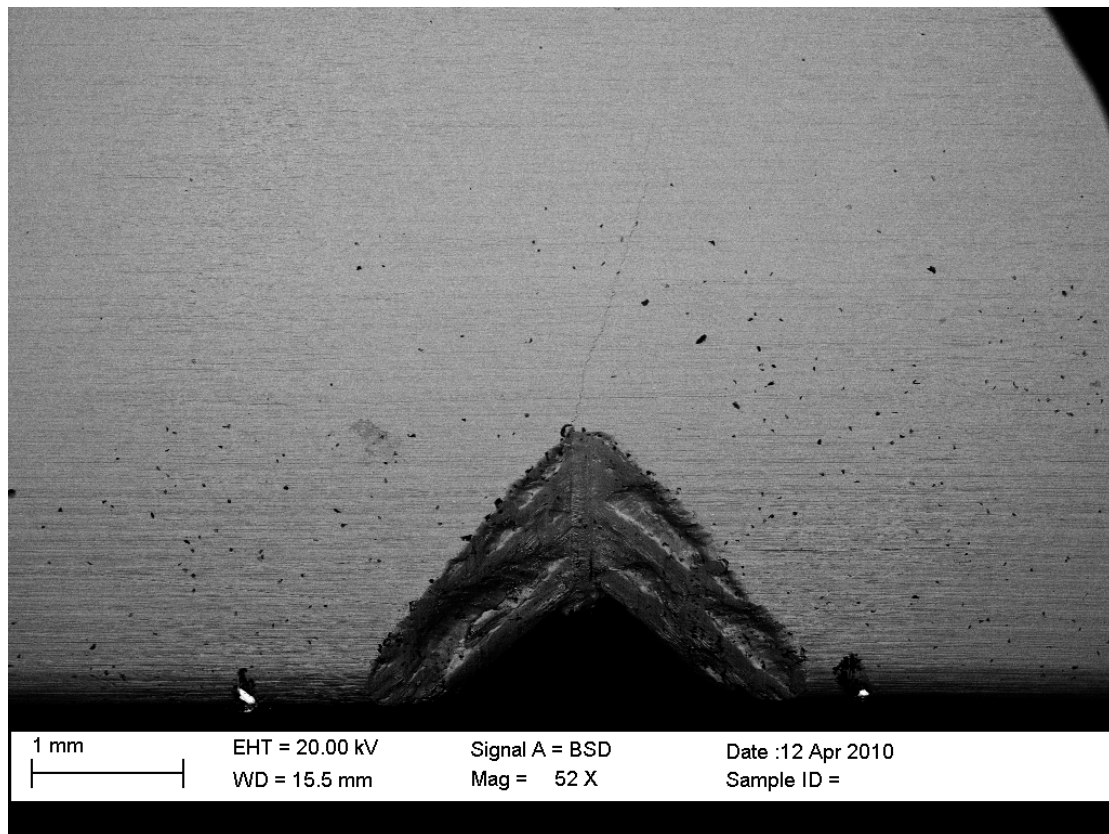


Figure 4.38: (c) FWHM plot for specimen S-12 with  $\Delta a=0.6$  mm.



**Figure 4.39:** (a) The synchrotron residual strain profiles parallel to the leading edge generated for a 45° FOD impact after applying combined (LCF+HCF) fatigue cycles,  $N=1439$  blocks, under  $S_{max}=430$  MPa. The notch depth for this specimen (S-8) is 0.78mm and  $\Delta a=2$  mm and (b) the corresponding FWHM plot.



**Figure 4.40:** SEM image for a 45° impact containing 2 mm long crack. The residual strains were measured along the white line and crack growth occurred along the blank line which is deviated by an angle of 20° from the notch centreline.

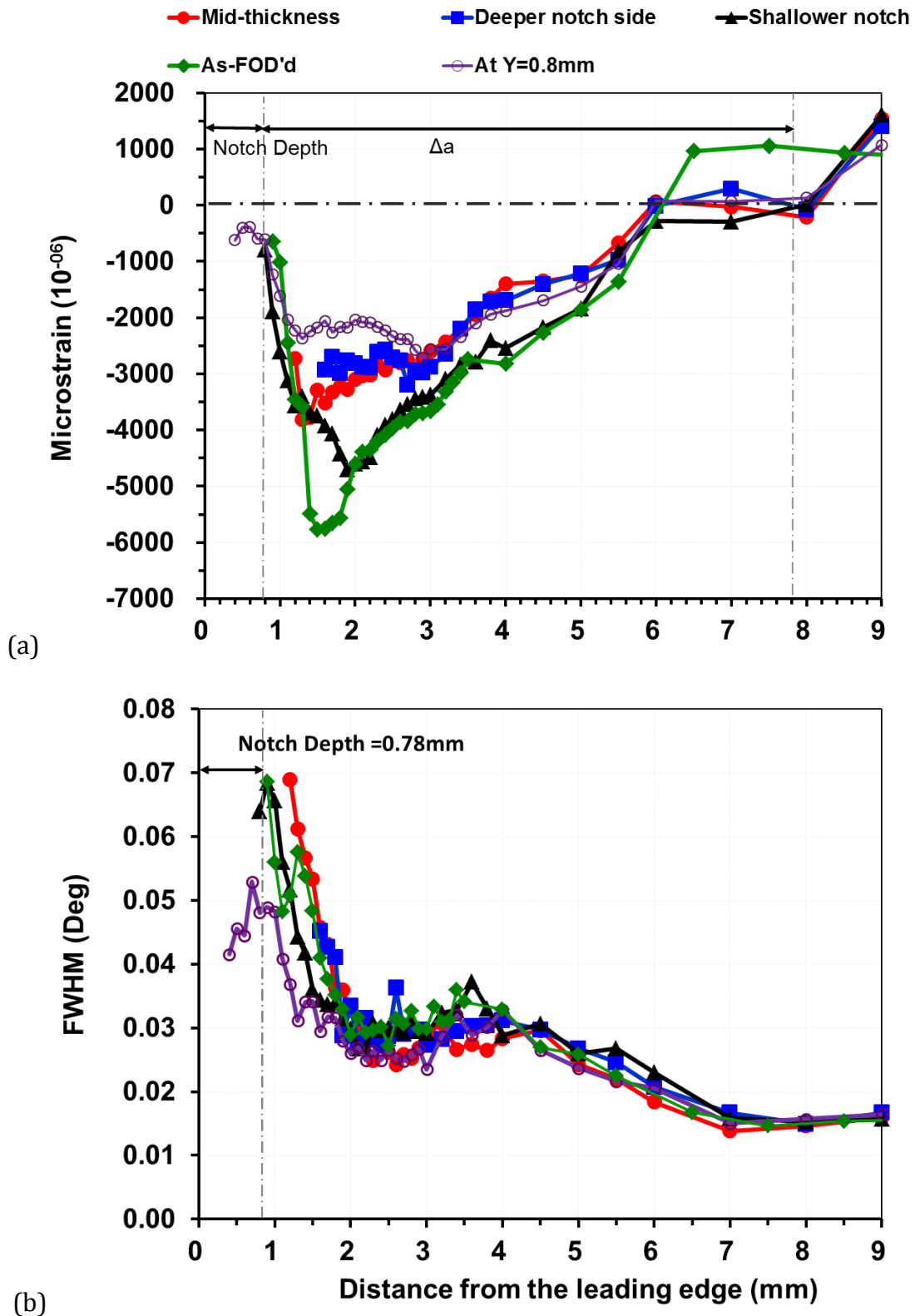


**Figure 4.41:** (a) Longitudinal depth resolved residual strain profiles, generated for a 45° FOD impact after applying combined (LCF+HCF) fatigue cycles,  $N=1262$  blocks, under  $S_{max}=434$  MPa. The notch depth for this specimen (S-11) is 0.78mm and  $\Delta a=7$ mm and (b) the corresponding FWHM plot.

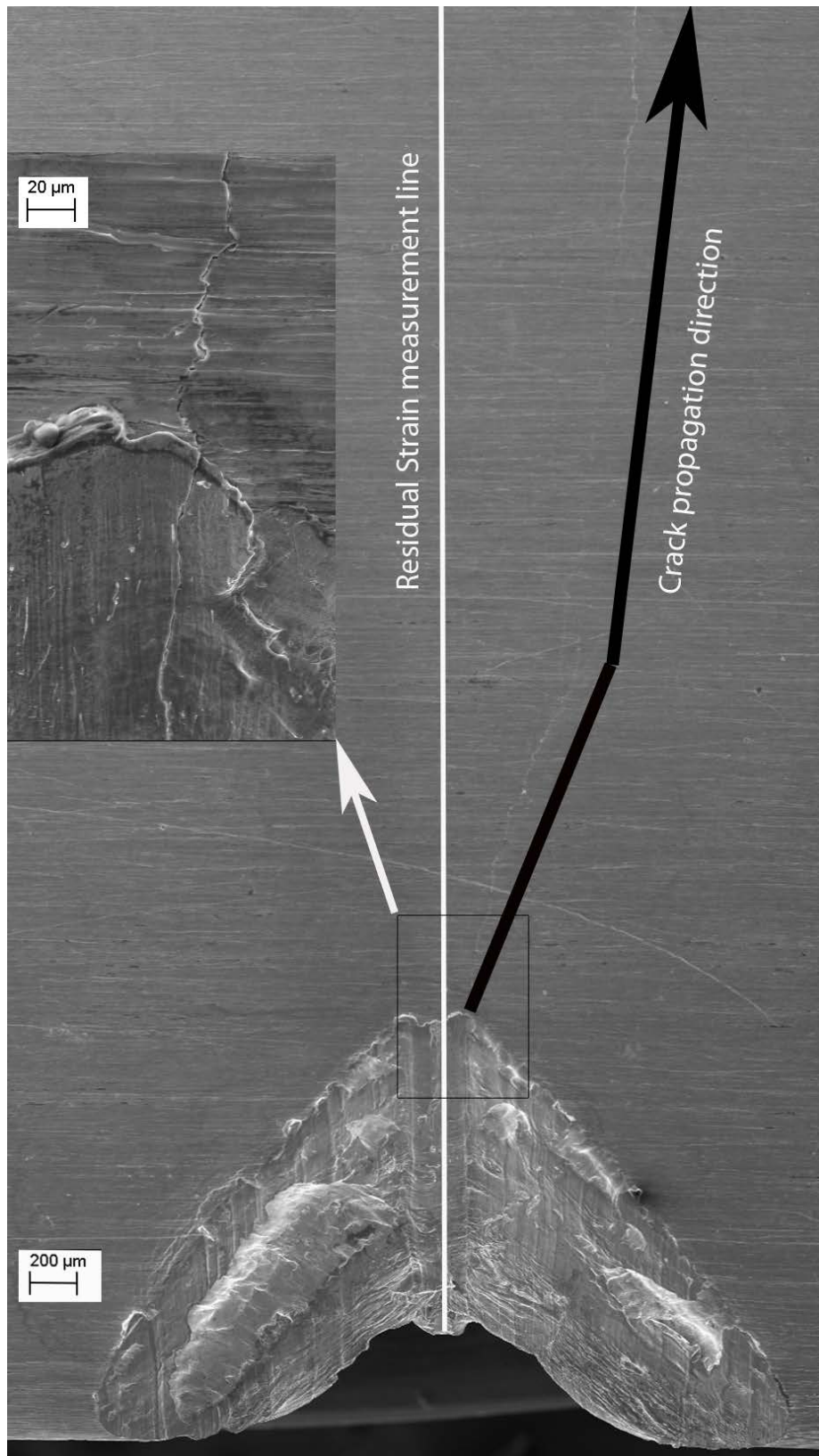


**Figure 4.42:** SEM image for a 45° FOD impact with a 7 mm crack showing residual stress measurement location and the crack path.

From the results presented above, it is evident that for both 0° and 45° impact conditions the residual strains are highly stable even to very long cracks. More than 60% of the original compressive residual stress remained even in the worst condition where a 7 mm crack was grown through an off-axis impacted specimen. Clearly, the residual stress introduced by LSP beyond 3 mm from the L.E has not been relaxed significantly in any of the cases studied. This has important implications concerning the fatigue crack growth behaviour and hence the life of the component which is discussed in the following paragraphs. Therefore, it is important to gain a comprehensive understanding of the origin of the residual stress stability observed here. There are two aspects: firstly the stability needs to be verified and then these results can be utilized in the predictions.

In the context of crack growth a key parameter is the stress intensity factor experienced by the crack tip. The effect of the residual stresses on the crack tip stress intensity,  $K_{res}$  is calculated in section 4.6.1.

The variation of the  $K_{res}$  with the crack length can also be utilized to determine the likely plastic zone size ahead of the crack tip. This may shed some light on the stability of the residual stress to crack growth. Consequently, the plastic zone sizes are estimated and their effect on the residual stress stability is discussed in section 4.7.

### **4.5.3 Summary**

High Energy Synchrotron X-ray diffraction has been used to evaluate the residual stress evolution with crack growth in a complex residual stress field, associated with LSP and FOD impacts, under solely LCF and CCF loading. It has been found that the residual stresses are highly stable in both 0° and 45° FOD impact conditions for short (< 1 mm) as well as long (> 1 mm) cracks, when a maximum applied stress of  $S_{\max}=435$  MPa has been used with CCF type loading. For 0° impact no significant relaxation was found for short or 2.2 mm long crack growth, however, for 45° impact approximately 30% relaxation was observed for long cracks. This infers that the residual stresses in 0° impacts are more stable than the 45° impacts. This might be one reason why 45° impacts are more damaging than the 0° impacts.

On the other hand, for solely LCF loading at  $R=0.1$ , 30% higher applied stress was required for crack propagation that resulted in the same level of relaxation indicating a high level of crack-closure effect at low R ratio. The residual stresses are highly stable even in the worst case scenario where a 7 mm (exceeds the extent of LSP'd region) long crack was grown.

## 4.6 FCG rate prediction

The aim of this section is to investigate how well the observed fatigue crack growth rates can be explained as a function of crack length on the basis of the measured residual stress fields for 0° and 45° FOD impacts.

### 4.6.1 Determination of stress intensity factor due to residual stress

The primary driving force for crack growth rate in a material can be characterized by the stress intensity factor range ahead of the crack tip according to Paris law (see section 2.3). The higher the magnitude of the stress intensity factor the faster the crack propagates. Compressive residual stresses can reduce this stress intensity factor range through crack face closure resulting in the retardation of crack growth. Therefore, to characterize the effect of residual stresses on the fatigue crack growth behaviour the knowledge of the effective stress intensity factor is necessary. This can be defined as the summation of the applied stress intensity factor and the stress intensity factor due to residual stress,  $K_{res}$ . For this reason the residual stress intensity factor,  $K_{res}$  for both 0° and 45° impact is evaluated using the weight function method, and presented in the following section 4.6. Subsequently, the effective stress intensity factor is used to predict the fatigue crack growth rate to compare with experimental FCG rates by our research partner (Spanrad 2011) (section 4.6.3).

As defined in section 2.3  $\Delta K_{app}$  is the nominally applied stress intensity factor range. If residual stresses are present in the material, the stress intensity experienced at the crack tip will be modified by a stress intensity factor that arises from the residual stress, known as  $K_{res}$ . In order to take into account the effect of residual stress on the fatigue crack growth, the magnitude of  $K_{res}$  needs to be determined first. This can be done analytically or using FEM. In this study,  $K_{res}$  was determined by the analytical method, and then compared with FEM results carried out by our research partner at Portsmouth (Spanrad 2011). According to Linear Elastic Fracture Mechanics (LEFM), the analytical solution for  $K_{res}$  was first given by Kaya and Erdogan (1980) for a single edge crack in an infinite plate based (neglecting the notch) on the superposition principle.

Accordingly,  $K_{res}$  can be found by integrating the residual stresses along the plane of the crack (at  $y=0$ ) as a function of distance from the leading edge,  $\sigma_{res}(x)$  and the weight function or Green function,  $m(x, a)$  for a through-thickness crack length  $a$ , which is expressed as (Tada et al 2000):

$$K_{res} = \int_0^a \sigma_{res}(x) \cdot m(x, a) dx \quad \text{Equation 4-1}$$

where for this geometry, the weight function is (Tada et al 2000)

Equation 4-2

$$m(x, a) = \frac{2}{\sqrt{\pi a}} \cdot \frac{G\left(\frac{x}{a}, \frac{a}{w}\right)}{\left(1 - \frac{a}{w}\right)^{3/2} \sqrt{1 - \left(\frac{x}{a}\right)^2}}$$

Where:

$$G\left(\frac{x}{a}, \frac{a}{w}\right) = g_1\left(\frac{a}{w}\right) + g_2\left(\frac{a}{w}\right) \cdot \left(\frac{x}{a}\right) + g_3\left(\frac{a}{w}\right) \cdot \left(\frac{x}{a}\right)^2 + g_4\left(\frac{a}{w}\right) \cdot \left(\frac{x}{a}\right)^3$$

$$g_1\left(\frac{a}{w}\right) = 0.46 + 3.06\left(\frac{a}{w}\right) + 0.84\left(1 - \frac{a}{w}\right)^5 + 0.66\left(\frac{a}{w}\right)^2 \left(1 - \frac{a}{w}\right)^2$$

$$g_2\left(\frac{a}{w}\right) = -3.52\left(\frac{a}{w}\right)^2$$

$$g_3\left(\frac{a}{w}\right) = 6.17 - 28.22\left(\frac{a}{w}\right) + 34.54\left(\frac{a}{w}\right)^2 - 14.39\left(\frac{a}{w}\right)^3 - \left(1 - \frac{a}{w}\right)^{\frac{3}{2}}$$

$$- 5.88\left(1 - \frac{a}{w}\right)^5 - 2.64\left(\frac{a}{w}\right)^2 \left(1 - \frac{a}{w}\right)^2$$

$$g_4\left(\frac{a}{w}\right) = -6.63 + 25.16\left(\frac{a}{w}\right) - 31.04\left(\frac{a}{w}\right)^2 + 14.41\left(\frac{a}{w}\right)^3 + 2\left(1 - \frac{a}{w}\right)^{\frac{3}{2}}$$

$$+ 5.04\left(1 - \frac{a}{w}\right)^5 + 1.98\left(\frac{a}{w}\right)^2 \left(1 - \frac{a}{w}\right)^2$$

where,  $w$  is the width of the specimen

This method assumes the stresses are zero within the region defined by the notch. In other words i.e. for 0° and 45° FOD impact the stresses are assumed to be zero for the first 1.5 mm and 0.8 mm (typical notch depth) from the L.E. respectively.

The longitudinal residual stress profile along the notch centreline arising for LSP and FOD is given in Figure 4.43 for 0° and 45° FOD impacts (taken from Figure 4.19 and Figure 4.9 respectively). The  $K_{res}$  calculation is based on a 1D analysis, therefore, only 1D residual stress is presented here.

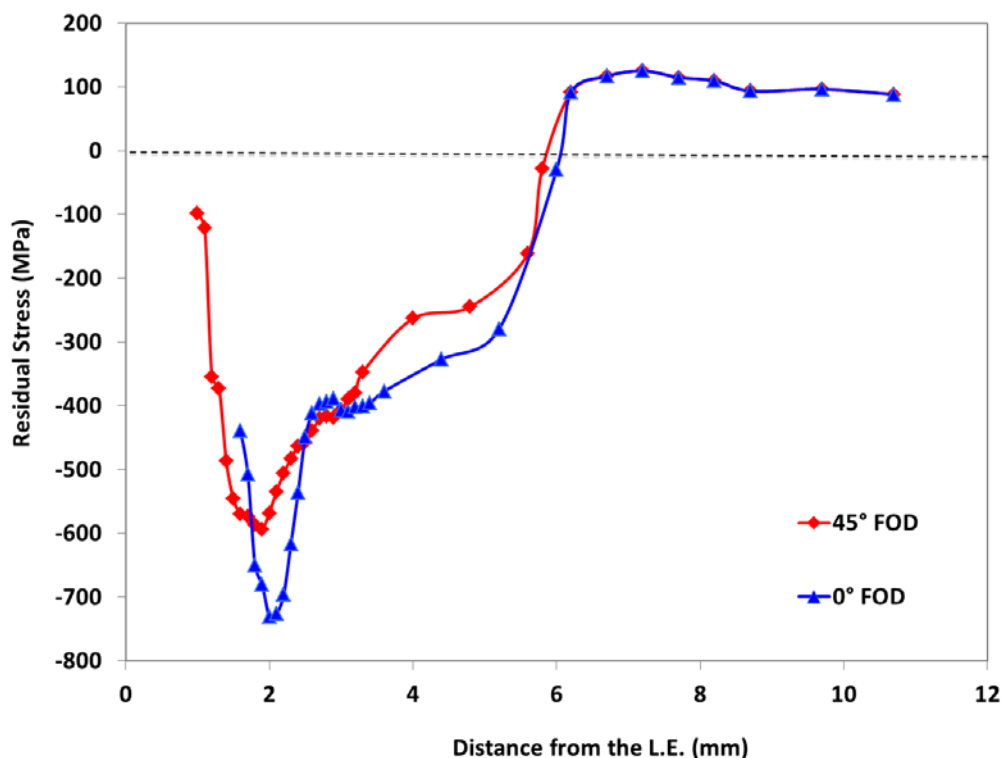


Figure 4.43: Longitudinal residual stress distribution for 0° and 45° impacts.

The  $K_{res}$  calculated as a function of crack length ( $a$ ) is shown in Figure 4.44 both for 0° and 45° impacts. Now the determination of  $\Delta K_{eff}$  depends on the extent to which  $K_{res}$  modifies the  $K_{min}$  in the cycle. This is illustrated in Figure 4.45 a-c, where Figure 4.50a represents the case where no RS is present in the structure:

Therefore, 
$$\Delta K = K_{max} - K_{min}$$

When residual stresses are present in the structure two situations can occur:

Case A. when no crack closure:

$$K_{min} + K_{res} > 0 \quad (\text{see Figure 4.45b})$$

$$\Delta K_{eff} = K_{max} - K_{min} \quad \text{Equation 4-3}$$

$$R_{eff} = (K_{min} + K_{res}) / (K_{max} + K_{res}) \quad \text{Equation 4-4}$$

Case B. when crack closure occurs

$$K_{min} + K_{res} < 0 \quad (\text{see Figure 4.45c})$$

$$\Delta K_{eff} = K_{max} + K_{res} \quad \text{Equation 4-5}$$

$$R_{eff} = (K_{min} + K_{res}) / (K_{max} + K_{res})$$

The situation becomes complex when a steep stress gradient exists along the crack path. Either of these two cases can be valid at different crack lengths depending on the value of the residual stress.

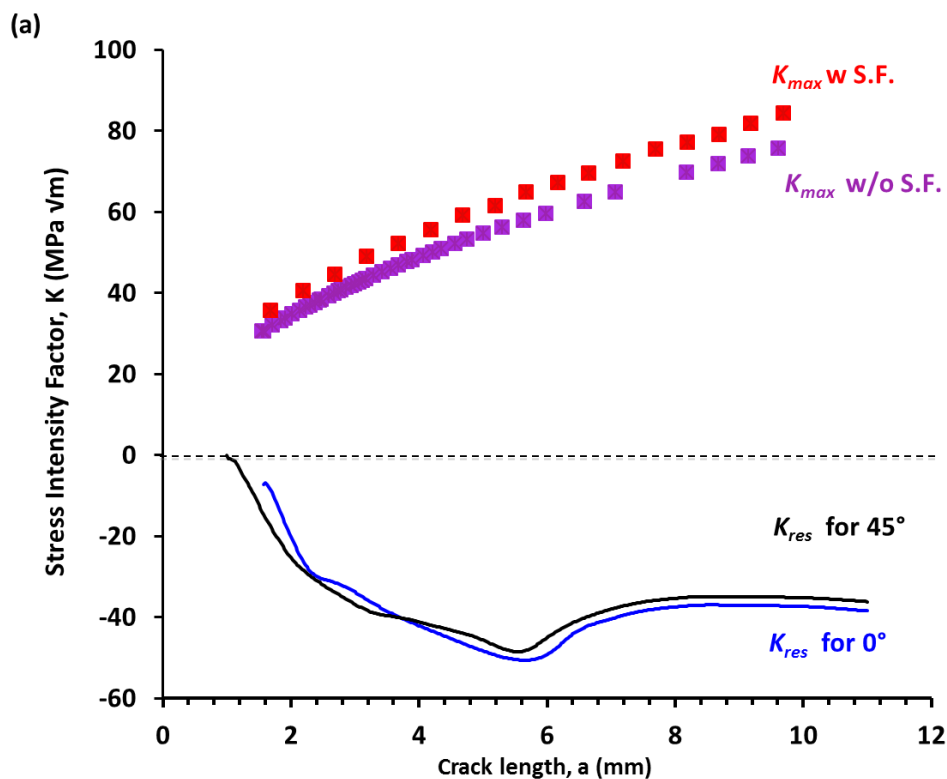


**Figure 4.44:** Nominally applied maximum stress intensity factor,  $K_{max}$  with and without considering the shape function (S.F.), calculated for a typical applied stress of  $S_{max} = 435$  MPa, and the variation of calculated  $K_{res}$  as a function of crack length for  $0^\circ$  and  $45^\circ$  FOD impact.

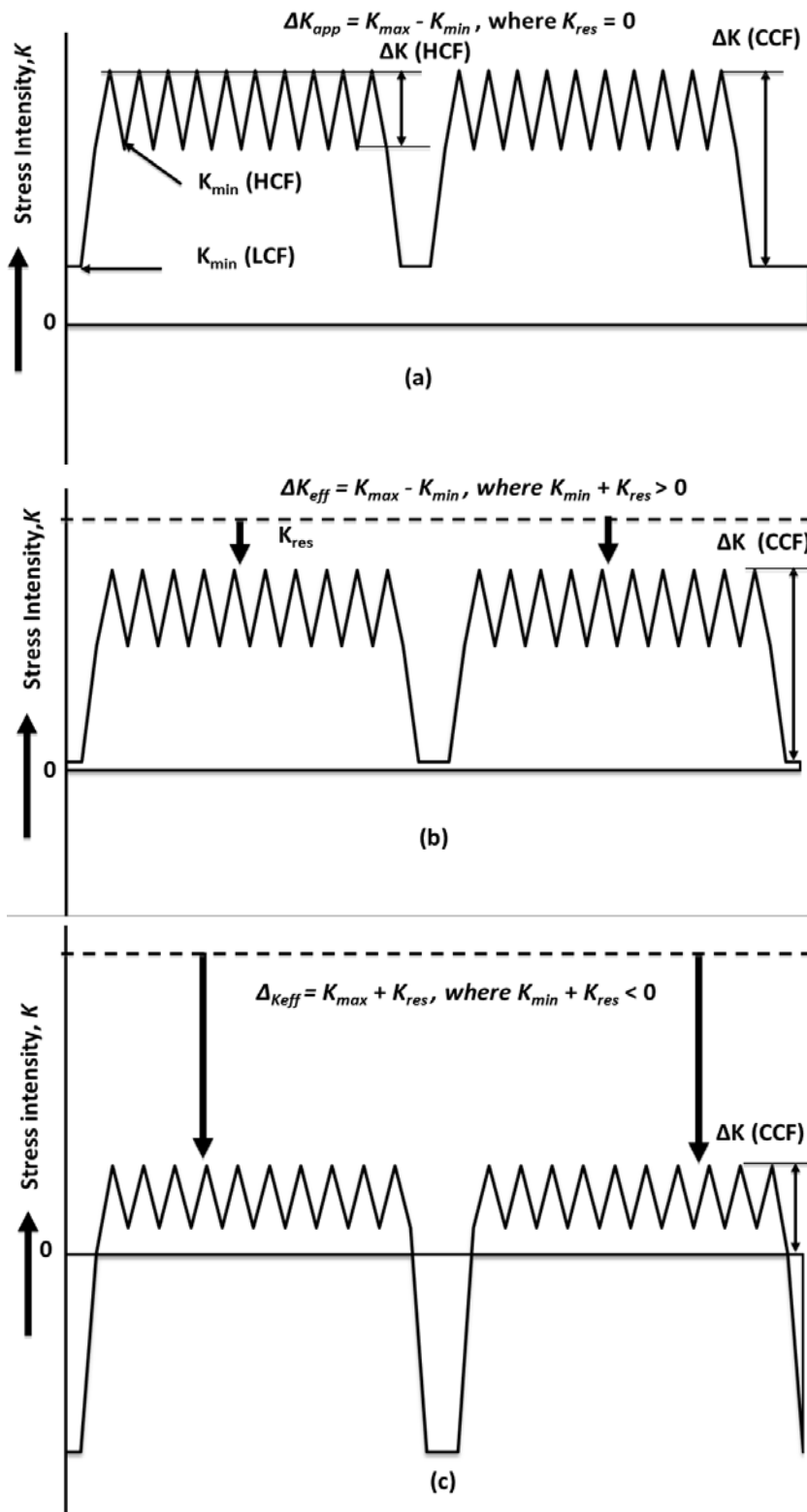


**Figure 4.45:** Determination of residual stress intensity factor range : (a) no residual stress. (b) when  $K_{min} + K_{res} > 0$  and (c) when  $K_{min} + K_{res} < 0$

Figure 4.46a and b shows the maximum applied stress intensity factor,  $K_{max}$  and the effective stress intensity factor range,  $\Delta K_{eff}$  at  $R=0.1$  (LCF) and  $R=0.7$  (HCF) in

a CCF block for  $0^\circ$  and  $45^\circ$  FOD impacts respectively. Here,  $K_{\max}$  values were calculated for  $S_{\max}=435\text{MPa}$ , a typical load used for combined cycle fatigue loading. At  $R=0.1$  the value of  $K_{\min} + K_{res}$  always remained negative. Therefore, Equation 4-5 was used to determine the  $\Delta K_{eff}$ . On the other hand, at  $R=0.7$ , the  $K_{\min} + K_{res}$  values outside the region of  $a= 2.2$  to  $6.2$  mm are positive, in which case Equation 4-4 was used where  $\Delta K_{eff} = \Delta K_{app}$ . It can be observed in Figure 4.46 that the  $\Delta K_{eff}$  values at two loading conditions varies significantly in the early crack growth regime and also when the crack exceeds the LSP'd region.

In CCF loading condition 1000 HCF cycles are superimposed onto 1 LCF cycle under a maximum applied load of  $S_{\max} = 435$  MPa. Therefore, the effective R-ratios are calculated separately for the LCF and HCF cycles within a CCF block, for  $0^\circ$  and  $45^\circ$  FOD impacts, and presented in Figure 4.47a-b respectively. It can be observed that in the LCF part of the cycle the  $R_{eff}$  values remain more negative along the crack length than the HCF part of the cycle. For example the minimum  $R_{eff}$  value is found as -3.5 for  $a=5$  mm for the LCF part of the cycle; whereas, for the HCF part of that cycle the  $R_{eff}$  value is -0.5 at that crack length. Since 1000 HCF cycles were superposed onto 1 LCF cycle at  $R = 0.7$ , the majority of the time in one CCF block the crack tip material experienced a relatively low negative R ratio where the crack-closure effect is generally minimal (Ritchie et al 1999). Consequently, the HCF part of a CCF cycle mostly contributes to the fatigue crack growth propagation. Hence, crack propagation easily occurred under CCF loading condition at an applied load of  $S_{\max} = 435$  MPa. On the other hand, under solely LCF conditions, at  $R=0.1$  no crack growth could not be detected at this load. This may be associated with the highly negative effective R ratios at the crack tip indicating high level of crack-closure effect. The fatigue limit stresses for solely LCF loading is 30% higher than the CCF loading condition (Figure 2.42). This means that only when the maximum applied stress was increased to  $S_{\max} = 586$  MPa the  $R_{eff}$  values were reduced resulting in the crack propagation. This implies that although slow, crack growth can occur at a negative R ratio. This can also be

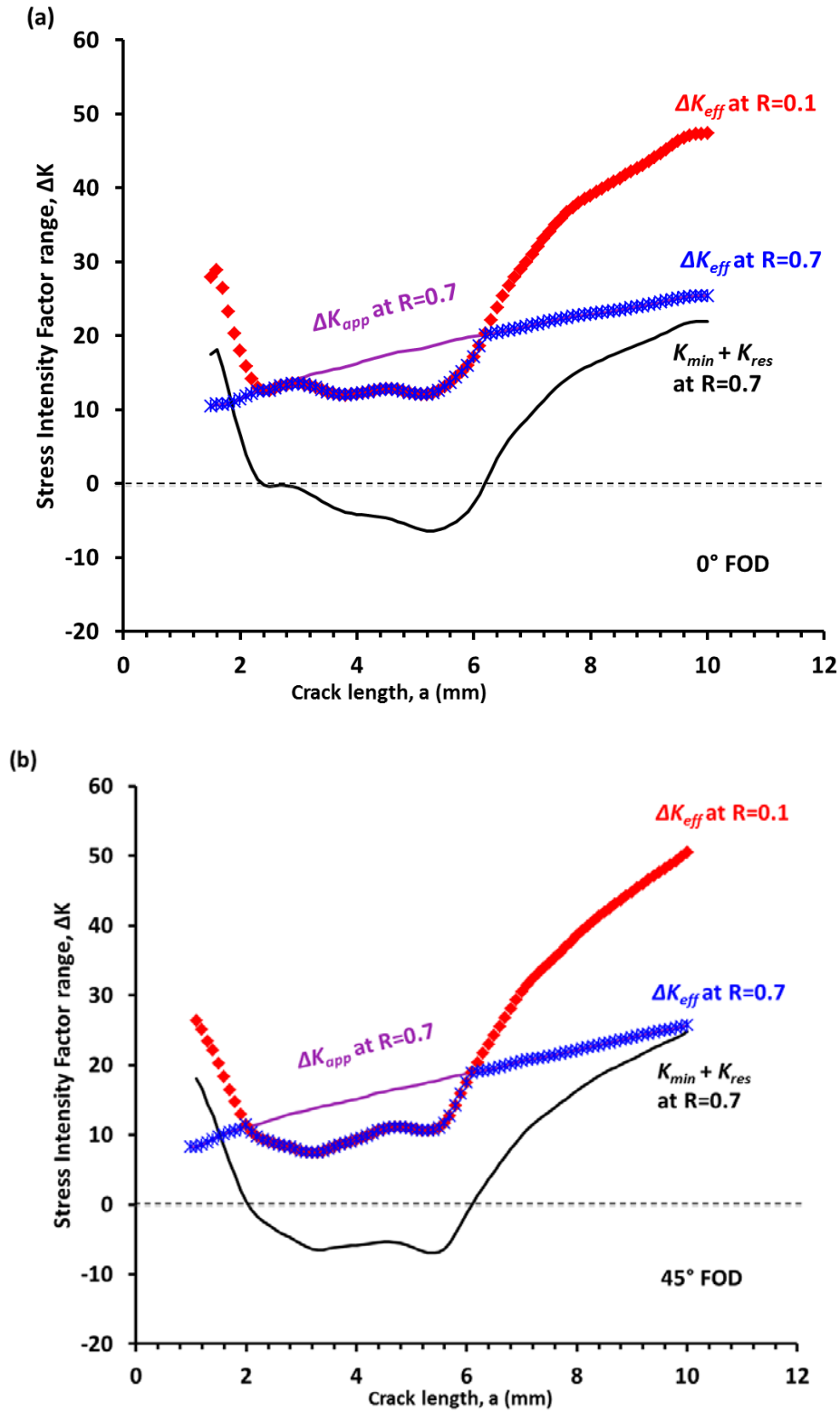
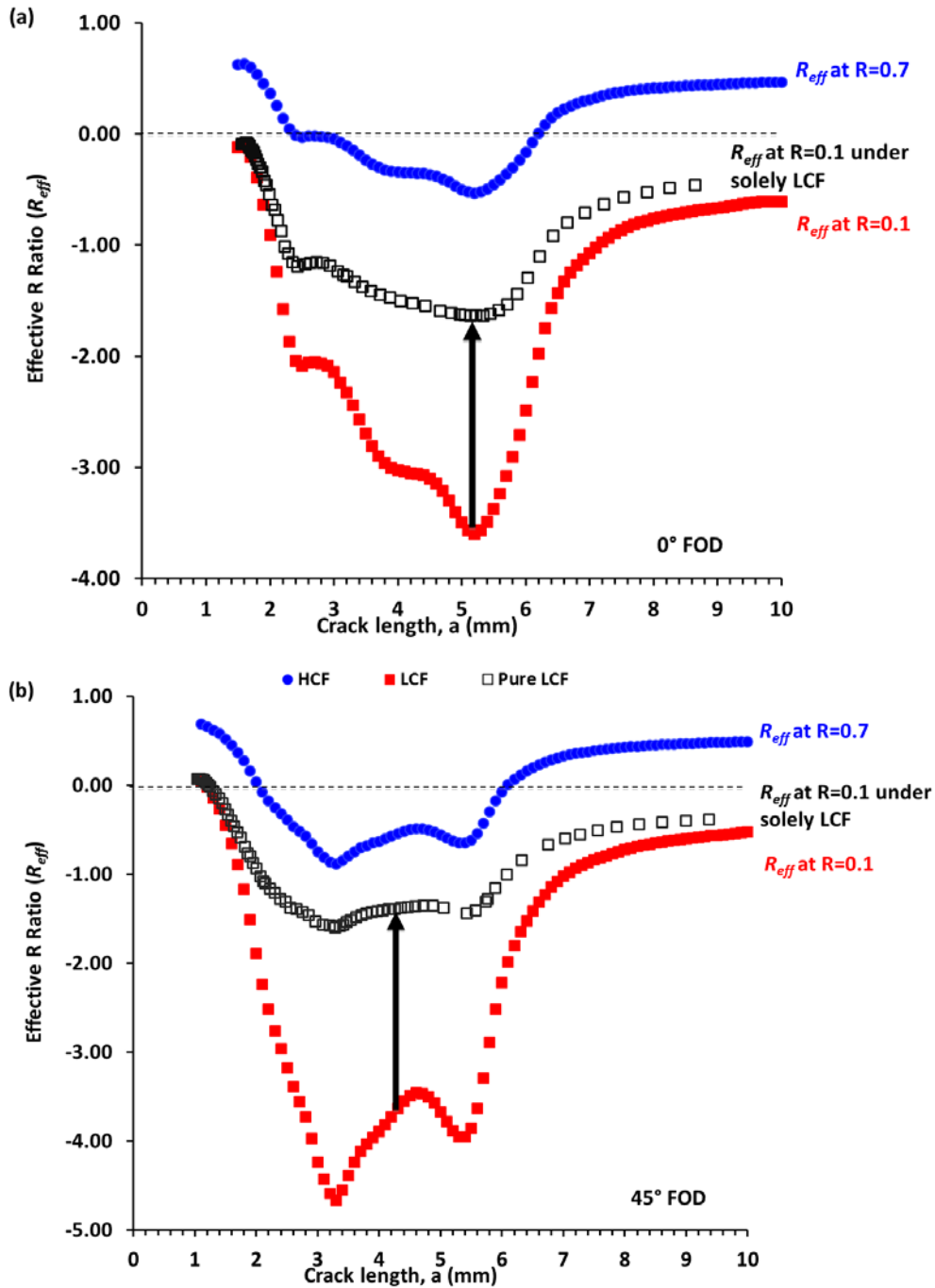


Figure 4.46: Variation of the effective stress intensity factor range,  $\Delta K_{eff}$  as a function of crack length at  $R=0.1$  (LCF) and  $R=0.7$  (HCF) for (a) for  $0^\circ$  impact and (b)  $45^\circ$  impact.



**Figure 4.47:** Effective R ratio as a function of crack length for LCF and HCF separately in a CCF block under  $S_{max} = 435$ , and also for solely LCF under  $S_{max} 586\text{MPa}$  for (a)  $0^\circ$  and (b)  $45^\circ$  impact.

correlated with experimental fatigue crack growth rates as a function of crack length given in Figure 2.43 where experimental crack growth data is shown as a function of crack length.

#### 4.6.2 Analytical model for FCG rate prediction

Fatigue crack growth rate in a material can be described by the well-recognised Paris growth law (Equation 4-7) (see section 2.3 for further explanation)

$$\frac{da}{dn} = C(\Delta K)^n \quad \text{Equation 4-6}$$

However, the Paris law does not take into account the effect of changing  $R$  ratio on the crack growth rate. For Ti-6Al-4V alloy it has been found that FCG rate increases with increasing  $R$  ratio (Ritchie et al 1999). Therefore, it is important to take into account the effect of  $R$  ratio in any FCG rate prediction model. To incorporate the influence of stress ratio the original Paris crack growth law was modified by Walker (1970) to give Equation 4-8:

$$\frac{da}{dn} = C \left( \Delta K_{app} (1 - R)^{(m-1)} \right)^n \quad \text{Equation 4-7}$$

where  $C$  and  $n$  are the Paris constants and  $m$  is a material constant.

In the current study the fatigue crack growth rates under solely LCF and CCF loading conditions are predicted using conventional crack growth data utilizing the modified Walker expression (Walker 1970), where the measured residual stress field associated with both the FOD impact, and the laser shock peening were taken into account. A simple approach to modify the Walker equation is described in the following paragraphs. As shown in the previous section the residual stresses are highly stable even when a 7 mm crack was grown; consequently, the residual stress relaxation was ignored in this analysis.

To examine whether benchmark FCG data obtained under zero residual stress can be used with Equation 4.8 to predict FCG rates in another case, experimental data as provided by Rolls-Royce (Schofield 2011). For benchmark Ti-6Al-4V the Paris constant  $C$  varies with  $R$  as shown in Table 4-3 but  $n$  remains constant with the  $R$  ratio (Schofield 2011). Therefore, a new constant  $C^*$  (independent of  $R$  ratio) as well as the value of  $m$  needs to be derived. This was achieved by best fitting the observed  $C$  vs.  $R$  curve (Figure 4.48). A best fit was achieved with  $C^* = 3.10E-09$  and  $m = 0.7$ .

To take into account the effect of residual stress, in the above equation  $\Delta K$  and  $R$  need to be replaced with the corresponding  $\Delta K_{eff}$  and  $R_{eff}$  to predict the growth rate in the residually stressed test piece. Therefore, Equation 4-8 becomes:

$$\frac{da}{dn} = 3.1 \times 10^{-9} \left( \Delta K_{eff} (1 - R_{eff})^{(0.7-1)} \right)^{3.5} \quad \text{Equation 4-8}$$

The crack growth rate for CCF block was calculated according to the following equation:

$$\frac{da}{dN} = \left( \frac{da}{dn} \right)_{LCF} + 1000 \times \left( \frac{da}{dn} \right)_{HCF} \quad \text{Equation 4-9}$$

**Table 4-3:** Benchmark data for of the Paris Constant  $C$  with  $R$  ratio for Ti-6Al-4V of leading edge microstructure (Schofield 2011)

R	C
-1	5.7235E-10
0	3.5862E-09
0.3	5.8862E-09
0.6	1.0486E-08
0.8	1.5862E-08

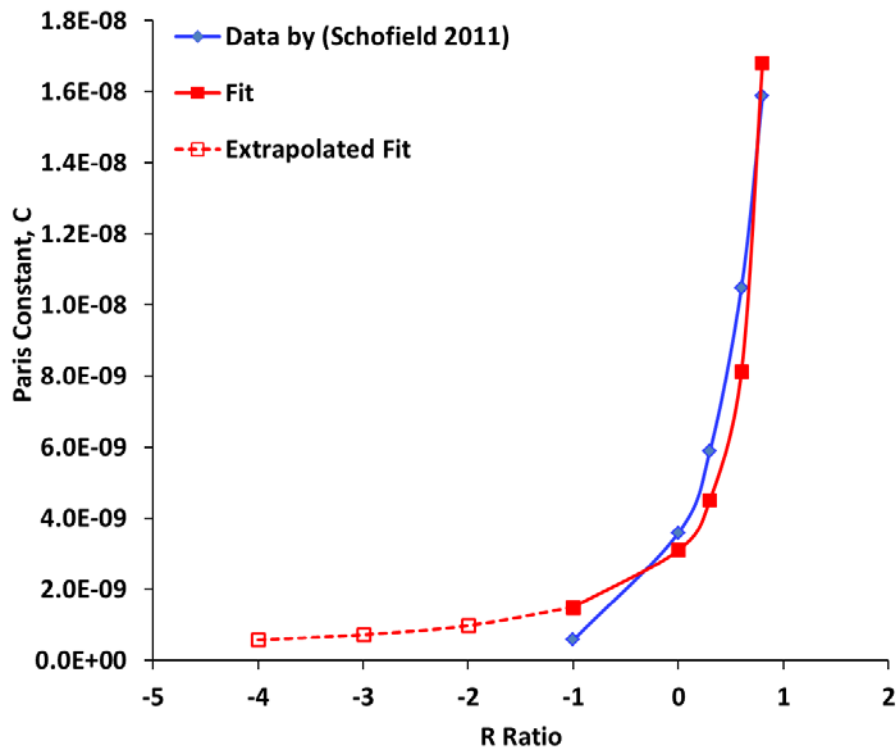


**Figure 4.48:** Variation of experimentally obtained Paris constant  $C$  with  $R$  ratio and the data fit to calculate the new constant  $C^*$  that is independent of  $R$  ratio.

#### 4.6.3 Comparison between predicted and experimental FCG rates

The fatigue crack growth (FCG) rates predicted under solely LCF are presented in Figure 4.49 and also compared with the experimental crack growth rate acquired by our research partner (Spanrad 2011). For comparison, the FCG rate for the benchmark Ti-6Al-4V was also calculated using the Paris constants provided by Schofield (2011). It shows that in both cases, the FCG rate in LSP+FOD specimens remains well below the benchmark behaviour due to the compressive residual stress assisted crack closure. It is evident that the predicted FCG rate is in good agreement with the experimental FCG rate for both  $0^\circ$  and  $45^\circ$ . However, contrary to the experimental FCG rates, the model predicts a higher FCG rate for the first 2.1 mm of the  $0^\circ$  FOD impact, and for the first 1.8 mm of the  $45^\circ$  FOD impact. This may be associated with the combined effect of multiple crack initiation that is prevalent in LSP'd Ti-6Al-4V (Spanrad & Tong 2011) and also the material threshold. The NASGRO equation (NASA 2000) may

be more appropriate to predict the FCG rate in this condition because it takes into account the combined effect of the threshold stress intensity factor  $\Delta K_{th}$  as well as the critical stress intensity factor  $\Delta K_C$ , which is yet to be studied for the LSP+FOD condition. Beyond this region the model predicts a lower FCG rate than experimental crack growth data. This is due to the fact that the prediction was based on the  $K_{res}$  estimated along the notch-centreline, but in reality crack growth did not occur along the notch centreline where residual stresses were measured, instead propagating along a path deviating by an angle of  $20^\circ$  from the notch bisector (see Figure 4.34 and Figure 4.42). In view of this,  $K_{res}$  was determined using the residual stress profile for only LSP treatment (i.e. without the effect of FOD) and the FCG rates were predicted accordingly. The grey dashed lines in Figure 4.49a and b show the predicted FCG rate using the LSP'd residual stress profile. Clearly, the prediction shows encouraging agreement with the experimental crack growth data with the only exception in the first 2 mm in both cases. It must be emphasized here that the  $K_{max}$  values at the notch root has been  $35 \text{ MPa } \sqrt{\text{m}}$  (as shown in Figure 4.44 ) with the assumption that a crack is growing from the L.E.. Practically crack initiates and subsequently propagates from the notch root where  $K_{max} = 0$ . A substantial value of  $K_{max}$  could only be found once the crack grows couple of times the notch root radius (Schofield 2011). This infers that the analytical value of  $\Delta K_{app}$  is too large near the notch, predicting faster crack growth rate within the first 0.5 mm from the notch root , and therefore may require more sophisticated future analysis. This might explain the discrepancy observed between the predicted and experimental FCG rates at the very early stage of crack growth. In addition, both  $\Delta K_{th}$  and  $\Delta K_C$  need to be taken into account to obtain a better prediction at the early stage of crack growth, which is beyond the scope of this project.

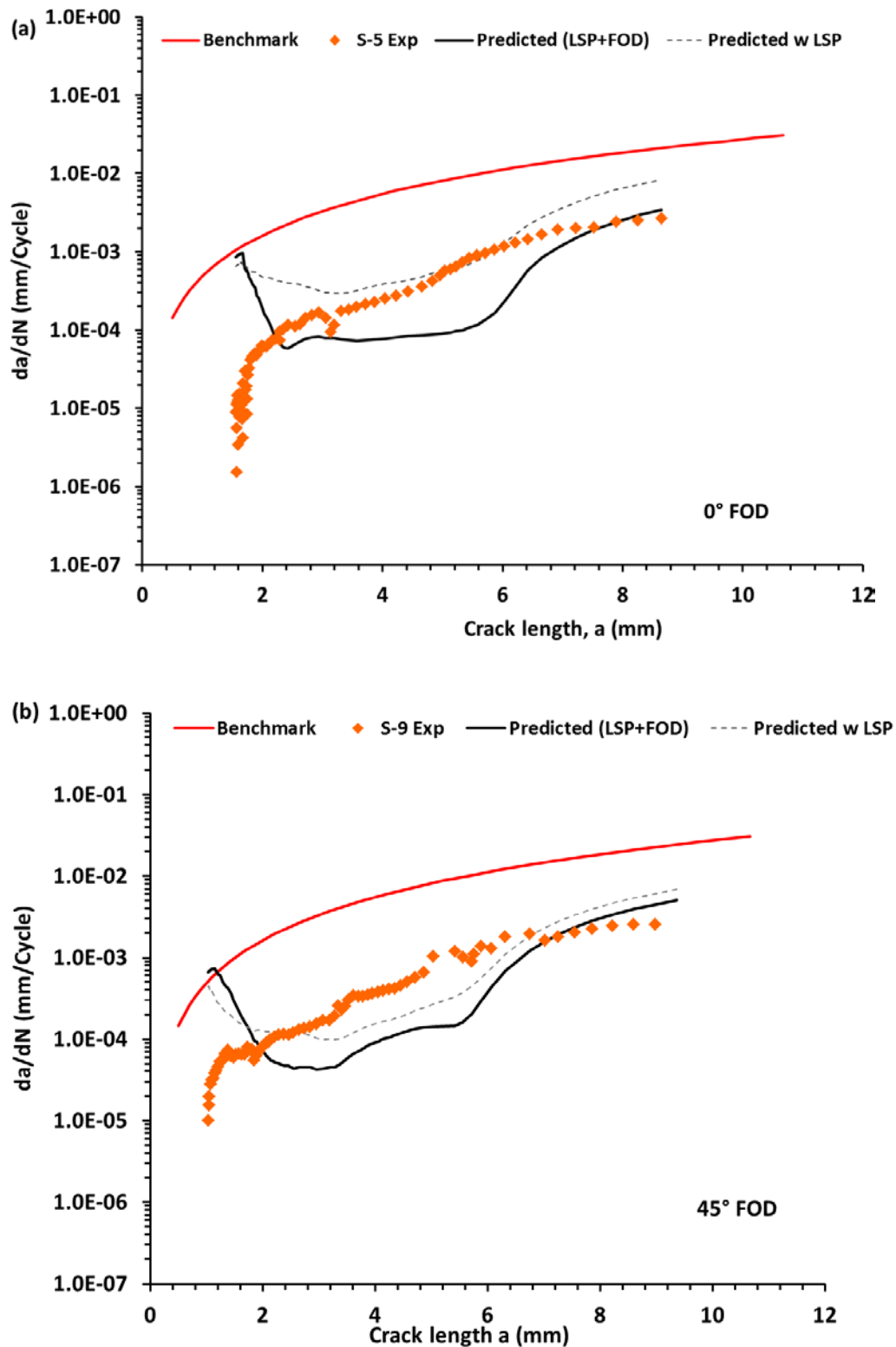


Figure 4.49: Comparison of the predicted and experimental fatigue crack growth rate as a function of crack length for (a)  $0^\circ$  and (b)  $45^\circ$  FOD under and applied stress of  $S_{max}=586$  MPa in LCF loading.

FCG rates were also predicted under combined cycle fatigue loading using Equation 4-10 (similar to the approach employed by (Hawkyard et al 1997)) that works well for materials without residual stress as shown in Figure 4.50 for benchmark Ti-64 . However, the interaction between LCF and HCF in a residual stress field is more complicated, at least at the early stage of crack growth that probably renders this equation invalid. In spite of this, this approach can serve as a good starting point to get a first approximation of the FCG rates.

Comparison between predicted and experimental FCG rates for 0° and 45° impacts are presented in Figure 4.50a and b respectively. Also shown are the experimental FCG rate in unpeened 0° FOD impact (notch depth was 0.8 mm). The prediction has a good agreement with the experimental FCG rates overall, however, the model overpredicts the FCG rate at the early stage crack growth and underpredicts the later/fast stages crack growth regime. In the early stage of crack growth regime, the discrepancy between the predicted and experimental crack growth rate is believed to be associated with the incapability of the model to take into account the effect of load history, material threshold and the critical stress intensity factor range that are yet to be studied in the present condition.

The difference in the FCG rate at the later stages (from 2 mm from the L.E. ) may be due to the residual stress distribution used for prediction. For  $K_{res}$  and hence  $\Delta K_{eff}$  calculation, residual stress distributions were taken along the notch centerline where peak compressive residual stresses are present. From the SEM image (see Figure 4.34, Figure 4.42) it can be observed that in both impact conditions, the crack never experienced the full-field peak residual compressive stress, but rather it bypassed this region and grew along a deviated route by an angle 15-20°. Therefore, it may be reasonable to utilize the residual stress profile associated with only LSP treatment in calculating  $K_{res}$  to achieve a safe prediction. These modified FCG rate predictions are also shown in Figure 4.50 using dashed grey lines. Now predictions are in an excellent agreement with the experimental results at the later stages of crack growth. This confirms that, using this approach, under CCF loading condition FCG rates can be predicted safely, if not accurately; if only the LSP'd residual stresses are known, without complex

and time consuming measurement of FOD'd residual stress as well as fatigue crack growth rates.

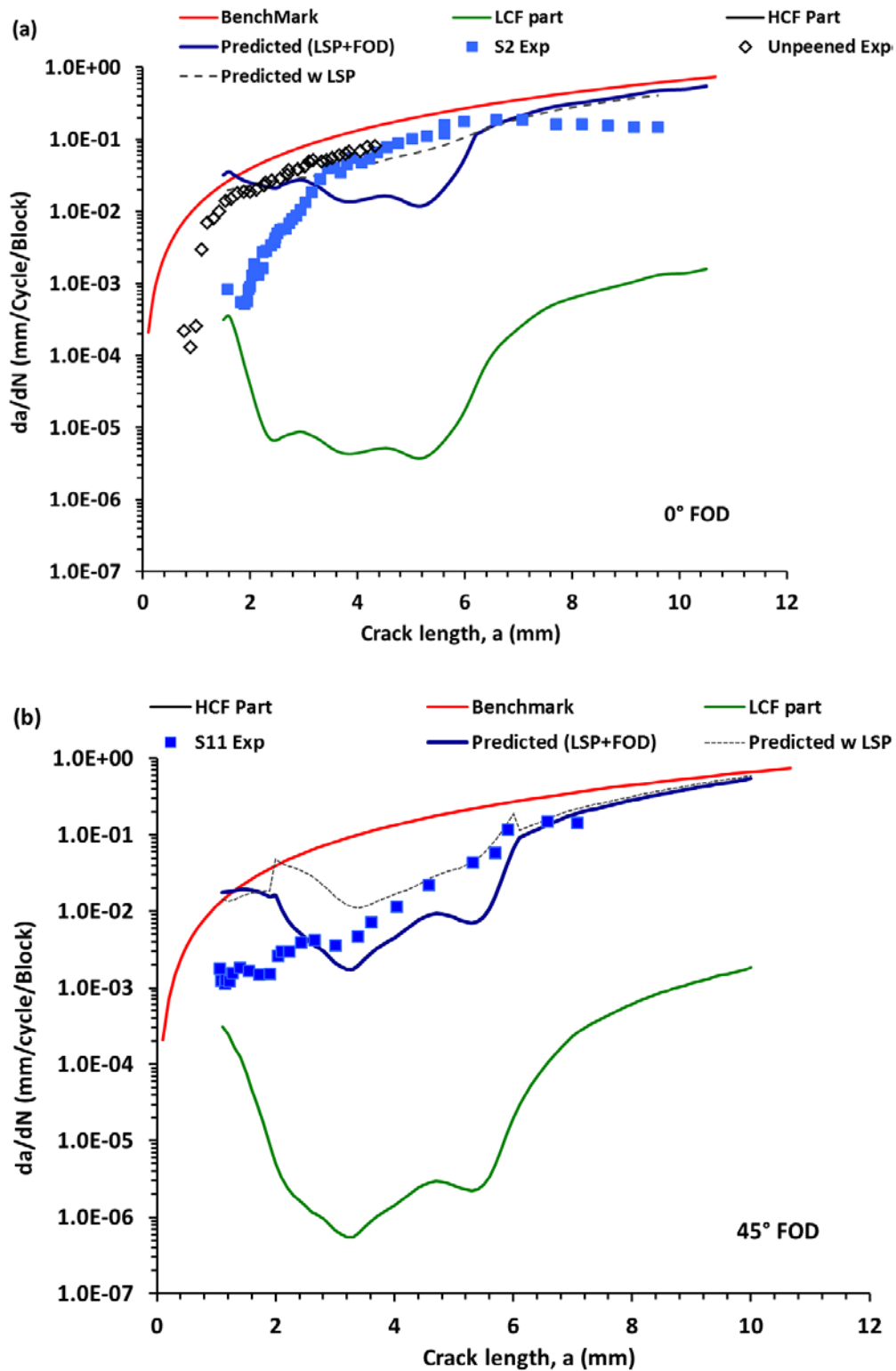


Figure 4.50: Comparison of the predicted and experimental FCG rate as a function of crack length for (a)  $0^\circ$  and (b)  $45^\circ$  FOD under and applied stress of  $S_{max}=435$  MPa in CCF.

Note here that the shape of the predicted FCG rate slightly differs between two impact conditions despite the similar shaped  $K_{res}$  profiles found for them (see Figure 4.46a). This may be associated with the difference in notch depth, or degree of initial plastic deformation between two impacts. Also shown in Figure 4.50 is the corresponding contribution of LCF part and HCF part in a combined cycle. It seems that HCF cycles mostly dominates the crack growth rate. This is not valid in the first 2 mm from the leading edge. In addition to this, the model does not take into account the effect of load history, threshold or critical stress intensity factor range. Despite neglecting these effects, the model captures the FCG rate quite well when the crack exceeds a distance of about 2 mm from the L.E.

#### 4.6.4 Summary

The effect of the residual stress associated with LSP and FOD impact on the fatigue crack growth rate has been predicted for  $0^\circ$  and  $45^\circ$  impact conditions, using analytical model based on Walker's expression. The stress intensity factor due to residual stress,  $K_{res}$  has been found using WFM method. A reasonable agreement was observed when  $K_{res}$  profile along the notch centreline was used. In this case, the model overpredicted the early crack growth regime and underpredicted the later crack growth regime. The discrepancy in the FCG rate between the experimental and prediction is believed to be due to multiple crack initiation, material threshold,  $\Delta K_{TH}$ , the critical stress intensity factor,  $K_C$ , and the nonlinear behaviour of cracks at this region. Further investigation of these parameters remained beyond the scope of this study. Nevertheless, it has been established that at the early stage of crack growth, in this case within the first 3 mm from the leading edge the superposition principle does not work due to nonlinear contact between the crack faces when the crack is fully or partially closed during the unloading cycle.

In the later stages of crack growth, the superposition works well where the crack is fully open. The discrepancy at this stage can be explained in terms of the actual crack path. In both  $0^\circ$  and  $45^\circ$  impact conditions, it seemed that the crack bypassed the large compressive region and grew along a less compressive region.

Therefore, the cracks only experienced the residual LSP'd residual compressive residual stress. Thus  $K_{res}$  was modified using the LSP'd residual stress. These modified FCG rate predictions show an excellent agreement with the experimental results at the later stages of crack growth. This confirms that, using this approach, under solely LCF and CCF loading conditions, FCG rates can be predicted safely, if not accurately, if only the LSP'd residual stresses are known, without any time consuming measurement of FOD'd residual stress or fatigue crack growth rate.

#### 4.7 Plastic Zone and Residual Stress Interactions

Laser shock peening induced compressive residual stresses have been found to affect the fatigue crack growth behaviour by delaying the crack initiation and by decelerating the crack propagation rate for aluminium alloys (Hatamleh et al 2007, Rubio-Gonzalez et al 2004, Tan et al 2004, Yang et al 2001), and also for Ti-6Al-4V alloy (Nalla et al 2003, Ruschau et al 1999, Shepard et al 2001, Zhang et al 2010). In order to incorporate the beneficial effect of the compressive residual stresses confidently into the damage tolerant design practice the compressive residual stresses need to be stable during the operation. If a significant amount of relaxation occurs during the first cycle as observed for AISI 4140 steel (Holzapfel et al 1998), LSP treatment would hardly provide any improvement against FOD related fatigue failure.

From the results presented so far it has been repeatedly observed that although the FOD induced compressive residual stresses relax (also previously reported by Boyce et al (2003)), LSP'd compressive stresses are highly stable. However one question still remains “why the compressive residual stresses do not relax as the crack grows”. Two reasons may be accounted for this: (i) a global elastic constraint exerted by the through thickness compressive residual stresses, and (ii) local plastic crack tip constraint.

The detailed analysis of the crack tip mechanics and the determination of the stress state at the crack tip are out of scope of this study. However, estimation of the plastic zone size can be one way to begin a discussion. In order to better understand the observed relaxation behaviour presented in sections 4.4.1 through 4.5, the plastic zone size ahead of the crack tip was sought. Under a monotonic load the width of the forward plastic zone  $r_p$  can be estimated using Equation 4-11 proposed by Rice back in 1967 (Rice 1967).

$$r_p = \frac{1}{\pi} \left( \frac{K_{\max}}{\sigma_y} \right)^2 \quad \text{Equation 4-10}$$

where  $K_{max}$  is the maximum applied stress intensity factor. In the case of cyclic loading the reverse plastic zone size,  $\Delta r_p$  can be derived as:

$$\Delta r_p = \frac{1}{4} r_p \quad \text{Equation 4-11}$$

This approach provides an estimate of the deformation zone ahead of the crack tip where no RS is present in the body. Where residual stresses are present such as in LSP+FOD'd specimens, so-called 'crack closure' can occur, which causes the actual stress intensity range  $\Delta K_{eff}$  to be reduced from the theoretical  $\Delta K$  that would be found if the crack were open at all times during a load cycle. The reverse plastic zone for an advancing fatigue crack in a residual stress field is given by McClung (1991):

$$\Delta r'_p = \frac{1}{\pi} \left( \frac{\Delta K_{eff}}{2\sigma_y + (\sigma_{cl} - \sigma_{min})} \right)^2 \quad \text{Equation 4-12}$$

Where;  $\Delta K_{eff}$  is the effective stress intensity factor range,  $\sigma_{cl}$  is the stress at the unloading cycle at which the crack faces first closes and  $\sigma_{min}$  is the minimum stress in the cycle. The details about determining the  $\Delta K_{eff}$  under LCF and HCF are given in Section 4.6. In this study 'crack-closure' stress,  $\sigma_{cl}$  was not explicitly measured. Nevertheless, Equation 4-13 is still valid with the assumption of  $\sigma_{cl} - \sigma_{min} = 0$  to estimate the maximum size of the plastically deformed zone ahead of the crack tip.

The variation of  $K_{max}$  as a function of crack length for simulated L.E. geometry is shown in Figure 4.51a for an applied stress of  $S_{max} = 435\text{MPa}$  under CCF loading conditions. Also, the corresponding forward plastic zone (PZS) size was estimated for the unpeened condition using Equation 4-11 to provide an estimate of the upper bound of the deformation zone size. The size and shape of the plastic zone ahead of the crack tip generally depends on the stress state (plane stress or plane strain) and the yield criterion (Suresh 1998). Since CRS reduces the applied stress intensity factor range, as shown in Figure 4.46, they will necessarily reduce the size of the plastic zone ahead of the crack tip according to the proportional relationship given in Equation 4-13. Therefore the PZS ahead of the crack tip in a residually stressed body should remain under the

PZS curve given in Figure 4.51a. Note that here a typical maximum stress,  $S_{\max} = 435\text{MPa}$  (represents the maximum stress used for CCF loading see section 4.7.2) was used for this calculation. It can be observed that the PZS increases with crack length.

The corresponding forward and reverse plastic zone sizes (using Equation 4-3) for peened and FOD'd specimens at angles of  $0^\circ$  and  $45^\circ$  are presented in Figure 4.51b. The compressive residual stresses result in a marked reduction in the PZSs. The maximum size of the reverse plastic zone is approximately  $100\ \mu\text{m}$  at the beginning of the crack growth, which then decreases with increasing crack length. Since the superposition principle was used to determine the stress intensity factor due to residual stress ( $K_{res}$ ), and hence the effective stress intensity factor range, the shape of the PZS profiles directly reflect the shape of corresponding residual stress profile. The validity of the weight function method in determining  $K_{res}$  is discussed in Section 4.7.3.

Figure 4.51b shows that the reverse PZS for both  $0^\circ$  and  $45^\circ$  impact conditions is similar with a maximum value of  $0.1\ \text{mm}$  where the crack just starts to grow. Simple superposition of the residual stress on the applied stress shows a reduction of PZS with increasing crack length, which is unrealistic from the energy release viewpoint. This means that when a fatigue crack starts to propagate (intergranular or transgranular) through a material the tractions along the crack faces need to be separate, which will release energy. The three dimensional force ahead of the crack tip will redistribute. The neighbouring grain ahead of the crack tip will necessarily be affected by the dissipation of energy. This is a very local effect. For this material the grain size of the  $\alpha$  phase is about  $25\ \mu\text{m}$  and the PZS is about 4 times this size. Only a few grains around the crack tip are plastically damaged.

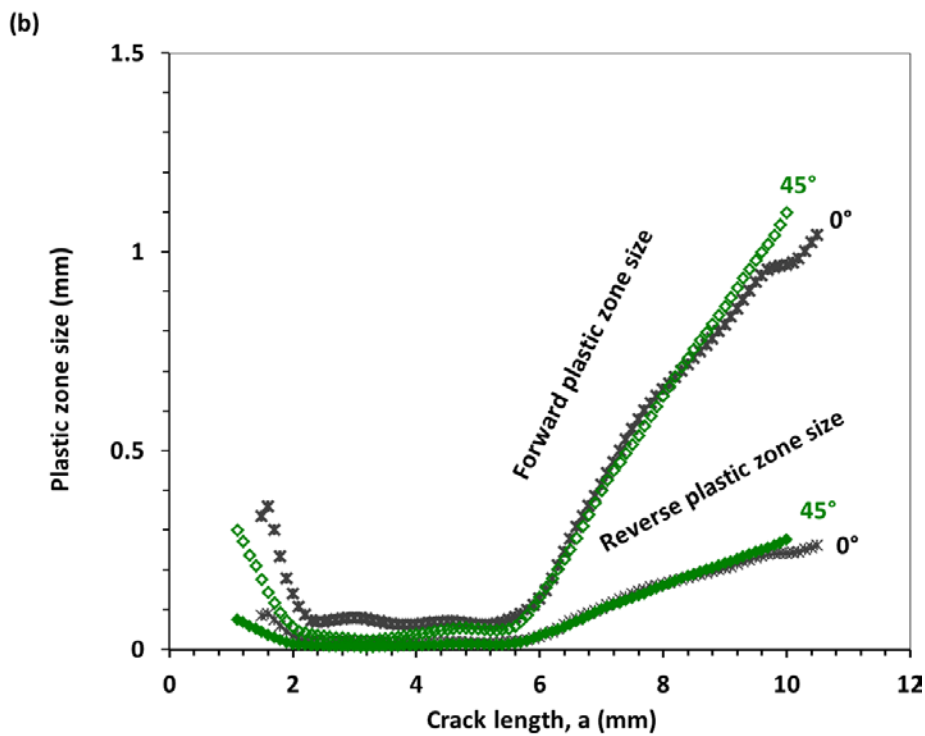
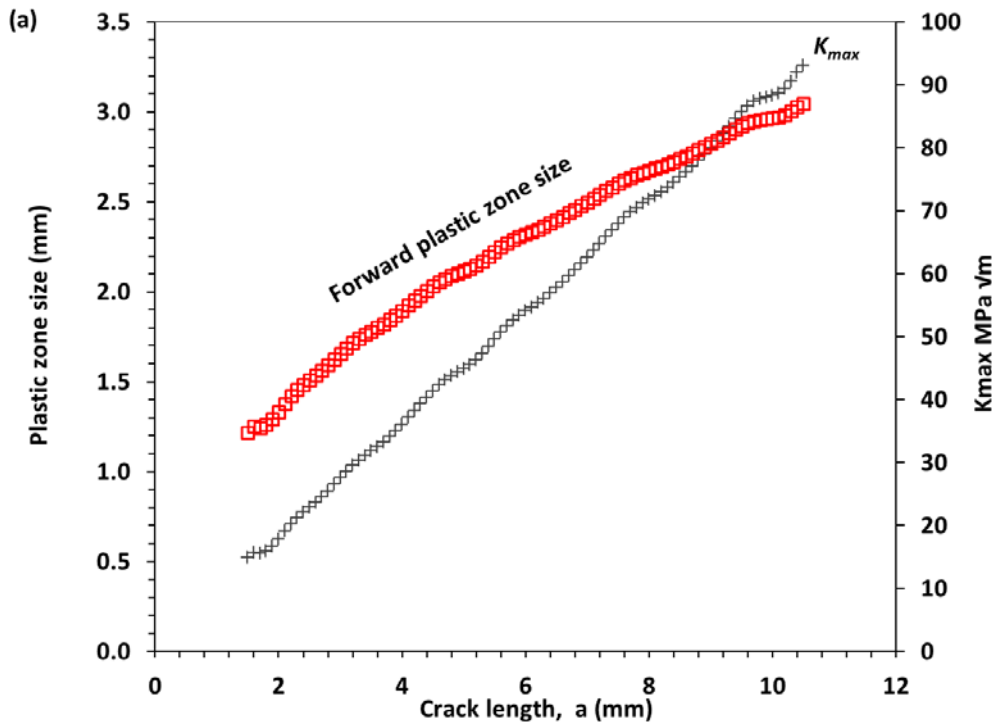
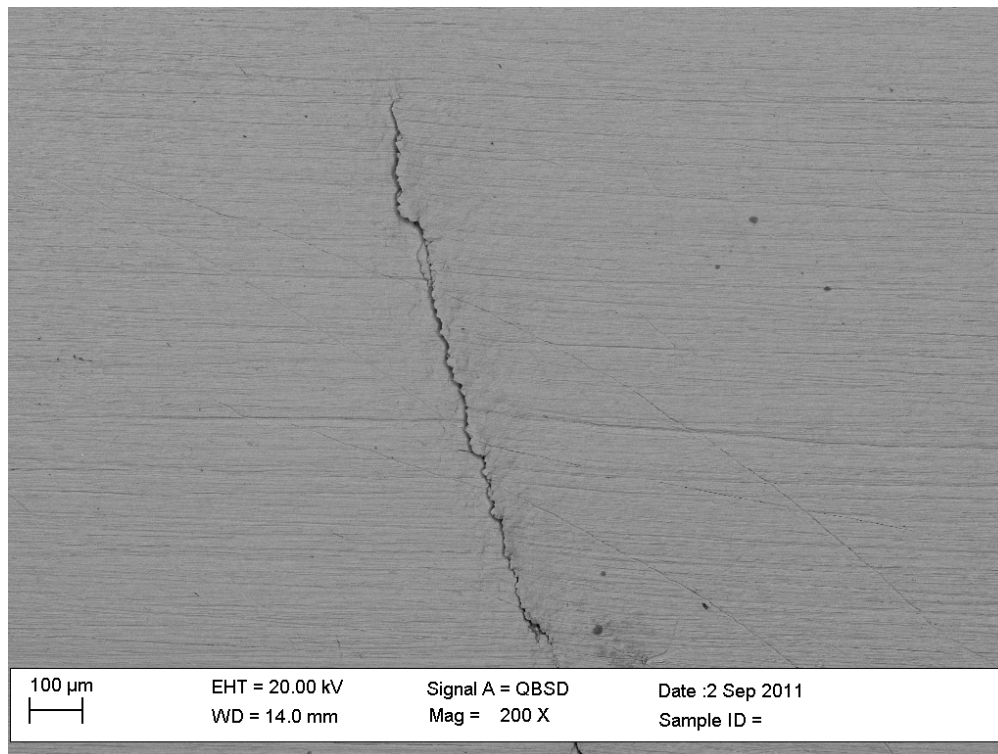


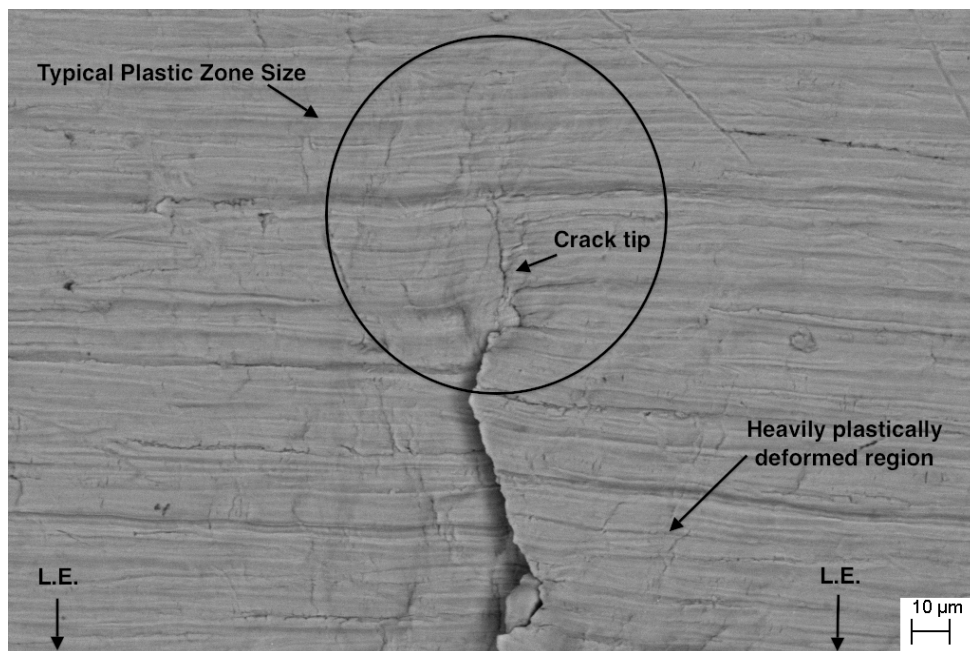
**Figure 4.51:** (a) Estimated variation of  $K_{max}$  and corresponding plastic zone size with crack length and (b) Forward and reverse plastic zone for both  $0^\circ$  and  $45^\circ$  impact, found using Equation 4-13 for CCF loading condition at  $S_{max} = 435 MPa$ .

An SEM image of the 2.2 mm crack is shown in Figure 4.52a with an enlarged

image of the crack tip in Figure 4.52b. The specimen was overloaded at  $S_{\max}=860$  MPa and clearly shows both a plastically damaged zone size ahead of the crack tip, and also the plastically damaged region at either side of the crack formed due to crack growth. It is important to note here that, the maximum applied stress for this specimen was twice as large as that used for the specimens (see Figure 4.32 Figure 4.42) studied in Section 4.7.2. It has been concluded in previous sections the residual strain relaxation increases with the applied load. The longitudinal residual strain field in this specimen is also shown in Figure 4.53a. Since relaxation is a strong function of the applied stress one might expect a larger plastic zone size at a higher load. The overloaded specimen provides evidence (Figure 4.53b) that this is not the case, residual strain relaxation is a strong function of applied load but not the PZS at least until crack exceed 6 mm from the L.E.. However, the plastic zone in Figure 4.52b is visible as a distribution of microcracks that extends up to about 40  $\mu\text{m}$  on either side of the crack, and this distance remains roughly constant along the length of the crack. This suggests that the plastic zone size remained constant during crack growth, which may be attributable to the CRS field. The crack itself is also more clearly visible (compared to the specimen in Figure 4.42) in the overloaded specimen as a result of some residual crack opening displacement.



(a)



(b)

**Figure 4.52:** SEM image showing the plastic zone ahead of the crack tip for an overloaded specimen ( $S-4$ ,  $S_{max} > 860\text{MPa}$ ) and heavily plastically deformed region at the crack tip and also at either side of the crack.

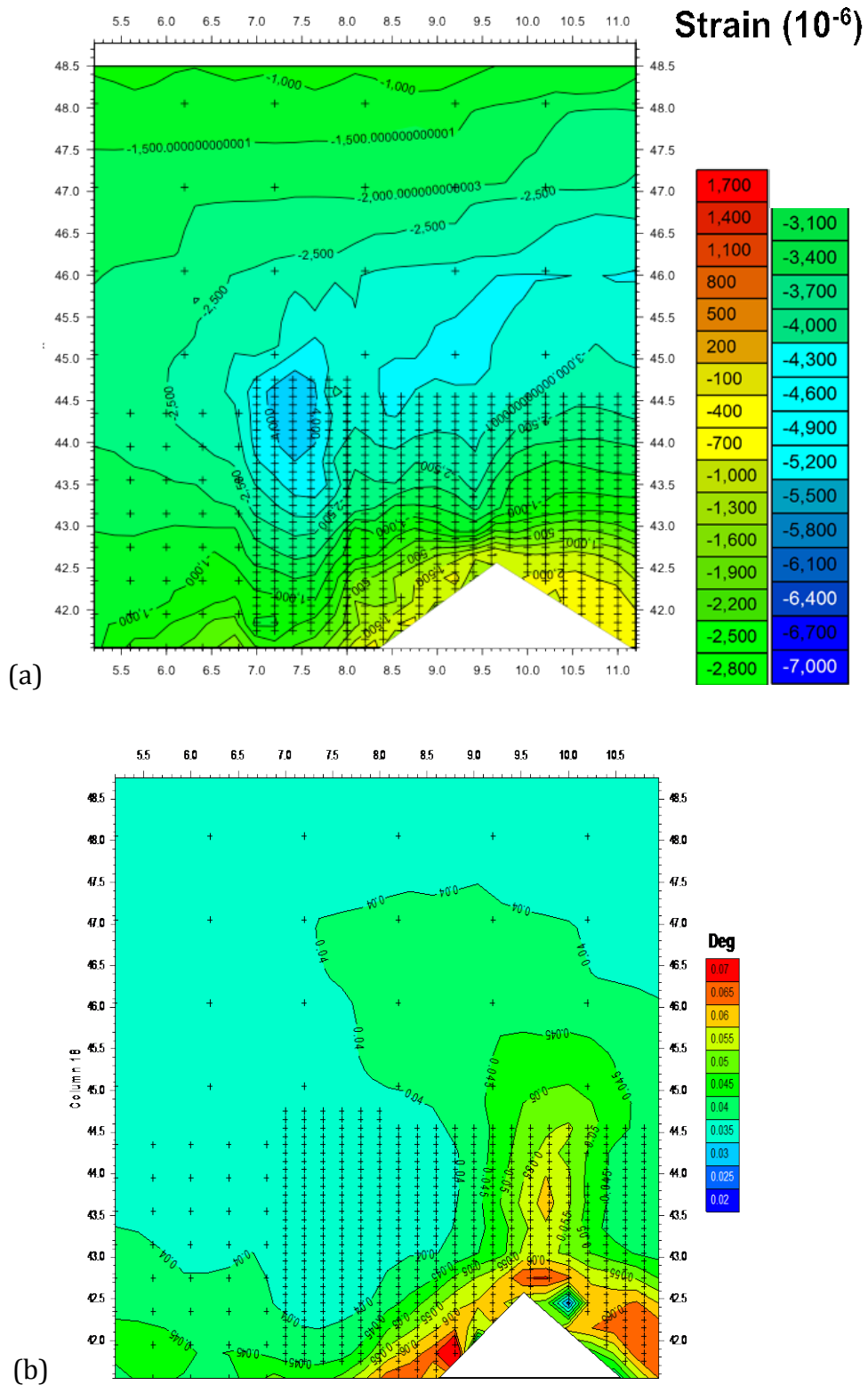


**Figure 4.53:** (a) Longitudinal residual strain distribution for overloaded specimen ( $S-4$ ,  $S_{max} > 860 \text{ MPa}$ ) (b) corresponding FWHM showing high degree of plastic work around the cracked region. The X and Y axis represents the distance along the L.E. and from the L.E. respectively.

**4.7.1 Summary**

The forward and reverse plastically deformed zone sizes are noticeably smaller compared to the stress free benchmark Ti-6Al-4V inferring the local effect on relaxation due to crack growth.

For a crack growing through a residual field the PZSs do not increase with the crack length.

## Chapter 5 Conclusions

Comparison of 0° and 45° in as FOD'd condition

The residual stress distribution around 0° and 45° FOD damages have been characterised by the synchrotron X-ray technique. The contour method was applied to the 0° FOD specimen and the results are compared. The following conclusions can be made:

1. Laser shock peening introduces compressive residual stresses with a value of  $0.5 \sigma_Y$  in the longitudinal direction (crack opening direction) of the aerofoil specimen. The maximum value of the residual stress is approximately  $0.6 \sigma_Y$ , which is found at a distance of 0.5 mm away from the leading edge.
2. High speed FOD impacts, both 0° and 45° superimposed additional residual stresses onto the initial LSP'd stresses predominantly at two key locations: a) a small tensile region at the flanks of the notch and b) a large compressive zone directly below the notch. The maximum compression observed was in the level of  $-0.8\sigma_Y$  and the maximum tension was  $0.2 \sigma_Y$ . No significant variation in terms of the size, shape or the position of these stress features were observed between 0° and 45° FOD notch. The magnitude of the compressive stresses introduced by 0° impacts was found to be slightly higher than that introduced by 45° impacts.
3. The  $\sigma_{yy}$  stress variation along the notch centreline was measured using the contour method for only LSP treatment and also for a 0° FOD specimen. The line profile was taken along the centreline. The stress profile generated by the contour method is consistent with that obtained by synchrotron diffraction technique. There is a small discrepancy of about 100 MPa observed between the two results at the root of the notch, which is largely due to the incapability of the contour method to provide correct stress near the surface.
4. FOD damage characterisation for both 0° and 45° impacts showed the evidence of loss of materials, material pileup, material folding, material

shearing and microcracks. Latter have been shown previously to be a preferred location of crack initiation cause causing premature failure (Rsuchau 2001).

5. In all cases, for both the impact conditions, that have been investigated in this study, with notch depths ranging from 0.63 to 1.55mm, the FOD related residual stress redistribution occurred in the first 3 mm from the leading edge. The rest of the region was remained unaltered.

### **RS Relaxation Behaviour due to cycling loading (prior to detectable crack)**

Residual strain evolution under solely LCF and CCF (LCF+HCF) type of loading has been mapped for 0° and 45° FOD impacts to investigate the relaxation behaviour of the beneficial compressive residual stress under cyclic loading where no cracks could be detected.

#### **Effect of LCF**

The residual strain relaxation has been measured extensively for 45° FOD impacts under solely LCF conditions. The following conclusions can be made:

1. 25% strain relaxation was observed when the specimen underwent  $10^5$  LCF cycles when the applied stress was increased from 521 MPa to 586 MPa.
2. The deeper side of the notch experienced extensive relaxation compared to the shallower side.
3. The residual strains largely remained unaffected beyond 4 mm from the L.E.
4. Anisotropic strain relaxation behaviour has been observed with the strains being more relaxed in the transverse direction than the longitudinal direction.

### **Effect of combined cycle fatigue on relaxation**

1. Residual strains in  $0^\circ$  impacts are found to be more stable than that in  $45^\circ$  impacts.
2. For  $0^\circ$  impact condition no significant relaxation has been observed after  $N = 1$  or  $N = 100$  at  $S_{\max} = 435$  MPa.
3. For  $45^\circ$  impacts no relaxation occurred after  $N = 100$  blocks at  $S_{\max} = 430$  MPa, however, when a 34% higher applied stress was used only  $N = 10$  blocks resulted in 30% relaxation.
4. The magnitude of applied load seems to have greater influence on the relaxation of residual stress under simplified combined cycled fatigue, compared to the total number of cycles applied in this study.
5.  $45^\circ$  impacts resulted in residual strain variation along the thickness.
6. Conclusion (No 2, 3 are 4) that has been made for the effect of LCF are also valid in this condition.

### **RS relaxation due to crack extension**

The residual strain relaxation behaviour has been examined for both short ( $a < 1$  mm) and long ( $a > 1$  mm) cracks under solely LCF ( $S_{\max} = 586$  MPa) as well as combined cycle fatigue ( $S_{\max} = 430$  MPa) loading conditions. The main finding of this section of the work can be summarised as follows:

1. No significant relaxation in the peak compressive residual strain has been observed due to short crack growth in both  $0^\circ$  and  $45^\circ$  impact conditions.
2. Approximately 35% relaxation has been found for long cracks.
3. Residual strains are found to be highly stable in the extreme condition where a 7 mm long crack was grown.
4. SEM images of the cracks showed that cracks deviated from the centreline by  $15^\circ - 20^\circ$ . This infers that cracks bypassed the region of peak

compressive residual strains that exist below the notch.

5. Results may suggest that only FOD related stress was completely relaxed, however, 80% of the stress associated with LSP treatment still remained unaltered.
6. The forward and reverse plastic zone sizes were found to be significantly smaller. This may be associated with far-field elastic constraint and also local crack tip constraint due to the compressive residual stress.

### **Fatigue crack growth rate prediction**

To assess the role of residual stress on the fatigue crack growth, and stress intensity factor due the residual stress,  $K_{res}$  has been determined using the weight function method (WFM). Effective stress intensity factor has been determined based on the superposition principle. FCG has been predicted using modified Walker's expression for both loading conditions and compared with the experimental FCG rates (Spanrad 2011). The following conclusions can be made:

1. When the FCG rates were predicted using  $K_{res}$  profile along the notch centreline, predictions seems to have a good agreement with the experimental FCG rates within the region of 2.2 mm to 6 mm from the L.E.. The model seems to over predict the FCG at the early stage of crack growth where the superposition principle may not be valid due to non-linear contacts of the crack faces.
2. Based on the observation of crack path deviation, fatigue crack growth rates were predicted for  $K_{res}$  for only LSP treatment and excellent agreement is found.

## Future Work

The knowledge of the residual stress distribution in any engineering structure plays a pivotal role in understanding the fatigue crack growth behaviour in that residual stress field. This study represents a significant contribution to the knowledge in the domain of residual stress that can serve as a foundation for further understanding the interaction between the fatigue crack growth and the residual stress they are embedded in. Some suggestions are made as follows:

- **Modelling of the residual stress relaxation**

The residual stress relaxation results for cyclic loading, small crack growth and long crack growth presented in this study can be used to develop and validate analytical or numerical modelling of LSP+FOD'd residual stress relaxation. Even though LSP'd residual stresses are found to be highly stable, it remains important to take into account the effect of the residual stress relaxation in determining the stress intensity factor due to residual stress,  $K_{res}$ . Afterwards, these  $K_{res}$  profiles can be used to determine effective stress intensity factor,  $\Delta K_{eff}$  and a better correlation can be obtained between the fatigue crack growth rate and the crack driving force.

- ***Establishing crack tip mechanics***

As we have seen the WFM method works well to determine the stress intensity factor near a crack tip within a residual stress field when a crack is fully open. However, when an advancing crack experiences compressive residual stress along its path, full or partial crack closure may occur (Beghini et al 1994). The validity of the WFM in determining  $K_{res}$  at the early stage of the crack growth is questionable due to the non-linear contact effects along the crack path. Where this happens, the superposition of residual stress onto the applied stress may not correspond to the actual stress field. To address this issue, crack tip mechanics need to be investigated in order to determine the stress state at the early stage of the crack growth.

- **Effect of microstructural damage on the crack growth**

Out of the four mechanisms of how FOD damage affects the fatigue life of aero engine components (Boyce et al 2001), the correlation between microstructural damage and the fatigue crack growth is the most challenging factor to assess quantitatively. Advanced characterization techniques that resolve at the scale of grain size such as 3D synchrotron X-ray microtomography can be one way to analyse microstructural damage. In an in-situ fatigue loading experiment, each stage of the damage accumulation, crack nucleation, initiation and propagation could be characterized during solely the LCF and CCF cycling. Thus accurate information could be determined in the following areas:

- Microstructural damage mechanisms and their effect on the fatigue crack growth.
- Accurate measurement of the crack opening displacements (COD). Hence, the stress intensity factor due to crack closure,  $K_{cl}$  could be ascertained.
- The interaction between LCF and HCF cycles in a combined cycle block can be established by measuring the fatigue crack extension during a LCF cycle and 1000 HCF cycle separately in a CCF block. Subsequently, a relationship between LCF and HCF assisted crack growth could be established to better predict the FCG rate at the early stage of crack growth.

- **Fractography**

Furthermore, SEM investigation of the fractured surfaces needs to be carried out to have a better understanding of the fatigue crack growth in the LSP+FOD'd residual stress field.

- **FCG rate prediction and damage-tolerant design**

The values of the threshold stress intensity factor,  $\Delta K_{TH}$  and the

critical stress intensity factor need to be established in the LSP+FOD condition. Once the  $\Delta K_{TH}$  and  $\Delta K_C$  values are found, the FCG rate predictions presented in section 4.6.2 can be extended by utilising the NASGRO equation (NASA 2000) that is capable of taking into account the relaxation of the residual stress, effect of R ratio, and  $\Delta K_{TH}$  and  $\Delta K_C$ .

## REFERENCES

- Altenberger I, Nalla RK, Noster U, Scholtes B, Ritchie RO. *7th Natl Turbine Engine High Cycle Fatigue Conference, Palm Springs, FL, 2002*, HCF.
- Bache MR, Bradshaw C, Voice W. 2003. Characterisation of foreign object damage and fatigue strength in titanium based aerofoil alloys. *Materials Science and Engineering A* 354: 199-206.
- Bache MR, Evans WJ, Voice W. 2002. The resistance to impact damage and subsequent fatigue response of two titanium alloys. *Materials Science and Engineering A* 333: 287-94.
- Balewski K, Brefeld W, Decking W, Franz H, Röhlsberger R, Weckert E. 2004. PETRAIII: A Low Emittance Synchrotron Radiation Source *EDMS Nr.: D00000000822371 Rev: A Ver: 1 Status: Freigegeben Dat.*, Desy, Hasylab, Hamburg.
- Beckmann F, Lippmann T, Metge J, Dose T, Donath T, et al. *Synchrotron Radiation Instrumentation, San Francisco, 2003*. AIP Conference Proceedings.
- Beghini M, Bertini L. 1990. Fatigue crack propagation through residual stress fields with closure phenomena. *Engineering Fracture Mechanics* 36: 379-87.
- Beghini M, Bertini L, Vitale E. 1994. Fatigue Crack Growth in Residual Stress Fields: Experimental Results and Modelling *Fatigue & Fracture of Engineering Materials & Structures* 17: 1433-44.
- Birkbeck JC. 2002. *Effects of FOD on the fatigue crack initiation of ballistically impacted titanium-aluminum(6)-vanadium(4) simulated engine blades*. University of Dayton, Dayton, OH.
- Blodgett MP, Yu F, Nagy PB. 2005. Eddy Current Nondestructive Residual Stress Assessment in Shot-Peened Nickel-Base Superalloys. *AIP Conference Proceedings* 760: 1347-54.

Bouchard R, Hupfeld D, Lippmann T, Neufeind J, Neumann HB, et al. 1998. A Triple-Crystal Diffractometer for High-Energy Synchrotron Radiation at the HASYLAB High-Field Wiggler Beamline BW5. *Journal of Synchrotron Radiation* 5: 90-101.

Boyce BL, Chen X, Hutchinson JW, Ritchie RO. 2001. The residual stress state due to a spherical hard-body impact. *Mechanics of Materials* 33: 441-54.

Boyce BL, Chen X, Peters JO, Hutchinson JW, Ritchie RO. 2003. Mechanical relaxation of localized residual stresses associated with foreign object damage. *Materials Science and Engineering A* 349: 48-58.

Brinker F, Kaul O. 2004. *Improvements of the Orbit Stability at DORIS III feedback photon radiation synchrotron synchrotron-radiation*. Presented at 9th European Particle Accelerator Conference, Lucerne, Switzerland.

Chahardehi A, Brennan FP, Steuwer A. 2010. The effect of residual stresses arising from laser shock peening on fatigue crack growth. *Engineering Fracture Mechanics* 77: 2033-39.

Chen X. 2005. Foreign object damage on the leading edge of a thin blade. *Mechanics of Materials* 37: 447-57.

Chen X, Hutchinson JW. 2001. Foreign object damage and fatigue crack threshold: Cracking outside shallow indents. *International Journal of Fracture* 107: 31-51.

Chu J, Rigsbee J, Banaś G, Lawrence F, Elsayed-Ali H. 1995. Effects of laser-shock processing on the microstructure and surface mechanical properties of hadfield manganese steel. *Metallurgical and Materials Transactions A* 26: 1507-17.

Clauer A. 1996. *Laser shock peening for fatigue resistance: Surface performance of titanium*. pp. 217-230. PA, USA.

Clauer AH, Walters CT, and Ford SC. 1983. *The Effects of Laser Shock Processing on the Fatigue Properties of 2024-T3 Aluminum*. pp. 7-22. Metals Park, Ohio:

American Society for Metals.

Cullity BD, Stock SR. 2001. *Elements of X-ray diffraction*. Pearson Education International.

Dane CB, Hackel LA, Daly J, Harrison J. 1998. Shot peening with lasers. *Advanced Materials and Processes* 153: 37-38.

Dejus RJ, Lai B, Khounsary A, Savoy R, Moog L, Gluskin E. 1994. Undulator A Characteristics and Specifications: Enhanced Capabilities ANL/APS/TB-17., Argonne National Laboratory.

Dieter GE. 1986. *Mechanical Metallurgy*. pp. 1-751. New York: McGraw-Hill Book Co. 398-400 pp.

Ding J, Hall RF, Byrne J, Tong J. 2007a. Fatigue crack growth from foreign object damage under combined low and high cycle loading. Part I: Experimental studies. *International Journal of Fatigue* 29: 1339-49.

Ding J, Hall RF, Byrne J, Tong J. 2007b. Fatigue crack growth from foreign object damage under combined low and high cycle loading. Part II: A two-parameter predictive approach. *International Journal of Fatigue* 29: 1350-58.

Duó P, Liu J, Dini D, Golshan M, Korsunsky AM. 2007. Evaluation and analysis of residual stresses due to foreign object damage. *Mechanics of Materials* 39: 199-211.

Edwards L. 2006. Influence of residual stress redistribution on fatigue crack growth and damage tolerant design. *Materials Science Forum* 524-525: 363-72.

El-Dasher BS, Zaleski TM, Gray JJ, Rybak SJ, Chen HL. 2006. Surface deformation behavior of beta solution treated and overaged Ti-6Al-4V during laser shock processing. *Journal of Applied Physics* 99.

Elber W. 1971. The significance of fatigue crack closure. In *Damage Tolerance in Aircraft Structures* pp. 230-42. : ASTM STP, 486.

Evans A, Kim SB, Shackleton J, Bruno G, Preuss M, Withers PJ. 2005. Relaxation of residual stress in shot peened Udimet 720Li under high temperature isothermal fatigue. *International Journal of Fatigue* 27: 1530-34.

Evans AD. 2007. *Residual stress characterisation of peened aerospace materials*. The University of Manchester, Manchester.

Fabbro R, Fournier J, Ballard P, Devaux D, Virmont J. 1990. Physical study of laser-produced plasma in confined geometry. *Journal of Applied Physics* 68: 775-84.

Fairand BP, Clauer A. 1976. Use of laser generated shocks to improve the properties of metals and alloys. *Industrial Applications of High Power Laser Technology* 86: 112-19.

Falub CV, Karimi A, Fontaine F, Kalss W. 2007. Fiber texture dependence of the anisotropic residual stress induced by lattice distortion in arc-evaporated Ti-Al-N thin films. *Reviews on Advanced Materials Science* 15: 105-10.

Farrahi GH, Majzoubi GH, Hosseinzadeh F, Harati SM. 2006. Experimental evaluation of the effect of residual stress field on crack growth behaviour in C(T) specimen. *Engineering Fracture Mechanics* 73: 1772-82.

Fitch AN. 2004. The High Resolution Powder Diffraction Beam Line at ESRF. *J. Res. Natl. Inst. Stand. Technol.* 109: 133-42.

Fitzpatrick M, Edwards L. 1998. Fatigue crack/residual stress field interactions and their implications for damage-tolerant design. *Journal of Materials Engineering and Performance* 7: 190-98-98.

Frankel PG. 2009. *Residual Stresses in Aerospace Components*. The University of Manchester, Manchester. 267 pp.

Ghidini T, Donne CD. 2007. Fatigue crack propagation assessment based on residual stresses obtained through cut-compliance technique. *Fatigue & Fracture of Engineering Materials & Structures* 30: 214-22.

Golden PJ, Hutson A, Sundaram V, Arps JH. 2007. Effect of surface treatments on fretting fatigue of Ti-6Al-4V. *International Journal of Fatigue* 29: 1302-10.

Guz AN, Makhort FG. 2000. The Physical Fundamentals of the Ultrasonic Nondestructive Stress Analysis of Solids. *International Applied Mechanics* 36: 1119-49.

Hall R, Byrne J, Zhao T, Tong J. 2008a. Influence of foreign object damage on fatigue crack growth of gas turbine aerofoils under complex loading conditions. *Fatigue and Fracture of Engineering Materials and Structures* 31: 386-97.

Hall R, Byrne J, Zhao T, Tong J. 2008b. Influence of foreign object damage on fatigue crack growth of gas turbine aerofoils under complex loading conditions. *Fatigue & Fracture of Engineering Materials & Structures* 31: 386-97.

Hammersley AP, Svensson SO, Hanfland M, Fitch AN, Hausermann D. 1996. Two-dimensional detector software: From real detector to idealised image or two-theta scan. *High Pressure Research: An International Journal* 14: 235-48.

Hammersley G, Hackel LA, Harris F. 2000. Surface prestressing to improve fatigue strength of components by laser shot peening. *Optics and Lasers in Engineering* 34: 327-37.

Hatamleh O, Lyons J, Forman R. 2007. Laser and shot peening effects on fatigue crack growth in friction stir welded 7075-T7351 aluminum alloy joints. *International Journal of Fatigue* 29: 421-34.

Hauk V. 1997. Structural and residual stress analysis by nondestructive methods, Elsevier. *Elsevier*.

Hawkyard M, Powell BE, Hussey I, Grabowski L. 1997. Fatigue crack growth under the conjoint action of major and minor stress cycles. *International Journal of Fatigue* 19: 722-22.

Holzapfel H, Schulze V, Vhringer O, Macherauch E. 1998. Residual stress relaxation in an AISI 4140 steel due to quasistatic and cyclic loading at higher

temperatures. *Materials Science and Engineering: A* 248: 9-18.

Hyde TR, Evans JT, Shaw BA. 2000. Effect of Stress and Heat Treatment on Magnetic Barkhausen Emission in Case Carburized Steels. *Materials Evaluation* 58: 985-90.

Jayaraman N, Prevey PS, Ravindranath R. 2005. Improved Damage Tolerance of Ti-6Al-4V Aero Engine Blades and Vanes Using Residual Compression by Design, Cincinnati, USA.

John R, Jata KV, Sadananda K. 2003. Residual stress effects on near-threshold fatigue crack growth in friction stir welds in aerospace alloys. *International Journal of Fatigue* 25: 939-48.

Johnson G. 2004. Matlab routines for the contour method.

Johnson G. 2008. *Residual stress measurements using the contour method. PhD thesis.* University of Manchester, Manchester.

Kaplan H. 1997. Laser Gauging Enters a Submicron World. *Photonics Spectra* 31 67-68.

Kaya AC, Erdogan F. 1980. Stress intensity factors and COD in an orthotropic strip. *International Journal of Fracture* 16: 171-90.

Kim SB, Evans A, Shackleton J, Bruno G, Preuss M, Withers PJ. 2005. Stress Relaxation of Shot-Peened UDIMET 720Li under Solely Elevated-Temperature Exposure and under Isothermal Fatigue. *Metallurgical and Materials Transactions A* 36: 3041-53.

King A. 2005. *Residual stress and damage characterisation in wide chord fan blades.* . University of Manchester, UK, Manchester.

King A, Steuwer A, Woodward C, Withers PJ. 2006. Effects of fatigue and fretting on residual stresses introduced by laser shock peening. *Materials Science and Engineering: A* 435-436: 12-18.

Korsunsky A, Liu J, Laundry D, Golshan M, Kim K. 2006. Residual elastic strain due to laser shock peening: synchrotron diffraction measurement. *The Journal of Strain Analysis for Engineering Design* 41: 113-20.

Laclare JL. 1994. Target Specifications and Performance of the ESRF Source. *Journal of Synchrotron Radiation*: 12-18.

Lai B, Khounsary A, Savoy R, Moog L, Gluskin E. 1993. Undulator A Characteristics and Specifications. *ANL/APS/TB-3*, Argonne National Laboratory.

Lathe C, Müller HJ, Schilling FR, Reichmann HJ, J. L. 2006. HARWI-II: A New High Pressure Beamline Equipped with a Large-Volume Press, MAX200x. *Synchrotron Radiation in Natural Science* 5: 111-14.

Lester HH, Aborn RH. 1925. Behaviour of iron crystals under load. *Army Ordnance* 6: 120-364.

Liljedahl CDM, Brouard J, Zanellato O, Irving PE, Fitzpatrick M, et al. 2007. *Weld Residual Stress Effects on Fatigue Crack Growth Behaviour of Aluminium Alloy 2024-T3* Presented at First International Conference on Damage Tolerance of Aircraft Structures, The Netherlands.

Lippmann T, Lottermoser L, Beckmann F, Martins RV, Dose T, et al. 2007. New developments at the Engineering Materials Science Beamline HARWI II, GKSS Forschungszentrum Geesthacht, Max-Planck-Str. 1, 21502 Geesthacht, Germany, Hamburg.

Liss K-D, Bartels A, Schreyer A, Clemens H. 2003. High-energy X-rays: a tool for advanced bulk investigations in materials science and physics. *Textures and Microstructures* 35: 219-52.

Liu Q, Yang CH, Ding K, Barter SA, Ye L. 2007. The effect of laser power density on the fatigue life of laser-shock-peened 7050 aluminium alloy. *Fatigue & Fracture of Engineering Materials & Structures* 30: 1110-24.

Macherauch E, Kloss KH. 1986. *Origin Measurements and Evaluation of Residual*

- Stress*. Presented at The International conference on residual stresses, Germany.
- Mall S, Hamrick IJL, Nicholas T. 2001. High cycle fatigue behavior of Ti-6Al-4V with simulated foreign object damage. *Mechanics of Materials* 33: 679-92.
- Martinez CM, Eylon D, Nicholas T, Thompson SR, Ruschau JJ, et al. 2002. Effects of ballistic impact damage on fatigue crack initiation in Ti-6Al-4V simulated engine blades. *Materials Science and Engineering A* 325: 465-77.
- Martinez S, Sathish S, Blodgett M, Shepard M. 2003. Residual stress distribution on surface-treated Ti-6Al-4V by X-ray diffraction. *Experimental Mechanics* 43: 141-47.
- Masse J-E, Barreau G. 1995. Laser generation of stress waves in metal. *Surface and Coatings Technology* 70: 231-34.
- Masson O, Dooryhee E, Cheary RW, Fitch AN. 2001. Instrumental Resolution Function of the ESRF Powder Diffraction Beamline BM16. *Materials Science Forum* 378-381: 300-07.
- McClung R, Newman JC. 1999. Advances in Fatigue Crack Closure Measurement and Analysis: Second Volume. In *STP1343-EB*, pp. 1-481: ASTM.
- McClung RC. 1991. CRACK CLOSURE AND PLASTIC ZONE SIZES IN FATIGUE. *Fatigue & Fracture of Engineering Materials & Structures* 14: 455-68.
- McClung RC. 2007. A literature survey on the stability and significance of residual stresses during fatigue. *Fatigue & Fracture of Engineering Materials & Structures* 30: 173-205.
- Molis SE, Clarke DR. 1990. Measurement of Stresses Using Fluorescence in an Optical Microprobe: Stresses around Indentations in a Chromium-Doped Sapphire. *Journal of the American Ceramic Society* 73: 3189-94.
- Montross CS, Wei T, Ye L, Clark G, Mai Y-W. 2002. Laser shock processing and its effects on microstructure and properties of metal alloys: a review. *International*

*Journal of Fatigue* 24: 1021-36.

Nalla RK, Altenberger I, Noster U, Liu GY, Scholtes B, Ritchie RO. 2003. On the influence of mechanical surface treatments--deep rolling and laser shock peening--on the fatigue behavior of Ti-6Al-4V at ambient and elevated temperatures. *Materials Science and Engineering A* 355: 216-30.

NASA. 2000. Fatigue crack growth computer program NASGRO Version 3.0—Reference manual. In *JSC-22267B*. Texas: Lyndon B. Johnson Space Center, NASA.

Nesemann H, Brefeld W, Brinker F, Decking W, Kaul O, Sarau B. *Particle Accelerator Conference, 1995., Proceedings of the 1995* 1995, 1: 195-97 vol.1.

Nicholas T. 2006. Foreign Object Damage In *High Cycle Fatigue*, pp. x-xiv. Oxford: Elsevier Science Ltd.

Nowell D. 2008. Ballistic simulation of foreign object damage on 20 fatigue specimens, Report, University of Oxford, University of Oxford, Oxford.

Nowell D, DuÛ P, Stewart IF. 2003. Prediction of fatigue performance in gas turbine blades after foreign object damage. *International Journal of Fatigue* 25: 963-69.

Noyan IC, Cohen JB. 1987. *Residual Stress - Measurement by Diffraction and Interpretation*. . Berlin: Springer-Verlag.

Oakley SY, Nowell D. 2007. Prediction of the combined high- and low-cycle fatigue performance of gas turbine blades after foreign object damage. *International Journal of Fatigue* 29: 69-80.

Owen A. 2002. *Synchrotron strain mapping: Aerospace applications*.

University of Manchester, Manchester.

Pao Y-H, Wu T-T, Gamer U. 1991. Acoustoelastic birefringences in plastically deformed solids. Part I. Theory 1. *Journal of Applied Mechanics, Transactions ASME* 58: 11-17.

Pasta S, Reynolds AP. 2008. Residual stress effects on fatigue crack growth in a Ti-6Al-4V friction stir weld. *Fatigue & Fracture of Engineering Materials & Structures* 31: 569-80.

Patterson E. 2001. Photoelasticity In *Encyclopedia of Materials: Science and Technology*, ed. KHJ Buschow. Oxford.

Elsevier

Peters JO, Ritchie RO. 2000. Influence of foreign-object damage on crack initiation and early crack growth during high-cycle fatigue of Ti-6Al-4V. *Engineering Fracture Mechanics* 67: 193-207.

Peters JO, Ritchie RO. 2001a. Foreign-object damage and high-cycle fatigue of Ti-6Al-4V. *Materials Science and Engineering A* 319-321: 597-601

Peters JO, Ritchie RO. 2001b. Foreign-object damage and high-cycle fatigue: role of microstructure in Ti-6Al-4V. *International Journal of Fatigue* 23: 413-21

Peyre P, Berthe L, Scherpereel X, Fabbro R. 1998. Laser-shock processing of aluminium-coated 55C1 steel in water-confinement regime, characterization and application to high-cycle fatigue behaviour. *Journal of Materials Science* 33: 1421-29

Peyre P, Fabbro R, Merrien P, Lieurade HP. 1996. Laser shock processing of aluminium alloys. Application to high cycle fatigue behaviour. *Materials Science and Engineering A* 210: 102-13

Pirling T, Bruno G, Withers PJ. 2006. SALSA--A new instrument for strain imaging in engineering materials and components. *Materials Science and Engineering: A* 437: 139-44

Polmear I. 1995. *Light Alloys—Metallurgy of Light Metals*

pp. 292. London: Arnold.

Prevèy PS. 2000. *The effect of cold work on the thermal stability of residual*

*compression in surface enhanced IN718*. . Presented at 20th ASM Materials Solutions Conference & Exposition, , St. Louis, Missouri. USA

Prevéy PS, Shepard MJ, Smith PR. *6th National Turbine Engine High Cycle Fatigue (HCF) Conference, Jacksonville, Florida, 2001*.

Prime M, Martineau RL. 2002. Mapping Residual Stresses After Foreign Object Damage Using The Contour Method. *Materials Science Forum* 404-407: 521-26

Prime MB. 2001. Cross-Sectional Mapping of Residual Stresses by Measuring the Surface Contour After a Cut. *Journal of Engineering Materials and Technology* 123: 162-68

Quinn S, Dulieu-Barton JM, Langlands JM. 2004. Progress in Thermoelastic Residual Stress Measurement. *Strain* 40: 127-33

Rankin JE, Hill MR, Hackel LA. 2003. The effects of process variations on residual stress in laser peened 7049 T73 aluminum alloy. *Materials Science and Engineering A* 349(1-2): 279-91.

Rice JR. 1967. Mechanics of crack tip deformation and extension by fatigue. In *Fatigue Crack Propagation*, pp. 247-309: ASTM STP 415

Ritchie, Davidson, Boyce, Campbell, Roder. 1999. High-cycle fatigue of Ti-6Al-4V. *Fatigue & Fracture of Engineering Materials & Structures* 22: 621-31

Rubio-González C, Ocaña JL, Gomez-Rosas G, Molpeceres C, Paredes M, et al. 2004. Effect of laser shock processing on fatigue crack growth and fracture toughness of 6061-T6 aluminum alloy. *Materials Science and Engineering A* 386: 291-95

Ruschau JJ, John R, Thompson SR, Nicholas T. 1999. Fatigue crack nucleation and growth rate behavior of laser shock peened titanium. *International Journal of Fatigue* 21: 199-209

Ruschau JJ, Nicholas T, Thompson SR. 2001. Influence of foreign object damage (FOD) on the fatigue life of simulated Ti-6Al-4 V airfoils. *International Journal of*

*Impact Engineering* 25: 233-50

Ruschau JJ, Thompson SR, Nicholas T. 2003. High cycle fatigue limit stresses for airfoils subjected to foreign object damage. *International Journal of Fatigue* 25: 955-62

Schell N. 2010. High Energy Materials Science at PETRA III. Hamburg

Schell N, Martins RV, Beckmann F, Ruhnau HU, Kiehn R, Schreyer A. 2008. The High Energy Materials Science Beamline at PETRA III. *Materials Science Forum* Stress Evaluation Using Neutrons and Synchrotron Radiation: 261-66

Schoenig FCJ, Soules JA, Chang H, DiCillo JJ. 1995. Eddy current measurement of residual stresses induced by shot peening in titanium Ti-6Al-4V. *Journal Name: Materials Evaluation; (United States); Journal Volume: 53:1; Medium: X; Size: Pages: 22-26*

Schofield J. 2011. Paris Law Constant. Derby

Servetti G, Zhang X. 2009. Predicting fatigue crack growth rate in a welded butt joint: The role of effective R ratio in accounting for residual stress effect. *Engineering Fracture Mechanics* 76: 1589-602

Shastri SD, Dejus RJ, Haeffner DR. 1998. Experimental Characterization of APS Undulator A at High Photon Energies (50–200 keV). *Journal of Synchrotron Radiation* 5: 67-71

Shepard M, Smith P, Amer M. 2001. Introduction of compressive residual stresses in Ti-6Al-4V simulated airfoils via laser shock processing. *Journal of Materials Engineering and Performance* 10: 670-78

Spanrad S, Tong J. 2011. Characterisation of foreign object damage (FOD) and early fatigue crack growth in laser shock peened Ti-6Al-4V aerofoil specimens. *Materials Science and Engineering: A* 528: 2128-36

Spanrad SK. 2011. *Fatigue Crack Growth in Laser Shock Peened Aerofoils*

- Subjected to Foreign Object Damage*. The University of Portsmouth, Portsmouth
- Srinivasan S, Garcia DB, Gean MC, Murthy H, Farris TN. 2009. Fretting fatigue of laser shock peened Ti-6Al-4V. *Tribology International* 42: 1324-29
- Suresh S. 1998. *Fatigue of materials*. Cambridge: Cambridge University Press.
- Tada H, Paris PC, Irwin GR. 2000. *The stress analysis of cracks handbook*. New York: The American Society of Mechanical Engineers.
- Tan Y, Wu G, Yang JM, Pan T. 2004. Laser shock peening on fatigue crack growth behaviour of aluminium alloy. *Fatigue & Fracture of Engineering Materials & Structures* 27: 649-56
- Thompson SR, Ruschau JJ, Nicholas T. 2001. Influence of residual stresses on high cycle fatigue strength of Ti-6Al-4V subjected to foreign object damage. *International Journal of Fatigue* 23: 405-12
- Torres M, A.,S., Voorwald H, J.,C. 2002. An evaluation of shot peening, residual stress and stress relaxation on the fatigue life of AISI 4340 steel. *International Journal of Fatigue* 24: 877-86
- Vaccari JA. 1992. Laser shocking extends fatigue life. *American Machinist* 62-64
- Walker E. 1970. The effect of stress ratio during crack propagation and fatigue for 2024-T3 and 7076-T6 aluminum In *Effect of environment and complex load history on fatigue life ASTM STP 462*, pp. 1-14. Philadelphia: American Society for Testing and Materials
- Warren BE, Averbach BL. 1950. The effect of cold-work distortion on x-ray patterns. *Journal of Applied Physics* 21: 595-99
- Warren BE, Averbach BL. 1952. The separation of cold-work distortion and particle size broadening in x-ray patterns [1]. *Journal of Applied Physics* 23: 497
- White RM. 1963. Elastic wave generation by electron bombardment or electromagnetic wave absorption. *Journal of Applied Physics* 34: 2123-24

Witek L. 2011. Crack propagation analysis of mechanically damaged compressor blades subjected to high cycle fatigue. *Engineering Failure Analysis* 18: 1223-32

Withers PJ. 2007. Residual stress and its role in failure. *Reports on Progress in Physics* 70: 2211-64

Withers PJ, Bhadeshia HKDH. 2001. Residual stress Part 1-Measurement techniques. *Materials Science & Technology* 17: 355-65

Withers PJ, Preuss M, Steuwer A, Pang JWL. 2007. Methods for obtaining the strain-free lattice parameter when using diffraction to determine residual stress. *Journal of Applied Crystallography* 40: 891-904

Wong AK. 2001. Stress distribution: analysis using thermoelastic effect In *Encyclopedia of Materials: Science and Technology*, ed. KHJ Buschow. Oxford

Elsevier

Xiong Y, Kelleher J, Frankel PG, Withers PJ. *ICRS8, Denver Colorado, 2008.*

Yang JM, Her YC, Han N, Clauer A. 2001. Laser shock peening on fatigue behavior of 2024-T3 Al alloy with fastener holes and stopholes. *Materials Science and Engineering: A* 298: 296-99

Young RJ. 2001. Residual stresses: measurement by Raman shifts. In *Encyclopedia of Materials: Science and Technology*, ed. KHJ Buschow. Oxford

Elsevier

Zhang XC, Zhang YK, Lu JZ, Xuan FZ, Wang ZD, Tu ST. 2010. Improvement of fatigue life of Ti-6Al-4V alloy by laser shock peening. *Materials Science and Engineering: A* 527: 3411-15

Zhang Y, Ganguly S, Edwards L, Fitzpatrick ME. 2004. Cross-sectional mapping of residual stresses in a VPPA weld using the contour method. *Acta Materialia* 52: 5225-32

Zhao ZB, Hershberger J, Yalisove SM, Bilello JC. 2002. Determination of residual

stress in thin films: a comparative study of X-ray topography versus laser curvature method. *Thin Solid Films* 415: 21-31

Zhuang WZ, Halford GR. 2001. Investigation of residual stress relaxation under cyclic load. *International Journal of Fatigue* 23: 31-37

#### APPENDIX-I

### **Conference presentations and journal articles produced during this project**

Zabeen, S., Preuss, M., Spanrad, S., Tong, J., Withers, P.J., 2010. Laser shock peening: A solution to foreign object damage problem. The second international conference on laser peening. San Francisco, CA, USA.

Zabeen, S., Preuss, M., Wang, H-T., Spanrad, S., Tong, J., Withers, P.J., 2009. A synchrotron x-ray study of residual strain distribution around foreign object damage in laser shock peened Ti-6Al-4V alloy. MECA SENS conference, Mito, Japan.

Spanrad, S., Tong, J., 2010. Characterization of foreign object damage (FOD) and early fatigue crack growth in laser shock peened Ti-6AL-4V aerofoil specimens. International Congress of Fatigue, Prague, Czech Republic.

Tong, J., Wang, H-T., Zhao, T., Spanrad, S., Hall, R., Byrne, J., 2008. FOD characterisation and its influence on FCG of aerofoils under HCF+LCF loading conditions. International Conference on Fatigue Damage of Structural Materials VI, Cape Cod, Hyannis, MA, US.

Spanrad, S., Tong, J., 2011. Characterization of foreign object damage (FOD) and early fatigue crack growth in laser shock peened Ti-6AL-4V aerofoil specimens. *Material Science and Engineering A* 528, 2128-2136

Spanrad, S., Tong, J., 2010. Characterization of foreign object damage (FOD) and early fatigue crack growth in laser shock peened Ti-6AL-4V aerofoil specimens. *Procedia Engineering*, Vol. 2: 1751-1759.

Zabeen, S., Preuss, M., Withers, P.J., Spanrad, S., Tong, J., Schofield, J., 2010.

Synchrotron strain mapping of the residual strain distribution around foreign object damage in laser shock peened Ti-6AL-4V alloy. Materials Science Forum, Vol. 652, 19-24.

Zabeen, S., Withers, P.J., Preuss, M. 2010. Residual Stress Relaxation in Laser Shock Peened and Foreign Object Damaged Ti-6Al-4V Under Complex Fatigue Loading, ECRS8, Riva Del Garda, Italy.

Zabeen, S., Preuss, M., Withers, P.J., 2011. The residual stress characterization of head-on and off-axis foreign object damages in laser shock Ti-6AL-4V alloy., Submission in progress.

## APPENDIX-II

**FOD impact conditions**

FOD impact parameters:

Impact angle: 0°

Edge First, 200m/s, 3.2mm cube impactor

Shot No.	Velocity (m/s)	Notch depth (mm)
1	195	1.55
2	192	1.37
3	193	1.40
4	193	1.12
5	196	1.49
6	204	1.49
7	199	1.54
8	202	1.48

Impact angle: 45°

Point First, 250m/s, 4.8mm cube impactor

Shot No.	Velocity (m/s)	Notch depth (mm)
1	240	0.75
2	247	0.63
3	247	0.73
4	247	0.86
5	245	0.82
6	250	0.79
7	247	0.78
8	239	0.83
9	247	0.82

## APPENDIX-III

**MATLAB fitting routine used to fit data from APS, HARWII and HEMS beamlines.**

```

% esrf_multifit
% Written by Ed Oliver, July 2002
% Uses built-in Matlab optimisation routines plus functions:
% pv_matfit_sb.m
% pk_voigt.m
% Edited by Francisco Garcia-Pastor, July 2006
% Added a residuals graph and erased error column from xrd data
% _____
_____

%clear all;close all;
%Just a quick try, remember to clear all if necessary
global a0 err;
%_____Get user
input_____

froot=input('Filename root: ','s');
idum=input('File numbers to fit [ FIRST LAST STEP(optional) ]: ');
istart=idum(1);iend=idum(2);if(length(idum)>2);istep=idum(3);else;istep=1;end;

cflag=input('Constrain background and slope to values fitted in first spectrum [y/n] (default=n)? ','s');
if isempty(cflag);cflag='n';end;

%_____Plot spectra, select fitting range and peak centres_____

dummy=int2str(istart+1000 );dummy=dummy(2:5);
fname=[froot dummy '.xrd'];fdata=load(fname);
tth=fdata(:,1);counts1=fdata(:,2);%err=fdata(:,3);

plot(tth,counts1);z=axis;z(1)=min(tth);z(2)=max(tth);axis(z);
hold on;

dummy=int2str(iend+10000);dummy=dummy(2:5);
fname=[froot dummy '.xrd'];fdata=load(fname);
tthend=fdata(:,1);counts2=fdata(:,2);%err=fdata(:,3);
plot(tth,counts2,'r');

legend('Initial spectrum','Final spectrum');

z=axis;
title('Select fitting range...');
[xdum,ydum]=ginput(1);
pltx=[xdum xdum];plty=[z(3) z(4)];plot(pltx,plty,'k--');
[xdum2,ydum]=ginput(1);
pltx=[xdum2 xdum2];plty=[z(3) z(4)];plot(pltx,plty,'k--');
xmin=min([xdum xdum2]);xmax=max([xdum xdum2]);

```

```

index=(tth>xmin)&(tth<xmax);
hold off;
plot(tth(index),counts1(index));

title('Click on peak centres (ENTER to finish):');
[xp,ydum]=ginput;
xp=sort(xp)';
npks=length(xp);
if ((xp>xmin)&(xp<xmax));else;disp('PEAKS ARE NOT WITHIN SELECTED
RANGE - RE-START!');break;end;

close all

a=[];aout=[];ae=[];aeout=[];

%_____MAIN
LOOP_____

for i=istart:iend;
dummy=int2str(i+10000);dummy=dummy(2:5);
fname=[froot dummy '.xrd'];fdata=load(fname);
tth=fdata(:,1);counts=fdata(:,2);%err=fdata(:,3);

index=(tth>=xmin)&(tth<=xmax);
tth=tth(index);counts=counts(index);%err=err(index);

%Guesstimates

slope=(counts(end)-counts(1))/(xmax-xmin);
bkgd=counts(1)-slope*xmin;

%Subtract sloping background, then look for maximum intensity of each
peak

cdum=counts-slope*tth-bkgd;

clear ibtwn;
for ii=1:npks-1
xbtwn=0.5*(xp(ii)+xp(ii+1));
xdum=abs(tth-xbtwn);
idum=find(xdum==min(xdum));
ibtwn(ii)=idum(1);
end

if npks==1;ibtwn=[1 length(tth)];else;ibtwn=[1 ibtwn
length(tth)];end;

for ii=1:npks;
cdum2=cdum(ibtwn(ii):ibtwn(ii+1));%Search for max intensity in
vicinity of peak only
tthdum=tth(ibtwn(ii):ibtwn(ii+1));
inty(ii)=max(cdum2);
idum=find(cdum2==inty(ii));
xp(ii)=tthdum(idum);

```

```

%Find FWHM
cdum3=abs(cdum2(1:idum)-inty(ii)/2);
indfw=find(cdum3==min(cdum3));
fw(ii)=2*(xp(ii)-tthdum(indfw));

if(i>istart);fw(ii)=(aout(end,4*(ii-
1)+3));end;%!!!!!!!!!!!!!!!!!!!!!!!!!!!!!!
eta(ii)=0.5;

end

a0=max(inty);inty=inty/a0;bkgd=bkgd/a0;slope=slope/a0;

guesspar=[];scalefac=[];
for ii=1:npks
guesspar=[guesspar xp(ii) inty(ii) fw(ii) eta(ii)];
scalefac=[scalefac 1 a0 1 1 ];

end
guesspar=[guesspar bkgd slope];
scalefac=[scalefac a0 a0];

figure(1);
options=optimset('tolx',1e-6,'tolf',1e-2);ub=[];lb=[];

ub=Inf*ones(size(guesspar));lb=-Inf*ones(size(guesspar));

if (cflag=='y'|cflag=='Y')&(i>istart);
gbg=bkgd0/a0;gslp=slope0/a0;
guesspar(end-1)=gbg;guesspar(end)=gslp;
lb(end-1)=min([gbg 1.0000001*gbg]);ub(end-1)=max([gbg
1.0000001*gbg]);
lb(end)=min([gslp 1.0000001*gslp]);ub(end)=max([gslp
1.0000001*gslp]);
end;

% This is the previous least-square fitting taking the "error" in
account;
%a=lsqcurvefit(@pv_matfit_sb,guesspar,tth,counts./err,lb,ub,options);

% This is the fitting line, the result 'a' has been scaled down on
the
% intensity column
a=lsqcurvefit(@pv_matfit_sb,guesspar,tth,counts,lb,ub,options);

% Calculate the errors from the alpha matrix;
edyda=pvdf_matfit_sb(tth,0,a,0,'dum');
%for ierr=1:size(edyda,2);edyda(:,ierr)=edyda(:,ierr)./err;end;
%Would this be ok? just erasing the /err?;
for ierr=1:size(edyda,2);edyda(:,ierr)=edyda(:,ierr);end;
alpha=(edyda' * edyda);
ae = diag(sqrt(alpha.^-1))';

%plot(tth,counts,'b+');hold on; plot(tth,pv_matfit_sb(a,tth).*err,'r-

```

```

');hold off;
plot(tth,counts,'b+');hold on; plot(tth,pv_matfit_sb(a,tth),'r-
');plot(tth,pv_matfit_sb(a,tth)-counts,'g-');hold off;
legend('Experimental Data','Fitting','Residuals');
%diff=counts-pv_matfit_sb(a,tth)

sera=max(counts);
sera2=max(pv_matfit_sb(a,tth));
resta=sera-sera2;

titl=['Spectrum no. ' int2str(i)];title(titl);

a=a.*scalefac;ae=ae.*scalefac;

if i==istart;slope0=a(end);bkgd0=a(end-1);end;

%test;
aout=[aout;a];

aeout=[aeout;ae];
%end test;

drawnow;

%disp(['Done spectrum ' int2str(i) ', chisq = ' num2str(chi2)]);
end

%
%
% OUTPUT
%
%!echo %runnum 2theta err intensity err fwhm err eta err bkgd slope >
temp2
output_suffix=input('Output Suffix: ','s');

runlist=[istart:iend]';
for i=1:npks;
    data_exp=runlist;
    for j=1:4;
        ind=4*(i-1)+j;
        data_exp=[data_exp aout(:,ind) aeout(:,ind)];
    end
    data_exp=[data_exp aout(:,end-1) aout(:,end)];

    %save temp data_exp -ascii;
    %eval(['!cat temp2 temp > ' froot 'fits.pk' int2str(i)]);

    filename=[froot output_suffix '_' int2str(i) '.csv'];
    dlmwrite(filename, data_exp, 'delimiter', '\t', 'precision',
'%.8f');
end

%!rm temp temp2

```